

---

***Microfluidic construction and operation of artificial cell  
chassis encapsulating living cells and pharmaceutical  
compounds towards their controlled interaction***

---

A thesis submitted to Cardiff University in candidature for the degree of

Doctor of Philosophy



**By Pantelitsa Dimitriou, BSc, MSc**

School of Engineering

Cardiff University

United Kingdom

**February 2023**



---

# Abstract

Droplet-based microfluidic devices can generate complex, soft-matter emulsion systems towards drug screening applications and artificial cell membrane studies. This thesis investigates a methodology for the eventual ‘programmed’ release of pharmaceuticals to treat breast cancer cells that are encapsulated and cultured within small diameter (<2 mm), artificial cell chassis hydrogel capsules. A pharmaceutical analogue was compartmentalised within smaller, membrane-bound, inner cores, that are arranged inside the overall hydrogel capsule. The membrane was based upon droplet interface bilayers (DIBs), which are widely employed for the study of artificial cell membrane transport properties. The whole capsule and contents were produced using enclosed 3D-printed multi-material, microfluidic devices. Methods to control the (programmed) release of compounds from the inner cores to the hydrogel shell, were investigated. The application-specific study was used as an exemplar for a more generally applicable model system.

Monolithic microfluidic devices were fabricated using 3D printing and filaments of cyclic olefin copolymer (COC) and nylon for the production of single, double and triple emulsions. With these devices, monodispersed single-emulsion microgels suitable for cell encapsulation were produced, whilst dual-junction devices generated double-emulsion capsules with a controlled number of oil cores. Multi-junction devices also produced triple emulsion, encapsulated droplet interface bilayers (eDIBs), which were subsequently monitored and characterised. Additionally, to demonstrate the ability of eDIBs to act as programmed pharmaceutical delivery systems, assays were performed to induce core release, using membrane modulation by lysolipids (LPC). Computational simulations and DIB electrophysiology experiments were performed to investigate the effect of LPC on the system. MCF-7 model breast cancer cells were encapsulated in alginate-collagen emulsion capsules and their viability was assessed. Moreover, multicellular tumour spheroids (MCTSs) in oil core microgels showed no response to tested doxorubicin concentrations, while proliferated at certain LPC concentrations. Encapsulated cells in eDIBs formed tumour spheroids, however, the DIB survival was low. The integration of living cells and artificial cell membranes within a single entity presents a hybrid model for studying their interaction, towards applications in synthetic biology and drug delivery/screening.

---

# Acknowledgements

First, I would like to thank my supervisor Prof. David Barrow for welcoming me to his laboratory, giving me the opportunity to carry out this research and guiding me through the past three years. I would also like to express my sincere gratitude to my supervisor Dr. Jin Li, for his day-to-day guidance and his help with introducing me to the field of microfluidics and 3D printing, when I first joined the program. They both encouraged me to become an independent researcher and explore my curiosities and interests. I am also appreciative for the opportunity they gave me to travel to the University of Trento in Italy to work with other researchers as part of the ACDC EU Horizon 2020 Project.

Major thanks to Dr. Oliver Castell and Dr. David Jamieson from the School of Pharmacy, for inviting me to the Castell group meetings during the final year of my project, which were remarkably insightful for my project. I would also like to thank Prof. Matthew Smalley and Dr. Giusy Tornillo for welcoming me to their cell culture facilities at the European Cancer Stem Cell Research Institute. I would like to thank Prof. Adrian Porch for giving me the opportunity to co-manage MEng projects and Prof. Arwyn Jones, for the fruitful discussions about the prospects of this project.

I would also like to thank Prof. Martin Hanczyc for the warm welcome to the ACDC Project and Dr. Catrin Williams for lending me cell culture equipment when they were needed the most.

The final year of my PhD project became more fun after getting to know some of my colleagues, which I would like to mention, including Matthew Colborne, Sofia Mavridou, Hind Alqahtani and Hannah Baird. With these people, I was not only able to share a laugh but also some insightful scientific discussions.

Thank you to Ryan, for your absolute patience and unconditional love. You always believed in me and for that, I am grateful.

Finally, Mum and Dad, thank you for your support, even from thousands of miles away, and thank you for making me the person and scientist I am today.

---

# Table of Contents

<b>Abstract</b> .....	<b>i</b>
<b>Acknowledgements</b> .....	<b>ii</b>
<b>Table of Contents</b> .....	<b>iii</b>
<b>Table of Figures</b> .....	<b>viii</b>
<b>List of Abbreviations</b> .....	<b>xiii</b>
<b>Chapter I</b> .....	<b>1</b>
<b>Introduction and literature review</b> .....	<b>1</b>
<b>1.1. Biological lipid membranes</b> .....	<b>2</b>
1.1.1. Phospholipids.....	3
1.1.2. Membrane Fluidity.....	4
<b>1.2. Lipid-based artificial cells</b> .....	<b>5</b>
1.2.1. Bottom-up artificial cells .....	5
1.2.2. Lipid vesicles as artificial cells .....	7
1.2.2.1. Vesicle fabrication .....	7
1.2.2.2. Lipid-based artificial cells.....	9
1.2.3. Liposomes as drug carriers .....	12
1.2.3.1. Stimuli-responsive liposomes .....	12
1.2.3.2. Tumour-Targeted liposomes.....	13
<b>1.3. Artificial cell membranes models</b> .....	<b>14</b>
1.3.1. Supported Lipid Bilayers (SLBs).....	14
1.3.2. Droplet-Hydrogel Bilayers (DHBs).....	14
1.3.3. Droplet-interface bilayers (DIBs) .....	15
<b>1.4. Artificial cell and living cell interactions</b> .....	<b>19</b>
<b>1.5. Breast Cancer</b> .....	<b>22</b>
1.5.1. Breast cancer cells.....	22
1.5.2. Hydrogel-based 3D cultures .....	24
1.5.2.1. Alginate.....	26
1.5.2.2. Collagen.....	27
<b>1.6. Microfluidics</b> .....	<b>28</b>
1.6.1. Droplet microfluidics .....	28
1.6.2. Droplet-forming geometries.....	30
1.6.2.1. T-junction.....	30
1.6.2.2. Flow-focusing .....	31
1.6.2.3. Co-flow junction .....	32

---

1.6.3. Applications of droplet microfluidics .....	33
1.6.3.1. Multiple emulsion production.....	33
1.6.3.2. Artificial cell DIB models.....	35
1.6.3.3. Cell encapsulation.....	35
1.6.3.4. Nanoparticle production .....	37
<b>1.7. 3D printing .....</b>	<b>38</b>
<b>1.8. Conclusion and scope of thesis.....</b>	<b>40</b>
<b>1.9. References.....</b>	<b>42</b>
<b>Chapter II .....</b>	<b>76</b>
<b>Fused Filament Fabricated (FFF) microfluidic devices for single, double, and triple emulsion hydrogel capsules .....</b>	<b>76</b>
<b>2.1. Chapter summary .....</b>	<b>76</b>
<b>2.2. Introduction.....</b>	<b>77</b>
<b>2.3. Materials and Methods.....</b>	<b>79</b>
2.3.1. Contact angle of COC and Nylon .....	79
2.3.2. Microfluidic device design, fabrication and operation .....	80
2.3.3. Production of Hydrogel capsules (H/O) using SE-MD .....	81
2.3.4. Production of Oil-in-Hydrogel capsules (O/H/O) using DE-MD .....	82
2.3.5. Production of Water-in-Oil-in-Hydrogel eDIB capsules (W/O/H/O) using TE-MD .....	82
<b>2.4. Results and Discussion .....</b>	<b>83</b>
2.4.1. Selection of filament materials .....	83
2.4.2. Contact angle (CA) measurements of COC and Nylon .....	83
2.4.3. Single emulsion microfluidic device (SE-MD) .....	85
2.4.3.1. Droplet frequency production.....	85
2.4.3.2. Hydrogel diameter .....	86
2.4.4. Double emulsion microfluidic device (DE-MD) .....	88
2.4.4.1. Single-core O/H/O .....	88
2.4.4.2. Multi-core O/H/O .....	90
2.4.5. Triple emulsion microfluidic device (TE-MD).....	93
2.4.5.1. CAD geometry dimensions Vs 3D-printed dimensions.....	94
2.4.5.2. eDIB formation, from the inside-out .....	96
2.4.5.2.1. 1 <sup>st</sup> droplet-forming junction .....	96
2.4.5.2.2. 2 <sup>nd</sup> droplet-forming junction .....	98
2.4.5.2.3. 3 <sup>rd</sup> droplet-forming junction and eDIB protocol optimisation .....	99
<b>2.5. Conclusion .....</b>	<b>104</b>
<b>2.6. References.....</b>	<b>105</b>

---

---

<b>Chapter III.....</b>	<b>112</b>
<b>Characterisation, post-processing and in-situ content release activation from encapsulated Droplet Interface Bilayer synthetic cell interiors.....</b>	<b>112</b>
<b>3.1. Chapter summary.....</b>	<b>112</b>
<b>3.2. Introduction.....</b>	<b>113</b>
<b>3.3. Materials and Methods.....</b>	<b>115</b>
3.3.1. Imaging of eDIBs.....	116
3.3.1.1. EVOS.....	116
3.3.1.2. OCT.....	116
3.3.2. Stability of eDIBs.....	116
3.3.3. eDIB core release using LPC.....	117
3.3.3.1. Leakage assay based on fluorescence decrease.....	117
3.3.3.2. Leakage assay based on fluorescence increase.....	117
3.3.4. COMSOL simulations on the LPC diffusion and core release.....	117
3.3.5. DIB electrophysiology.....	119
<b>3.4. Results and Discussion.....</b>	<b>120</b>
3.4.1. Encapsulated Droplet Interface Bilayer (eDIB) characterisation.....	120
3.4.2. Optical Coherence Tomography (OCT) imaging of eDIBs.....	123
3.4.3. Centrifugation and temperature stability tests.....	126
3.4.4. Active core content release assays using lysophosphatidylcholine (LPC).....	129
3.4.5. The effect of low LPC concentrations (1 $\mu$ M and 10 $\mu$ M) on eDIBs.....	133
3.4.6. COMSOL simulations on the LPC transport and core release in an eDIB-like design.....	135
3.4.6.1. Threshold concentration for core release activation (2D).....	136
3.4.6.2. Porosity of the hydrogel shell (2D).....	137
3.4.6.3. Hydrogel shell thickness ( $t_H$ ) (2D).....	138
3.4.6.4. 3D simulation.....	141
3.4.6.5. Practical versus computational results.....	142
3.4.7. DIB electrophysiology.....	144
<b>3.5. Conclusion.....</b>	<b>150</b>
<b>3.6. References.....</b>	<b>151</b>
<b>Chapter IV.....</b>	<b>157</b>
<b>From primary to tertiary emulsion microcapsules for tumour-related studies and potential compartmentalised drug screening capsules.....</b>	<b>157</b>
<b>4.1. Chapter summary.....</b>	<b>157</b>
<b>4.2. Introduction.....</b>	<b>158</b>

---

---

<b>4.3. Materials and Methods.....</b>	<b>160</b>
4.3.1. Cell Culture.....	160
4.3.2. Microfluidic device fabrication.....	160
4.3.3. Reagent preparation for microfluidic experiments .....	160
4.3.4. Microfluidic setup and production of cell-laden capsules .....	161
4.3.5. Cell counting and encapsulation matrix preparation.....	161
4.3.6. Culturing the cell-laden capsules.....	162
4.3.7. Cell proliferation assays and drug treatments .....	162
4.3.7.1. MCF-7 culture in ALG, ALGCOL and ALGCOL OCCs .....	162
4.3.7.2. DOX <sub>IC50</sub> and LPC <sub>IC50</sub> determination of MCF-7 2D cultures .....	163
4.3.7.3. DOX and LPC treated 3D cultures in vesALGCOL OCCs .....	163
4.3.8. Tf-488 ligand treated MCF-7 cultures .....	163
4.3.8.1. 2D culture .....	163
4.3.8.2. 3D culture in OCCs.....	164
4.3.9. Live/dead Cytotoxicity Assay.....	164
4.3.10. Light Sheet Fluorescent microscopy (LSFM).....	164
4.3.11. EVOS fluorescent imaging .....	165
4.3.12. Statistical Analysis.....	165
<b>4.4. Results and Discussion .....</b>	<b>166</b>
4.4.1. Microfluidically produced cell-laden single emulsion microgels.....	166
4.4.2. ALG, ALGCOL and ALGCOL OCCs .....	168
3.3.1.3. MCF-7 culture and spheroid formation in ALG, ALGCOL and ALGCOL OCCs .....	168
3.3.1.4. CellTiter Blue (CTB) Metabolic Assay of MCF-7 cells.....	171
3.3.1.5. LSFM live/dead cell staining and intensity quantification .....	172
4.4.3. Oil-core capsules (OCCs) as a novel 3D culture model .....	176
4.4.4. Vesicle-containing, alginate-collagen type I oil-core capsules (vesALGCOL OCCs).....	177
4.4.4.1. Doxorubicin treatment .....	178
4.4.4.2. Lysophosphatidylcholine treatment .....	180
4.4.4.3. Transferrin-488 (Tf-488) labelling of 2D and 3D cultures .....	182
4.4.5. Cell and Droplet Interface Bilayer (DIB) fate in eDIBs capsules.....	184
4.4.5.1. Live/dead staining of MCF-7-laden eDIBs.....	186
4.4.6. The ‘Droplet Incubator’ and its applications .....	193
<b>4.5. Conclusion .....</b>	<b>195</b>
<b>4.6. References.....</b>	<b>196</b>
<b>Chapter V .....</b>	<b>207</b>
<b>Concluding remarks .....</b>	<b>207</b>

---

---

<b>5.1. Summary of findings .....</b>	<b>207</b>
5.1.1. Fused Filament Fabricated (FFF) microfluidic devices for single, double, and triple emulsion hydrogel capsules.....	207
5.1.2. Characterisation, post-processing and in-situ content release activation from encapsulated Droplet Interface Bilayer synthetic cell interiors.....	208
5.1.3. From primary to tertiary emulsion microcapsules for tumour-related studies and potential compartmentalised drug screening capsules.....	210
<b>5.2. Future work.....</b>	<b>212</b>
5.2.1. Short-term future work .....	212
5.2.2. Long-term future work.....	213
<b>5.3. Concluding statement.....</b>	<b>216</b>
<b>Appendices.....</b>	<b>219</b>

---

# Table of Figures

## Chapter I

Figure 1. 1: Examples of phospholipids categorised by their shape and curvature. ....	3
Figure 1. 2: Construction of artificial or synthetic cells divided into the top-down and bottom-up approaches.....	6
Figure 1. 3: Fabrication methods for lipid GUVs. ....	8
Figure 1. 4: Bottom-up constructed vesicles as artificial cell membrane models.....	11
Figure 1. 5: Methods for fabricating artificial lipid bilayer membrane models. ....	15
Figure 1. 6: DIB-based multisomes for artificial cell membrane studies.....	18
Figure 1. 7: Protocell-living cell interaction models using various approaches. ....	21
Figure 1. 8: Schematic of the breast tissue and formation of carcinoma. ....	23
Figure 1. 9: Tissue culture morphology in 2D versus 3D (scaffold and scaffold-free). ....	24
Figure 1. 10: Alginate crosslinking using divalent cations of calcium ( $\text{Ca}^{2+}$ ). ....	26
Figure 1. 11: Droplet formation using the T-junction at the three different flow-regimes. ....	30
Figure 1. 12: Droplet formation using flow-focusing junctions. ....	31
Figure 1. 13: Droplet formation with co-flow microfluidic junctions. ....	32
Figure 1. 14: Illustrations showing single and complex emulsions of different structures.....	33
Figure 1. 15: Diverse microfluidic devices for producing complex emulsions. ....	34
Figure 1. 16: Cell encapsulation using droplet-forming microfluidic devices and applications.....	36
Figure 1. 17: Schematics of stereolithography (SLA) and fused filament fabrication (FFF) 3D printing methods.....	39

## Chapter II

Figure 2. 1: Contact angle (CA) setup. ....	79
Figure 2. 2: Flow chart showing the fabrication steps of 3D-printed devices ..... 81	81
Figure 2. 3: The smooth and rough surfaces of the 3D-printed parts and the CA of COC and Nylon substrates.....	84
Figure 2. 4: SE-MD experimental device, setup and droplet production affected by the inlet flow rates. ....	85
Figure 2. 5: Images of different microgels produced using SE-MD and various flow rate ratio combinations.....	86
Figure 2. 6: The effect of various flow rate combinations on microgel production using 3D-printed SE-MD, further analysis of monodispersity and correlation between droplet frequency and diameter .....	87

---

Figure 2. 7: DE-MD experimental setup and device dimensions for single oil-core hydrogel-shell production .....	89
Figure 2. 8: Production of multi-core O/H/O capsules using the DE-MD and the effect of different flow rates on the number of encapsulated cores.....	91
Figure 2. 9: Images of various single and multi-core capsules produced using DE-MD.....	92
Figure 2. 10: The final TE-MD and its dimensions utilised for triple emulsion capsule and eDIB formation.....	93
Figure 2. 11: Microscopy images of the 3D-printed, COC, TE-MD channels and comparisons with the CAD assigned dimensions .....	94
Figure 2. 12: 3D printing infill patterns and nozzle travel of cylinder geometries .....	95
Figure 2. 13: Calcein/buffer droplet formation in 12.5 mg/ml DOPC/Hex (W/O) at the 1 <sup>st</sup> droplet-forming junction of the TE-MD.....	96
Figure 2. 14: COC microfluidic component of the TE-MD consisting of the 1 <sup>st</sup> junction for DIB formation, and the serpentine for lipid monolayer/bilayer assembly (dashed line box) .....	97
Figure 2. 15: Nylon microfluidic component of the TE-MD responsible for enclosing the DIBs in single oil droplets, by an alginate phase .....	98
Figure 2. 16: Schematics of the microfluidic channel sequence without and with DPPC vesicles, starting from the lipid monolayer assembly to the DIB formation, encapsulation and eDIB production.....	99
Figure 2. 17: Time-lapse images of eDIB formation with different final concentration of DPPC vesicles in the alginate phase (AP3).....	101
Figure 2. 18: Microfluidically formed eDIBs using 6.5 mg/ml final DPPC concentration in alginate shell and 30 mg/ml DOPC in Hex as the middle oil phase .....	101
Figure 2. 19: Images of eDIBs created using the final protocol.....	103

### Chapter III

Figure 3. 1: Photographs of the TE-MD developed in Chapter II for triple emulsion eDIB production. ....	115
Figure 3. 2: COMSOL designed geometry of the 2D model explaining the rationale behind the simulations. ....	118
Figure 3. 3: eDIBs with calcein/buffer cores produced using dual-material 3D-printed microfluidic devices. ....	120
Figure 3. 4: Merging of the inner aqueous cores encapsulated in eDIBs.....	121
Figure 3. 5: eDIB capsules with different lipid oil compositions exhibit distinct morphologies.....	122
Figure 3. 6: eDIB orthogonal views and 3D reconstructed image using OCT imaging. ....	124
Figure 3. 7: Contact angles and 3D location extracted from an individual eDIB following OCT imaging and analysis.....	125

---

Figure 3. 8: eDIBs with encapsulated cores of diameters less than 100 $\mu\text{m}$ , imaged at 0 hrs and 48 hrs after centrifugation.....	126
Figure 3. 9: eDIBs with encapsulated cores of diameters greater than 200 $\mu\text{m}$ , imaged at different timepoints after centrifugation.....	127
Figure 3. 10: Fluorescent images of eDIBs exposed to temperatures ranging from 30 to 80 $^{\circ}\text{C}$ for 30 minutes.....	128
Figure 3. 11: LPC concentration dependant release of encapsulated cores in eDIBs, according to the fluorescence decrease assay.....	130
Figure 3. 12: LPC concentration dependant release of encapsulated cores in eDIBs, according to the fluorescence increase assay.....	131
Figure 3. 13: Schematic representation of the LPC effect on the lipid bilayer of an eDIB. ....	132
Figure 3. 14: Effects of 1 $\mu\text{M}$ and 10 $\mu\text{M}$ LPC on the internal cores of eDIB.....	134
Figure 3. 15: The effect of the LPC concentration (1, 10, 100, 1000 $\mu\text{M}$ ) on the inner droplet intensity decrease, depending on the LPC threshold value defined within the model.....	137
Figure 3. 16: Diffusive flux of LPC (100 $\mu\text{M}$ ) at a point near the lipid bilayer, where the decrease of the porosity and increase of the shell thickness exhibits delayed LPC concentration build-up at the lipid bilayer .....	139
Figure 3. 17: 2D concentration contour plots at $t= 180$ min for the LPC and internal cores, resulting from different hydrogel shell thicknesses ( $t_H$ ) .....	140
Figure 3. 18: 2D and 3D simulation comparisons focusing on the LPC and inner core concentrations.. .....	141
Figure 3. 19: Plotted wet (practical) and dry (computational) laboratory data for the LPC triggered core release over 14 hours. ....	143
Figure 3. 20: DIB electrophysiology setup and control bilayer formation. ....	144
Figure 3. 21: Lipid bilayer amplification and expansion in the presence of 100 $\mu\text{M}$ LPC in the trans droplet of the DIB electrophysiology setup.....	145
Figure 3. 22: DIB electrophysiology experiments with 500 $\mu\text{M}$ and 1000 $\mu\text{M}$ of LPC in the trans droplet, resulted in bilayer failure. ....	146
Figure 3. 23: Illustration of the hypothesis related to the fusion of LPC micelles with the lipid bilayer of the DIB during electrophysiology experiments.....	148
Figure 3. 24: DIB electrophysiology current traces and occurrences under an applied potential of +/- 20 mV in buffer-buffer and buffer-100 $\mu\text{M}$ LPC.....	148
Figure 3. 25: Electrophysiology experiment on a bilayer formed between a DPPC-containing gelled alginate droplet (trans) and a 100 $\mu\text{M}$ LPC buffer droplet (cis).....	149

*Chapter IV*

---

Figure 4. 1: Light sheet fluorescent microscope sample chamber .....	165
Figure 4. 2: Analysis of the polydisperse cell-laden ALG and ALGCOL microgels .....	167
Figure 4. 3: Bright Field images of MCF-7 cells in ALG, ALGCOL and ALGCOL OCC at different timepoints, leading to tumour spheroid formation. ....	169
Figure 4. 4: MCF-7 tumour spheroid area over time starting from the 6th day of culture in ALG, ALGCOL and ALGCOL OCCs.....	170
Figure 4. 5: Graphs of the proliferation profiles of MCF-7 in ALG, ALGCOL and ALGCOL OCCs determined by the CTB metabolic assay.....	171
Figure 4. 6: LSFM images and intensity analysis relating to MCTS formation (Day 1 and 15).....	174
Figure 4. 7: LSFM images of individual MCF-7 MCTSs formed after 15 days of culture in ALG, ALGCOL and ALGCOL OCCs.....	175
Figure 4. 8: Model graph showing the higher oxygen concentration closer to the surface of the culture medium. ....	177
Figure 4. 9: Bright field images of vesALGCOL OCCs, before and after MCTS formation.....	178
Figure 4. 10: Doxorubicin response of a 2D culture and 3D cultured MCF-7 MCTSs in vesALGCOL OCCs.....	179
Figure 4. 11: Fluorescent images of control (0 $\mu$ M) and 5-day DOX treated (4.37 $\mu$ M) MCTSs in vesALGCOL OCCs.....	180
Figure 4. 12: LPC response of a 2D culture and 3D cultured MCF-7 MCTSs in vesALGCOL OCCs. ....	181
Figure 4. 13: Green fluorescent channel images (LHS) and bright-field images (RHS) of MCF-7 cells in 2D and 3D MCTS cultures, after the uptake of Tf-488. ....	183
Figure 4. 14: Bright field and dark field images of cell-laden eDIB capsules before and after MCTS formation.....	185
Figure 4. 15: Live/dead staining of MCF-7 cells in eDIBs cultured for 24 hours after encapsulation (day 1), at two different cell densities.....	187
Figure 4. 16: Multiple views of a two-core eDIB, with live/dead stained MCF-7 cells (day 1), imaged using LSFM (eDIB is embedded in agarose).....	188
Figure 4. 17: Live (green) and dead (red) stained clusters and MCTSs developed in eDIBs on days 5 and 6 of culture. ....	189
Figure 4. 18: eDIB imaged using LSFM with live(green) and dead(red) stained MCF-7 cells and MCTSs on the 8 <sup>th</sup> day of culture.....	190
Figure 4. 19: Bright field and dark field images (GFP(calcein)+TexasRed(sulfB) obtained using EVOS imaging setup.....	191
Figure 4. 20: Droplet incubator (DI) technology experimental design, summarising cell encapsulation in eDIBs (day 0), cell culture up to a desired timepoint (day 6) and subsequent activation of aqueous core release and subsequent DI readout. ....	194

---

---

*Chapter V*

Figure 5. 1: Application examples for the DI capsule, where the synthetic cell component (purple and blue cores represent two different populations) and ECM component serve diverse roles. .... 216

---

## *List of Abbreviations*

The following table lists commonly used abbreviations throughout this thesis. Some abbreviations are not listed here but are defined when first mentioned in the text.

<b>2D</b>	Two-dimensional
<b>3D</b>	Three-dimensional
<b>AR20</b>	Silicone oil
<b>C<sub>a</sub></b>	Capillary number
<b>CA</b>	Contact angle
<b>CAD</b>	Computer-aided design
<b>CMC</b>	Critical micelle concentration
<b>COC</b>	Cyclic Olefin Copolymer
<b>CV</b>	Coefficient of variance
<b>DE-MD</b>	Double emulsion microfluidic device
<b>DHB</b>	Droplet hydrogel bilayer
<b>DIB</b>	Droplet Interface Bilayer
<b>DNA</b>	Deoxyribonucleic acid
<b>DOPC</b>	Dioleoyl-phosphatidylcholine
<b>DOX</b>	Doxorubicin
<b>DPhPC</b>	Diphytanoyl-phosphatidylcholine
<b>DPPC</b>	Dipalmitoyl-phosphatidylcholine
<b>ECM</b>	Extracellular Matrix
<b>eDIB</b>	encapsulated Droplet Interface Bilayer
<b>Em</b>	Emission wavelength
<b>Ex</b>	Excitation wavelength
<b>FDM</b>	fused deposition modelling
<b>FFF</b>	Fused Filament Fabrication
<b>GUVs</b>	Giant unilamellar vesicles
<b>Hex</b>	Hexadecane
<b>IVTT</b>	In-vitro transcription translation
<b>LPC</b>	Lysophosphatidylcholine
<b>LSFM</b>	Light sheet fluorescent microscopy
<b>LUVs</b>	Large unilamellar vesicles
<b>MCTS</b>	Multicellular Tumour Spheroid
<b>MScL</b>	Mechanosensitive channel

---

<b>OCT</b>	Optical coherence tomography
<b>PC</b>	Phosphatidylcholine
<b>PDMS</b>	Polydimethylsiloxane
<b>PE</b>	Phosphatidylethanolamine
<b>PLA</b>	Poly(lactic acid)
<b>PLA<sub>2</sub></b>	Phospholipase A <sub>2</sub>
<b>PMMA</b>	Polymethylmethacrylate
<b>PS</b>	Phosphatidylserine
<b>PVA</b>	Polyvinyl alcohol
<b>Q<sub>c</sub></b>	Flow rate of the continuous phase
<b>Q<sub>d</sub></b>	Flow rate of the dispersed phase
<b>SE-MD</b>	Single emulsion microfluidic device
<b>SLA</b>	Stereolithography
<b>SLBs</b>	Supported lipid bilayers
<b>SUVs</b>	Small unilamellar vesicles
<b>TE-MD</b>	Triple emulsion microfluidic device
<b>T<sub>m</sub></b>	Phase Transition Temperature
<b>UV</b>	Ultraviolet
<b>αHL</b>	Alpha-hemolysin
<b>γ</b>	Surface tension

# *Chapter I*

## *Introduction and literature review*

---

Engineered systems inspired by biology are often employed in the fields of cell mimicry and tissue culture models. Cell mimicry focuses on the imitation of native cellular structures and functionalities, through miniaturised artificial systems, using non-living engineered materials (bottom-up)<sup>1</sup>. These systems are usually referred to as artificial cells, synthetic cells or protocells. Tissue culture models, on the other hand, utilise bioinspired materials to fabricate artificial environments with similar properties to the native environments of living cells<sup>2</sup>. Thus, one field focuses on the construction of artificial cells, while the other focuses on the creation of artificial extracellular environments.

One of the primary constituents of biological membranes and widely used in bottom-up artificial cell construction is the phospholipid membrane. The assembly of synthetic phospholipid membranes produces robust cell-mimicking models, including lipid vesicles (or known as liposomes), and isolated phospholipid cell membranes. Some of the aims of such models include the study of autonomous cellular functionalities and the investigation of membrane/bilayer interplay and their interaction with drug molecules<sup>3,4</sup>. Many seek to investigate communication routes between protocells and living cells by developing hybrid models<sup>5</sup>, however only a handful of published work focuses on the interaction with cultured tissues.

One primary aim of tumour tissue culture models is to combat drug resistance, an underlying challenge related to cancer progression and metastasis<sup>6</sup>. Bioinspired hydrogels can resemble the dynamics of biological tissues<sup>7</sup>, hence can recreate the *in-vivo* tumour microenvironment, artificially. So far, drug-laden liposome treatments are the main form of lipid-based artificial cells which have established interactions with cultured tumours<sup>8</sup>.

Droplet microfluidics is an important enabler towards the automation and high yield of *in-vitro* platforms<sup>9,10</sup>. While high-resolution microfluidic devices are costly and require advanced technical skills and labour, 3D printing offers a tool, though at lower resolution and accuracy, for rapid device fabrication to simplify the process of a prototype development. The following paragraphs examine the bottom-up construction of lipid-based artificial cell models and their contribution in applications, such as synthetic biology and their interaction with living cells. An overview of the development of three-dimensional tumour formation and support materials often used, is also provided. Some applications of droplet microfluidics are discussed, including, the production of multiple emulsions, droplet interface bilayers (DIBs) and cell encapsulation for cancer studies. Finally, examples of common 3D printing methods are briefly discussed, as an introduction to Chapter II of this thesis.

## 1.1. Biological lipid membranes

Cells were first discovered by Robert Hooke in 1665 and later on, around the 1830s, Schleiden and Schwann, established that cells are the primary unit of any living entity on planet Earth <sup>11</sup>. The contents of biological cells are held within a semi-permeable membrane composed of lipids, proteins and carbohydrates, known as plasma membrane. This encloses the cytoplasm and organelles such as mitochondria, which are energy-producing organelles, the nucleus that holds the genetic material (DNA) and ribosomes, which facilitate protein synthesis. Some organelles have their own semi-permeable membrane. The ratio of the membrane components (e.g., lipids and proteins) is variable between organisms and their location within the organism. For example, the amount of proteins and lipids in the plasma membrane of most mammalian cells, is roughly the same (~ 50 %), while the ratio of proteins to lipids in the mitochondrial membranes is higher <sup>12-14</sup>.

The cellular membranes have fluid properties to allow lateral diffusion of proteins and lipids, and medial diffusion of molecules, therefore the study of their interactions is essential. Phospholipids are amphiphilic molecules, meaning they possess a hydrophilic and a hydrophobic region, and hold a large fraction of the total lipids in the membrane. The organisation of proteins and lipids within the membranes guides cells to execute a series of functions, such as the activation of extracellular and intracellular signalling pathways and the stimulation of morphological changes, including cell migration and division <sup>15</sup>. Levental and Lyman 2022, discussed how amphiphilic proteins prefer to be surrounded by phospholipids with a well-matched hydrophobic thickness <sup>16</sup>. Phospholipids reorganise to match the tension and packing of the protein nano-environment required for protein conformational changes, which in turn mediate cellular functions.

Phospholipids along with other lipids (sphingomyelin, glycolipids, cholesterol) are assembled in lipid monolayers. The cellular membrane comprises of two lipid monolayers, known as the lipid bilayer, which holds the membrane's components. Cellular membranes permit the exchange of nutrients and gas via passive diffusion, or via interactions of molecules (ions and ligands) with membrane proteins <sup>3</sup>. Some extracellular molecules can interact with the cell's surface, and via receptor-mediated endocytosis, cells can uptake molecules and ligands into their cytoplasm by inward membrane budding. Therefore, the biological lipid membrane regulates communication between the extracellular and the intracellular environment, through the exchange of information. The well-orchestrated cellular pathways, as well as the complexity of cell membranes and compartmentalised organelles, raise scientific questions related to their nature, specificity and interactions with environmental cues. Thus, research fields, including, but not limited to, synthetic biology, biophysics, engineering and molecular biology, aim to develop novel systems for better understanding the nature and functions of cells.

### 1.1.1. Phospholipids

Phospholipids, which constitute a major element of biological membranes, are amphiphilic molecules with a polar phosphate headgroup (hydrophilic) and non-polar (hydrophobic) fatty acid tails. In an aqueous solution, phospholipids self-arrange to shield the hydrophobic tails and expose the headgroup. But, when surrounded by a non-polar solvent (e.g. hydrocarbon and oils), the hydrophobic tails of phospholipids are exposed and self-assembled to shield the polar headgroup. Phospholipids may possess a negative charge, or be zwitterionic with zero net charge.

Phosphatidylcholine (PC), phosphatidylethanolamine (PE) and phosphatidylserine (PS) are three examples of phospholipids found in the cell membrane of animal and plant cells. At physiological pH, PC and PE are zwitterionic, while PS is negatively charged. Lipids and phospholipids self-assemble into different molecular shapes depending on their structure and environment. This is known as lipid polymorphism and it is a characteristic that can influence the stress, pressure and shape of lipid membranes<sup>15</sup>. When phospholipids are isolated into polar (water) and non-polar (oils) solvents, they organise into distinct structures, and one key factor is the head-to-tail volume ratio. For example, PC and PS self-assemble into lamellar lipid bilayers upon hydration, due to their cylindrical shape (no curvature) (**Figure 1.1A**)<sup>17</sup>. On the other hand, PE has a smaller head group, leading to lipid membranes with conical structures (negative curvature) (**Figure 1.1C**). This arrangement of PE phospholipids is

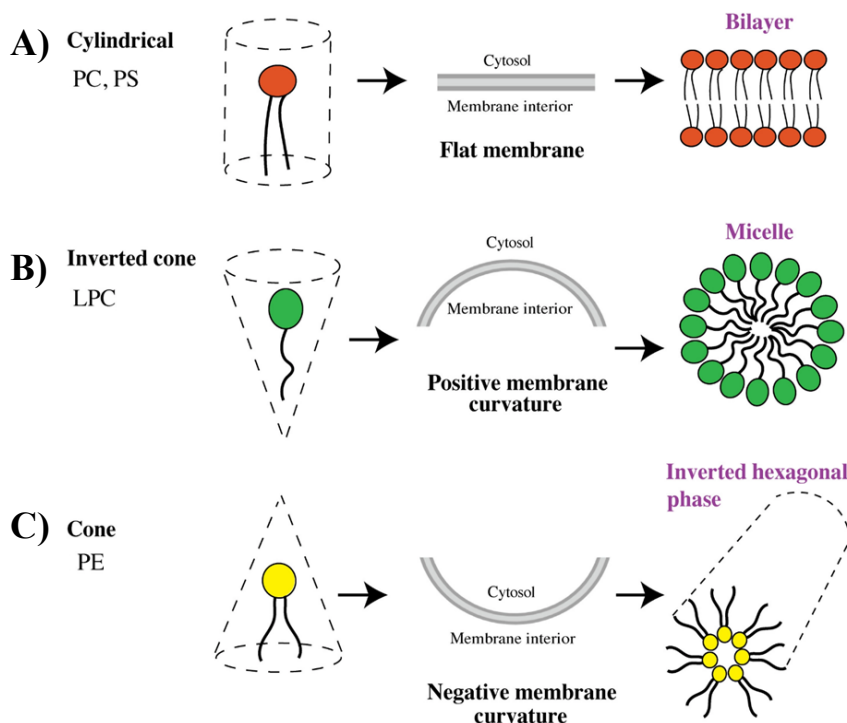


**Figure 1.1:** Examples of phospholipids categorised by their shape and curvature. **A)** Cylindrical shaped phospholipids (PC, PS) have similar head to tail ratio which results in the formation of lamellar flat phospholipid bilayers. **B)** Phospholipids like LPC are inverted cone shaped with larger head group than the tail, forming micelles of positive curvature. **C)** PE phospholipids are cone shaped, with larger tail group than the head group, forming inverted hexagonal phase of negative curvature. Image adapted from<sup>17</sup>.

also known as an inverted hexagonal phase, which formation has been attributed to elevated temperatures and longer acyl chains<sup>18</sup>. Lysolipids, such as lysophosphatidylcholine (LPC) are phospholipids with a single hydrophobic tail and form micelles due to their inverted cone-like shape (positive curvature) (**Figure 1. 1B**).

### **1.1.2. Membrane Fluidity**

Scientists often use the Fluid Mosaic model to explain the organisation and functions of biological cell membranes. One of the characteristics of cell membranes is their fluidity and it is important for the lateral diffusion of membrane components<sup>19</sup>. The fluidity is affected by the lipid composition (saturated and unsaturated lipids), the presence of cholesterol and temperature<sup>20</sup>. Saturated phospholipids tend to have straight hydrophobic tails, while unsaturated lipids possess bent fatty acyl chains, due to the double bond between carbon atoms<sup>21</sup>. Additionally, lipid membranes with unsaturated phospholipids and phospholipids with short fatty acid tails, give rise to membranes with increased fluidity<sup>16,22</sup>. The presence of cholesterol makes a cellular membrane less fluid affecting the lateral diffusion of proteins and phospholipids<sup>23</sup>. Lastly, temperature affects the fluidity of phospholipid membranes, where phospholipids are closely packed at low temperatures and loosely packed at higher temperatures<sup>20</sup>. Therefore, phospholipids have a critical temperature, above which their physical state changes from gel to liquid, and this is known as the phase transition temperature ( $T_m$ ).

## 1.2. Lipid-based artificial cells

Artificial cells were first developed in 1957, by Thomas M. S. Chang, who captured haemoglobin and red blood cell enzymes in polymeric membranes using emulsification methods<sup>24</sup>. After this, a lot of attention was given to the fabrication of artificial cells, bringing us to an era where artificial cells are ubiquitously studied. In order for an artificial cell to signify as ‘alive’, it requires to have three main elements, including a semi-permeable membrane which allows material exchange (e.g. gas and nutrients), genetic matter for evolutionary purposes, and pathways which can energise, maintain and renew the cell, as well as process information<sup>25</sup>. Until today, no fully functional and autonomous artificial cell has been publicly reported that obtains all three features.

Additionally, artificial cells have been categorised as ‘typical’ or ‘non-typical’, depending on their internal features and morphologies. For example, the term ‘typical’ describes artificial cells which possess similar structure to living cells and can support some essential features, such as material metabolism, self-reproduction and evolution<sup>1</sup>. The term ‘non-typical’ refers to engineered materials and environments, also referred to as ‘cell mimics’, that simulate cellular characteristics of biological cells (functions, membrane, shape), without any structural restraints<sup>25</sup>.

### 1.2.1. Bottom-up artificial cells

A key aim within the research field of artificial cells is to impart new functionalities upon either engineered natural cells through a top-down approach, or using bottom-up constructed protocells from non-living elements<sup>26</sup>. In top-down approaches, the genetic material of natural cells is minimised, altered or replaced with new genetic material to obtain a ‘minimal’ cell with at least the ability to survive<sup>1</sup>. On the other hand, bottom-up approaches aim to formulate ‘living’ artificial cells using non-living materials, which increases the complexity of the system (**Figure 1.2**). The term ‘artificial cell’ is used interchangeably within the field, with other terms like, ‘synthetic cell’ and ‘protocell’, although protocells are usually developed only by bottom-up approaches. On the other hand, the terms ‘artificial’ and ‘synthetic’ are used for both bottom-up and top-down developed constructs.

Bottom-up constructed artificial cells, may be imparted with one or more cell-like features. This can be achieved through the organisation of reactions and the control of chemically-mediated communication, within internal compartmentalised structures<sup>27,28</sup>. The formation of artificial cells relies on the self-organisation of molecules, forming membrane-bound droplets with amphiphilic lipids, polymers and nanoparticles<sup>29</sup>, as well as, membrane-free systems from coacervation<sup>30,31</sup>. Hence, with amphiphilic molecules and appropriate complexes, several vesicle-based protocell models have been developed, including lipid vesicles or liposomes<sup>32</sup>, polymersomes<sup>33</sup>, proteinosomes<sup>34</sup>, colloidosomes<sup>35</sup>, and coacervates<sup>36</sup>. In the attempt to create these systems, bottom-up artificial cells have been constructed by supplying semi-permeable membranes, genetic circuit entrapment for engineering proteins and energy molecules (i.e., ATP) for the execution of metabolic reactions. The following

section reviews and discusses bottom-up constructed lipid-based vesicles, which are referred to as ‘artificial’, ‘synthetic’ cells or ‘protocells’.

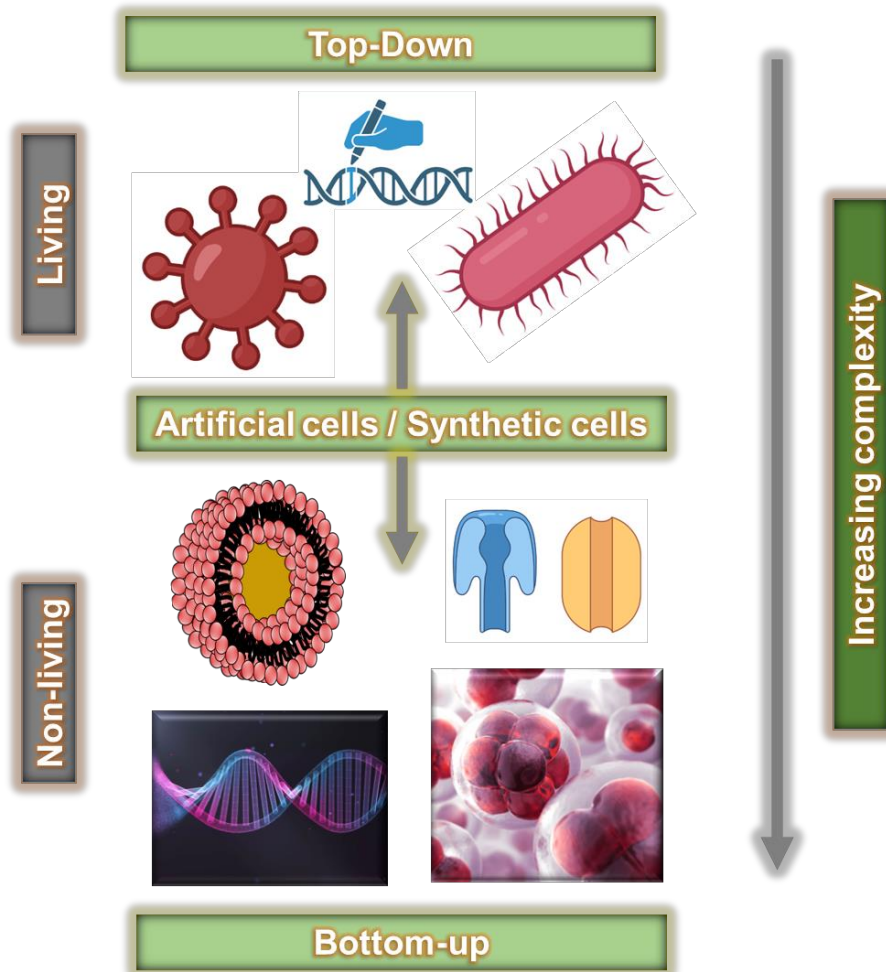


**Figure 1. 2: Construction of artificial or synthetic cells divided into the top-down and bottom-up approaches.** Top-down methods involve the editing of the genome of living organisms and is considered a less complex approach. Synthetic cells created using non-living matter (phospholipids, macromolecules, DNA, emulsion systems, polymers, etc) is described by the bottom-up strategy, which increases the complexity of the system. Most images within the figure above were created using Microsoft 365 and BioRender.com.

## 1.2.2. Lipid vesicles as artificial cells

Vesicles take part in cellular endocytosis and exocytosis, which is either the uptake or secretion of material, respectively, in the form of enclosed lipid membrane fragments. They are one of the most frequently studied structure of artificial cells and they can be fabricated in different sizes and forms. Their sizes can vary from giant unilamellar vesicles (GUVs  $> 1 \mu\text{m}$ ) to large unilamellar vesicles (LUVs, 100 nm to 1  $\mu\text{m}$ ) and small unilamellar vesicles (SUVs  $< 100 \text{ nm}$ )<sup>3</sup>. Additionally, compartmentalised formats of lipid vesicles, such as multilamellar (MLVs) and multivesicular vesicles (MVVs) also exist and often used.

The main component of these vesicles is the phospholipid molecules and for engineering artificial cells, their composition can be variable, depending on the application. The cylindrical structure of PC allows them to form stable bilayers<sup>18</sup>, hence they are used as a large fraction in most lipid-based artificial cell studies. Dioleoyl-phosphatidylcholine (DOPC), Diphytanoyl-phosphatidylcholine (DPhPC) and dipalmitoyl-phosphatidylcholine (DPPC) are widely used phospholipids for the construction and study of artificial cells and membranes. The approximate  $T_m$  of DOPC is  $-17 \text{ }^\circ\text{C}$ , of DPPC is  $41 \text{ }^\circ\text{C}$ , while there is no reported  $T_m$  for DPhPC between  $-120$  and  $120 \text{ }^\circ\text{C}$ <sup>37</sup>. Lipid vesicle formation and their application as artificial cells are discussed in the following sections.

### 1.2.2.1. Vesicle fabrication

GUVs are widely operated as artificial cell platforms, since they are of the same magnitude and diameter as biological cells. All GUV fabrication methods have in common the self-assembly of the amphiphilic molecules around an aqueous solution, which are illustrated in **Figure 1.3** These methods include the thin-film hydration method, electroformation, phase-transfer and droplet microfluidics. The hydration method and the electroformation method, utilise the same principle of membrane swelling in the presence of a buffer solution, although the latter approach has the dry lipid film deposited onto an indium tin oxide (ITO)-coated glass to which an electric field is applied<sup>3</sup>. The primary advantage of the phase transfer method is the control over the lipid composition of the inner and outer leaflets of the vesicle<sup>38</sup>, whilst miniaturised microfluidic devices offer high-throughput liposome production. Both, phase-transfer and droplet-microfluidic production of lipid GUVs are capable to control the formation of compartmentalised lipid-based artificial cell constructs<sup>39,40</sup>. Microfluidic principles, devices and applications will be discussed later in this chapter.

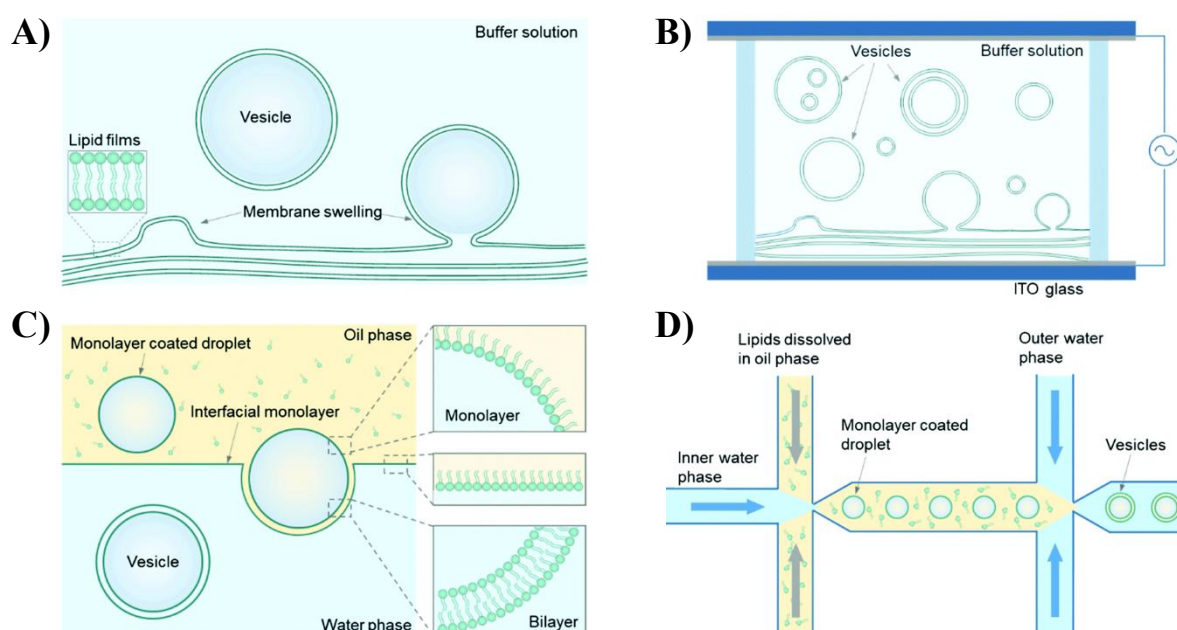


**Figure 1. 3: Fabrication methods for lipid GUVs.** *A) Thin film hydration method requires a dry lipid film, which in the presence of buffer starts to swell and form GUVs with aqueous core. B) Electroformation uses alternating current electric field to form GUVs following membrane swelling when buffer is added. C) GUVs formed using phase transfer between immiscible solutions stabilised by lipids. The transfer of a water droplet coated with a lipid monolayer to an oil- water solution with a lipid interface, can form lipid bilayers and subsequently GUVs. D) GUV production using droplet-microfluidic channels. This requires a lipid-containing oil phase which breaks up the inner aqueous phase into droplets, followed by an outer water phase for vesicle formation. Image adapted from <sup>[3]</sup>.*

### 1.2.2.2. Lipid-based artificial cells

Phospholipid vesicles take up a large proportion in the exploration of artificial cells, simply due to their mimicking properties of biological cell membranes. Designed lipid vesicles/liposomes can protect encapsulants and 'hold' transmembrane proteins to facilitate and regulate communication between the intravesicular and extravesicular environment. Despite the analogy to living cells and biocompatibility, some of their disadvantages as artificial cell membranes include increased sensitivity and permeability, reduced stability and chemical compatibility<sup>41</sup>.

Regardless, liposomes have established a baseline, paving the way into developing complex bottom-up artificial cells. One of the first scientific accomplishments in the field was the cell-free protein synthesis in liposomes, which has been extensively studied since the early 2000s<sup>42,43</sup>. Within the artificial cell research area, the protein synthesis from living cells is emulated by expressing protein pores or channels inside lipid vesicles, which subsequently assemble spontaneously into the membrane to facilitate communication across the lipid bilayer<sup>44</sup>. Additionally, in the attempt to study cell division, Kuruma, *et al.* 2009 encapsulated enzyme-producing pathways in liposomes to stimulate autonomous membrane growth<sup>45</sup>. Zhu and Szostak, 2009 demonstrated the growth of MLVs by incorporating fatty acid micelles and produced daughter vesicles through agitation<sup>46</sup>. Sakuma, *et al.* 2010, employed a temperature dependant phase-separation approach in GUVs with lipid compositions of varying curvature and  $T_m$ , to control their morphological changes (vesicle adhesion, pore formation and budding)<sup>47</sup>. These publications utilised lipid vesicles to investigate membrane dynamics, therefore, represent robust artificial cell membrane models.

In more recent years, lipid-based artificial cells have adopted more complex sequential reactions, which involve aforementioned phospholipid membranes, cell-free synthesis, transmembrane proteins and other. Such complex systems may contain *de-novo* enzymatic cascades, molecule and protein synthesis, stimulated by predefined factors similar to native cells.

Experimentally, transmembrane proteins are frequently incorporated into the membranes of lipid-based vesicle systems. Two most commonly used are, pore-forming toxin  $\alpha$ -hemolysin ( $\alpha$ HL) and mechanosensitive channels (MscL), which are derived from the bacterium of *Staphylococcus aureus* and *Escherichia coli* (*E.coli*), respectively. Enhanced insertion of  $\alpha$ HL in lipid vesicles has been associated with the presence of PC phospholipids and cholesterol<sup>48,49</sup>. Hilburger, *et al.* 2019, externally introduced micelles to liposomes encapsulating an 'inactive' form of  $\alpha$ HL (low concentrations of cholesterol) and induced enhanced core release, hence controlling the permeability of the vesicles in response to external signals (**Figure 1.4A**)<sup>50</sup>. A nested artificial cell network was reported by Hindley, *et al.* 2020, who introduced  $\alpha$ HL pores into cholesterol-free GUVs encapsulating phospholipase A<sub>2</sub> (PLA<sub>2</sub>) and additional LUVs with membrane-embedded MscL channels<sup>40</sup>. Externally added calcium ions transported through the  $\alpha$ HL pore into the lumen of the GUV, interacted with PLA<sub>2</sub> to produce

LPC lipids, which led to the opening of the MScL channel, through membrane pressure instabilities (Figure 1. 4)

Moreover, the natural protein synthesis of living cells, known as transcription-translation, is another system being explored using artificial cells<sup>51,52</sup>. While others utilise cell extracts for *in-vitro* transcription-translation (IVTT) protein expression<sup>53</sup>, Dwidar, *et al.* 2019, utilised an alternative bottom-up (from scratch) approach. He and colleagues encapsulated different IVTT systems in liposomal artificial cells, which were responsive to an externally introduced molecule that would initiate protein expression<sup>54</sup>. Eventually the liposomes, either expressed a reporter fluorescent molecule, or released small molecules through the formation of pores after expression, or were self-destructed<sup>54</sup>.

Furthermore, signal transduction between natural cells regulates cell communication, as well as autonomous behaviour and has indeed been recapitulated in protocells<sup>55,56</sup>. Artificial cell populations in the form of GUVs have been exploited to simulate cell-cell communication, through either paracrine or contact dependant signalling. An example includes the production of signalling molecules in GUVs, and their diffusion to receiver GUVs, which translated the signal into an optical readout<sup>57</sup>. As opposed to Buddingh, *et al.* 2020, signal transduction established by Chakraborty and Wegner 2021, showed a population of bioluminescent artificial cells inducing lysis of the receiving artificial cells, upon direct contact<sup>58</sup>.

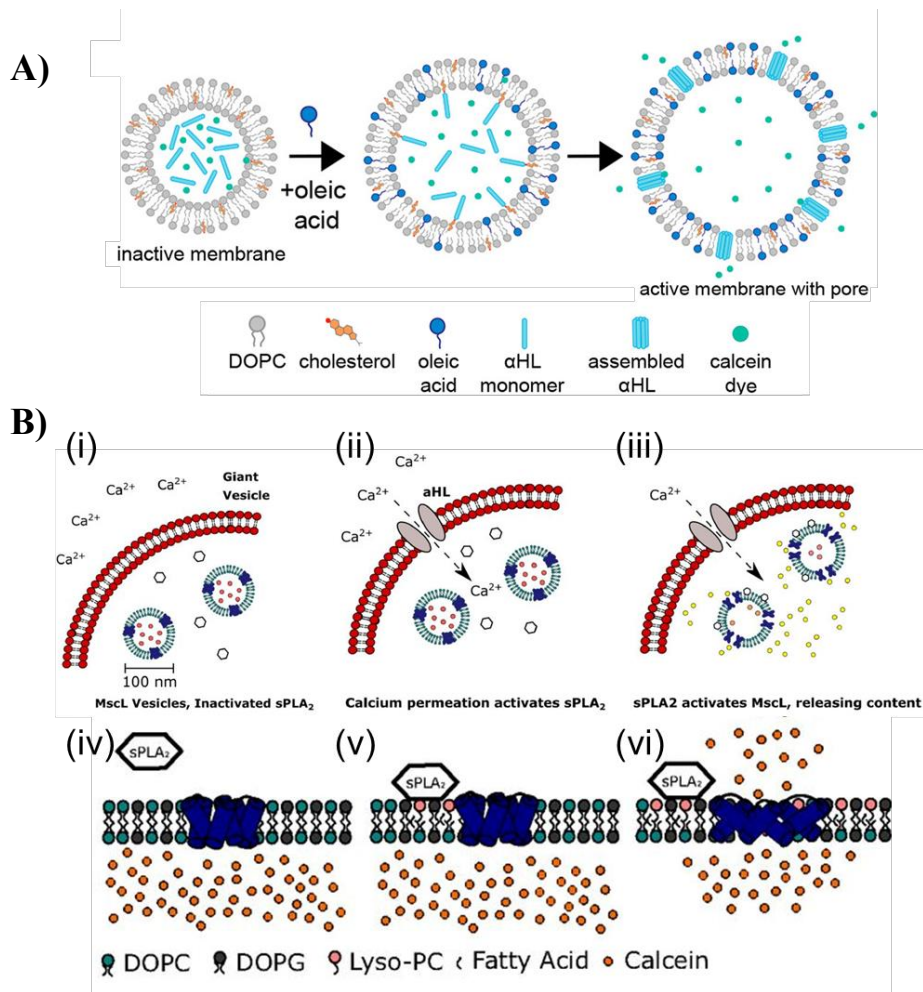


**Figure 1. 4: Bottom-up constructed vesicles as artificial cell membrane models. A)** SUVs with  $\alpha$ HL monomers (inactive) encapsulating fluorescently quenched dye, calcein. The external addition of oleic acid as micelles alters the membrane tension and induces the formation of  $\alpha$ HL pores (active), leading to enlarged vesicles and fluorescent signal, due to the release of the quenched dye. Image adapted from <sup>[50]</sup>. **B)** Nested artificial cell network of a GUV encapsulating LUVs and PLA<sub>2</sub> in its lumen. The externally added Ca<sup>2+</sup> passes into the lumen through the  $\alpha$ HL pore (i-ii), to cause the conversion of phosphatidylcholines to Lyso-PC, by PLA<sub>2</sub> (iv,v). Then, the presence of Lyso-PC in the membrane induces pressure changes and activates MscL of the LUVs to release their content (iii,vi). Image adapted from <sup>[40]</sup>.

### 1.2.3. Liposomes as drug carriers

Due to their biocompatibility, properties and adaptability, lipid-based synthetic cells, have been applied to pharmaceutical processes, where compartmentalised liposomes act as storage units and drug-vehicles<sup>59,60</sup>. Liposomes can encapsulate hydrophobic and hydrophilic drugs, which may be released in a controlled manner compared to bulk solutions, posing an effective and safe drug delivery method<sup>8</sup>. The designed drug-laden liposomes may host special agents (phospholipids and particles sensitive to environmental conditions), hence the system can be integrated with orchestrated susceptibilities, resulting to ‘turn ON’ type of engineered liposomes. These are known as stimuli-responsive liposomes. Several works demonstrated the feasibility of employing artificial cells as smart carriers in anticancer drug delivery and screening, through targeting specific cell lines using membrane functionalisation<sup>61,62</sup>. The pivotal contributor in achieving bottom-up artificial cells as drug carriers is the combination of synthetic biology and nanomedicine to engineer systems with long blood circulation, tissue site specific and sub-cellular specific characteristics, therefore targeting unhealthy tissues, while avoiding harm to healthy tissues<sup>63</sup>.

#### 1.2.3.1. Stimuli-responsive liposomes

Liposomes serve as effective drug delivery vehicles, due to their unique characteristics, such as structural fluidity, low toxicity and non-immunogenicity, making them ideal platforms for hydrophilic and hydrophobic drug encapsulation<sup>64</sup>. A broadly used example of stimuli-responsive liposomes are thermo-sensitive liposomes (TSLs), which rely upon the phase transition of phospholipids,  $T_m$ , where above this characteristic  $T_m$ , liposomal contents leak out<sup>65</sup>. The addition of lysolipids and polymers into liposomes can reduce the transition temperature to that which is much closer to physiological temperatures<sup>66,67</sup>. Some other external stimuli for inducing liposomal responses include ultrasound<sup>68,69</sup>, magnetic fields<sup>70,71</sup>, near-infrared (NIR) light<sup>72,73</sup>, and ultraviolet (UV) radiation<sup>74</sup>. Most of these rely on the heating of liposomes and the transition from the gel phase to the leaky fluid phase.

Various stimuli-responsive liposome constructs can release encapsulated content under external effects, whether they are composed of susceptible lipids, polymers, or other particles. It is of considerable importance that drug-laden and stimuli-responsive liposomes, function effectively, but simultaneously ensure that the external stimulus does not induce undesired effects upon the host tissue. Liposomes can be tailored to target specific tissues and initiate drug release locally by passive means<sup>75</sup>, based on the characteristics and expression of the targeted cells; an example includes cancerous tissue<sup>76</sup>.

### **1.2.3.2. Tumour-Targeted liposomes**

Therapies involving tumour-targeted liposomes follow either passive or active accumulation at cancerous tissues. Active accumulation is driven by the immobilisation of special ligands to liposomes, whose receptor is highly expressed at the tumour microenvironment <sup>77</sup>. Antibodies, peptides and DNA have been functionalised on liposomes and used as tumour-targeted ligands <sup>78</sup>. Some examples of overexpressed cell surface receptors in tumours include transferrin <sup>79</sup>, epidermal growth factor receptors (EGFR) <sup>80</sup> and human epidermal growth factor receptor 2 (HER-2) <sup>81</sup>. By targeting these receptors and guiding selective endocytosis and drug release upon contact <sup>82</sup>, issues associated with safety, efficacy in cancer theranostics and suffering of pre-clinical animal models can be reduced. Furthermore, the tumour microenvironment differs from normal, healthy tissues, due to its altered characteristics, such as acidic pH, higher temperatures, enhanced enzymatic activity and hypoxia <sup>83</sup>. Several researchers have developed drug-loaded, ligand-carrying liposomes that can endogenously release drugs upon contact with such characteristics <sup>76,84</sup>.

### 1.3. Artificial cell membranes models

Apart from lipid vesicles, other models have been developed to study the cell membrane, which include supported lipid bilayers (SLBs), droplet-interface bilayers (DIBs) and droplet-hydrogel bilayers (DHBs). Electrophysiology is widely used in combination with artificial cell membrane models to study membrane properties, protein pores, ionic and molecular transport<sup>85</sup>. This technique originates from the electrical properties of organs and cells, which Sakmann and Neher first established by detecting the ionic flow through single cell membranes, in 1981<sup>86</sup>. This is an essential tool combined with tailored planar lipid bilayers, SLB, DHB and DIBs<sup>87</sup>. The following sections focus on the overall fabrication and use of such cell membrane models, where more focus is paid to findings using the DIB approach.

#### 1.3.1. Supported Lipid Bilayers (SLBs)

SLBs are planar lipid bilayers formed on a solid substrate. The formation of the SLB relies on the spontaneous adsorption of vesicles on a treated substrate. Such lipid bilayer platforms are compatible with various post-processing methods which are surface sensitive including atomic force microscopy (AFM)<sup>88</sup> and fluorescence<sup>89</sup>. Vesicle fusion from a buffer solution is the most commonly used method for producing SLBs<sup>90,91</sup>, but other researchers developed alternative fabrication methods. Jackmann and Cho, 2020, presented the solvent-assisted lipid bilayer (SALB) and bicelle (mixture of short and long lipids) adsorption methods for producing SLBs on a wider variety of substrates and claimed to form SLB quicker and easier (**Figure 1. 5A**)<sup>92</sup>. Despite the limited compatibility of SLBs with solid substrates, they are still widely studied for understanding lipid membranes and bilayer functionalisation through macromolecules<sup>93</sup>.

#### 1.3.2. Droplet-Hydrogel Bilayers (DHBs)

Besides solid surfaces, thin hydrogel films have been used as a substrate for planar bilayer formation. In the presence of phospholipids in the surrounding oil, an aqueous droplet is deposited onto a hydrogel film forming a droplet-hydrogel bilayer (DHB) (**Figure 1. 5B**), which when compared to other artificial membrane models, has been reported to last for several weeks<sup>19</sup>. This method is compatible with single-molecule fluorescence microscopy<sup>94</sup>, single-channel recordings<sup>95</sup> and has been utilised for the study and activation of ion channels and large pores<sup>96,97</sup>. Modelling artificial lipid bilayers using DHBs appears to be an attractive method for developing and investigating asymmetric lipid bilayers, while incorporating proteoliposomes<sup>96</sup> and cell components into the hydrogel substrate<sup>98</sup>. Finally, the DHB experiments can be executed on a range of materials, from glass to milled poly(methyl methacrylate) (PMMA) and 3D-printed substrates<sup>99</sup>.

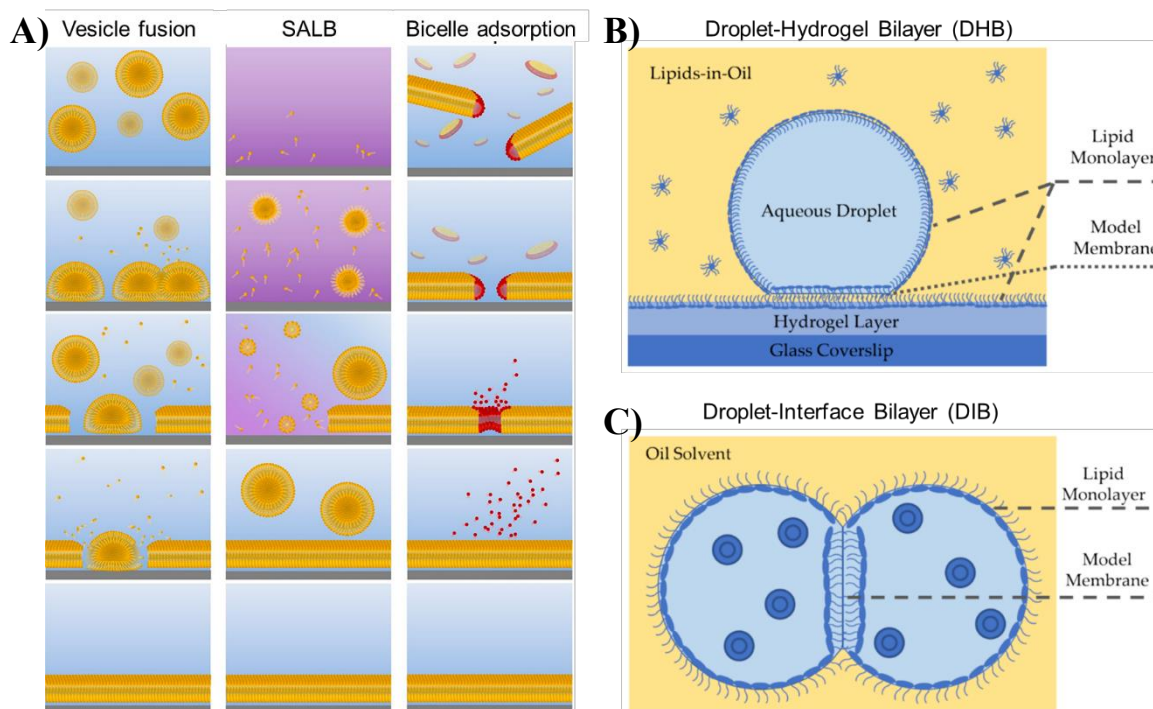


**Figure 1.5: Methods for fabricating artificial lipid bilayer membrane models.** **A)** Three approaches for forming SLBs. Vesicle fusion relies on the spontaneous adsorption of vesicles from the buffer solution onto a treated surface. SALB requires the incremental replacement of the lipid-containing organic solvent with buffer. Image adapted from [92]. Bicelle adsorption uses a suspension of bicelles formed by short (red) and long (yellow) chained phospholipids. **B)** DHB model, where the model lipid bilayer membrane is formed between a hydrogel-coated (usually agarose) glass surface and an aqueous droplet surrounded by a lipid-containing oil. Image adapted from [85]. **C)** DIB model membrane formed by two contacting aqueous droplets in the presence of lipids, either in the oil solvent or inside the droplets as vesicles (blue particles). Each droplet is coated by a lipid monolayer, when two aqueous droplets come in contact the oil is replaced and a lipid bilayer is formed. Image adapted from [85].

### 1.3.3. Droplet-interface bilayers (DIBs)

DIBs are an alternative and versatile method for fabricating artificial cell membrane models in a lipid-containing oil environment (**Figure 1.5C**). They are commonly applied and can be created using a ‘lipid-in’ or a ‘lipid-out’ approach, which describes the location of lipids in the system, whether they are inside (in the form of vesicles) or outside the droplets, respectively. Both of these approaches are also employed in DHB formation. The ‘lipid-out’ method forms identical lipid bilayer leaflets, while asymmetric bilayers can be formed using the ‘lipid-in’ approach, which is of great significance since most biological cells and organelles have distinct inner and outer leaflet compositions. Similar to DHBs, the DIBs are compatible with electrical recordings, however they are not compatible with single-molecule fluorescence microscopy<sup>100</sup>. DIB resembles a standard procedure and the simplest model for studying the electrical activity through nanometre-thick lipid membranes with varying lipid and protein compositions.

Symmetric and asymmetric bilayer formation in DIBs offers a robust and facile method for probing artificial cell membranes. Many studies have focused on the examination of lipid compositions and the implementation of ion channels and transmembrane pores. For example, asymmetric DIBs

rendering oppositely charged leaflets were investigated in the presence of a transmembrane outer membrane protein (OmpG) and showed how gating effects were more active when the protein was inserted from the negatively charged leaflet <sup>101</sup>. More recently, Lee and Bayley, 2022, showed that the orientation of another transmembrane protein (OmpF) inserted into an asymmetric DIB was independent of the lipid composition and that the translocation of a toxin through the pore dependent on the presence of lipopolysaccharides <sup>4</sup>. In earlier years, an attempt was made to reconstruct double membranes, which are highly relevant in the study of gram-negative bacteria <sup>100</sup>, while more recently, Allen, *et al.* 2022 reported a method for emerging multi-layered DIBs <sup>102</sup>. The concept of multi-layered membranes was applied in vesicles <sup>103</sup>, but yet, there have not been claims of a functional multi-layered DIB model membrane, with additional cell-mimicking characteristics.

Free of transmembrane protein pores DIB translocation studies have also been carried out <sup>104</sup>. The translocation of small molecular weight substances depends on the degree of permeability through the membrane of living cells. Therefore, researchers utilised DIB systems to show the dependence of permeability on the phospholipid structure and composition (saturated or unsaturated acyl chain, charged or uncharged head) and also reported that results vary according to the oil solution used <sup>105</sup>. Fluorescence microscopy is compatible and widely utilised with the DIB devices, however it requires labelling agents. Recently, in the attempt to develop a pharmaceutically compatible, label-free, DIB platform, Strutt, *et al.* 2022, studied the permeability of compounds, using a UV detection device integrated with a DIB system <sup>106</sup>.

Additionally, droplets surrounded by lipid monolayers can be arranged in a series, or in arrays, to form DIB networks. These facilitate a network of sequential reactions, in which transport of molecules is assisted by the presence of transmembrane proteins or passive diffusion. Others have utilised magnetic particles to dynamically manipulate the rearrangement of a DIB network, in order to form new membranes *in-situ* <sup>107</sup>. Such external manipulation can potentially act as a reaction initiator. Magnetic manipulation was also established by Li, *et al.* 2022, where a levitated DIB network was magnetically locked to activate MscL channels and demonstrated network communication <sup>108</sup>. By combining multiple external manipulation techniques of levitated DIB networks (heating, micro-centrifugation, magnetic actuation), they developed a ‘droplet laboratory’ for mimicking cellular functionalities <sup>108</sup>. As opposed to DIB models with protein pores only at an open state, such as the earlier mentioned  $\alpha$ HL, single DIBs and networks have been developed with embedded MscL channels. The open/close state of MscL channels can be manipulated by chemical <sup>109,110</sup>, and physical actuators <sup>111</sup>. Thus, such mechanosensitive channels offer means of on-demand communication in artificial membrane models. As reported by Strutt, *et al.* 2021, MscL channels in DIBs exhibited a dependency on the membrane’s asymmetry, where they remained open in the presence of single-tailed LPC lipids in one of the leaflets <sup>112</sup>.

Moreover, IVTT cell-free protein expression has been successfully accomplished in individual DIBs and DIB networks, using light activation <sup>100,113,114</sup>. Others, by translating the molecular transport

of neurons into an agarose-based biomaterial device with DIBs at different ends, it was possible to produce a synthetic neural network, capable of signal transmission, moving one step closer to synthetic tissue bioelectronic devices <sup>115</sup>.

The compartmentalisation of cellular contents is an important feature of living cells aimed to be recapitulated in protocells and membrane models like DIBs. One of the main issues associated with DIBs, is the fact that they are formed in oil, rather than in aqueous environments. Therefore, researchers have developed ways to permit the isolation of DIBs within an aqueous external environment. In this way the aqueous environment can facilitate communication between adjacent lipid-segregated aqueous phases. These compartmentalised structures were first defined by Villar, *et al.* 2011, as multisomes <sup>116,117</sup>, and since then have been explored using various methods and tools (**Figure 1.6A**). Encapsulated DIBs form communicating compartments and have been achieved either by placing the DIBs (in oil) on a Teflon wire loop surrounded by water <sup>118</sup>, or using multi-phase droplet microfluidics <sup>119</sup>.

The Teflon wire loop method relies on the suspension of an oil droplet in an aqueous environment, held in place by the Teflon-coated wire. Using this method, Booth, *et al.* 2019 transported a molecule from one compartment of a DIB into the other, where an ion sensitive pore was *in-situ* expressed and assembled into the lipid bilayer in contact with the external aqueous environment <sup>120</sup>. The pore was then activated on-demand through the external addition of an ionic solution. Cazimoglu, *et al.* 2021 showed parallel chemical communication between reaction-containing DIBs and the aqueous environment <sup>118</sup> (**Figure 1.6B**). They formulated a DIB network of compartments with  $\alpha$ HL pores, responsible for signal transduction, sensing (process 1) and enzymatic reactions (process 2), which were activated by the molecules present in the aqueous environment (lactose,  $\text{Ca}^{2+}$  or  $\text{Mg}^{2+}$ ) <sup>118</sup>.

Following the same concept around the isolation of cell membrane models in physiological environments, DIBs were encapsulated in hydrogels to mimic networks, from proto-organelles to prototissues <sup>121</sup>. Such hydrogel encapsulated DIBs (eDIBs) have been generated using primarily droplet microfluidics and integrated with cell mimicking functions, presenting free-standing artificial cell models. Droplet-microfluidics and sequential emulsification yielded eDIBs with controlled number of cores, whilst communication between the inner and outer environments, was enabled through the *in-situ* assembly of nanopores at the lipid bilayer interfaces (**Figure 1.6C**) <sup>122</sup>. The customisation of eDIBs broadens their application which led to the development of magnetically polarised hierarchical artificial cell chassis <sup>123</sup>, formation of bioluminescent detection platforms for thermal DNA amplification <sup>124</sup> and high-throughput membrane screening studies using the synergy of pore-forming peptides <sup>125</sup>.

Compartmentalised structures, including vesicles and DIBs can be shaped within artificial cell consortia, as a counterpart to natural cells and organelles. Their integration with living cells would explore emergent and collective behaviours to direct higher level activities.

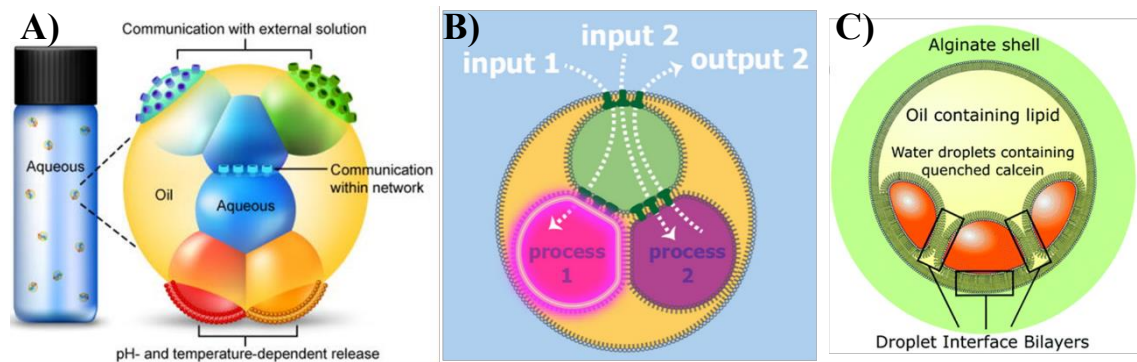


**Figure 1. 6: DIB-based multisomes for artificial cell membrane studies.** **A)** The first suggested DIB multisome model in an aqueous solution, consisting of aqueous cores, pores for communication with the external environment (top), within the network (middle) and tailored interfaces with sensitivity to pH and temperature for controlled release (bottom). Image adapted from <sup>[116]</sup>. **B)** DIB encapsulated by an aqueous environment for executing two different processes with a signal transduction droplet (green) acting as the mediator. In this schematic, process 1 was activated (pink fluorescence) by input 1 in the external aqueous environment. Image adapted from <sup>[118]</sup>. **C)** Encapsulated DIB (eDIB) with a hydrogel alginate shell produced using droplet-microfluidic technology, where lipid bilayers are formed between adjacent aqueous phases (droplets and hydrogel shell). The droplet interface bilayers indicate possible sites of pore assembly. Image adapted from <sup>[122]</sup>.

#### 1.4. Artificial cell and living cell interactions

Bottom-up artificial cell studies focus on non-biological materials, but very often cell-derived components are also involved. Cell membranes derived from natural cells can decorate nanoparticles and act as camouflaged drug delivery vehicles<sup>126,127</sup>. Membranes derived from cancer cells<sup>61</sup>, and red blood cells<sup>128</sup>, managed to be used as surface mimics<sup>25</sup>, while materials like soft polymers have been used as shape mimics<sup>129</sup>. On the contrary, recent scientific interests lay in the interactions between artificial and living cells, aiming communication and stimulation between entities.

Systematic advances have been made in developing hybrid models of interacting artificial cells with either bacteria or mammalian living cells. Lentini, *et al.* 2014 compiled ‘chemical translator’ artificial cells, which induced a response in *Escherichia coli* bacteria, only when aHL pore were expressed within the artificial cells<sup>130</sup>. Quorum sensing is the ‘language’ of bacteria when existing within the same environment, which is a great method to evaluate communication between artificial cells and bacteria<sup>131,132</sup>. Interestingly, lipid-based artificial cells have mediated a two-way communication between bacterial populations, through the synthesis and release of quorum sensing signals<sup>133</sup>. One of the most recent and fascinating coacervate-based artificial cell system, which involved living bacteria was developed by Xu, *et al.* 2022<sup>134</sup>. They transformed a membrane-less coacervate, to a bacteriogenic protocell with proto-organelles, a DNA-containing proto-nucleus and other cellular components, which ultimately formed an irregular more cell-like morphology, as shown in **Figure 1. 7A**.

The application of stimuli-responsive liposomes earlier discussed, is not limited to drug delivery and treatments. Engineering artificial cells sensitive to the external environment (light, heat), paves the way in programming communication routes between artificial cells and living cells within hybrid systems<sup>135</sup>. By combining top-down genetic manipulation, and bottom-up non-living matter constructs, complex and environment-responsive hybrid systems can be developed<sup>136</sup>.

To enable efficient interactions, artificial cells and living cells need to be appropriately integrated within their cell signalling range<sup>137</sup>. The exchange between non-contacting artificial cells and natural cells can be assisted by molecular diffusion from one population to the other. A reaction, which is widely used in synthetic biology and hybridisation concepts, but not limited to, is the glucose oxidation reaction<sup>138</sup>. In many cases, this involves one population (sender) being introduced to external molecules, which can be catalysed and converted into a secondary substance, to which the second population (receiver) is susceptible. This has been characterised as a ‘population hybridisation’ or ‘distributed population’ method<sup>5,139</sup>. Qian, *et al.* 2021, investigated the transfer of enzymatically produced fluorescent probes from hydrogel-based artificial cells to liver cells, leading to light-emitting cell cultures<sup>140</sup>. Within the same group, scientists simulated energy production in hydrogels by encapsulating mitochondria and enzymes, capable of producing energy *in-situ*<sup>141</sup>. Another approach involves the direct contact and organisation of the artificial cell and living cell populations, for material

exchange and communication, which has been achieved using acoustic standing wave patterning<sup>142,143</sup>. This has been described as ‘network hybridisation’ or ‘contact-dependant’ interactions<sup>5,139</sup>.

The nano and micro-scale production of artificial cells permits their encapsulation within living cells, or vice-versa. Hybrid models that take this form are recognised as ‘embedded’ or ‘nested’ hybridisation methods<sup>5,139</sup>. An example includes the encapsulation of a single mammalian cell within a vesicle, to couple the intracellular hydrolysis of lactose to glucose, to a non-biological fluorescence-producing pathway (**Figure 1. 7B**)<sup>144</sup>. Additionally, the vesicle acted as a defence mechanism for the cell in the presence of toxic molecules. Another example of embedded hybridisation, involved the encapsulation of cyanobacteria in vesicles to act as converters of light into energy, which in turn initiated an intravesicular reaction<sup>145</sup>. Finally, living cells can be bound within artificial cells via DNA tags<sup>146</sup>.

Cellular differentiation is an event that occurs in maturing cells with altering gene expressions, affected by physical (extracellular matrix) and chemical (stimulants) cues<sup>147</sup>. As in all biological cells, the extracellular environment is one of the primary determinants of cell differentiation<sup>148</sup>, a fact which was employed for the differentiation of neuron cells using artificial cells as mediators or initiators<sup>149</sup>. Toparlak, *et al.* 2020, established not only the communication of mammalian cells and artificial cells but also, achieved differentiation of neural cells, by introducing artificial cells with expressed large protein pores and factors that drove differentiation<sup>149</sup>.

With the increasing precision of bioengineering, complex artificial cell colonies or prototissues can be constructed to facilitate artificial-natural cell interactions. Prototissue models can be programmed to have precise, arrangement and geometries<sup>150</sup>, and be responsive to external stimuli to trigger sequential biochemical reactions<sup>113,151–153</sup>. Recently, pioneer studies demonstrate that DIB prototissue models can be utilised to explore the metabolic pathway of natural cells and the developmental processes of organs<sup>154</sup>. These synthetic multi-compartment tissues are aimed at applications in tissue engineering<sup>155</sup>, while 3D bioprinting offers control over the position, as well as the dimensionality (2D or 3D-printed DIB networks)<sup>156,157</sup>. The organisation of different cell lines can be controlled, which is vital in mimicking *in-vitro* tissue and organ formation<sup>156</sup>. To recapitulate the mechanics of the extracellular matrix (ECM), Graham, *et al.* 2017 utilised agarose-based bioinks to print two populations of mammalian cells in a controlled pattern, forming 3D DIB networks (**Figure 1. 7C**), while maintaining their viability and functionality<sup>158</sup>. Using a similar approach, but using a bioink more accurately representative of the *in-vivo* ECM, Zhou, *et al.* 2020, accomplished the formation of 3D-printed neural stem cell-laden DIB networks, which differentiated into stimulus-responsive brain tissues<sup>154</sup>. Hence, it is recognised that 3D bioprinting can support the fabrication of multifunctional DIB networks, where the compartments can be stimuli-responsive, or encapsulate connecting pores, reagents, as well as living cells<sup>159–161</sup>.

As discussed in earlier sections of this chapter, some aims of artificial cell research include the development of novel drug carriers, *in-situ* drug synthesisers and perhaps reporters. Hence, their

implementation as advanced tools would benefit areas in biosensing <sup>162,163</sup>, smart drug delivery <sup>164</sup>, and therapeutics <sup>165,166</sup>. Artificial cell membrane models, such as SLBs, have been used in combination with living cells, to study target-specific coatings and membrane-bound interactions <sup>167</sup>. Furthermore, artificial cells have been engineered to produce toxic proteins on-site while being incubated with breast cancer tumours leading to their suppression <sup>168,169</sup>. Moreover, an interesting area is the programmability of bacteria into synthetic bacteria to target cancer cells and kill upon contact, towards cancer therapy <sup>166</sup>. From a clinical perspective, soft protocells may offer possibilities as implants either for tissue regeneration or pathology treatments <sup>170</sup>. Lastly, engineering cellular behaviours, through communicating artificial cells, or perhaps the opposite, can be the key towards next-generation programmable drug treatments.

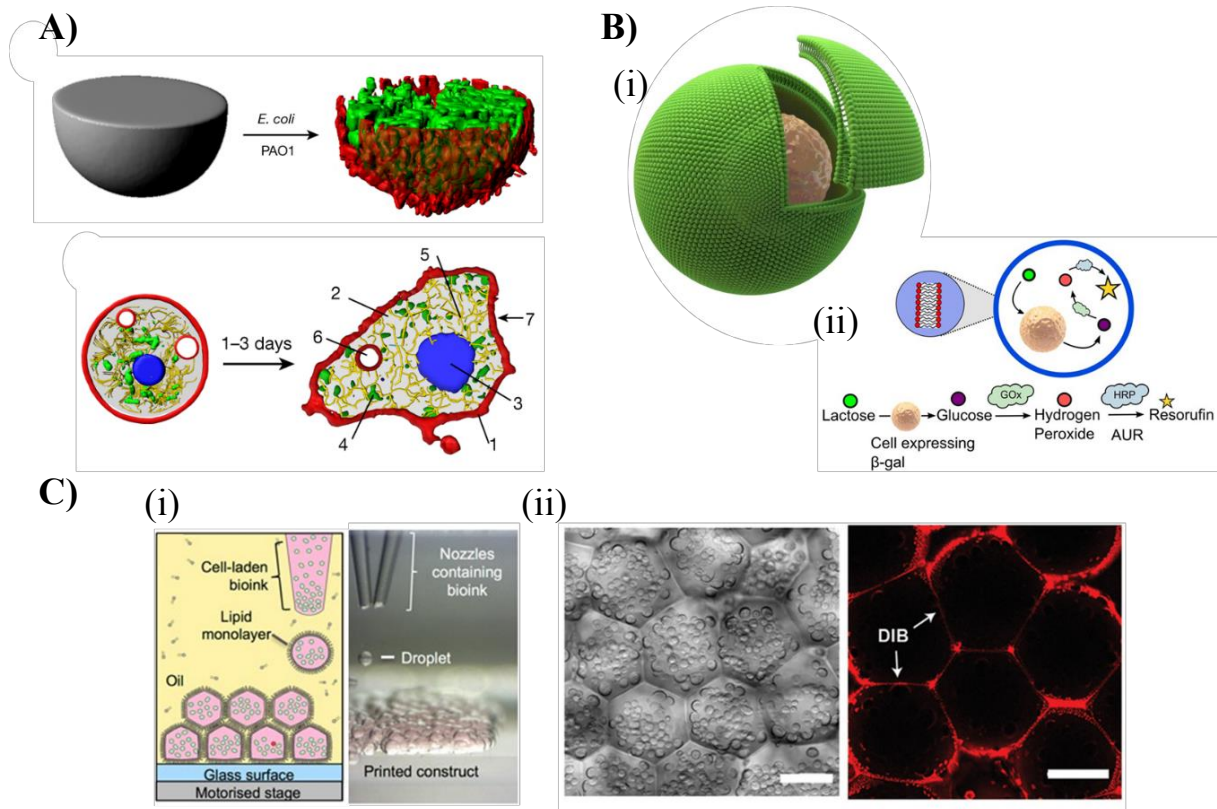


**Figure 1. 7: Protocell-living cell interaction models using various approaches.** **A)** (i) Bacteria in coacervates rearranged spontaneously in either the periphery or the cores (green: *Escherichia coli*, red: *Pseudomonas aeruginosa*). (ii) Spherical protocell adopted a cell-like morphology over time (coacervate outer membrane (1), proto-cytoplasm (2), proto-nucleus (3), *E. coli* cells (4), proto-cytoskeleton (5), membrane bound proto-organelle (6), amoeba-like morphology (7). Image adapted from <sup>[134]</sup>. **B)** (i) Example of embedded hybridisation, where a mammalian cell is encapsulated within a liposome. (ii) The cell catalyses the lactose to glucose, which activates a reaction inside the liposome, leading to the production of a fluorescent agent (resorufin). Image adapted from <sup>[144]</sup>. **C)** (i) 3D-printed DIB networks with mammalian cells encapsulated in the bioink (ii) Printed DIB network, left: bright field image, right: red fluorescent labelled lipids. Scale bar is 100  $\mu\text{m}$ . Image adapted from <sup>[158]</sup>.

## 1.5. Breast Cancer

One of the most frequently diagnosed forms of cancer in females is breast cancer, which develops in the breast tissue area. According to Public Health England, breast cancer is in the top five cancer types with the most 5-year survival rates in England reported between 2014 and 2019 (>85 %) <sup>171</sup>. During the Covid-19 pandemic outbreak in 2020, the number of diagnosed cases of cancer had dropped considerably compared to the previous year, due to the paused services and refused referrals <sup>172,173</sup>.

Breast cancer is treated using 4 different approaches including radiotherapy, chemotherapy, hormone therapy and cancer-targeted pharmaceuticals. Radiotherapy uses high-energy radiation in the form of X-rays to kill cancer cells locally, either applied internally or externally <sup>174</sup>. Hormone therapy targets hormone receptors expressed by breast cancer cells, which receptors facilitate breast cancer survival and growth <sup>175</sup>. Examples of these hormonal receptors in breast cancer, include the estrogen receptor (ER) and progesterone receptor (PR). In addition, chemotherapy, involves drugs usually delivered through the blood stream, slowing down cancer cell division <sup>176,177</sup>. Unlike hormonal and chemotherapeutic anti-cancer drugs, cancer-targeted therapy, aims to fight breast cancer cells by targeting their selective receptors. An example of an overexpressed receptor in some breast cancer cells, is the human epidermal growth factor receptor 2 (HER-2) <sup>178</sup>. The therapy of choice is determined depending on the gene expression of the breast cancer cell line after biopsy, as well as the health condition of the patient.

### 1.5.1. Breast cancer cells

Cell lines are characterised based on their gene and receptor expression, which can determine the treatment approach. Some examples of breast cancer cell lines that express different receptors are MCF-7, MDA-MB-231 and SK-BR-3. For example, MCF-7 cells express ER and PR, but no HER-2, while SK-BR-3 do not express ER nor PR, but does HER-2, and MDA-MB-231 express none of these receptors <sup>179</sup>. Based on their surface receptors, these cell lines are categorised as Luminal A, HER-2 positive and triple negative B, for MCF-7, SK-BR-3 and MDA-MB-231, respectively <sup>180</sup>. MCF-7 cells are considered to be less aggressive and more responsive to therapies than other cell lines <sup>181</sup>. Tumour formation is initiated by mutation occurrences *in-situ* within the milk ducts (or lobules) of the mammary glands (ductal carcinoma *in-situ*), which develops into invasive ductal carcinoma (IDC), as illustrated in **Figure 1. 8** <sup>182</sup>. Because the tumour is formed in the glands of the breast, it is also referred to as adenocarcinoma. The underlying issue with cancer pathologies is the drug resistance developed by tumours during the course of treatment.

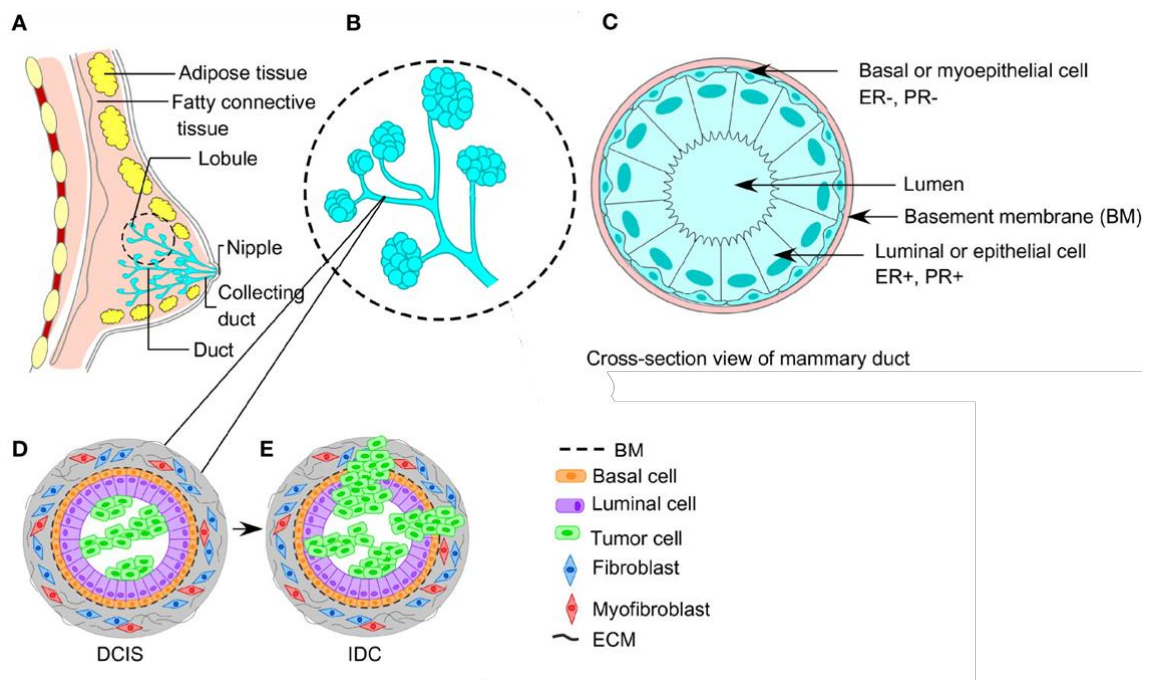


**Figure 1. 8: Schematic of the breast tissue and formation of carcinoma.** **A)** Anatomical cross section of the breast. **B)** Mammary milk ducts and lobules **C)** Cross-section of the mammary duct, noting the lumen, the basement membrane surrounding the duct, luminal cells which express ER and PR (ER+, PR+), while the basal cells do not express these receptors (ER-, PR-). **D)** Initial stages of ductal carcinoma in-situ (DCIS), cellular mutations lead to the differentiation of cells into tumour cells. **E)** As the carcinoma progresses, it starts to invade the basement membrane, becoming invasive ductal carcinoma (IDC). Image adapted from <sup>[182]</sup>.

Conventional cancer studies are performed in two-dimensional (2D) cultures, which technique has been around since the start of the 20<sup>th</sup> century <sup>183</sup>. This technique has led to outstanding medicinal developments over the past century, although pathologies such as cancer require more complex and realistic platforms than monolayer cultures. By introducing the third dimension to cell culture systems (3D culture), cell-cell junctions become more realistic, and it is possible to maintain cell culture simplicity, using scaffold-free methods (**Figure 1. 9**). However, when an ECM is incorporated in the form of hydrogels, cells are reinforced mechanically through the interactions with the ECM, which is vital in the *in-vivo* tumour microenvironments and tissue engineering applications (**Figure 1. 9B**) <sup>184</sup>. Characteristics such as cell morphology, proliferation, drug resistance and more, strongly differ between 3D and 2D cultured systems, which are only formed on a flat tissue-treated surface <sup>185</sup>. Therefore, anti-cancer drug resistance research emphasises on the development of novel adjuvant drugs and realistic tissue culture models to simulate and study the behaviour of cancers <sup>176,185,186</sup>. *In-vivo* mimicking platforms in cancer research include tumour-on-a-chip devices and 3D multicellular tumour spheroid (MCTS) cultures <sup>187</sup>, with hydrogels as one of the primary materials used as the ECM.

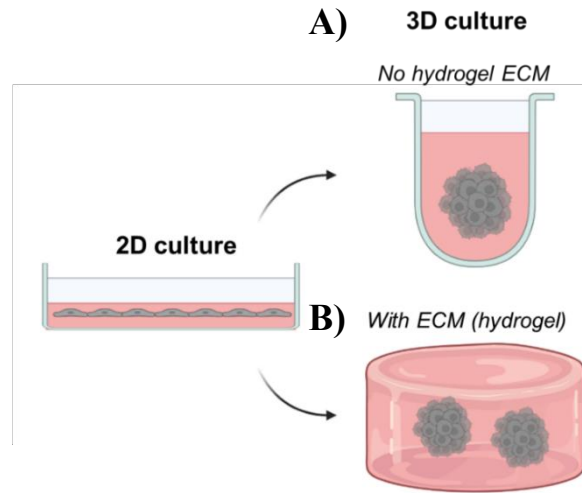


**Figure 1. 9: Tissue culture morphology in 2D versus 3D (scaffold and scaffold-free).** Monolayer cellular arrangement in 2D does not accurately mimic the formation of tissue in the body, while 3D cultures are more realistic. 3D cultures can be formed (A) in liquid media without the incorporation of an ECM, or (B) with hydrogel as the ECM to simulate the surrounding tissue of the tumour. Image recreated using BioRender.com.

### 1.5.2. Hydrogel-based 3D cultures

Natural polymers originate from natural sources, often rendering them highly biocompatible, with gelling conditions dependent on ionic interactions, pH and temperature. Polysaccharides and proteins derived from plant and animal tissues have been used in tumour-related studies to replicate *in-vivo* tumour microenvironment characteristics.

The majority of natural polymers derived from the ECM of tissues and organs include proteins. Matrigel is a basement membrane extracellular (BME) matrix protein extract, which can be derived from Engelbreth-Holm-Swarm (EHS) mouse sarcoma and consists of laminin, collagen type IV and other proteins<sup>188</sup>. Collagen type I is another major protein present in the ECM of tissues and improves cellular attachment and invasion in MCTS studies<sup>189,190</sup>. Polysaccharides are also used as hydrogels to replicate the structural characteristics of *in-vivo* tissues. Polysaccharides including alginate, chitosan<sup>191</sup>, hyaluronic acid<sup>192</sup>, and agarose<sup>193</sup>, cover a range of hydrogels that have a demonstrated ability to promote cancer cell growth and MCTS formation. The current interest in hydrogel composites as a platform for MCTS formation and drug testing is increasing. Hybrid protein and polysaccharide hydrogel scaffolds generate *in-vitro* 3D MCTSs, where their formulation and mixing ratio can affect directly the physical properties of the hydrogel (porosity and pore interconnectivity) and the subsequent MCTS formation<sup>194,195</sup>. Although numerous proteins and polysaccharides have been reported to promote MCTSs, only the alginate and collagen are discussed along with some of their fundamental characteristics. **Table 1. 1** summarises the advantages and disadvantages of protein, polysaccharide, and hybrid hydrogels.

*Table 1. 1: Advantages and disadvantages of protein, polysaccharide and hybrid hydrogels.*

Hydrogel	Advantages	Disadvantages	Ref.
<b>Proteins</b>	<ul style="list-style-type: none"> <li>• Biocompatible, biodegradable</li> <li>• Provide cell adhesion sites</li> <li>• Encourage cell proliferation</li> <li>• Physical crosslinking</li> <li>• Ideal for cell dynamics and migration</li> <li>• Angiogenesis promotion in MCTS systems</li> </ul>	<ul style="list-style-type: none"> <li>• Batch-to-batch variations</li> <li>• Low mechanical properties</li> </ul>	196,197
<b>Polysaccharides</b>	<ul style="list-style-type: none"> <li>• Biocompatible, biodegradable</li> <li>• Easily functionalised</li> <li>• Some are bio adhesive</li> <li>• Structural support of cells</li> <li>• Mild gelation conditions</li> </ul>	<ul style="list-style-type: none"> <li>• Batch-to-batch variations</li> <li>• Lack of cell adhesive ligands</li> </ul>	196,198, 199
<b>Hybrids</b>	<ul style="list-style-type: none"> <li>• Improved mechanical properties</li> <li>• Improved pore interconnectivity</li> <li>• Cell adhesion sites available</li> <li>• Tunable characteristics</li> <li>• Realistic recapitulation of tissue stiffness</li> <li>• Good pore interconnectivity</li> </ul>	<ul style="list-style-type: none"> <li>• Crosslinking mechanisms may be difficult to achieve</li> <li>• May be difficult to tune physicochemical characteristics</li> </ul>	200–202

### 1.5.2.1. Alginate

Alginate is a polyanionic polymer extracted from brown seaweed and is probably the most commonly used hydrogel in numerous fields. The molecular structure of alginate consists of  $\beta$ -D-mannuronic acid (M) and  $\alpha$ -L-Guluronic acid (G) residues, forming polysaccharide chains with GG, GM and MM sequences<sup>203</sup>. The compositional ratio of G/M in the alginate and its molecular weight, depend on the source from which the polymer was isolated from, and defines the physical properties of the alginate hydrogel<sup>204</sup>. For example, alginate rich in G blocks, results in stiffer hydrogels, while alginate with larger M block fractions has increased water solubility and tends to be more flexible<sup>205</sup>. During ionic crosslinking of alginate, divalent cations, such as  $\text{Ca}^{2+}$  and  $\text{Ba}^{2+}$ , bind to the GG sequences of alginate, causing the structure to fold and form the ‘egg box’ structure, as illustrated in **Figure 1. 10**<sup>206,207</sup>. These conformational changes of the polymer chains lead to the formation of a biocompatible and biodegradable hydrogel, making alginate a strong candidate for biomaterial applications.

The molecular chains of alginate can follow ionic crosslinking through internal or external gelation approaches. The latter relates to the alginate solution encountering divalent cations, which crosslink the alginate at a degree that depends on the diffusion of the ions through the alginate phase<sup>208</sup>. The internal gelation on the other hand, involves the slow release of divalent cations from an alginate mixture with chelating agents, usually upon protonation<sup>207</sup>. The great mechanical properties of alginate hydrogels and their simple crosslinking methods, have permitted their application in cell encapsulation and tumour spheroid formation<sup>209</sup>. However, when it comes to MCTS proliferation and invasion studies, alginate is frequently used in combination with cell adhesive peptides, through simple mixing or covalent crosslinking<sup>210</sup>.

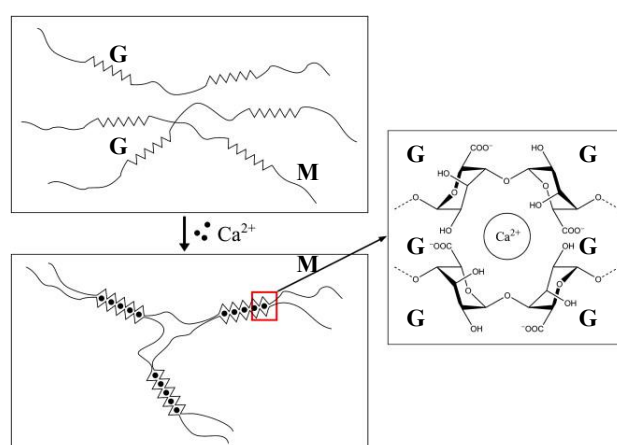


**Figure 1. 10: Alginate crosslinking using divalent cations of calcium ( $\text{Ca}^{2+}$ ).** During ionic crosslinking, the  $\text{Ca}^{2+}$  binds to the GG sequences, bringing close the linear alginate polysaccharide chains to form the ‘egg box’ structure. Image adapted from [206].

### 1.5.2.2. Collagen

Collagen is a triple helix protein and is the most abundant protein in mammals. Collagen type I protein is the main form of collagen type present in the ECM of tissues, such as bone, tendon and cornea<sup>189</sup>. Amongst all collagen types, type I, is considered the primarily investigated and utilised in biomedical engineering<sup>211</sup>. It is soluble in acid, while at neutral pH it undergoes fibrillogenesis, forming an opaque gel<sup>212</sup>. Neutralised collagen solutions can be hindered from gelling by keeping the solution on ice, but when temperature is raised to 20-37 °C, fibrils start to build up a network resulting to collagen gelation<sup>213</sup>. Collagen type I provides ligands important for cell attachment and growth, thus it is widely utilised as an ECM material for MCTS formation. Zhao, *et al.* 2019 used the hanging drop method for MCTS formation and utilised collagen gels to study the migrating and invasive behaviour of 3D breast cancer tissues<sup>214</sup>. In addition, tumour vascularisation and drug resistance of breast cancers have been explored using collagen-containing hydrogels<sup>194</sup>.

Protein/polysaccharide hybrid hydrogels have been reported to accurately mimic the *in-vivo* tumour microenvironment, due to the improved mechanical properties and cellular adhesion sites provided. Liu, *et al.* 2018, claimed that their collagen-alginate 3D gel system performed better than commercial invasion-promoting hydrogels, such as Matrigel, by showing the invasion of fibroblasts followed by tumour cells<sup>201</sup>. In fact, by altering the CaCl<sub>2</sub> gelling solution, they were able to match almost perfectly the stiffness of *in-vivo* tumours (~4000 Pa)<sup>215</sup>. Increasing the concentration of collagen ( $\geq 1.5$  mg/ml) or alginate ( $\geq 2$  %), increases the stiffness of the hydrogel, which consequently decreased the proliferation of MCF-7 cells according to Agarwal, *et al.* 2017<sup>194,215</sup>. Therefore, the gelation method and concentrations, as well as the collagen to alginate ratio affects the mechanical properties of *in-vitro* tumours<sup>200</sup>. The well-characterised alginate and collagen offer a relatively easy and versatile method for developing MCTSs, since they provide physicochemical attributes to recreate the *in-vivo* physiology and invasion of tumours.

## 1.6. Microfluidics

Microfluidic technology is now a well-studied field with multidisciplinary applications. Miniaturised devices of such technology are characterised by patterned, micro-scale, fluid-restricting channels. The forerunners of microfluidic fabrication include the techniques of silicon manufacturing, integrated circuits and photolithography invented in the 1950s<sup>216</sup>. The complementary applications of these fields led to advances in microelectronics, microanalysis, biodefence and molecular biology<sup>217</sup>. Indeed, the military expressed a great interest in these technologies and funded this research, which led to the development of miniaturised microelectromechanical systems (MEMS). Since then, scientists worked into reducing the large size of integrated circuits, in order to develop portable platforms for applications, such as medicine. Then came Andreas Manz and colleagues in 1990s, who revolutionised laboratory-on-a-chip (LOC) applications, by developing and introducing the concept of miniaturised Total Chemical Analysis System ( $\mu$ -TAS), promoting efficient and reduced volume analysis and separation of chemical samples<sup>218</sup>. Monophasic systems, including  $\mu$ -TAS, are also known as single-phase microfluidics<sup>219</sup>.

During the uprising period of microfluidic technology, devices were fabricated with silicon substrates, similar to microelectronic devices. Using the photolithography technique, a silicon wafer with a photoresist layer is used in combination with a photomask, which creates a pattern on the wafer upon UV exposure. Other techniques for the fabrication of silicon-based microfluidic devices include thin film deposition and etching<sup>220</sup>, which rely on the addition or removal of material, respectively. Due to the high costs of silicon substrates, they are often replaced with other affordable materials, such as polymethylmethacrylate (PMMA), polydimethylsiloxane (PDMS), glass and others<sup>221</sup>. Yet, the fabrication of microfluidic devices using these techniques and materials remained complex, which led to the development of soft lithography and the use of cheap, easy-to-produce and transparent elastomers, including PDMS<sup>222</sup>. Until today, PDMS micromoulding is the most widely used microfluidic device fabrication method in academia. Microfluidics are now famously studied and applied in major fields, leading to breakthroughs in digital microfluidics, organ-on-a-chip and paper-based microfluidics<sup>223</sup>. More recently, microfluidic engineers have expressed an interest in 3D printing as an alternative microfluidic device rapid fabrication method<sup>224</sup>.

### 1.6.1. Droplet microfluidics

Fluid flow behaviour in the micro-scale is differentiated from the fluid behaviour in the macroscale. Although, any fluid flow with density ( $\rho$ ), velocity ( $u$ ), viscosity ( $\mu$ ) and characteristic length ( $L$ ), can be described by the dimensionless Reynolds number ( $Re$ ) (*Equation 1.1*)<sup>225</sup>. The  $Re$  number creates a correlation between the inertial and viscous forces, which determines the nature of the fluidic stream.

$$R_e = \frac{\rho u L}{\mu} \quad (1.1)$$

At high  $R_e$  values, the inertial forces are dominant, producing a non-predictable mixing of the fluid, known as a turbulent flow, which is a phenomenon that abundantly occurs at the macroscale. On the other hand, most microfluidic systems are usually governed by low  $R_e$  values, defined as a laminar flow, due to the micro-scale dimensions and the dominance by viscous forces. If a fluid was to be imagined flowing within a tube in a laminar fashion, the fluid appears as smooth layers, with zero velocity at the walls and maximum velocity at the centre of the tube.

Droplet microfluidics is one of the daughter fields of microfluidics, which is governed by the production of droplets using immiscible phases. Small volume droplets are generated, and due to the microscale of microfluidics and the high surface area to volume ratio, accelerated reactions can occur<sup>226</sup>. Within this daughter field, droplet sorting and mixing are utilised in order to separate distinct populations of droplets and facilitate reactions, respectively<sup>225</sup>. Segmented flows is another regime which also relies on immiscible phases, where discrete and separated volumes of fluid, flow along the continuous channel of microfluidic devices, with applications as bioreactors and high-throughput chemical analysis<sup>227–229</sup>.

When developing a droplet-microfluidic system, care must be taken over the material of the microfluidic channels, depending on the type of emulsion created, as well as the properties of fluids being involved. The formation of an emulsion in droplet-microfluidics is described by a dispersed phase, which is the fluid to be broken into droplets, and a continuous phase, which shears and carries the droplets. Water-in-oil (W/O) and oil-in-water (O/W) are the simplest single emulsion examples, which require channels with hydrophobic and hydrophilic wetting properties, respectively, for their stable formation. In order to keep an emulsion stable, hydrophilic and hydrophobic surfactants may be introduced, which can also minimise the effect of droplet coalescence<sup>230</sup>. The presence of surfactants, the viscosity ( $\mu$ ) and most importantly, the size of droplet-forming orifice, influence the diameter and uniformity of the produced droplet population. Additionally, the interfacial tension ( $\gamma$ ) between the two immiscible phases affects the droplet break-up. These fluid and system parameters, and their influence on the droplet dynamics, are described by the dimensionless Capillary number ( $C_\alpha$ ), which defines the relationship between viscous forces to interfacial tension forces (*Equation 1.2*):

$$C_\alpha = \frac{\mu u}{\gamma} \quad (1.2)$$

where  $u$ , is the velocity of the continuous phase. The  $C_\alpha$ , varies between microfluidic systems and droplet break-up occurs, when the  $C_\alpha$ , exceeds a critical  $C_\alpha$ <sup>226</sup>. In microscale T-junctions and flow-focusing junctions, the  $C_\alpha$  is usually considerably lower than 1 ( $\ll 1$ )<sup>231</sup>. At low  $C_\alpha$ , the interfacial

tension forces dominate over the viscous forces, while at high  $C_a$ , the viscous forces are dominant, which makes droplet formation more difficult. Therefore velocity, viscosity and surface tension are important parameters which can determine the nature and regime of droplet formation.

## 1.6.2. Droplet-forming geometries

There are three different hydrodynamic focusing junctions that lead to droplet formation. These include, T-shape, flow-focusing and co-flow junctions. These junctions vary in their geometry and arrangement, but all have in common the ability to host a dispersed and a continuous phase, which meet, and periodically break the dispersed phase into droplets, which continue to flow in a single downstream main channel<sup>232,233</sup>.

### 1.6.2.1. T-junction

The droplet-forming geometry considered to be the simplest, is the T-junction. This consists of two channels that meet perpendicularly (at  $90^\circ$ ), or in modified channels meet at an angle ( $0^\circ - 180^\circ$ ). As the dispersed phase enters the downstream channel, the shear forces of the continuous phase attempt to lengthen the dispersed phase, forming a neck with increased pressure, leading to droplet break-up. The formation regime of the droplet will vary depending on factors including the  $C_a$ , as well as the channel width ratio<sup>234</sup>. For example, at high  $C_a$ , the T-junction generates droplets, with diameter smaller than the main channel and near the orifice (dripping regime), while at low  $C_a$ , the droplet diameter exceeds the channel diameter, resulting to an upstream pressure build-up that causes droplet pinch-off (squeezing regime)<sup>235</sup>. However, when the flow rates are increased further, jetting regimes can occur, where droplets are pinched-off further downstream away from the orifice. These droplet-forming regimes are illustrated in **Figure 1. 11**<sup>233</sup>.

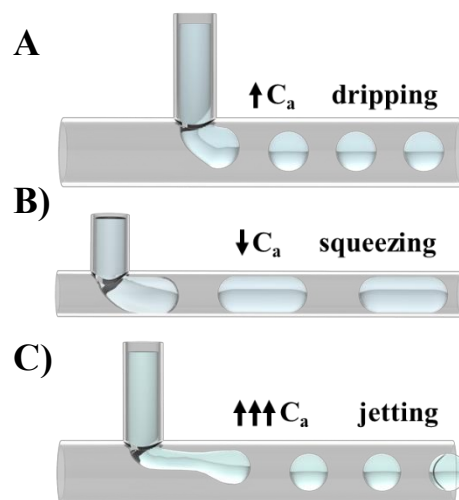


**Figure 1. 11: Droplet formation using the T-junction at the three different flow-regimes. A) Dripping regime occurring at high capillary number ( $\uparrow C_a$ ). B) Squeezing regime occurring at low capillary number ( $\downarrow C_a$ ) and C) Jetting regime at very high capillary number ( $\uparrow\uparrow\uparrow C_a$ ), where the shear forces dominate. Images were adapted from Elveflow<sup>[233]</sup>.**

### 1.6.2.2. Flow-focusing

Flow-focusing droplet-forming junctions focus the fluid flow into a narrow orifice defined by the geometrical design. The dispersed phase and two opposite-in-direction continuous phases of a planar flow-focusing junction, meet at a cross-section, where droplet formation is initiated. As the continuous phases elongate the dispersed phase into the narrow region, the inner phase forms a neck, on which high pressure is exerted, leading to pinch-off by Plateau–Rayleigh instability (**Figure 1. 12A**). Flow-focusing geometries offer a more controlled way of producing uniform, smaller droplets <sup>236</sup>. Similar to the T-junction, the flow-focusing junction, exhibits dripping and jetting behaviours, depending on the  $C_\alpha$ , whereas at very low  $C_\alpha$  values, the droplet generation is geometrically driven, producing droplets much larger than the narrow region <sup>236,237</sup>. Additionally, the fabrication of flow-focusing junctions in one plane, requires the surface treatment of the fluidic walls to ensure stable emulsion. This led to the development of axisymmetric flow-focusing junctions, also known as non-planar junctions (**Figure 1. 12B**), which generate smaller and more uniform droplets compared to planar junctions <sup>238</sup>, while others utilised them to produce multiple emulsions, by avoiding channel surface treatments <sup>239,240</sup>.

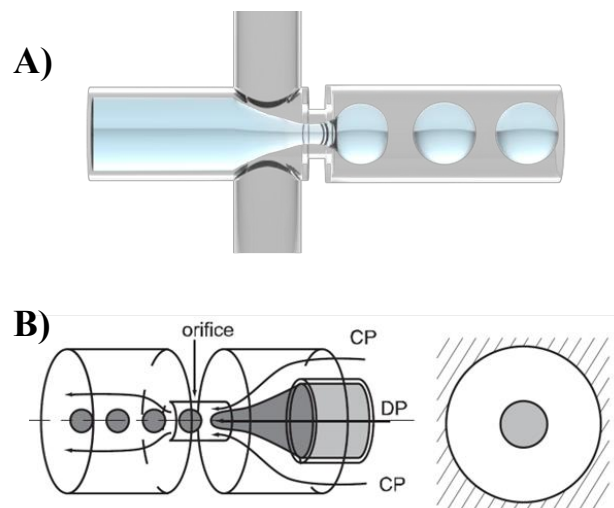


**Figure 1. 12: Droplet formation using flow-focusing junctions.** **A)** Planar flow-focusing junction showing droplet formation following the dripping regime. Images were adapted from Elveflow <sup>[2331]</sup>. **B)** Non-planar or axisymmetric flow-focusing junction, where the dispersed phase orifice (grey) has a very small cross section, and it is completely surrounded by the outer phase (white). Image adapted from <sup>[238]</sup>.

### 1.6.2.3. Co-flow junction

This droplet-forming geometry relies on the co-axial arrangement of the dispersed phase channel aligned within a larger continuous phase channel (**Figure 1. 13**). Similar to the other droplet-forming geometries, the  $C_\alpha$  number can predict the droplet formation regime. In co-flow focusing channels, the flow rate of the two immiscible phases has a greater effect on the size of the droplets, compared to the viscosity<sup>236</sup>. Droplet break-up near the orifice of the inner channel (dripping), occurs at high continuous phase flow rates, while droplets broken up further away from the tip of the inner channel (jetting), takes place with higher dispersed phase flow rates. Therefore, droplet formation relies more on the interplay between the shear stresses induced by the continuous phase and the interfacial tension, leading to either dripping or jetting regimes. One of the main benefits of using co-flow for periodic droplet formation, is the fact that the dispersed fluid is completely surrounded by the continuous fluid, meaning that the channel wetting properties do not influence droplet formation and stability. For this reason, many have employed this geometry for the formation of multiple emulsions, as they require fluidic channels with specific and alternating surface wetting properties<sup>241</sup>.

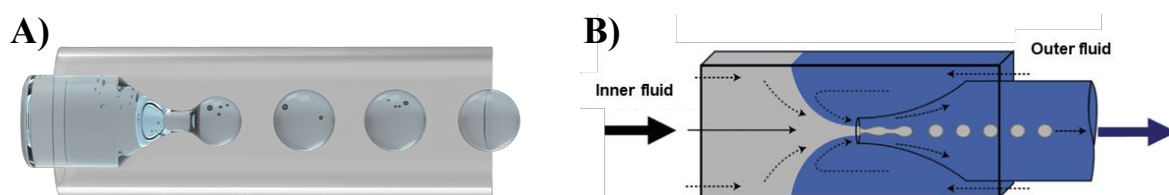


**Figure 1. 13: Droplet formation with co-flow microfluidic junctions. A)** Dripping regime, where droplet break-up happens very close to the orifice of the dispersed phase (dripping). Images were adapted from Elveflow<sup>[233]</sup>. **B)** Droplet formation occurs, with the outer fluid introduced from the opposite direction and hydrodynamic forces focus the dispersed phase into the orifice. This figure shows the transition from the dripping regime to the jetting regime, as the break-up occurs some distance from the orifice. Image adapted from<sup>[241]</sup>.

### 1.6.3. Applications of droplet microfluidics

#### 1.6.3.1. Multiple emulsion production

The formation of multiple emulsions using conventional methods, such as mechanical agitation have limited control over the emulsion size and uniformity<sup>242</sup>. Microfluidic devices on the other hand offer controlled formation of hierarchically structured multiple emulsions by alternating between the channel wetting properties, leading to the precise generation of emulsions, one-by-one<sup>241</sup>. By encapsulating single emulsions (W/O or O/W) with subsequent immiscible phases, double (O/W/O), triple (W/O/W/O) and higher order emulsions can be generated, as shown in **Figure 1. 14**. To achieve the formation and conservation of multiple emulsions, stabilizing agents are required. These can be in the form of surfactants, viscosity altering or gelling agents, that prevent coalescence and ensure stable emulsification<sup>243</sup>. One of the advantages of complex emulsion production using microfluidics, is the precision over the number, size and composition of the encapsulated cores<sup>244</sup>.

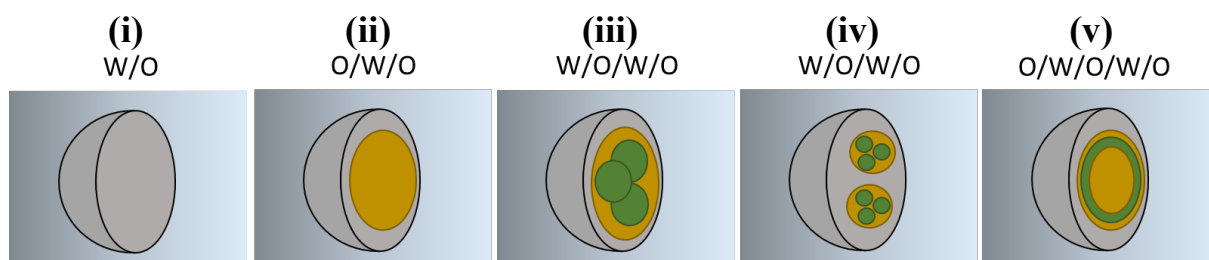


**Figure 1. 14: Illustrations showing single and complex emulsions of different structures.** Grey and green spheres are water phases, yellow resembles oil, and the outer light blue/grey phase is oil in all examples. (i) Single emulsion (W/O), (ii) double emulsion (O/W/O), (iii) triple emulsion (W/O/W/O), (v) concentric quadruple emulsion (O/W/O/W/O). The emulsions' structure can be altered using appropriate flow rates for example the triple emulsion in (iv).

Multiple emulsions can be produced using the aforementioned droplet-forming geometries (T-junction, flow-focusing, co-flow) and other more recently invented bifurcated geometries<sup>245</sup>. One of the earliest double emulsion systems with controlled dual-core population, was produced by Okushima, *et al.* 2004 using two T-junctions in series<sup>246</sup>. Since then, by ensuring the correct surface modifications, high-order emulsions have been produced with different microfluidic devices fabricated with techniques, such as glass capillaries (**Figure 1. 15A**)<sup>241,247,248</sup>, PDMS moulding<sup>249,250</sup>, PMMA milling<sup>251</sup>, and 3D-printing (**Figure 1. 15B&C**)<sup>123,252,253</sup>. Soft and robust triple emulsion hydrogels, have been produced using surface treated capillaries<sup>254</sup>, while others utilised hybrid devices to produce all aqueous complex emulsions<sup>255</sup>. Even though capillary microfluidic devices generate highly monodispersed and precise multiple emulsions, their fabrication is labour intensive and requires advanced technical skills<sup>253</sup>. By modifying the surface wetting properties of PDMS microfluidic channels, highly monodispersed single to quintuple emulsions have been formed<sup>249,256</sup>. Interestingly, others have integrated single emulsion devices to form multiple emulsions, by employing methods such as drop-by-drop engulfing<sup>257</sup>, or controlled 3D droplet printing<sup>258</sup>. It should be noted that numerical studies are particularly

important to be conducted, in order to explore and understand further the effects of interfacial tension and viscous forces around complex emulsion formation <sup>259,260</sup>. The compartmentalisation using emulsion microfluidics facilitates the high-throughput encapsulation and storage of reagents, which are valuable in applications such as food industry <sup>261</sup>, pharmaceuticals and cosmetics <sup>230</sup>, as well as cell encapsulation <sup>250</sup> and drug delivery <sup>262</sup>.

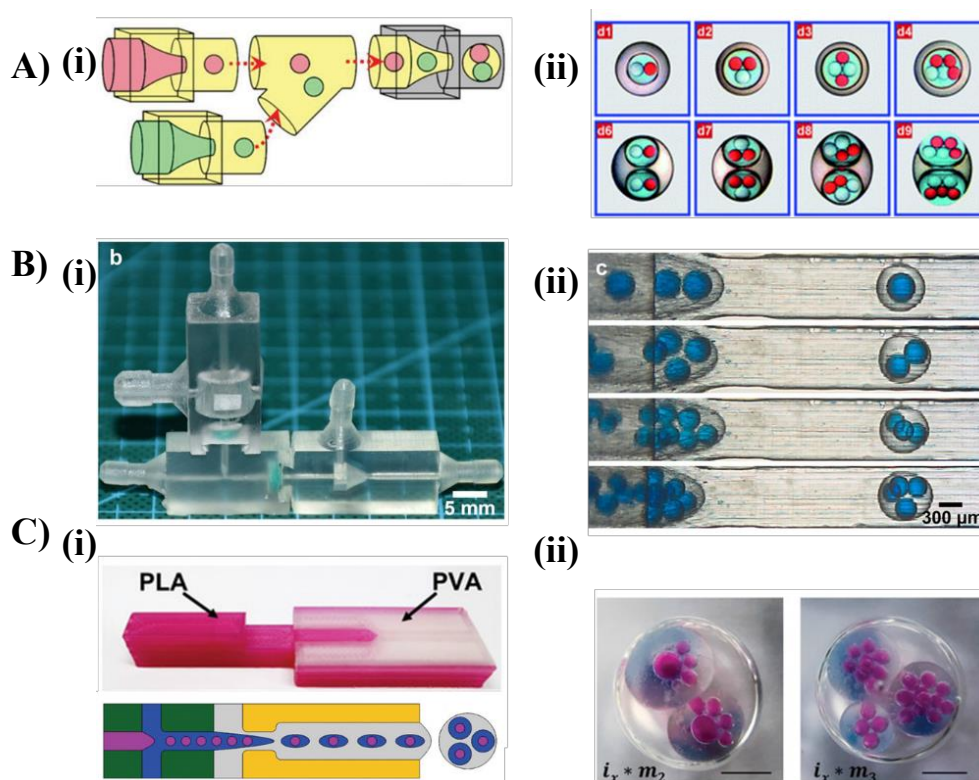


**Figure 1. 15: Diverse microfluidic devices for producing complex emulsions.** **A)** (i) Glass capillary microfluidic device manifold of cylindrical capillaries in cube capillaries, (ii) facilitated production of triple emulsions of controlled and precise number, ratio, and composition of internal compartments. Image adapted from <sup>[248]</sup>. **B)** (i) Assembled multi-module microfluidic device fabricated using 3D printing stereolithography, (ii) generated double emulsions with control over the number of aqueous blue cores. Image adapted from <sup>[253]</sup>. **C)** (i) Fused filament fabricated 3D-printed microfluidic device made of polylactic acid (PLA) and polyvinyl alcohol (PVA) filaments, (ii) produced approximately 3 mm diameter triple emulsions with control number of cores. Image adapted from <sup>[123]</sup>.

### 1.6.3.2. Artificial cell DIB models

In comparison to other fabrication methods, droplet microfluidics has the advantage of high-throughput production of constructs such as DIBs, multisomes and vesicles for cell mimicry studies<sup>119,144</sup>. Apart from high yield, microfluidics offer control over the compartments' volume, structure and composition<sup>263,264</sup>. Thereby, the precision control afforded by the use of microfluidics, provides a versatile platform to develop new cell-like functionalities, such as membrane properties<sup>265</sup>, sequential biochemical reactions<sup>266</sup>, cell-free gene expression<sup>267</sup>, and protein synthesis<sup>268</sup>. These are wonderful examples for artificial cell model applications, as earlier discussed, which in fact have been utilised in combination with droplet-microfluidics. For example, Elani, *et al.* 2016 used a hydrophobic and hydrophilic treated PDMS microfluidic device to produce double emulsion multisomes and achieved chemical synthesis through the communicating compartments of the DIB<sup>119</sup>. By using microfluidic technology to produce DIB multisomes, they were able to scale-up their experiments. Similarly, Baxani, *et al.* 2016 utilised custom-made hybrid (3D-printed/glass capillary) microfluidic devices to produce triple emulsion eDIBs, with transmembrane pores embedded in the artificial membranes for communication with the external environment<sup>122</sup>. Hence, microfluidically produced DIBs may be implement in high-throughput artificial cell membrane studies<sup>125</sup>, contact angle investigations<sup>269</sup>, or as stand-alone small bioreactor capsules<sup>124</sup>. Finally, DIB can be trapped in microfluidic wells or arrays for parallel artificial cell membrane studies<sup>270,271</sup>, aiming to evoke lab-on-a-chip applications<sup>106</sup>.

### 1.6.3.3. Cell encapsulation

Multiphase droplet-based microfluidics is a method extensively applied for cell encapsulation, as it is governed by the automated formation of cell-laden droplets<sup>272,273</sup>. High-throughput cell encapsulation techniques are needed for cell and tissue analysis and microfluidics serve as a useful platform<sup>274</sup>. Single cell and multiple cell encapsulation protocols have been established using microfluidics and hydrogels, in order to investigate cellular behaviour within a designated ECM, and to study cell-cell and cell-ECM interactions<sup>275,276</sup>. The application of microfluidics in cell culture studies allows for experimental flexibility and agility, whilst the minimised resource consumption, is of considerable benefit in pharmaceutical research, due to the high costs and demanding precision of drugs<sup>277</sup>.

Entrapped cells in confined hydrogel beads produced using microfluidic technology, can be analysed on or off-chip<sup>274</sup>. The combination of droplet-forming geometries, liquid polymers and biocompatible crosslinking, results in the formation of biological scaffolds for the cellular growth into 3D cultures<sup>278,279</sup>. Relatively simple T-junction microfluidic geometries are widely used for cell encapsulation in hydrogels, due to the increased monodispersity of produced droplets<sup>280,281</sup>. Although, flow-focusing junction geometries are preferred platforms for cell encapsulation, due to the sophisticated control over gelation, protection of cells from potential harmful environments, as well as

the reduced shear stresses applied compared to T-junctions<sup>281–283</sup>. Moreover, the density and viscosity of reagents flowing through microfluidic channels are important parameters that influence the dynamics of cell encapsulation<sup>284</sup>. With the appropriate manipulation of these fluid properties and the droplet-forming geometry, core-shell hydrogel spatial arrangements can be produced for multi-cell line encapsulation towards *in-vitro* organ studies (**Figure 1. 16B**)<sup>232,285,286</sup>. Agarwal, *et al.* 2017 used droplet-based microfluidic devices to form MCF-7 microtumours in a collagen core surrounded by an alginate shell (**Figure 1. 16C**)<sup>194</sup>. These microcapsules were formed at the junction of five microfluidic channels and when these capsules developed microtumours, they assessed anticancer drugs based on 3D vascularisation experiments. Additionally, microfluidic devices like organ-on-a-chip, can integrate complex fluidic circuitry and multi-functionalism that is required for high yield cancer studies<sup>232,277,287</sup>. Therefore, droplet-based microfluidic devices can diversify the architectural format of cell-laden scaffolds to better simulate *in-vivo* tissue complexity<sup>194</sup>, and increase efficiency to target rapid patient-specific treatments (**Figure 1. 16A**)<sup>288</sup>.

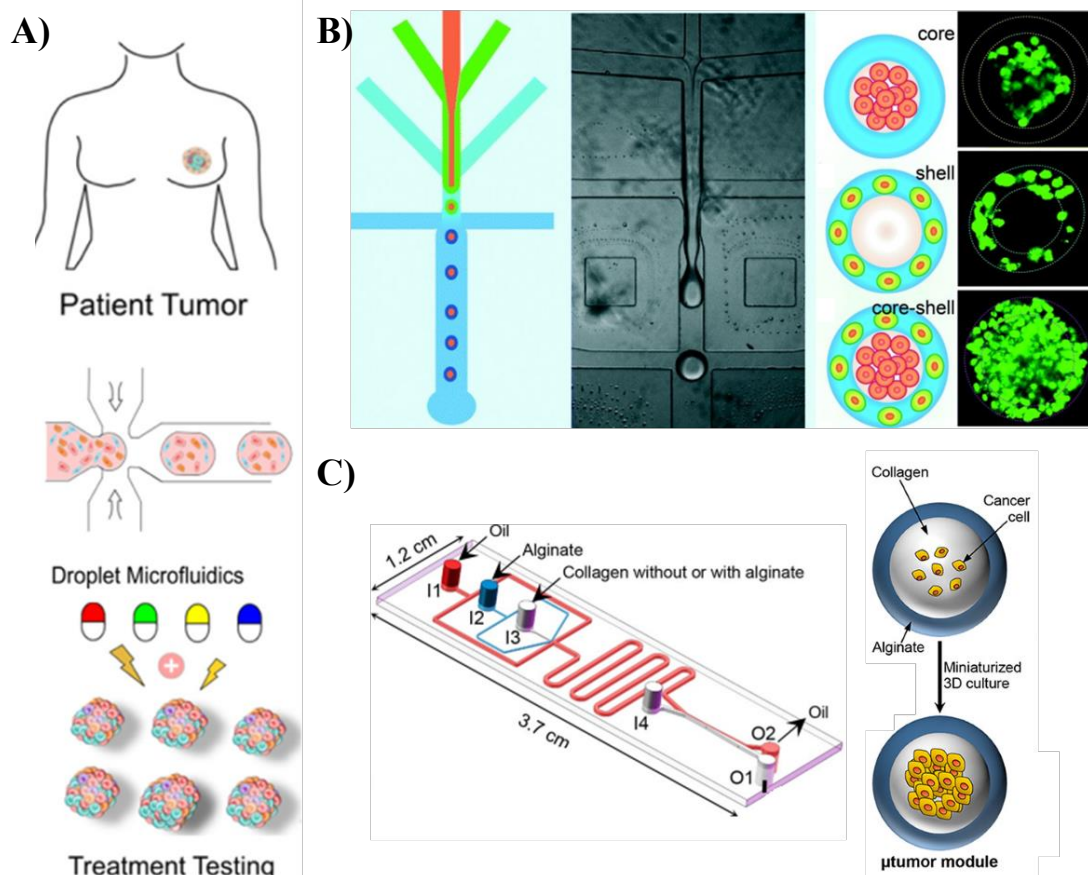


**Figure 1. 16: Cell encapsulation using droplet-forming microfluidic devices and applications.** *A)* The rationale behind the combination of droplet microfluidics, hydrogels, and cancer cell encapsulation in order to produce high-throughput personalised drug treatments. Image adapted from [288]. *B)* Microfluidic assisted formation of liver-in-a-droplet, where different cell lines are encapsulated in the core and shell of the capsule. Image adapted from [285]. *C)* A droplet-forming microfluidics device for the formation of MCTSs in collagen-core and alginate-shell capsules for 3D tumour vascularisation and drug resistance studies. Image adapted from [194].

#### **1.6.3.4. Nanoparticle production**

With more recent advances in nanofabrication, nano-scale droplet-forming junctions can be integrated within conventional microfluidic circuits to produce monodisperse nanoparticles for intracellular drug delivery and preclinical drug screening <sup>289,290</sup>. With advancing new materials and complex emulsion microfluidics, sophisticated microparticles can be constructed with hierarchical structures, towards programmable drug encapsulation with selective release processes. These efforts are one step forward to manufacture smart drug microcarriers that harness on-demand active targeting and enable quantity-controlled release of drugs for cancer therapy.

Depending on the nature and scale of the final product, the fabrication of particles varies. For example, cell-sized polymer and liposomal particles are produced using droplet-forming junctions to control size, monodispersity and structure, as opposed to conventional agitation methods. Although, for drug delivery systems, the scale of particles needs to fall down to the nanoscale, but the channel dimensions and insufficient production frequency of droplet-forming microfluidic devices, make this technology unfit, in most cases. At least this is the case with less sophisticated microfluidic device fabrication methods than nanofabrication <sup>291</sup>. Therefore, polymer and lipid nanoparticles have been produced using microfluidic devices integrated with chaotic advection modules, to improve mixing of aqueous and organic solutions that lead to the formation of the particles <sup>292,293</sup>. Such devices are microfluidic hydrodynamic focusing (MHF) <sup>294</sup>, which rely on the characteristic diffusion length between an aqueous solution and an organic solution, and staggered herringbone micromixers (SHM) <sup>295,296</sup>. Drug-loaded nanoscale polymer particles and liposomes produced using MHF and SHM devices, have reached tumour sites due to their very narrow size, and their sufficient encapsulation efficacy <sup>296,297</sup>, renders them as key contributors in combating cancer.

## 1.7. 3D printing

Fabrication of microfluidic devices in the last 25 to 30 years has been diverse, due to the variable characteristics between fabrication techniques. Photolithography is expensive, time costly and requires a clean room, micromachining utilises expensive equipment and is moderately automatic, while 3D-printing is fast, but yields channels of poor resolution<sup>298</sup>. According to Elvira, *et al.* 2022, up to the year 2021, almost 6000 publications had utilised PDMS microfluidic devices, of which almost 600 articles were related to droplet microfluidics<sup>298</sup>. This signifies that PDMS moulding is worldwide used, due to its biocompatibility, transparency, adaptability with other materials and ease of fabrication<sup>225</sup>. Interestingly, the growing interest in 3D printing has led to its use as a fabrication method in droplet microfluidics, although technical improvements are yet to be made<sup>299</sup>.

Rapid prototyping or 3D printing became a beneficial innovation for many industrial and research areas, including automotive<sup>300</sup>, construction systems<sup>301,302</sup>, biomedical engineering<sup>303–305</sup> and others. The most famously used 3D printing approaches, are stereolithography (SLA) and fused deposition modelling (FDM), also known as fused filament fabrication (FFF). Others include, multiJet modelling (MJM) and selective laser sintering (SLS). The manufacturing processes between the mentioned techniques strongly differ, but they all follow the same principle of layer-by-layer deposition. The layer-by-layer deposition refers to the deposition and solidification process, where one layer of material is deposited and solidified before another layer is added.

Microfluidic devices have been fabricated using SLA and FDM 3D printing<sup>253,306</sup>. During the SLA printing process, UV light is emitted into a bath of photocurable resin to solidify the structure of the designed part (**Figure 1. 17A**), while FFF uses a printing nozzle from which melted plastic is being extruded (**Figure 1. 17B**). As opposed to SLA, FFF devices usually do not require any cleaning, post processing or curing, unless degradable support material was also printed. Hence, FFF 3D-printed microfluidic devices would be ready and functional instantly after printing. Other advantages for making microfluidic devices with FFF, rather than SLA, is the ability to print and fuse multiple materials. This is particularly beneficial in microfluidic formation of multiple emulsions, using plastics of different wetting properties<sup>123</sup>. Additionally, the resolution of SLA printed channels (~100  $\mu\text{m}$ ) is better than that of FFF (~500  $\mu\text{m}$ )<sup>298</sup>, although many have reported clogging of SLA microchannels by the cured resin<sup>307,308</sup>.

The limitations of 3D printing as a technology, make FFF cumbersome to explore as a fabrication technique for microfluidic devices. Lack of transparency and reduced printing resolution of 3D FFF constitute as some of these major challenges<sup>299</sup>. The printing of opaque plastic filaments limits optical characterisation of the fluid flow and on-chip occurring events. However, less opaque filaments, such as PLA and Cyclic olefin copolymer (COC) have been reported to result in microfluidic devices with glass-like bottom surfaces<sup>309,310</sup>. Nevertheless, this method of rapid prototyping offers versatility and multiple material printing, which is indispensable in specific applications of microfluidics.

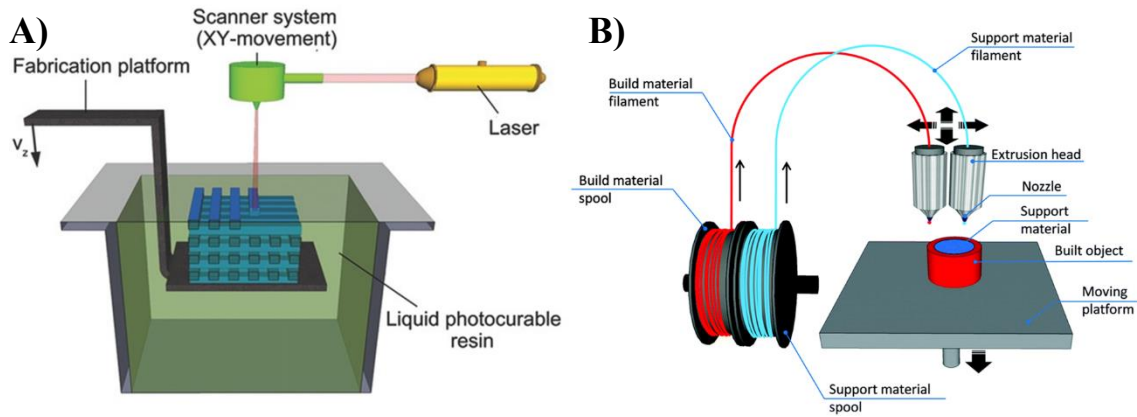


**Figure 1. 17: Schematics of stereolithography (SLA) and fused filament fabrication (FFF) 3D printing methods. A)** For SLA printing, the UV light source is emitted into a bath of resin and crosslinks the resin according to the programmed design. The laser source can be emitted from the top (as shown in the figure) or from the bottom (not shown). Image adapted from <sup>[303]</sup>. **B)** FFF or FDM 3D printing fabricates the designed dual-material part by melting the plastic filament material and extruding it from the nozzle onto a moving platform. Image adapted from <sup>[301]</sup>.

Foreseen enhancements of affordable 3D printing technologies would benefit multidisciplinary laboratories around the world to explore the application of microfluidic circuits. Droplet microfluidic devices in fields like cell encapsulation and synthetic biology, would replace the repeated manual pipetting with automated system production. Additionally, 3D printing would be valued in research that requires proof of concept and prototypes, before advancing to more complicated manufacturing approaches.

## 1.8. Conclusion and scope of thesis

Based on the overview of the current literature, we have entered a generation of advanced systems in synthetic biology and *in-vitro* tumour investigation. Research within the field of synthetic biology has made remarkable advancements in the construction of artificial cells and membrane models from non-living matter, thus the next step would be the integration with matured living systems. Exploring and mimicking functionalities of living cells, and the development of novel and programmable drug carriers are some of the focuses within the area of artificial cells. The co-culture of tumour spheroids and protocells may have applications in, but not limited to, drug resistance studies. As demonstrated by the literature overview, microfluidic circuits and emulsion-generating devices are powerful tools compatible with applications, such as bioengineering and synthetic biology. Although, prototype fluidic circuit fabrication suffers from long and complicated procedures, which can be resolved with rapid prototyping.

This thesis aims to bring together multiple disciplines including microfluidic engineering, synthetic biology and tissue engineering. The project desired the production of multiple emulsions using monolithic, multi-material, 3D Fused Filament Fabricated (FFF) microfluidic devices, suitable for the formation of artificial cell chassis (i.e., encapsulated Droplet Interface bilayers, eDIBs) and the encapsulation and survival of breast cancer cells. The rest of the thesis comprises of five chapters described below.

In Chapter II, three 3D-printed droplet-forming microfluidic devices were designed and performed. The first microfluidic device was used to produce monodispersed alginate hydrogel microbeads using a filament considered as hydrophobic. The second device produced double emulsion capsules with controlled number of oil cores and an alginate shell using dual-material printing, while the final device was utilised to form triple emulsion eDIB capsules (W/O/W/O). The complex emulsification was established by using surfactants and hydrophobic/hydrophilic filaments.

In Chapter III, the same protocol for eDIB production was employed. The produced eDIBs were characterised in terms of their dimensions and stability under different conditions. Additionally, an on-demand core release (from the eDIBs) protocol was established using lysolipids, which altered the fluidity of the lipid bilayers, leading to the bursting of the inner cores. The effect of lysolipids on the lipid bilayer was also assessed based on electrophysiology traces of a DIB membrane model.

In Chapter IV, all the devices developed in Chapter II were applied for the encapsulation of breast cancer cells and 3D tumour spheroid formation in hydrogel capsules. Collagen type I was also added to the hydrogel. Tumour formation and proliferation was characterised using microscopy and a metabolic assay. 3D tumours in oil-core, hydrogel-shell capsules were treated with an anticancer drug, lysolipids and a fluorescent conjugate. eDIBs encapsulating cells and tumours were assessed in terms of their survival and structural integrity. The chapter then introduces a model named as ‘Droplet

Incubator', as standalone capsules for the encapsulation and co-culture of artificial cell membranes and living cells.

The final Chapter V examines the findings from all the earlier chapters, presents limitations and suggests future work.

## 1.9. References

1. Jiang, W., Wu, Z., Gao, Z., Wan, M., Zhou, M., Mao, C. & Shen, J. Artificial Cells: Past, Present and Future. *ACS Nano* **16**, 15705–15733 (2022).
2. Clegg, J. R., Wagner, A. M., Shin, S. R., Hassan, S., Khademhosseini, A. & Peppas, N. A. Modular fabrication of intelligent material-tissue interfaces for bioinspired and biomimetic devices. *Progress in Materials Science* **106**, 100589 (2019).
3. Lu, Y., Allegri, G. & Huskens, J. Vesicle-based artificial cells: materials, construction methods and applications. *Materials Horizons* **9**, 892–907 (2022).
4. Lee, S. & Bayley, H. Reconstruction of the Gram-Negative Bacterial Outer-Membrane Bilayer. *Small* **18**, 2200007 (2022).
5. Mukwaya, V., Mann, S. & Dou, H. Chemical communication at the synthetic cell/living cell interface. *Commun Chem* **4**, 1–12 (2021).
6. Ran, R., Middelberg, A. P. J. & Zhao, C.-X. Microfluidic synthesis of multifunctional liposomes for tumour targeting. *Colloids and Surfaces B: Biointerfaces* **148**, 402–410 (2016).
7. Sant, S. & Johnston, P. A. The production of 3D tumor spheroids for cancer drug discovery. *Drug Discovery Today: Technologies* **23**, 27–36 (2017).
8. Saraf, S., Jain, A., Tiwari, A., Verma, A., Panda, P. K. & Jain, S. K. Advances in liposomal drug delivery to cancer: An overview. *Journal of Drug Delivery Science and Technology* **56**, 101549 (2020).
9. Dimitriou, P., Li, J., Tornillo, G., McCloy, T. & Barrow, D. Droplet Microfluidics for Tumor Drug-Related Studies and Programmable Artificial Cells. *Global Challenges* **5**, 2000123 (2021).
10. Amirifar, L. *et al.* Droplet-based microfluidics in biomedical applications. *Biofabrication* **14**, 022001 (2022).
11. Ding, Y., Wu, F. & Tan, C. Synthetic Biology: A Bridge between Artificial and Natural Cells. *Life* **4**, 1092–1116 (2014).

12. Virtanen, J. A., Cheng, K. H. & Somerharju, P. Phospholipid composition of the mammalian red cell membrane can be rationalized by a superlattice model. *Proc Natl Acad Sci U S A* **95**, 4964–4969 (1998).
13. Dupuy, A. D. & Engelman, D. M. Protein area occupancy at the center of the red blood cell membrane. *Proc. Natl. Acad. Sci. U.S.A.* **105**, 2848–2852 (2008).
14. Schenkel, L. C. & Bakovic, M. Formation and Regulation of Mitochondrial Membranes. *Int J Cell Biol* **2014**, 709828 (2014).
15. Frolov, V. A., Shnyrova, A. V. & Zimmerberg, J. Lipid Polymorphisms and Membrane Shape. *Cold Spring Harbor Perspectives in Biology* **3**, a004747–a004747 (2011).
16. Levental, I. & Lyman, E. Regulation of membrane protein structure and function by their lipid nano-environment. *Nat Rev Mol Cell Biol* 1–16 (2022).
17. Zhukovsky, M. A., Filograna, A., Luini, A., Corda, D. & Valente, C. Phosphatidic acid in membrane rearrangements. *FEBS Letters* **593**, 2428–2451 (2019).
18. Hafez, I. M. & Cullis, P. R. Roles of lipid polymorphism in intracellular delivery. *Advanced Drug Delivery Reviews* **47**, 139–148 (2001).
19. Thompson, J. R., Heron, A. J., Santoso, Y. & Wallace, M. I. Enhanced Stability and Fluidity in Droplet on Hydrogel Bilayers for Measuring Membrane Protein Diffusion. *Nano Lett.* **7**, 3875–3878 (2007).
20. Los, D. A., Mironov, K. S. & Allakhverdiev, S. I. Regulatory role of membrane fluidity in gene expression and physiological functions. *Photosynth Res* **116**, 489–509 (2013).
21. Ballweg, S. & Ernst, R. Control of membrane fluidity: the OLE pathway in focus. *Biological Chemistry* **398**, 215–228 (2017).
22. Harayama, T. & Riezman, H. Understanding the diversity of membrane lipid composition. *Nat Rev Mol Cell Biol* **19**, 281–296 (2018).
23. Yang, S.-T., Kreutzberger, A. J. B., Lee, J., Kiessling, V. & Tamm, L. K. The role of cholesterol in membrane fusion. *Chem Phys Lipids* **199**, 136–143 (2016).
24. Chang, T. M. S. 1957 Report on “Method for Preparing Artificial Hemoglobin Corpuscles”. *Artificial Cells* (2007).

25. Artificial cells: from basic science to applications. *Materials Today* **19**, 516–532 (2016).
26. Parrilla-Gutierrez, J. M., Tsuda, S., Grizou, J., Taylor, J., Henson, A. & Cronin, L. Adaptive artificial evolution of droplet protocells in a 3D-printed fluidic chemorobotic platform with configurable environments. *Nature Communications* **8**, 1144 (2017).
27. Lyu, Y., Peng, R., Liu, H., Kuai, H., Mo, L., Han, D., Li, J. & Tan, W. Protocells programmed through artificial reaction networks. *Chem. Sci.* **11**, 631–642 (2020).
28. Powell, K. Biology from Scratch. *Nature* **563**, 172–175 (2018).
29. Lombardo, D., Calandra, P., Pasqua, L. & Magazù, S. Self-Assembly of Organic Nanomaterials and Biomaterials: The Bottom-Up Approach for Functional Nanostructures Formation and Advanced Applications. *Materials (Basel)* **13**, (2020).
30. Song, Y., Michaels, T. C. T., Ma, Q., Liu, Z., Yuan, H., Takayama, S., Knowles, T. P. J. & Shum, H. C. Budding-like division of all-aqueous emulsion droplets modulated by networks of protein nanofibrils. *Nature Communications* **9**, 2110 (2018).
31. Martin, N., Douliez, J.-P., Qiao, Y., Booth, R., Li, M. & Mann, S. Antagonistic chemical coupling in self-reconfigurable host–guest protocells. *Nature Communications* **9**, 3652 (2018).
32. Kamiya, K. & Takeuchi, S. Giant liposome formation toward the synthesis of well-defined artificial cells. *J. Mater. Chem. B* **5**, 5911–5923 (2017).
33. Seo, H. & Lee, H. Spatiotemporal control of signal-driven enzymatic reaction in artificial cell-like polymersomes. *Nat Commun* **13**, 5179 (2022).
34. Zhao, C., Zhu, M., Fang, Y., Liu, X., Wang, L., Chen, D. & Huang, X. Engineering proteinosomes with renewable predatory behaviour towards living organisms. *Materials Horizons* **7**, 157–163 (2020).
35. Park, J. H., Galanti, A., Ayling, I., Rochat, S., Workentin, M. S. & Gobbo, P. Colloidosomes as a Protocell Model: Engineering Life-Like Behaviour through Organic Chemistry. *European Journal of Organic Chemistry* **2022**, e202200968 (2022).
36. Zhang, Y., Chen, Y., Yang, X., He, X., Li, M., Liu, S., Wang, K., Liu, J. & Mann, S. Giant Coacervate Vesicles As an Integrated Approach to Cytomimetic Modeling. *J. Am. Chem. Soc.* **143**, 2866–2874 (2021).

- 
37. Phase Transition Temperatures for Glycerophospholipids. *Avanti Polar Lipids*  
<https://avantilipids.com/tech-support/physical-properties/phase-transition-temps>.
  38. Perez Jimenez, A. I., Challier, L., Aït-Yahiatène, E., Delacotte, J., Labbé, E. & Buriez, O. Selective Electrochemical Bleaching of the Outer Leaflet of Fluorescently Labeled Giant Liposomes. *Chemistry – A European Journal* **23**, 6781–6787 (2017).
  39. Elani, Y., Gee, A., Law, R. V. & Ces, O. Engineering multi-compartment vesicle networks. *Chem. Sci.* **4**, 3332–3338 (2013).
  40. Hindley, J. W., Law, R. V. & Ces, O. Membrane functionalization in artificial cell engineering. *SN Appl. Sci.* **2**, 593 (2020).
  41. Gaur, D., Dubey, N. C. & Tripathi, B. P. Biocatalytic self-assembled synthetic vesicles and coacervates: From single compartment to artificial cells. *Advances in Colloid and Interface Science* **299**, 102566 (2022).
  42. Yu, W., Sato, K., Wakabayashi, M., Nakaishi, T., Ko-Mitamura, E. P., Shima, Y., Urabe, I. & Yomo, T. Synthesis of functional protein in liposome. *J Biosci Bioeng* **92**, 590–593 (2001).
  43. Stano, P. Gene Expression Inside Liposomes: From Early Studies to Current Protocols. *Chemistry – A European Journal* **25**, 7798–7814 (2019).
  44. Hamada, S., Tabuchi, M., Toyota, T., Sakurai, T., Hosoi, T., Nomoto, T., Nakatani, K., Fujinami, M. & Kanzaki, R. Giant vesicles functionally expressing membrane receptors for an insect pheromone. *Chem. Commun.* **50**, 2958–2961 (2014).
  45. Kuruma, Y., Stano, P., Ueda, T. & Luisi, P. L. A synthetic biology approach to the construction of membrane proteins in semi-synthetic minimal cells. *Biochim Biophys Acta* **1788**, 567–574 (2009).
  46. Zhu, T. F. & Szostak, J. W. Coupled Growth and Division of Model protocell membranes. *J. Am. Chem. Soc.* **131**, 5705–5713 (2009).
  47. Sakuma, Y., Taniguchi, T. & Imai, M. Pore Formation in a Binary Giant Vesicle Induced by Cone-Shaped Lipids. *Biophysical Journal* **99**, 472–479 (2010).
  48. Watanabe, M., Tomita, T. & Yasuda, T. Membrane-damaging action of staphylococcal alpha-toxin on phospholipid-cholesterol liposomes. *Biochim Biophys Acta* **898**, 257–265 (1987).

49. Valeva, A. *et al.* Evidence that clustered phosphocholine head groups serve as sites for binding and assembly of an oligomeric protein pore. *J Biol Chem* **281**, 26014–26021 (2006).
50. Hilburger, C. E., Jacobs, M. L., Lewis, K. R., Peruzzi, J. A. & Kamat, N. P. Controlling Secretion in Artificial Cells with a Membrane AND Gate. *ACS Synth. Biol.* **8**, 1224–1230 (2019).
51. Rampioni, G., D'Angelo, F., Leoni, L. & Stano, P. Gene-Expressing Liposomes as Synthetic Cells for Molecular Communication Studies. *Frontiers in Bioengineering and Biotechnology* **7**, (2019).
52. Vibhute, M. A., Schaap, M. H., Maas, R. J. M., Nelissen, F. H. T., Spruijt, E., Heus, H. A., Hansen, M. M. K. & Huck, W. T. S. Transcription and Translation in Cytomimetic Protocells Perform Most Efficiently at Distinct Macromolecular Crowding Conditions. *ACS Synth. Biol.* **9**, 2797–2807 (2020).
53. Fukumoto, M. & Tonooka, T. Construction of an Artificial Cell Capable of Protein Expression at Low Temperatures Using a Cell Extract Derived from *Pseudomonas fluorescens*. *Processes* **9**, 212 (2021).
54. Dwidar, M., Seike, Y., Kobori, S., Whitaker, C., Matsuura, T. & Yokobayashi, Y. Programmable Artificial Cells Using Histamine-Responsive Synthetic Riboswitch. *J. Am. Chem. Soc.* **141**, 11103–11114 (2019).
55. Peruzzi, J. A., Galvez, N. R. & Kamat, N. P. Engineering transmembrane signal transduction in synthetic membranes using two-component systems. 2022.10.30.514420 Preprint at <https://doi.org/10.1101/2022.10.30.514420> (2022).
56. Chen, C., Wang, X., Wang, Y., Tian, L. & Cao, J. Construction of protocell-based artificial signal transduction pathways. *Chem. Commun.* **57**, 12754–12763 (2021).
57. Buddingh', B. C., Elzinga, J. & van Hest, J. C. M. Intercellular communication between artificial cells by allosteric amplification of a molecular signal. *Nat Commun* **11**, (2020).
58. Chakraborty, T. & Wegner, S. V. Cell to Cell Signaling through Light in Artificial Cell Communities: Glowing Predator Lures Prey. *ACS Nano* **15**, 9434–9444 (2021).
59. Arrabito, G., Ferrara, V., Bonasera, A. & Pignataro, B. Artificial Biosystems by Printing Biology. *Small* **16**, 1907691 (2020).

60. Mj, Y.-D., M, G.-G., C, L., Aj, U., Tl, A. & L, H.-R. Recent advances in compartmentalized synthetic architectures as drug carriers, cell mimics and artificial organelles. *Colloids Surf B Biointerfaces* **152**, 199–213 (2017).
61. Fang, R. H., Hu, C.-M. J., Luk, B. T., Gao, W., Copp, J. A., Tai, Y., O'Connor, D. E. & Zhang, L. Cancer Cell Membrane-Coated Nanoparticles for Anticancer Vaccination and Drug Delivery. *Nano Lett.* **14**, 2181–2188 (2014).
62. Deng, N.-N., Yelleswarapu, M., Zheng, L. & Huck, W. T. S. Microfluidic Assembly of Monodisperse Vesosomes as Artificial Cell Models. *J. Am. Chem. Soc.* **139**, 587–590 (2017).
63. Lussier, F., Staufer, O., Platzman, I. & Spatz, J. P. Can Bottom-Up Synthetic Biology Generate Advanced Drug-Delivery Systems? *Trends in Biotechnology* **39**, 445–459 (2021).
64. Sun, H., Guo, X., Zeng, S., Wang, Y., Hou, J., Yang, D. & Zhou, S. A multifunctional liposomal nanoplatform co-delivering hydrophobic and hydrophilic doxorubicin for complete eradication of xenografted tumors. *Nanoscale* **11**, 17759–17772 (2019).
65. Yatvin, M., Weinstein, J., Dennis, W. & Blumenthal, R. Design of liposomes for enhanced local release of drugs by hyperthermia. *Science* **202**, 1290–1293 (1978).
66. Sandstrom, M., Ickenstein, L., Mayer, L. & Edwards, K. Effects of lipid segregation and lysolipid dissociation on drug release from thermosensitive liposomes. *Journal of Controlled Release* **107**, 131–142 (2005).
67. Lu, T. & ten Hagen, T. L. M. Inhomogeneous crystal grain formation in DPPC-DSPC based thermosensitive liposomes determines content release kinetics. *Journal of Controlled Release* **247**, 64–72 (2017).
68. Gray, M. D. *et al.* Focused Ultrasound Hyperthermia for Targeted Drug Release from Thermosensitive Liposomes: Results from a Phase I Trial. *Radiology* **291**, 232–238 (2019).
69. Wang, L., Zhu, B., Huang, J., Xiang, X., Tang, Y., Ma, L., Yan, F., Cheng, C. & Qiu, L. Ultrasound-targeted microbubble destruction augmented synergistic therapy of rheumatoid arthritis via targeted liposomes. *J. Mater. Chem. B* **8**, 5245–5256 (2020).

70. Hardiansyah, A., Yang, M.-C., Liu, T.-Y., Kuo, C.-Y., Huang, L.-Y. & Chan, T.-Y. Hydrophobic Drug-Loaded PEGylated Magnetic Liposomes for Drug-Controlled Release. *Nanoscale Research Letters* **12**, 355 (2017).
71. Vlasova, K. Yu. *et al.* Magnetic liposome design for drug release systems responsive to super-low frequency alternating current magnetic field (AC MF). *Journal of Colloid and Interface Science* **552**, 689–700 (2019).
72. Wiraja, C., Mathiyazhakan, M., Movahedi, F., Upputuri, P. K., Cheng, Y., Pramanik, M., Yang, L., Becker, D. L. & Xu, C. Near-infrared light-sensitive liposomes for enhanced plasmid DNA transfection. *Bioengineering & Translational Medicine* **1**, 357–364 (2016).
73. Shen, S. *et al.* Magnetic liposomes for light-sensitive drug delivery and combined photothermal–chemotherapy of tumors. *J. Mater. Chem. B* **7**, 1096–1106 (2019).
74. Sharma, N. & Kumar, V. A NOVEL CLASS OF PHOTOTRIGGERABLE LIPOSOMES CONTAINING PACLITAXEL FOR THE TREATMENT OF SKIN CANCER. *Journal of Drug Delivery and Therapeutics* **7**, 1–3 (2017).
75. Alavi, M. & Hamidi, M. Passive and active targeting in cancer therapy by liposomes and lipid nanoparticles. *Drug Metabolism and Personalized Therapy* **34**, (2019).
76. Liu, Y., Chen, X.-G., Yang, P.-P., Qiao, Z.-Y. & Wang, H. Tumor Microenvironmental pH and Enzyme Dual Responsive Polymer-Liposomes for Synergistic Treatment of Cancer Immuno-Chemotherapy. *Biomacromolecules* **20**, 882–892 (2019).
77. Attia, M. F., Anton, N., Wallyn, J., Omran, Z. & Vandamme, T. F. An overview of active and passive targeting strategies to improve the nanocarriers efficiency to tumour sites. *Journal of Pharmacy and Pharmacology* **71**, 1185–1198 (2019).
78. Moosavian, S. A. & Sahebkar, A. Aptamer-functionalized liposomes for targeted cancer therapy. *Cancer Letters* **448**, 144–154 (2019).
79. Wei, Y., Gu, X., Sun, Y., Meng, F., Storm, G. & Zhong, Z. Transferrin-binding peptide functionalized polymersomes mediate targeted doxorubicin delivery to colorectal cancer in vivo. *Journal of Controlled Release* **319**, 407–415 (2020).

80. Haeri, A., Zalba, S., ten Hagen, T. L. M., Dadashzadeh, S. & Koning, G. A. EGFR targeted thermosensitive liposomes: A novel multifunctional platform for simultaneous tumor targeted and stimulus responsive drug delivery. *Colloids and Surfaces B: Biointerfaces* **146**, 657–669 (2016).
81. Behravan, N., Zahedipour, F., Jaafari, M. R., Johnston, T. P. & Sahebkar, A. Lipid-based nanoparticulate delivery systems for HER2-positive breast cancer immunotherapy. *Life Sciences* **291**, 120294 (2022).
82. Jain, A. & Jain, S. K. Advances in Tumor Targeted Liposomes. *CMM* **18**, 44–57 (2018).
83. Mu, L.-M., Ju, R.-J., Liu, R., Bu, Y.-Z., Zhang, J.-Y., Li, X.-Q., Zeng, F. & Lu, W.-L. Dual-functional drug liposomes in treatment of resistant cancers. *Advanced Drug Delivery Reviews* **115**, 46–56 (2017).
84. Jose, A., Ninave, K. M., Karnam, S. & Venuganti, V. V. K. Temperature-sensitive liposomes for co-delivery of tamoxifen and imatinib for synergistic breast cancer treatment. *Journal of Liposome Research* **29**, 153–162 (2019).
85. El-Beyrouthy, J. & Freeman, E. Characterizing the Structure and Interactions of Model Lipid Membranes Using Electrophysiology. *Membranes* **11**, 319 (2021).
86. Hamill, O. P., Marty, A., Neher, E., Sakmann, B. & Sigworth, F. J. Improved patch-clamp techniques for high-resolution current recording from cells and cell-free membrane patches. *Pflugers Arch.* **391**, 85–100 (1981).
87. Taylor, G., Nguyen, M.-A., Koner, S., Freeman, E., Collier, C. P. & Sarles, S. A. Electrophysiological interrogation of asymmetric droplet interface bilayers reveals surface-bound alamethicin induces lipid flip-flop. *Biochimica et Biophysica Acta (BBA) - Biomembranes* **1861**, 335–343 (2019).
88. Attwood, S. J., Choi, Y. & Leonenko, Z. Preparation of DOPC and DPPC Supported Planar Lipid Bilayers for Atomic Force Microscopy and Atomic Force Spectroscopy. *Int J Mol Sci* **14**, 3514–3539 (2013).
89. Galush, W. J., Nye, J. A. & Groves, J. T. Quantitative Fluorescence Microscopy Using Supported Lipid Bilayer Standards. *Biophysical Journal* **95**, 2512–2519 (2008).

90. Hardy, G. J., Nayak, R. & Zauscher, S. Model cell membranes: Techniques to form complex biomimetic supported lipid bilayers via vesicle fusion. *Current Opinion in Colloid & Interface Science* **18**, 448–458 (2013).
91. Lind, T. K., Cárdenas, M. & Wacklin, H. P. Formation of Supported Lipid Bilayers by Vesicle Fusion: Effect of Deposition Temperature. *Langmuir* **30**, 7259–7263 (2014).
92. Jackman, J. A. & Cho, N.-J. Supported Lipid Bilayer Formation: Beyond Vesicle Fusion. *Langmuir* **36**, 1387–1400 (2020).
93. Sut, T. N., Yoon, B. K., Jeon, W.-Y., Jackman, J. A. & Cho, N.-J. Supported lipid bilayer coatings: Fabrication, bioconjugation, and diagnostic applications. *Applied Materials Today* **25**, 101183 (2021).
94. Parperis, C. & Wallace, M. I. Chapter Fifteen - Single-molecule imaging of pore-forming toxin dynamics in droplet interface bilayers. in *Methods in Enzymology* (ed. Heuck, A. P.) vol. 649 431–459 (Academic Press, 2021).
95. Heron, A. J., Thompson, J. R., Mason, A. E. & Wallace, M. I. Direct Detection of Membrane Channels from Gels Using Water-in-Oil Droplet Bilayers. *J. Am. Chem. Soc.* **129**, 16042–16047 (2007).
96. Rosholm, K. R., Baker, M. A. B., Ridone, P., Nakayama, Y., Rohde, P. R., Cuello, L. G., Lee, L. K. & Martinac, B. Activation of the mechanosensitive ion channel MscL by mechanical stimulation of supported Droplet-Hydrogel bilayers. *Sci Rep* **7**, 45180 (2017).
97. Senior, M. J. T., Monico, C., Weatherill, E. E., Gilbert, R. J., Heuck, A. P. & Wallace, M. I. Single-molecule tracking of perfringolysin O assembly and membrane insertion uncoupling. *The FEBS Journal* **290**, 428–441 (2023).
98. Leptihn, S., Thompson, J. R., Ellory, J. C., Tucker, S. J. & Wallace, M. I. In Vitro Reconstitution of Eukaryotic Ion Channels Using Droplet Interface Bilayers. *J. Am. Chem. Soc.* **133**, 9370–9375 (2011).
99. Bruin, A. de, S. Friddin, M., Elani, Y., J. Brooks, N., V. Law, R., M. Seddon, J. & Ces, O. A transparent 3D printed device for assembling droplet hydrogel bilayers (DHBs). *RSC Advances* **7**, 47796–47800 (2017).

100. Bayley, H., Cronin, B., Heron, A., Holden, M. A., Hwang, W., Syeda, R., Thompson, J. & Wallace, M. Droplet interface bilayers. *Mol Biosyst* **4**, 1191–1208 (2008).
101. Hwang, W. L., Chen, M., Cronin, B., Holden, M. A. & Bayley, H. Asymmetric Droplet Interface Bilayers. *J. Am. Chem. Soc.* **130**, 5878–5879 (2008).
102. E. Allen, M., Albon, J. & Elani, Y. Layer-by-layer assembly of multi-layered droplet interface bilayers (multi-DIBs). *Chemical Communications* **58**, 60–63 (2022).
103. Ip, T., Li, Q., Brooks, N. & Elani, Y. Manufacture of Multilayered Artificial Cell Membranes through Sequential Bilayer Deposition on Emulsion Templates. *ChemBioChem* **22**, 2275–2281 (2021).
104. Gehan, P. *et al.* Penetratin translocation mechanism through asymmetric droplet interface bilayers. *Biochimica et Biophysica Acta (BBA) - Biomembranes* **1862**, 183415 (2020).
105. Faugeras, V., Duclos, O., Bazile, D. & Thiam, A. R. Membrane determinants for the passive translocation of analytes through droplet interface bilayers. *Soft Matter* **16**, 5970–5980 (2020).
106. Strutt, R., Sheffield, F., E. Barlow, N., J. Flemming, A., D. Harling, J., V. Law, R., J. Brooks, N., C. Barter, L. M. & Ces, O. UV-DIB: label-free permeability determination using droplet interface bilayers. *Lab on a Chip* **22**, 972–985 (2022).
107. Makhoul-Mansour, M. M., El-Beyrouthy, J. B., Mao, L. & Freeman, E. C. Enhancing membrane-based soft materials with magnetic reconfiguration events. *Sci Rep* **12**, 1703 (2022).
108. Li, J. *et al.* Building programmable multicompartment artificial cells incorporating remotely activated protein channels using microfluidics and acoustic levitation. *Nat Commun* **13**, 4125 (2022).
109. Barriga, H. M. G., Booth, P., Haylock, S., Bazin, R., Templer, R. H. & Ces, O. Droplet interface bilayer reconstitution and activity measurement of the mechanosensitive channel of large conductance from *Escherichia coli*. *J. R. Soc. Interface.* **11**, 20140404 (2014).
110. Haylock, S., Friddin, M. S., Hindley, J. W., Rodriguez, E., Charalambous, K., Booth, P. J., Barter, L. M. C. & Ces, O. Membrane protein mediated bilayer communication in networks of droplet interface bilayers. *Commun Chem* **3**, 1–8 (2020).

111. Najem, J. S., Dunlap, M. D., Rowe, I. D., Freeman, E. C., Grant, J. W., Sukharev, S. & Leo, D. J. Activation of bacterial channel MscL in mechanically stimulated droplet interface bilayers. *Sci Rep* **5**, 13726 (2015).
112. Strutt, R., Hindley, J. W., Gregg, J., Booth, P. J., Harling, J. D., Law, R. V., Friddin, M. S. & Ces, O. Activating mechanosensitive channels embedded in droplet interface bilayers using membrane asymmetry. *Chem. Sci.* **12**, 2138–2145 (2021).
113. Booth, M. J., Restrepo Schild, V., Box, S. J. & Bayley, H. Light-patterning of synthetic tissues with single droplet resolution. *Sci Rep* **7**, (2017).
114. Allen-Benton, M., Findlay, H. E. & Booth, P. J. Probing membrane protein properties using droplet interface bilayers. *Exp Biol Med (Maywood)* **244**, 709–720 (2019).
115. Hoskin, C. E. G., Schild, V. R., Vinals, J. & Bayley, H. Parallel transmission in a synthetic nerve. *Nat. Chem.* **14**, 650–657 (2022).
116. Villar, G., Heron, A. J. & Bayley, H. Formation of droplet networks that function in aqueous environments. *Nat Nanotechnol* **6**, 803–808 (2011).
117. Villar, G. & Bayley, H. Functional Droplet Interface Bilayers. in *Encyclopedia of Biophysics* (ed. Roberts, G. C. K.) 861–868 (Springer, 2013).
118. Cazimoglu, I., Booth, M. J. & Bayley, H. A Lipid-Based Droplet Processor for Parallel Chemical Signals. *ACS Nano* **15**, 20214–20224 (2021).
119. Elani, Y., Solvas, X. C. I., Edel, J. B., Law, R. V. & Ces, O. Microfluidic generation of encapsulated droplet interface bilayer networks (multisomes) and their use as cell-like reactors. *Chem. Commun.* **52**, 5961–5964 (2016).
120. Booth, M. J., Cazimoglu, I. & Bayley, H. Controlled deprotection and release of a small molecule from a compartmented synthetic tissue module. *Commun Chem* **2**, 142 (2019).
121. Bayoumi, M., Bayley, H., Maglia, G. & Sapro, K. T. Multi-compartment encapsulation of communicating droplets and droplet networks in hydrogel as a model for artificial cells. *Sci Rep* **7**, 45167 (2017).

122. Baxani, D. K., Morgan, A. J. L., Jamieson, W. D., Allender, C. J., Barrow, D. A. & Castell, O. K. Bilayer Networks within a Hydrogel Shell: A Robust Chassis for Artificial Cells and a Platform for Membrane Studies. *Angewandte Chemie International Edition* **55**, 14240–14245 (2016).
123. Li, J., Baxani, D. K., Jamieson, W. D., Xu, W., Rocha, V. G., Barrow, D. A. & Castell, O. K. Formation of Polarized, Functional Artificial Cells from Compartmentalized Droplet Networks and Nanomaterials, Using One-Step, Dual-Material 3D-Printed Microfluidics. *Advanced Science* **7**, 1901719 (2020).
124. Hardinge, P., Baxani, D. K., McCloy, T., Murray, J. A. H. & Castell, O. K. Bioluminescent detection of isothermal DNA amplification in microfluidic generated droplets and artificial cells. *Sci Rep* **10**, 21886 (2020).
125. Baxani, D. K., Jamieson, W. D., Barrow, D. A. & Castell, O. K. Encapsulated droplet interface bilayers as a platform for high-throughput membrane studies. *Soft Matter* **18**, 5089–5096 (2022).
126. Nie, D. *et al.* Cancer-Cell-Membrane-Coated Nanoparticles with a Yolk–Shell Structure Augment Cancer Chemotherapy. *Nano Lett.* **20**, 936–946 (2020).
127. Jin, J. & Bhujwalla, Z. M. Biomimetic Nanoparticles Camouflaged in Cancer Cell Membranes and Their Applications in Cancer Theranostics. *Frontiers in Oncology* **9**, (2020).
128. Hu, C.-M. J., Zhang, L., Aryal, S., Cheung, C., Fang, R. H. & Zhang, L. Erythrocyte membrane-camouflaged polymeric nanoparticles as a biomimetic delivery platform. *Proceedings of the National Academy of Sciences* **108**, 10980–10985 (2011).
129. Merkel, T. J. *et al.* Using mechanobiological mimicry of red blood cells to extend circulation times of hydrogel microparticles. *Proc Natl Acad Sci U S A* **108**, 586–591 (2011).
130. Lentini, R. *et al.* Integrating artificial with natural cells to translate chemical messages that direct E. coli behaviour. *Nat Commun* **5**, (2014).
131. Gardner, P. M., Winzer, K. & Davis, B. G. Sugar synthesis in a protocellular model leads to a cell signalling response in bacteria. *Nature Chem* **1**, 377–383 (2009).
132. Schwarz-Schilling, M., Aufinger, L., Mückl, A. & Simmel, F. C. Chemical communication between bacteria and cell-free gene expression systems within linear chains of emulsion droplets. *Integrative Biology* **8**, 564–570 (2016).

133. Lentini, R. *et al.* Two-Way Chemical Communication between Artificial and Natural Cells. *ACS Cent. Sci.* **3**, 117–123 (2017).
134. Xu, C., Martin, N., Li, M. & Mann, S. Living material assembly of bacteriogenic protocells. *Nature* **609**, 1029–1037 (2022).
135. Gispert, I., Hindley, J. W., Pilkington, C. P., Shree, H., Barter, L. M. C., Ces, O. & Elani, Y. Stimuli-responsive vesicles as distributed artificial organelles for bacterial activation. *Proc. Natl. Acad. Sci. U.S.A.* **119**, e2206563119 (2022).
136. Jahnke, K. *et al.* Proton gradients from light-harvesting *E. coli* control DNA assemblies for synthetic cells. *Nat Commun* **12**, 3967 (2021).
137. Campàs, O. *et al.* Quantifying cell-generated mechanical forces within living embryonic tissues. *Nature Methods* **11**, 183–189 (2014).
138. Suzuki, Lee, Loew, Takahashi-Inose, Okuda-Shimazaki, Kojima, Mori, Tsugawa, W. & Sode, K. Engineered Glucose Oxidase Capable of Quasi-Direct Electron Transfer after a Quick-and-Easy Modification with a Mediator. *International Journal of Molecular Sciences* **21**, 1137 (2020).
139. Elani, Y. Interfacing Living and Synthetic Cells as an Emerging Frontier in Synthetic Biology. *Angew Chem Int Ed Engl* **60**, 5602–5611 (2021).
140. Qian, X., Westensee, I. N., Fernandes, C. C. & Städler, B. Enzyme Mimic Facilitated Artificial Cell to Mammalian Cell Signal Transfer. *Angewandte Chemie International Edition* **60**, 18704–18711 (2021).
141. Westensee, I. N., Brodzkij, E., Qian, X., Marcelino, T. F., Lefkimmatis, K. & Städler, B. Mitochondria Encapsulation in Hydrogel-Based Artificial Cells as ATP Producing Subunits. *Small* **17**, 2007959 (2021).
142. Wang, X., Tian, L., Du, H., Li, M., Mu, W., Drinkwater, B. W., Han, X. & Mann, S. Chemical communication in spatially organized protocell colonies and protocell/living cell micro-arrays. *Chem. Sci.* **10**, 9446–9453 (2019).
143. Wang, X., Tian, L., Ren, Y., Zhao, Z., Du, H., Zhang, Z., Drinkwater, B. W., Mann, S. & Han, X. Chemical Information Exchange in Organized Protocells and Natural Cell Assemblies with Controllable Spatial Positions. *Small* **16**, 1906394 (2020).

144. Elani, Y., Trantidou, T., Wylie, D., Dekker, L., Polizzi, K., Law, R. V. & Ces, O. Constructing vesicle-based artificial cells with embedded living cells as organelle-like modules. *Scientific Reports* **8**, 4564 (2018).
145. Yang, B., Li, S., Mu, W., Wang, Z. & Han, X. Light-Harvesting Artificial Cells Containing Cyanobacteria for CO<sub>2</sub> Fixation and Further Metabolism Mimicking. *Small* **n/a**, 2201305 (2022).
146. Jahnke, K., Weiss, M., Frey, C., Antona, S., Janiesch, J.-W., Platzman, I., Göpfrich, K. & Spatz, J. P. Programmable Functionalization of Surfactant-Stabilized Microfluidic Droplets via DNA-Tags. *Advanced Functional Materials* **29**, 1808647 (2019).
147. Streuli, C. Extracellular matrix remodelling and cellular differentiation. *Current Opinion in Cell Biology* **11**, 634–640 (1999).
148. Jain, D., Mattiassi, S., Goh, E. L. & Yim, E. K. F. Extracellular matrix and biomimetic engineering microenvironment for neuronal differentiation. *Neural Regen Res* **15**, 573–585 (2019).
149. Toparlak, O. D. & Mansy, S. S. Progress in synthesizing protocells. *Exp Biol Med (Maywood)* **244**, 304–313 (2019).
150. Alcinesio, A., Meacock, O. J., Allan, R. G., Monico, C., Restrepo Schild, V., Cazimoglu, I., Cornall, M. T., Krishna Kumar, R. & Bayley, H. Controlled packing and single-droplet resolution of 3D-printed functional synthetic tissues. *Nature Communications* **11**, 2105 (2020).
151. Challita, E. J., Najem, J. S., Monroe, R., Leo, D. J. & Freeman, E. C. Encapsulating Networks of Droplet Interface Bilayers in a Thermoreversible Organogel. *Sci Rep* **8**, (2018).
152. Gobbo, P., Patil, A. J., Li, M., Harniman, R., Briscoe, W. H. & Mann, S. Programmed assembly of synthetic protocells into thermoresponsive prototissues. *Nature Materials* **17**, 1145–1153 (2018).
153. Li, Q., Li, S., Zhang, X., Xu, W. & Han, X. Programmed magnetic manipulation of vesicles into spatially coded prototissue architectures arrays. *Nature Communications* **11**, 232 (2020).
154. Zhou, L., Wolfes, A. C., Li, Y., Chan, D. C. W., Ko, H., Szele, F. G. & Bayley, H. Lipid-Bilayer-Supported 3D Printing of Human Cerebral Cortex Cells Reveals Developmental Interactions. *Advanced Materials* **32**, 2002183 (2020).

155. Villar, G., Graham, A. D. & Bayley, H. A Tissue-Like Printed Material. *Science* **340**, 48–52 (2013).
156. Murphy, S. V. & Atala, A. 3D bioprinting of tissues and organs. *Nature Biotechnology* **32**, 773–785 (2014).
157. Booth, M. J. & Bayley, H. 3D-printed synthetic tissues. *The Biochemist* **38**, 16–19 (2016).
158. Graham, A. D. *et al.* High-Resolution Patterned Cellular Constructs by Droplet-Based 3D Printing. *Scientific Reports* **7**, 7004 (2017).
159. Krishna Kumar, R. *et al.* Droplet printing reveals the importance of micron-scale structure for bacterial ecology. *Nat Commun* **12**, 857 (2021).
160. Alcinesio, A., Cazimoglu, I., Kimmerly, G. R., Restrepo Schild, V., Krishna Kumar, R. & Bayley, H. Modular Synthetic Tissues from 3D-Printed Building Blocks. *Advanced Functional Materials* **32**, 2107773 (2022).
161. Alcinesio, A., Krishna Kumar, R. & Bayley, H. Functional Multivesicular Structures with Controlled Architecture from 3D-Printed Droplet Networks. *ChemSystemsChem* **4**, e202100036 (2022).
162. Boyd, M. A. & Kamat, N. P. Designing Artificial Cells towards a New Generation of Biosensors. *Trends Biotechnol* **39**, 927–939 (2021).
163. Zhang, S., Contini, C., Hindley, J. W., Bolognesi, G., Elani, Y. & Ces, O. Engineering motile aqueous phase-separated droplets via liposome stabilisation. *Nat Commun* **12**, 1673 (2021).
164. Diltemiz, S. E., Tavafoghi, M., Barros, N. R. de, Kanada, M., Heinämäki, J., Contag, C., Seidlits, S. K. & Ashammakhi, N. Use of artificial cells as drug carriers. *Mater. Chem. Front.* **5**, 6672–6692 (2021).
165. Zou, D., Wang, H., Liu, X., Xu, Z. P., Roberts, M. S. & Zhao, C.-X. Artificial cells for the treatment of liver diseases. *Acta Biomaterialia* **130**, 98–114 (2021).
166. Lim, B., Yin, Y., Ye, H., Cui, Z., Papachristodoulou, A. & Huang, W. E. Reprogramming Synthetic Cells for Targeted Cancer Therapy. *ACS Synth. Biol.* **11**, 1349–1360 (2022).
167. Hao, J., Zhao, W., Oh, J. M. & Shen, K. A Pillar-Free Diffusion Device for Studying Chemotaxis on Supported Lipid Bilayers. *Micromachines* **12**, 1254 (2021).

168. Krinsky, N., Kaduri, M., Zinger, A., Shainsky-Roitman, J., Goldfeder, M., Benhar, I., Hershkovitz, D. & Schroeder, A. Synthetic Cell-like Particles Synthesize Therapeutic Proteins Inside Tumors. *Adv Healthc Mater* **7**, e1701163 (2018).
169. Hernandez Bücher, J. E., Staufer, O., Ostertag, L., Mersdorf, U., Platzman, I. & Spatz, J. P. Bottom-up assembly of target-specific cytotoxic synthetic cells. *Biomaterials* **285**, 121522 (2022).
170. Chen, G. *et al.* Implanted synthetic cells trigger tissue angiogenesis through de novo production of recombinant growth factors. *Proceedings of the National Academy of Sciences* **119**, e2207525119 (2022).
171. Cancer survival in England for patients diagnosed between 2014 and 2018, and followed up to 2019. *GOV.UK* <https://www.gov.uk/government/statistics/cancer-survival-in-england-for-patients-diagnosed-between-2014-and-2018-and-followed-up-until-2019/cancer-survival-in-england-for-patients-diagnosed-between-2014-and-2018-and-followed-up-to-2019>.
172. Mahase, E. Covid-19: Urgent cancer referrals fall by 60%, showing “brutal” impact of pandemic. *BMJ* m2386 (2020).
173. Morris, E. J. A. *et al.* Impact of the COVID-19 pandemic on the detection and management of colorectal cancer in England: a population-based study. *The Lancet Gastroenterology & Hepatology* **6**, 199–208 (2021).
174. Sadeghi, Enferadi, M. & Shirazi, A. External and internal radiation therapy: Past and future directions. <https://cancerjournal.net/article.asp?issn=0973-1482;year=2010;volume=6;issue=3;spage=239;epage=248;aulast=Sadeghi> (2010).
175. Caffa, I. *et al.* Fasting-mimicking diet and hormone therapy induce breast cancer regression. *Nature* **583**, 620–624 (2020).
176. Wang, H. & Mao, X. Evaluation of the Efficacy of Neoadjuvant Chemotherapy for Breast Cancer. *DDDT Volume* **14**, 2423–2433 (2020).
177. Varghese, E., Samuel, S. M., Líšková, A., Samec, M., Kubatka, P. & Büsselberg, D. Targeting Glucose Metabolism to Overcome Resistance to Anticancer Chemotherapy in Breast Cancer. *Cancers* **12**, 2252 (2020).

178. Swain, S. M., Shastry, M. & Hamilton, E. Targeting HER2-positive breast cancer: advances and future directions. *Nat Rev Drug Discov* 1–26 (2022).
179. Dai, X., Cheng, H., Bai, Z. & Li, J. Breast Cancer Cell Line Classification and Its Relevance with Breast Tumor Subtyping. *J. Cancer* **8**, 3131–3141 (2017).
180. Smith, S. E., Mellor, P., Ward, A. K., Kendall, S., McDonald, M., Vizeacoumar, F. S., Vizeacoumar, F. J., Napper, S. & Anderson, D. H. Molecular characterization of breast cancer cell lines through multiple omic approaches. *Breast Cancer Research* **19**, 65 (2017).
181. Parsian, M., Mutlu, P., Taghavi Pourianazar, N., Yalcin Azarkan, S. & Gunduz, U. Investigation of the Therapeutic Effects of Palbociclib Conjugated Magnetic Nanoparticles on Different Types of Breast Cancer Cell Lines. *Cel. Mol. Bioeng.* (2023).
182. Saha, T. & Lukong, K. E. Breast Cancer Stem-Like Cells in Drug Resistance: A Review of Mechanisms and Novel Therapeutic Strategies to Overcome Drug Resistance. *Frontiers in Oncology* **12**, (2022).
183. Jensen, C. & Teng, Y. Is It Time to Start Transitioning From 2D to 3D Cell Culture? *Frontiers in Molecular Biosciences* **7**, (2020).
184. Chae, S., Hong, J., Hwangbo, H. & Kim, G. The utility of biomedical scaffolds laden with spheroids in various tissue engineering applications. *Theranostics* **11**, 6818–6832 (2021).
185. Boinapalli, Y., Shankar Pandey, R., Singh Chauhan, A. & Sudheesh, M. S. Physiological relevance of in-vitro cell-nanoparticle interaction studies as a predictive tool in cancer nanomedicine research. *International Journal of Pharmaceutics* **632**, 122579 (2023).
186. Nunes, A. S., Barros, A. S., Costa, E. C., Moreira, A. F. & Correia, I. J. 3D tumor spheroids as in vitro models to mimic in vivo human solid tumors resistance to therapeutic drugs. *Biotechnology and Bioengineering* **116**, 206–226 (2019).
187. Moccia, C. & Haase, K. Engineering Breast Cancer On-chip—Moving Toward Subtype Specific Models. *Frontiers in Bioengineering and Biotechnology* **9**, (2021).
188. Badea, M. A., Balas, M., Hermenean, A., Ciceu, A., Herman, H., Ionita, D. & Dinischiotu, A. Influence of Matrigel on Single- and Multiple-Spheroid Cultures in Breast Cancer Research. *SLAS DISCOVERY: Advancing the Science of Drug Discovery* **24**, 563–578 (2019).

189. Li, Y. & Kumacheva, E. Hydrogel microenvironments for cancer spheroid growth and drug screening. *Sci. Adv.* **4**, eaas8998 (2018).
190. Nguyen-Ngoc, K.-V., Cheung, K. J., Brenot, A., Shamir, E. R., Gray, R. S., Hines, W. C., Yaswen, P., Werb, Z. & Ewald, A. J. ECM microenvironment regulates collective migration and local dissemination in normal and malignant mammary epithelium. *Proceedings of the National Academy of Sciences* **109**, E2595–E2604 (2012).
191. Tsai, C.-W., Wang, J.-H. & Young, T.-H. Core/shell multicellular spheroids on chitosan as in vitro 3D coculture tumor models. *Artificial Cells, Nanomedicine, and Biotechnology* **46**, S651–S660 (2018).
192. Nakod, P. S., Kim, Y. & Rao, S. S. Three-dimensional biomimetic hyaluronic acid hydrogels to investigate glioblastoma stem cell behaviors. *Biotechnology and Bioengineering* **117**, 511–522 (2020).
193. Mirab, F., Kang, Y. J. & Majd, S. Preparation and characterization of size-controlled glioma spheroids using agarose hydrogel microwells. *PloS one* **14**, (2019).
194. Agarwal, P. *et al.* Microfluidics Enabled Bottom-Up Engineering of 3D Vascularized Tumor for Drug Discovery. *ACS Nano* **11**, 6691–6702 (2017).
195. Alagha, A., Nourallah, A. & Hariri, S. Characterization of dexamethasone loaded collagen-chitosan sponge and in vitro release study. *Journal of Drug Delivery Science and Technology* **55**, 101449 (2020).
196. Thakuri, P. S., Liu, C., Luker, G. D. & Tavana, H. Biomaterials-Based Approaches to Tumor Spheroid and Organoid Modeling. *Advanced Healthcare Materials* **7**, 1700980 (2018).
197. Liu, K., Wiendels, M., Yuan, H., Ruan, C. & Kouwer, P. H. J. Cell-matrix reciprocity in 3D culture models with nonlinear elasticity. *Bioactive Materials* **9**, 316–331 (2022).
198. Diekjürgen, D. & Grainger, D. W. Polysaccharide matrices used in 3D in vitro cell culture systems. *Biomaterials* **141**, 96–115 (2017).
199. Habanjar, O., Diab-Assaf, M., Caldefie-Chezet, F. & Delort, L. 3D Cell Culture Systems: Tumor Application, Advantages, and Disadvantages. *International Journal of Molecular Sciences* **22**, 12200 (2021).

- 
200. Wang, J.-Z., Zhu, Y.-X., Ma, H.-C., Chen, S.-N., Chao, J.-Y., Ruan, W.-D., Wang, D., Du, F. & Meng, Y.-Z. Developing multi-cellular tumor spheroid model (MCTS) in the chitosan/collagen/alginate (CCA) fibrous scaffold for anticancer drug screening. *Materials Science and Engineering: C* **62**, 215–225 (2016).
201. Liu, C., Lewin Mejjia, D., Chiang, B., Luker, K. E. & Luker, G. D. Hybrid collagen alginate hydrogel as a platform for 3D tumor spheroid invasion. *Acta Biomaterialia* **75**, 213–225 (2018).
202. Bonnesœur, S., Morin-Grognet, S., Thoumire, O., Cerf, D. L., Boyer, O., Vannier, J.-P. & Labat, B. Hyaluronan-based hydrogels as versatile tumor-like models: Tunable ECM and stiffness with genipin-crosslinking. *Journal of Biomedical Materials Research Part A* **108**, 1256–1268 (2020).
203. Smidsrød, O. Molecular basis for some physical properties of alginates in the gel state. *Faraday Discussions of the Chemical Society* **57**, 263–274 (1974).
204. *Food polysaccharides and their applications*. (CRC/Taylor & Francis, 2006).
205. Zhang, C., Li, M., Rauf, A., Khalil, A. A., Shan, Z., Chen, C., Rengasamy, K. R. R. & Wan, C. Process and applications of alginate oligosaccharides with emphasis on health beneficial perspectives. *Critical Reviews in Food Science and Nutrition* **63**, 303–329 (2023).
206. Paques, J. P. Alginate Nanospheres Prepared by Internal or External Gelation with Nanoparticles. in *Microencapsulation and Microspheres for Food Applications* 39–55 (Elsevier, 2015).
207. Cao, L., Lu, W., Mata, A., Nishinari, K. & Fang, Y. Egg-box model-based gelation of alginate and pectin: A review. *Carbohydrate Polymers* **242**, 116389 (2020).
208. Alginate Nanospheres Prepared by Internal or External Gelation with Nanoparticles. *Microencapsulation and Microspheres for Food Applications* 39–55 (2015).
209. Domenici, G., Eduardo, R., Castillo-Ecija, H., Orive, G., Montero Carcaboso, Á. & Brito, C. PDX-Derived Ewing's Sarcoma Cells Retain High Viability and Disease Phenotype in Alginate Encapsulated Spheroid Cultures. *Cancers* **13**, 879 (2021).
210. Blanco-Fernandez, B., Gaspar, V. M., Engel, E. & Mano, J. F. Proteinaceous Hydrogels for Bioengineering Advanced 3D Tumor Models. *Advanced Science* **8**, 2003129 (2021).
211. Henriksen, K. & Karsdal, M. A. Chapter 1 - Type I Collagen. in *Biochemistry of Collagens, Laminins and Elastin* (ed. Karsdal, M. A.) 1–11 (Academic Press, 2016).
-

212. Friess, W. Collagen – biomaterial for drug delivery1Dedicated to Professor Dr. Eberhard Nürnberg, Friedrich-Alexander-Universität Erlangen-Nürnberg, on the occasion of his 70th birthday.1. *European Journal of Pharmaceutics and Biopharmaceutics* **45**, 113–136 (1998).
213. Yang, Y., Motte, S. & Kaufman, L. J. Pore size variable type I collagen gels and their interaction with glioma cells. *Biomaterials* **31**, 5678–5688 (2010).
214. Zhao, L., Xiu, J., Liu, Y., Zhang, T., Pan, W., Zheng, X. & Zhang, X. A 3D Printed Hanging Drop Dripper for Tumor Spheroids Analysis Without Recovery. *Sci Rep* **9**, 19717 (2019).
215. Paszek, M. J. *et al.* Tensional homeostasis and the malignant phenotype. *Cancer Cell* **8**, 241–254 (2005).
216. Zimmerman, W. B. J. *Microfluidics: History, Theory and Applications*. (Springer Science & Business Media, 2006).
217. Whitesides, G. M. The origins and the future of microfluidics. *Nature* **442**, 368–373 (2006).
218. Manz, A., Graber, N. & Widmer, H. M. Miniaturized total chemical analysis systems: A novel concept for chemical sensing. *Sensors and Actuators B: Chemical* **1**, 244–248 (1990).
219. Ren, C. & Lee, A. CHAPTER 1 History and Current Status of Droplet Microfluidics. 1–14 (2020)
220. Lei, K. F. Materials and Fabrication Techniques for Nano- and Microfluidic Devices. in *Microfluidics in Detection Science* (eds. Labeed, F. H. & Fatoyinbo, H. O.) 0 (The Royal Society of Chemistry, 2014).
221. Hou, X. *et al.* Interplay between materials and microfluidics. *Nat Rev Mater* **2**, 1–15 (2017).
222. Whitesides, G. Microfluidics in Late Adolescence. Preprint at <https://doi.org/10.48550/arXiv.1802.05595> (2018).
223. Battat, S., Weitz, D. A. & Whitesides, G. M. An outlook on microfluidics: the promise and the challenge. *Lab Chip* **22**, 530–536 (2022).
224. Amin, R., Knowlton, S., Hart, A., Yenilmez, B., Ghaderinezhad, F., Katebifar, S., Messina, M., Khademhosseini, A. & Tasoglu, S. 3D-printed microfluidic devices. *Biofabrication* **8**, 022001 (2016).
225. Convery, N. & Gadegaard, N. 30 years of microfluidics. *Micro and Nano Engineering* **2**, 76–91 (2019).

226. Teh, S.-Y., Lin, R., Hung, L.-H. & Lee, A. P. Droplet microfluidics. *Lab Chip* **8**, 198 (2008).
227. Barrow, D. A., Harries, N., Jones, T. G. & Bouris, K. Microfluidic device and methods for construction and application. (2012).
228. Stanley, C. E., Wootton, R. C. R. & deMello, A. J. Continuous and Segmented Flow Microfluidics: Applications in High-throughput Chemistry and Biology. *CHIMIA* **66**, 88–88 (2012).
229. He, Y., Kim, K.-J. & Chang, C. Segmented Microfluidic Flow Reactors for Nanomaterial Synthesis. *Nanomaterials* **10**, 1421 (2020).
230. Garti, N. & Lutz, R. Chapter 14 - Recent progress in double emulsions. in *Interface Science and Technology* (ed. Petsev, D. N.) vol. 4 557–605 (Elsevier, 2004).
231. Montessori, A., Lauricella, M., La Rocca, M., Succi, S., Stolovicki, E., Ziblat, R. & Weitz, D. Regularized lattice Boltzmann multicomponent models for low capillary and Reynolds microfluidics flows. *Computers & Fluids* **167**, 33–39 (2018).
232. Chen, Z., Kheiri, S., Young, E. W. K. & Kumacheva, E. Trends in Droplet Microfluidics: From Droplet Generation to Biomedical Applications. *Langmuir* **38**, 6233–6248 (2022).
233. Digital microfluidics: microfluidic droplet and emulsion science. *Elveflow* <https://www.elveflow.com/microfluidic-reviews/droplet-digital-microfluidics/digital-microfluidics-microfluidic-droplet-emulsion-science/>.
234. Trantidou, T., Friddin, M. S., Salehi-Reyhani, A., Ces, O. & Elani, Y. Droplet microfluidics for the construction of compartmentalised model membranes. *Lab Chip* **18**, 2488–2509 (2018).
235. Venkateshwarlu, A. & Bharti, R. P. Effects of capillary number and flow rates on the hydrodynamics of droplet generation in two-phase cross-flow microfluidic systems. *Journal of the Taiwan Institute of Chemical Engineers* **129**, 64–79 (2021).
236. Shang, L., Cheng, Y. & Zhao, Y. Emerging Droplet Microfluidics. *Chem. Rev.* **117**, 7964–8040 (2017).
237. Anna, S. L. & Mayer, H. C. Microscale tipstreaming in a microfluidic flow focusing device. *Physics of Fluids* **18**, 121512 (2006).

238. Takeuchi, S., Garstecki, P., Weibel, D. B. & Whitesides, G. M. An Axisymmetric Flow-Focusing Microfluidic Device. *Advanced Materials* **17**, 1067–1072 (2005).
239. Gu, H., Duits, M. H. G. & Mugele, F. Droplets Formation and Merging in Two-Phase Flow Microfluidics. *Int J Mol Sci* **12**, 2572–2597 (2011).
240. Rotem, A., Abate, A. R., Utada, A. S., Steijn, V. V. & Weitz, D. A. Drop formation in non-planar microfluidic devices. *Lab Chip* **12**, 4263–4268 (2012).
241. Shah, R. K. *et al.* Designer emulsions using microfluidics. *Materials Today* **11**, 18–27 (2008).
242. Vladislavljević, G. T., Al Nuamani, R. & Nabavi, S. A. Microfluidic Production of Multiple Emulsions. *Micromachines* **8**, 75 (2017).
243. Agrawal, A., Kulkarni, S. & Sharma, S. B. Recent advancements and applications of multiple emulsions. *Int J of Adv Pharm* **4**, (2015).
244. Kim, J.-W., Han, S. H., Choi, Y. H., Hamonangan, W. M., Oh, Y. & Kim, S.-H. Recent advances in the microfluidic production of functional microcapsules by multiple-emulsion templating. *Lab Chip* **22**, 2259–2291 (2022).
245. Li, J. & Barrow, D. A. A new droplet-forming fluidic junction for the generation of highly compartmentalised capsules. *Lab Chip* **17**, 2873–2881 (2017).
246. Okushima, S., Nisisako, T., Torii, T. & Higuchi, T. Controlled Production of Monodisperse Double Emulsions by Two-Step Droplet Breakup in Microfluidic Devices. *Langmuir* **20**, 9905–9908 (2004).
247. Kim, S.-H. & Weitz, D. A. One-Step Emulsification of Multiple Concentric Shells with Capillary Microfluidic Devices. *Angewandte Chemie International Edition* **50**, 8731–8734 (2011).
248. Wang, W., Xie, R., Ju, X.-J., Luo, T., Liu, L., Weitz, D. A. & Chu, L.-Y. Controllable microfluidic production of multicomponent multiple emulsions. *Lab Chip* **11**, 1587–1592 (2011).
249. Abate, A. R. & Weitz, D. A. High-Order Multiple Emulsions Formed in Poly(dimethylsiloxane) Microfluidics. *Small* **5**, 2030–2032 (2009).
250. Brower, K. K., Khariton, M., Suzuki, P. H., Still, C. I., Kim, G., Calhoun, S. G. K., Qi, L. S., Wang, B. & Fordyce, P. M. Double Emulsion Picoreactors for High-Throughput Single-Cell Encapsulation and Phenotyping via FACS. *Anal. Chem.* **92**, 13262–13270 (2020).

251. Nawar, S., K. Stolaroff, J., Ye, C., Wu, H., Thai Nguyen, D., Xin, F. & A. Weitz, D. Parallelizable microfluidic dropmakers with multilayer geometry for the generation of double emulsions. *Lab on a Chip* **20**, 147–154 (2020).
252. Martino, C., Berger, S., Wootton, R. C. R. & deMello, A. J. A 3D-printed microcapillary assembly for facile double emulsion generation. *Lab Chip* **14**, 4178–4182 (2014).
253. Ji, Q., Zhang, J. M., Liu, Y., Li, X., Lv, P., Jin, D. & Duan, H. A Modular Microfluidic Device via Multimaterial 3D Printing for Emulsion Generation. *Sci Rep* **8**, 4791 (2018).
254. Lee, S., Hamonangan, W. M., Kim, J. H. & Kim, S.-H. Soft and Tough Microcapsules with Double-Network Hydrogel Shells. *Advanced Functional Materials* **32**, 2203761 (2022).
255. Jeyhani, M., Thevakumaran, R., Abbasi, N., Hwang, D. K. & Tsai, S. S. H. Microfluidic Generation of All-Aqueous Double and Triple Emulsions. *Small* **16**, 1906565 (2020).
256. Trantidou, T., Elani, Y., Parsons, E. & Ces, O. Hydrophilic surface modification of PDMS for droplet microfluidics using a simple, quick, and robust method via PVA deposition. *Microsyst Nanoeng* **3**, 1–9 (2017).
257. Deng, N.-N., Wang, W., Ju, X.-J., Xie, R., A. Weitz, D. & Chu, L.-Y. Wetting-induced formation of controllable monodisperse multiple emulsions in microfluidics. *Lab on a Chip* **13**, 4047–4052 (2013).
258. Chen, L. *et al.* Emulsion Designer Using Microfluidic Three-Dimensional Droplet Printing in Droplet. *Small* **17**, 2102579 (2021).
259. Nabavi, S. A., Vladislavljević, G. T., Gu, S. & Ekanem, E. E. Double emulsion production in glass capillary microfluidic device: Parametric investigation of droplet generation behaviour. *Chemical Engineering Science* **130**, 183–196 (2015).
260. Yu, W., Li, B., Liu, X. & Chen, Y. Hydrodynamics of triple emulsion droplet generation in a flow-focusing microfluidic device. *Chemical Engineering Science* **243**, 116648 (2021).
261. Muschiolik, G. Multiple emulsions for food use. *Current Opinion in Colloid & Interface Science* **12**, 213–220 (2007).
262. Huang, D., Wang, J., Che, J., Wen, B. & Kong, W. Ultrasound-responsive microparticles from droplet microfluidics. *Biomedical Technology* **1**, 1–9 (2023).

263. Sato, Y. & Takinoue, M. Creation of Artificial Cell-Like Structures Promoted by Microfluidics Technologies. *Micromachines* **10**, 216 (2019).
264. Linsenmeier, M. *et al.* Dynamics of Synthetic Membraneless Organelles in Microfluidic Droplets. *Angewandte Chemie International Edition* **58**, 14489–14494 (2019).
265. Karamdad, K., Hindley, J. W., Bolognesi, G., Friddin, M. S., Law, R. V., Brooks, N. J., Ces, O. & Elani, Y. Engineering thermoresponsive phase separated vesicles formed via emulsion phase transfer as a content-release platform. *Chem. Sci.* **9**, 4851–4858 (2018).
266. Wang, H., Zhao, Z., Liu, Y., Shao, C., Bian, F. & Zhao, Y. Biomimetic enzyme cascade reaction system in microfluidic electrospray microcapsules. *Science Advances* **4**, eaat2816 (2018).
267. Aufinger, L. & Simmel, F. C. Artificial Gel-Based Organelles for Spatial Organization of Cell-Free Gene Expression Reactions. *Angewandte Chemie International Edition* **57**, 17245–17248 (2018).
268. Ayoubi-Joshaghani, M. H., Dianat-Moghadam, H., Seidi, K., Jahanban-Esfahalan, A., Zare, P. & Jahanban-Esfahlan, R. Cell-free protein synthesis: The transition from batch reactions to minimal cells and microfluidic devices. *Biotechnology and Bioengineering* **117**, 1204–1229 (2020).
269. Fujiwara, S., Shoji, K., Watanabe, C., Kawano, R. & Yanagisawa, M. Microfluidic Formation of Honeycomb-Patterned Droplets Bounded by Interface Bilayers via Bimodal Molecular Adsorption. *Micromachines* **11**, 701 (2020).
270. Schlicht, B. & Zagnoni, M. Droplet-interface-bilayer assays in microfluidic passive networks. *Sci Rep* **5**, 9951 (2015).
271. Czekalska, M. A., Kaminski, T. S., Makuch, K. & Garstecki, P. Passive and parallel microfluidic formation of droplet interface bilayers (DIBs) for measurement of leakage of small molecules through artificial phospholipid membranes. *Sensors and Actuators B: Chemical* **286**, 258–265 (2019).
272. Tan, Y.-C., Fisher, J. S., Lee, A. I., Cristini, V. & Lee, A. P. Design of microfluidic channel geometries for the control of droplet volume, chemical concentration, and sorting. *Lab Chip* **4**, 292–298 (2004).

273. Matuła, K., Rivello, F. & Huck, W. T. S. Single-Cell Analysis Using Droplet Microfluidics. *Advanced Biosystems* **4**, 1900188 (2020).
274. Tenje, M., Porras Hernández, A. M., Searle, S. S., Johansson, S., Barbe, L., Antfolk, M. & Pohlitz, H. A practical guide to microfabrication and patterning of hydrogels for biomimetic cell culture scaffolds. *Organs-on-a-Chip* **2**, 100003 (2020).
275. Kamperman, T., Karperien, M., Le Gac, S. & Leijten, J. Single-Cell Microgels: Technology, Challenges, and Applications. *Trends in Biotechnology* **36**, 850–865 (2018).
276. Enck, K., Rajan, S. P., Aleman, J., Castagno, S., Long, E., Khalil, F., Hall, A. R. & Opara, E. C. Design of an Adhesive Film-Based Microfluidic Device for Alginate Hydrogel-Based Cell Encapsulation. *Ann Biomed Eng* **48**, 1103–1111 (2020).
277. Zhang, Z. & Nagrath, S. Microfluidics and cancer: are we there yet? *Biomed Microdevices* **15**, 595–609 (2013).
278. Li, W. *et al.* Microfluidic fabrication of microparticles for biomedical applications. *Chem. Soc. Rev.* **47**, 5646–5683 (2018).
279. Zhu, K., Yu, Y., Cheng, Y., Tian, C., Zhao, G. & Zhao, Y. All-Aqueous-Phase Microfluidics for Cell Encapsulation. *ACS Appl. Mater. Interfaces* **11**, 4826–4832 (2019).
280. Tan, W.-H. & Takeuchi, S. Monodisperse Alginate Hydrogel Microbeads for Cell Encapsulation. *Advanced Materials* **19**, 2696–2701 (2007).
281. Ling, S. D., Geng, Y., Chen, A., Du, Y. & Xu, J. Enhanced single-cell encapsulation in microfluidic devices: From droplet generation to single-cell analysis. *Biomicrofluidics* **14**, 061508 (2020).
282. Hidalgo San Jose, L. Microfluidic production of stem-cell microcapsules for spinal cord injury repair. (Cardiff University, 2017).
283. Nooranidoost, M. & Kumar, R. Geometry Effects of Axisymmetric Flow-Focusing Microchannels for Single Cell Encapsulation. *Materials* **12**, 2811 (2019).
284. Nooranidoost, M., Haghshenas, M., Muradoglu, M. & Kumar, R. Cell encapsulation modes in a flow-focusing microchannel: effects of shell fluid viscosity. *Microfluid Nanofluid* **23**, 31 (2019).

285. Yu, L., Grist, S. M., Nasser, S. S., Cheng, E., Hwang, Y.-C. E., Ni, C. & Cheung, K. C. Core-shell hydrogel beads with extracellular matrix for tumor spheroid formation. *Biomicrofluidics* **9**, (2015).
286. Chen, Q., Utech, S., Chen, D., Prodanovic, R., Lin, J.-M. & Weitz, D. A. Controlled assembly of heterotypic cells in a core-shell scaffold: organ in a droplet. *Lab Chip* **16**, 1346–1349 (2016).
287. Tsai, H.-F., Trubelja, A., Shen, A. Q. & Bao, G. Tumour-on-a-chip: microfluidic models of tumour morphology, growth and microenvironment. *Journal of The Royal Society Interface* **14**, 20170137 (2017).
288. Wu, Z. *et al.* Rapid Microfluidic Formation of Uniform Patient-Derived Breast Tumor Spheroids. *ACS Appl. Bio Mater.* **3**, 6273–6283 (2020).
289. Colombo, S., Beck-Broichsitter, M., Bøtker, J. P., Malmsten, M., Rantanen, J. & Bohr, A. Transforming nanomedicine manufacturing toward Quality by Design and microfluidics. *Advanced Drug Delivery Reviews* **128**, 115–131 (2018).
290. Toprakcioglu, Z., Challa, P. K., Morse, D. B. & Knowles, T. Attoliter protein nanogels from droplet nanofluidics for intracellular delivery. *Sci. Adv.* **6**, eaay7952 (2020).
291. Lölsberg, J., Linkhorst, J., Cinar, A., Jans, A., Kuehne, A. J. C. & Wessling, M. 3D nanofabrication inside rapid prototyped microfluidic channels showcased by wet-spinning of single micrometre fibres. *Lab Chip* **18**, 1341–1348 (2018).
292. Shrimal, P., Jadeja, G. & Patel, S. A review on novel methodologies for drug nanoparticle preparation: Microfluidic approach. *Chemical Engineering Research and Design* **153**, 728–756 (2020).
293. Shepherd, S. J., Issadore, D. & Mitchell, M. J. Microfluidic formulation of nanoparticles for biomedical applications. *Biomaterials* **274**, 120826 (2021).
294. Jahn, A., Vreeland, W. N., Gaitan, M. & Locascio, L. E. Controlled Vesicle Self-Assembly in Microfluidic Channels with Hydrodynamic Focusing. *J. Am. Chem. Soc.* **126**, 2674–2675 (2004).
295. Zhang, L., Chen, Q., Ma, Y. & Sun, J. Microfluidic Methods for Fabrication and Engineering of Nanoparticle Drug Delivery Systems. *ACS Appl. Bio Mater.* **3**, 107–120 (2020).

296. Kimura, N., Maeki, M., Sato, Y., Ishida, A., Tani, H., Harashima, H. & Tokeshi, M. Development of a Microfluidic-Based Post-Treatment Process for Size-Controlled Lipid Nanoparticles and Application to siRNA Delivery. *ACS Appl. Mater. Interfaces* **12**, 34011–34020 (2020).
297. Dong, Y.-D., Tchung, E., Nowell, C., Kaga, S., Leong, N., Mehta, D., Kaminskas, L. M. & Boyd, B. J. Microfluidic preparation of drug-loaded PEGylated liposomes, and the impact of liposome size on tumour retention and penetration. *Journal of Liposome Research* **29**, 1–9 (2019).
298. S. Elvira, K., Gielen, F., H. Tsai, S. S. & M. Nightingale, A. Materials and methods for droplet microfluidic device fabrication. *Lab on a Chip* **22**, 859–875 (2022).
299. Oropallo, W. & Piegler, L. A. Ten challenges in 3D printing. *Engineering with Computers* **32**, 135–148 (2016).
300. Bogue, R. The changing face of the automotive robotics industry. *Industrial Robot: the international journal of robotics research and application* **49**, 386–390 (2022).
301. Ambrosi, A. & Pumera, M. 3D-printing technologies for electrochemical applications. *Chem. Soc. Rev.* **45**, 2740–2755 (2016).
302. Ali, Md. H., Issayev, G., Shehab, E. & Sarfraz, S. A critical review of 3D printing and digital manufacturing in construction engineering. *Rapid Prototyping Journal* **28**, 1312–1324 (2022).
303. Billiet, T., Vandenhaute, M., Schelfhout, J., Van Vlierberghe, S. & Dubruel, P. A review of trends and limitations in hydrogel-rapid prototyping for tissue engineering. *Biomaterials* **33**, 6020–6041 (2012).
304. Pavan Kalyan, B. & Kumar, L. 3D Printing: Applications in Tissue Engineering, Medical Devices, and Drug Delivery. *AAPS PharmSciTech* **23**, 92 (2022).
305. Liu, Y., Hu, Q., Dong, W., Liu, S., Zhang, H. & Gu, Y. Alginate/Gelatin-Based Hydrogel with Soy Protein/Peptide Powder for 3D Printing Tissue-Engineering Scaffolds to Promote Angiogenesis. *Macromolecular Bioscience* **22**, 2100413 (2022).
306. Morgan, A. J. L., Jose, L. H. S., Jamieson, W. D., Wymant, J. M., Song, B., Stephens, P., Barrow, D. A. & Castell, O. K. Simple and Versatile 3D Printed Microfluidics Using Fused Filament Fabrication. *PLOS ONE* **11**, e0152023 (2016).

307. Chen, P.-C., Chen, P.-T. & Vo, T. N. A. Using Stereolithographic Printing to Manufacture Monolithic Microfluidic Devices with an Extremely High Aspect Ratio. *Polymers* **13**, 3750 (2021).
308. Ahmed, I., Sullivan, K. & Priye, A. Multi-Resin Masked Stereolithography (MSLA) 3D Printing for Rapid and Inexpensive Prototyping of Microfluidic Chips with Integrated Functional Components. *Biosensors* **12**, 652 (2022).
309. Romanov, V., Samuel, R., Chaharlang, M., Jafek, A. R., Frost, A. & Gale, B. K. FDM 3D Printing of High-Pressure, Heat-Resistant, Transparent Microfluidic Devices. *Anal. Chem.* **90**, 10450–10456 (2018).
310. Kotz, F., Mader, M., Dellen, N., Risch, P., Kick, A., Helmer, D. & Rapp, B. E. Fused Deposition Modeling of Microfluidic Chips in Polymethylmethacrylate. *Micromachines* **11**, 873 (2020).

## *Chapter II*

# *Fused Filament Fabricated (FFF) microfluidic devices for single, double, and triple emulsion hydrogel capsules*

---

### **2.1. Chapter summary**

This chapter focuses on the design, fabrication, optimisation and execution of 3D-printed droplet-forming microfluidic devices. Three microfluidic devices were designed for either single or dual-material 3D printing. By combining the FFF microfluidic printed devices and alginate hydrogel crosslinking, single, double and triple emulsion microgel capsules were produced. Product characterisation such as the droplet frequency, droplet size, structural integrity and other, were investigated and discussed. The microfluidic devices developed in this chapter, were further explored for cell encapsulation experiments in Chapter IV. Additionally, the triple emulsion device, aimed the stable emulsification of encapsulated Droplet Interface Bilayers (eDIBs). These emulsions enclosed aqueous internal compartments that were segregated by artificial lipid membranes. The eDIB structure presents an artificial cell chassis, however, the eDIBs formulated in this chapter were intended for encapsulating living cells.

## 2.2. Introduction

Precision droplet-microfluidic devices for microgel production are often fabricated by stereolithography (SLA) or polydimethylsiloxane (PDMS) moulding<sup>1-4</sup>. However, these fabrication techniques possess limitations, including possible reactions with non-polar solutions, post-fabrication processing, device assembly, and the incapability of printing multiple materials<sup>5,6</sup>. Fused Filament Fabrication (FFF), or Fused Deposition Modelling (FDM), is a rapid prototyping technique based on layer-by-layer deposition and fusion of melted plastic filament. One of the main advantages of FFF, is that FFF parts and devices are fabricated rapidly and are usually ready-to-use, unless degradable support material was also printed (e.g. polyvinyl alcohol, PVA support)<sup>7</sup>. Although, when compared to SLA and PDMS, FFF devices usually lack transparency, hence compromising the visualisation of the channel restricted flow.<sup>8</sup> On that note, transparent filaments are commercially available and with the appropriate manipulation of the printing setup, channel visualisation can be enhanced<sup>9</sup>. With regard to 3D-printed microfluidic channels, the resolution is often poor, but it can be improved by altering the print settings and providing the appropriate tools for controlling the variables (environment, materials storage) that influence the quality of the printed module.

Although transparent FFF microfluidic device manufacturing and optimisation may be challenging, FFF 3D printers facilitate dual-material printing, which is of significant value for achieving high-order emulsions<sup>10</sup>. Multiple emulsion architectures have applications in drug delivery, reagent compartmentalisation, multi-cellular cultures and synthetic biology<sup>2,11-13</sup>. Alginate is widely used in droplet-microfluidics as an encapsulation matrix, due to its biocompatibility, handling convenience, and its amenability to flexible crosslinking<sup>14</sup>. Usually, the gelation process will determine the monodispersity of single emulsion microgels and the stability of high-order emulsions. Moreover, the addition of interfacial tension-altering molecules, known as surfactants, are essential in emulsification systems<sup>15</sup>. Phospholipids are a class of surfactants<sup>15</sup>, which may be used in the formation of complex emulsion capsules, such as the previously reported encapsulated droplet interface bilayers (eDIBs)<sup>16</sup>. eDIB models published in earlier years obtained large diameters ( $> 3 \mu\text{m}$ ) and were generated by hybrid fluidic circuits or double emulsion FFF microfluidic devices<sup>10,16</sup>.

This chapter reports the formation and gelation of single, double and triple emulsion microgels, using monolithic 3D FFF droplet-microfluidic devices, made out of cyclic olefin copolymer (COC) and Nylon filaments. These filament materials were fused together to alter between the wetting properties of the droplet-forming junctions and channels, leading to stable multiple emulsions. Three types of microfluidic devices were fabricated. The first device was investigated to obtain microgels suitable for cell encapsulation (presented in Chapter IV), while the second microfluidic device was used for the formation of oil-in-hydrogel-in-oil (O/H/O) emulsions with either single or multiple internal

compartments. Finally, free-standing eDIBs were produced using the third device, consisting of three consecutive 3D FFF droplet-forming junctions, with no surface modifications and W/O/H/O emulsions.

### 2.3. Materials and Methods

Each 3D Fused Filament Fabricated (FFF) microfluidic device generated a different emulsion system and was named accordingly. The devices are listed in **Table 2. 1** with their acronyms explained as follows; the *emulsion order* (single emulsion (**SE**), double emulsion (**DE**) or triple emulsion (**TE**))-*Microfluidic Device (MD)*. For example, the microfluidic device that produced double emulsion hydrogel capsules (O/H/O) will have the acronym of DE-MD.

*Table 2. 1: A list of the microfluidic devices utilised across the project.*

Device acronym	Filament	On-chip emulsion	Off-chip end-product
SE-MD	COC*	Single H/O	Hydrogel capsules
DE-MD	Nylon/COC	Double O/H/O	Oil-in-Hydrogel capsules
TE-MD	COC/Nylon/COC	Triple W/O/H/O	Water-in-Oil-in-Hydrogel capsules

\*COC = Cyclin Olefin Copolymer, W = water, O = oil, H= hydrogel, / indicates one order of emulsion

#### 2.3.1. Contact angle of COC and Nylon

Contact angle (CA) measurements for cyclic olefin copolymer (COC) (Creemelt, Grade 8007, TOPAS) and Nylon 3D-printed samples were collected according to BS EN 828:2013. The contact angle measuring system comprised of an optical tensiometer, OneAttention Theta Lite (**Figure 2. 1A**). The samples were printed as blocks with dimensions 3 cm x 3 cm x 0.1 cm, using the Ultimaker S5 Pro Buddle and the same print settings as the microfluidic devices (**Table 2. 2**). The samples were printed on a glass platform, after a thin layer of polyvinyl alcohol (PVA) glue was applied. Each block sample was cleaned after fabrication with deionised (DI) water and 70% ethanol to remove residual PVA glue and dust. Each sample was positioned on the OneAttention platform and a 2  $\mu$ l water drop was placed

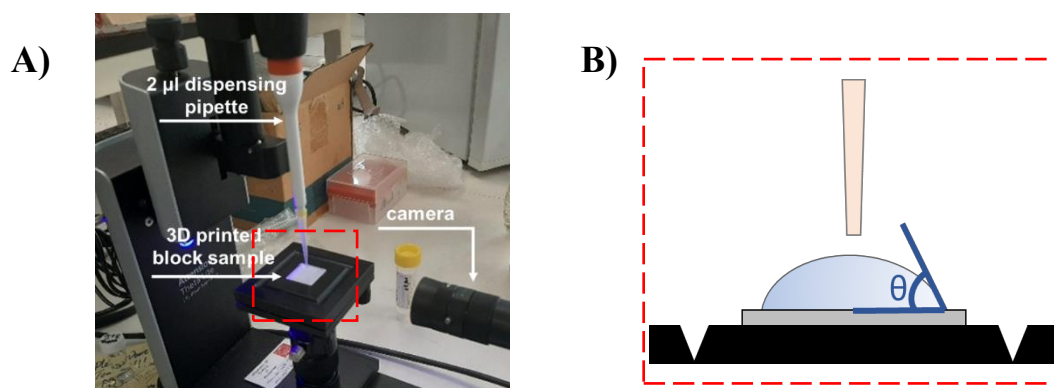


**Figure 2. 1: Contact angle (CA) setup.** **A)** OneAttention Theta Lite optical tensiometer setup for CA measurements. **B)** A schematic of the camera's front view for CA ( $\theta$ ) measurements between the 2 $\mu$ l water droplet and 3D-printed part (grey area).

on each surface of the sample (top and bottom). Measurements of the contact angle (CA) were taken by the camera over 10 s, starting as soon as the 2  $\mu$ l water drop was placed on each surface (**Figure 2. 1B**). The top and bottom surface of four (n=4) 3D-printed block samples of COC and Nylon were tested for the contact angle. COC wafer (unknown manufacturer) was also used for contact angle measurements, as reference for COC. The reported CAs are the average over 1 s immediately after the water droplet touches the surface. This was chosen, because the water droplet starts to evaporate after deposition and the CA changes since the water can flow through the micro-scale gaps.

### 2.3.2. Microfluidic device design, fabrication and operation

All microfluidic devices were designed using COMSOL Multiphysics (versions 5.4-5.6) and fabricated using the Ultimaker S5 Pro Bundle. Each design was exported from COMSOL Multiphysics software as an .STL file and imported into CURA slicing software. In CURA, the print settings were assigned as summarised in **Table 2. 2**, to generate a G-CODE file for the 3D printer. **Figure 2. 2**, summarises the device fabrication steps, starting from the Computer Aided Design (CAD) to the printing and ready-to-use microfluidic device. A thin layer of PVA glue was applied to the glass platform of the 3D printer, before a device of Nylon was fabricated. All devices after printing were stored with silica gel sachets. Each liquid phase was delivered to the microfluidic device using SGE gas-tight glass syringes loaded onto positive displacement syringe pumps (KD Scientific). The SGE syringes were connected directly to the 3D-printed microfluidic inlets using polytetrafluoroethylene (PTFE) tubing ( $\varnothing = 1.58$  mm). A small amount of ultraviolet (UV) resin was applied to each inlet to seal the fluidic connection and was cured with a UV torch (365 nm). The microfluidic flows from day-to-day experiments were imaged using a Dino-Lite Edge USB microscope, unless otherwise stated.

*Table 2. 2: COC and Nylon print settings assigned within CURA software for Ultimaker S5 3D printer. These setting were used for all experiments and microfluidic devices.*

	COC*	Nylon*
<b>Speed</b>	25 mm/s	20 mm/s
<b>Infill</b>	100 % (0.69 mm)	100 % (0.69 mm)
<b>Initial Layer Height</b>	0.18 mm	0.18 mm
<b>Layer height</b>	0.06 mm	0.06 mm
<b>Line width</b>	0.22 mm	0.23 mm
<b>Wall line width</b>	0.22 mm	0.23 mm
<b>Material Flow</b>	100 %	100 %
<b>Fan Speed</b>	100 %	10 %
<b>Printing temperature</b>	255 °C	245 °C
<b>Build plate temperature</b>	85 °C	85 °C

\*Brim Tower for Dual Printing was enabled

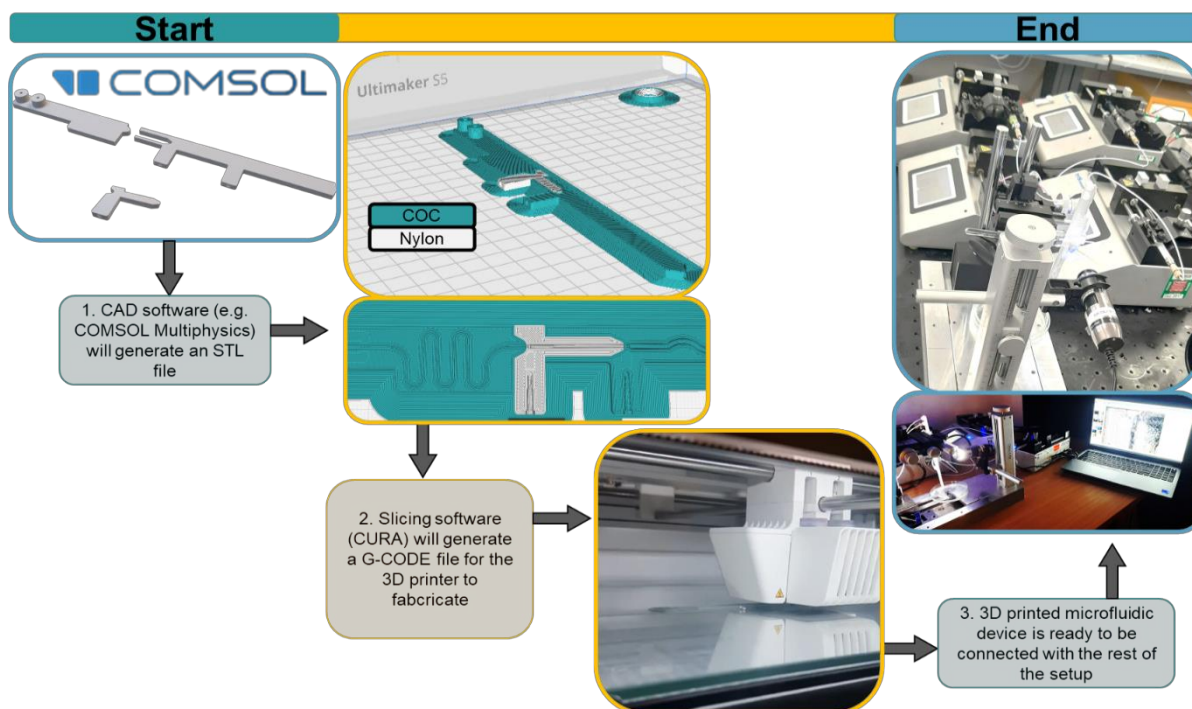


**Figure 2. 2:** Flow chart showing the fabrication steps of 3D-printed devices. Step 1-2 are basic practice for rapid prototyping. The engineer uses COMSOL or other CAD software (e.g., SolidWorks) to design the microfluidic devices, which can be an assembly of various pieces. Each piece is imported to a slicing program to assign the appropriate materials (COC or Nylon) and a G-code is generated using each assigned printing profile (Step 1). The 3D printer translates the G-code commands and fabricates the device (Step 2). After fabrication the microfluidic device is ready to be assembled with the rest of the microfluidic setup and for experiments to begin (Step 3).

### 2.3.3. Production of Hydrogel capsules (H/O) using SE-MD

The single emulsion-microfluidic device (SE-MD) from **Figure 2. 4A** was utilised to produce capsules of alginate hydrogel. This COC device consisted of a single droplet-forming T-junction (**Figure 2. 4B**). The dispersed phase is cut off by the continuous phase and the droplets undergo on-chip gelation in a serpentine mixing outlet channel (**OC1**). The dispersed phase consisted of 1 % w/v alginate (**API**) in 0.9 % w/v sodium chloride (NaCl) solution. The continuous oil phase (**OPI**) was a  $\text{Ca}^{2+}$ -infused mineral oil emulsion, prepared by mixing an aqueous solution of 1 g/ml  $\text{CaCl}_2$  and mineral oil at 1:9 volume ratio, plus 1.2 % SPAN 80 surfactant. This mixture was stirred for at least 10 minutes using a magnetic stirrer and plate, creating a  $\text{Ca}^{2+}$ -infused nanoemulsion. During experiments, the outlet orifice was slightly submerged in 0.2 M  $\text{CaCl}_2$ . The flow rates of the dispersed and continuous phases ranged between 1-5 ml/hr and 10-50 ml/hr, respectively. All reagents were purchased from Merck, unless otherwise stated.

### 2.3.4. Production of Oil-in-Hydrogel capsules (O/H/O) using DE-MD

Double emulsion-microfluidic devices (DE-MDs) were optimised to make oil-core, alginate-shell capsules (**Figure 2. 7**). The device consisted of two droplet-forming junctions. The first was a T-junction, identical to the one of the SE-MD (**Figure 2. 4B**) but was designed without the serpentine mixing channel, and printed as a straight channel with Nylon filament, instead. At the 1<sup>st</sup> droplet-forming junction, the oil phase (**OP2**) was broken into droplets, by a 2 % w/v or 2.5 % w/v alginate phase (**AP2**), creating an O/H emulsion. The oil phase was a mixture of hexadecane (Hex) (code: H6703) and silicone oil (AR20) (code: 10836) at a ratio of 2:1. Occasionally, the hexadecane was dyed with oil-red O (code: O0625) at various concentrations (not mentioned) for visualisation purposes. The O/H emulsion was pinched-off at a COC flow-focusing junction (**Figure 2. 7B** - 2<sup>nd</sup> droplet-forming junction), by a Ca<sup>2+</sup>-infused nanoemulsion (1:9 or 1: 6), as described in Section 2.3.3 (**OC2**), forming O/H/O. The outlet was submerged in a 0.2 M CaCl<sub>2</sub> bath for completing gelation and collecting the capsules. The oil and hydrogel flow rates were manipulated accordingly to obtain an incremental increase of oil core number. All reagents were purchased from Merck, unless otherwise stated.

### 2.3.5. Production of Water-in-Oil-in-Hydrogel eDIB capsules (W/O/H/O) using TE-MD

The triple emulsion-microfluidic device (TE-MD) (**Figure 2. 10**) was used to form triple emulsion eDIB capsules. The inner water phase (**WP3**) consisted of a buffer solution of 0.05 M HEPES, 0.15 M potassium chloride (KCl), 200 µM of sulforhodamine B (SulFB) ( $M_w = 580.65$  g/mol) or calcein ( $M_w = 622.53$  g/mol). The middle oil phase (**OP3**) consisted of 1,2-di-oleoyl-sn-glycero-3-phosphocholine (DOPC, P6354,  $M_w = 786.11$  g/mol) in a mixture of hexadecane (Hex) and silicone oil AR20 or Hex alone (12.5 mg/ml or 30 mg/ml). DOPC was first dispersed in hexadecane following the thin film lipid hydration method suggested by the manufacturer <sup>17</sup>. Briefly, the DOPC powder was dissolved in chloroform and evaporated using a gentle nitrogen stream until a thin film of lipids was formed. The DOPC film was subjected to a vacuum for at least 30 minutes to evaporate any residual chloroform and then released under nitrogen gas. Hex volume was added to the DOPC film depending on the final concentration needed, or whether AR20 was going to be added too. The shell phase (**AP3**) consisted of 1 – 1.5 % w/v alginate and 1,2-dipalmitoyl-sn-glycero-3-phosphocholine (DPPC, 850355C,  $M_w = 734.04$  g/mol) vesicles (0.5 mg/ml – 12.5 mg/ml). The DPPC vesicle solution was prepared using the thin film lipid hydration method, but the vacuum period was extended to a minimum of 3 hours or overnight (~15 hours). Following the nitrogen gas vacuum release, the DPPC film was dispersed in the buffer solution, vortexed for 30 seconds and sonicated in a water bath at 55 °C for 15 min or until a milky solution was obtained without crystals. The vesicle solution was kept at 4 °C and used within 1 week. Before use they were diluted with the appropriate volume of buffer and alginate to

achieve desired concentrations. Like the SE-MD and DE-MD, the gelation of alginate was achieved using a  $\text{Ca}^{2+}$ -infused nano-emulsion (1:9) (**OC3** + **OC4**). The microfluidic setup and execution, aimed at the formation of 1-2 mm diameter eDIBs, with water compartments segregated by artificial lipid membranes (i.e., droplet interface bilayers or DIBs).

## **2.4. Results and Discussion**

### **2.4.1. Selection of filament materials**

Generally, microfluidic device manufacturing is dominated by the use of soft lithography with polydimethylsiloxane (PDMS), by which large-scale production is doubtful<sup>18</sup>. On the contrary, 3D Fused Filament Fabrication (FFF) offers an automated alternative method for rapid prototyping microfluidic devices, with a large selection of filament materials. Multi-material 3D-printed microfluidic chips were reported to have satisfactory performance, however, most of the reported 3D-printed microfluidic devices are single material, as they are believed to have improved pressure resistance compared to PDMS/glass devices<sup>9,19</sup>. To ensure successful dual-filament microfluidic device manufacturing, the printed filaments need to fuse together during printing. Some examples of filament pairs that exhibited good adhesion are polylactic acid (PLA)-polyvinyl alcohol (PVA), PLA-Nylon and thermoplastic polyurethane (TPU)-acrylonitrile butadiene styrene (ABS)<sup>20-22</sup>. In fact, PLA-PVA and PLA-Nylon have been reported to generate multiple emulsions<sup>10,22</sup>. PVA is a water-soluble polymer, which degrades in the presence of water, limiting the duration and consistency of microfluidic experiments. This drawback of PVA, presented Nylon as an attractive filament to use as the hydrophilic channels. The main advantage of Nylon is that it is not water-soluble, and it minimally reacts with organic solutions (e.g. ethanol), oil and hydrocarbons<sup>23-25</sup>. However, it is hygroscopic, meaning it absorbs moisture, which directly influences the quality of 3D-printed nylon filament, unless the environment has low humidity levels<sup>26</sup>. PLA filament is commonly used in 3D FFF. Microfluidic mixers and channels have been fabricated with it; however, it is slightly opaque once printed. In comparison to PLA, cyclic olefin copolymer (COC) was preferred due to its biocompatibility<sup>27</sup>, chemical resistance<sup>28</sup> and transparency. Moreover, it was reported that COC has low water absorption compared to PDMS and PMMA, promising stability and consistency, but the downside of COC is its reactive nature with non-polar solvents<sup>29</sup>.

### **2.4.2. Contact angle measurements of COC and Nylon**

Droplet formation and multiple emulsion systems using microfluidic devices rely largely on the wettability of the channels which can be characterised by the contact angle. The contact angles (CAs)

of 3D-printed Nylon substrates, 3D-printed COC substrate, and commercially available compression moulded COC wafer, were measured and listed in **Table 2. 3**.

The measurements of the bottom and top faces of the 3D-printed samples (**Figure 2. 3A**), reveal how the contact with the glass substrate increased the CA by  $16.1^\circ$  for COC and  $12.9^\circ$  for Nylon. The printed side facing the glass (bottom) yielded a lower surface roughness ( $R_a \downarrow$ ), compared to the tougher top surface ( $R_a \uparrow$ ). The  $R_a$  is a measurement that describes the texture of a surface with peaks, although this was not measured as part of this project. In the nanoscale, hydrophobicity ( $CA \geq 90^\circ$ ) and superhydrophobicity ( $CA \geq 150^\circ$ ) have been correlated with high  $R_a$ <sup>30,31</sup>. However, in the microscale of 3D-printed components, the higher the  $R_a$ , the more hydrophilic a surface can be<sup>32,33</sup>, which agrees with the findings in **Table 2. 3**. These observations could be a result of the capillary action occurring between the aqueous droplet and the 3D-printed rough surface of the sample. The internal microfluidic channels are more likely to possess higher  $R_a$ , with values closer to the top surface of the measured samples. Therefore, the CAs for COC and Nylon are considered to be  $77.8^\circ \pm 1.1$  and  $45.5^\circ \pm 0.7$ , respectively (**Figure 2. 3B**). Injection moulded COC parts have CA of approximately  $90^\circ$ <sup>34</sup>, hence roughly  $7^\circ$  higher than that of the measured COC wafer. This difference could be due to the COC grade and type of sample tested. Such samples have been used as substrates for milling and found that the contact angle could be varied between  $76^\circ$  and  $109^\circ$  by manipulating the milling parameters<sup>30</sup>. Finally, according to the manufacturer Ultimaker, the Nylon filament has polyamide 6/66 grade, which has been reported to have a contact angle of approximately  $68^\circ$ <sup>35</sup>, which is considerably higher than the CAs measured here

**Table 2. 3: Contact angles values for all tested materials ( $n=3$  per surface and  $\pm$  indicates the uncertainty of the average CA).**

Surface	Contact Angle
COC <sub>top</sub>	$77.8^\circ \pm 1.1^\circ$
COC <sub>bottom</sub>	$93.9^\circ \pm 0.3^\circ$
Nylon <sub>top</sub>	$45.5^\circ \pm 0.7^\circ$
Nylon <sub>bottom</sub>	$58.4^\circ \pm 1.6^\circ$
COC wafer	$82.8^\circ \pm 2.4^\circ$

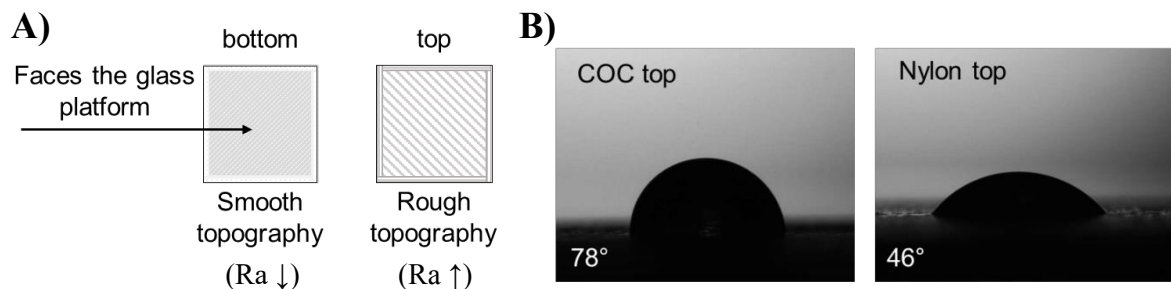


**Figure 2. 3: The smooth and rough surfaces of the 3D-printed parts and the CA of COC and Nylon substrates. A) Schematic of the 3D-printed samples (bottom and top view) used for CA measurements, noting that the bottom face contacting the glass substrate has a smoother topography ( $R_a \downarrow$ ) than the top face ( $R_a \uparrow$ ). B) Images of the water droplet on COC<sub>top</sub> ( $78^\circ$ ) and Nylon<sub>top</sub> ( $46^\circ$ ) 3D-printed samples, as acquired through the camera setup.**

### 2.4.3. Single emulsion microfluidic device (SE-MD)

Alginate microgel bead production was achieved using the 3D-printed COC microfluidic device shown in **Figure 2. 4A-C**. The biocompatibility of COC renders it as a highly suitable microfluidic device material for further cell encapsulation experiments, but first, the droplet frequency and droplet diameter needed to be evaluated. The oil phase (OP1) and alginate phase (AP1) flow rates were varied as mentioned in Section 2.3.3, to assess droplet pinch-off at the T-junction (**Figure 2. 4B**).

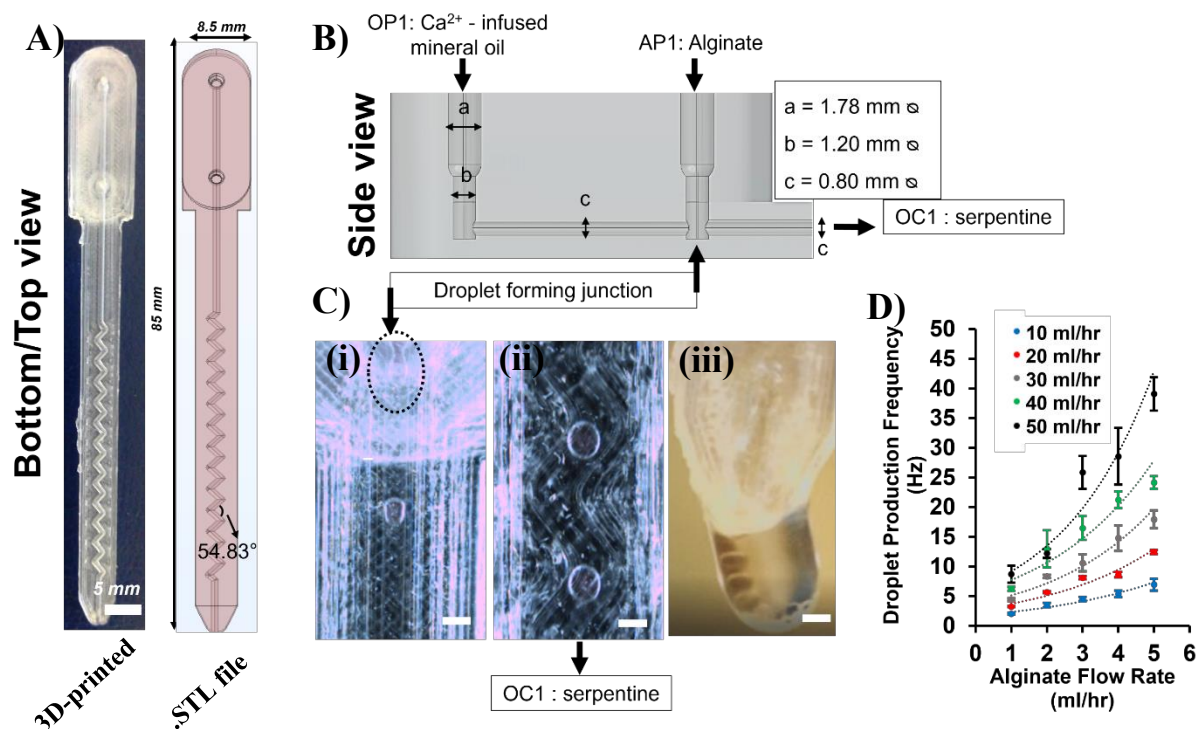


**Figure 2. 4: SE-MD experimental device, setup and droplet production affected by the inlet flow rates.** **A)** COC microfluidic device with a carrier serpentine channel utilised for microgel production (angle between intersecting channels is 54.83 °). LHS: Bottom view of the 3D-printed device and RHS: Top view of the STL file generated by CAD software. **B)** Side view of the designated T-junction for microgel production **C)** COC images taken by the mega speed camera where the dotted circle indicates the site of the droplet breakup (i), and its subsequent flow in the serpentine channel (ii), and eventually exiting through the orifice (iii) into the collection container (scale bars are 1 mm). **D)** Line/dotted graph of the relationship between the droplet frequency production (Hz) against the alginate dispersed flow rate ( $n=20$  per flow rate combination).

#### 2.4.3.1. Droplet frequency production

For each applied flow rate ratio (OP1:AP1), the droplet production frequency was captured using the MegaSpeed camera (at 600 FPS) (**Figure 2. 4C(i)-(ii)**). The video recordings of 5s duration were processed in Fiji ImageJ, where a macro was generated to measure the droplet generation frequency based on the grey value intensity changes (*Appendix 2.A*). The droplet frequency increased as the flow rates of either OP1 or AP1 was increased (**Figure 2. 4D**). It was also observed that an increase in the continuous flow, OP1 affected the production frequency to a greater extent than the dispersed phase, AP1. For example, the flow rate combination of 50:5 (ml/hour), produced droplets almost 6 times faster than the 10:5 (ml/hour) combination.

### 2.4.3.2. Hydrogel diameter

The same flow rate variations were applied to investigate the size of the droplets after gelation. Alginate droplet partial gelation occurred on-chip and then exited the outlet (**Figure 2. 4C(iii)**) into a 0.2 M CaCl<sub>2</sub> bath to complete gelation<sup>36</sup>. When transferred into a container with deionised water, the microgels' diameter from each set of flow rates was imaged using a GXM-XDY-2 inverted microscope. Microgel diameter was measured using Fiji ImageJ and the microgels of nine flow rate combinations (10:1, 10:3, 10:5, 30:1, 30:3, 30:5, 50:1, 50:3, 50:5) are shown in **Figure 2. 5**.

The diameter for each set of flow rates was plotted against the dispersed phase and the continuous carrier oil phase (**Figure 2. 6A&B**). The orange highlighted diameter measurements and coefficient of variation (CV) from **Figure 2. 6A-Table A** and **Figure 2. 6B-Table B**, show that the most suitable flow rate ratio for producing monodisperse capsules of diameter approximately 510  $\mu\text{m}$ , is 30:5 ml/hr (**Figure 2. 6C**). It should be noted that **Figure 2. 6A** reveals some instabilities on the microgel diameter at flow rate ratios of 50:3, 40:3 and 30:3. However, there is no clear explanation for this phenomenon. Finally, the inverse relationship between the droplet frequency and droplet diameter with the increase of the carrier phase flow rate is illustrated in **Figure 2. 6D**, confirming that the higher the carrier oil flow rate, the larger the production frequency and the smaller the droplet diameter.

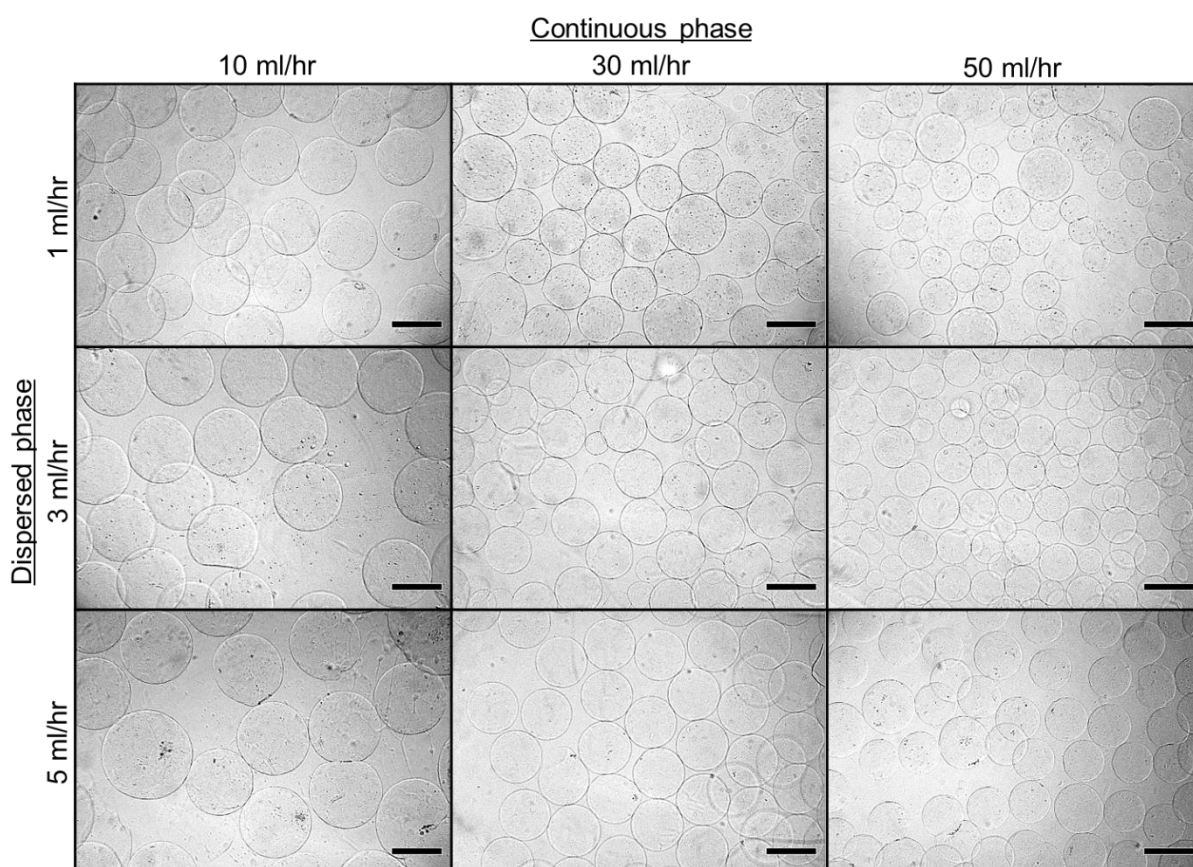


**Figure 2. 5:** Images of different microgels produced using SE-MD and various flow rate ratio combinations. Microgels of 9 out of 25 flow rate combinations captured with the GXM-XDY-2 inverted microscope. Each image corresponds to a dispersed flow noted on the LHS (horizontal grouping) and a continuous flow (vertical grouping). Scale bar denotes 500  $\mu\text{m}$ .

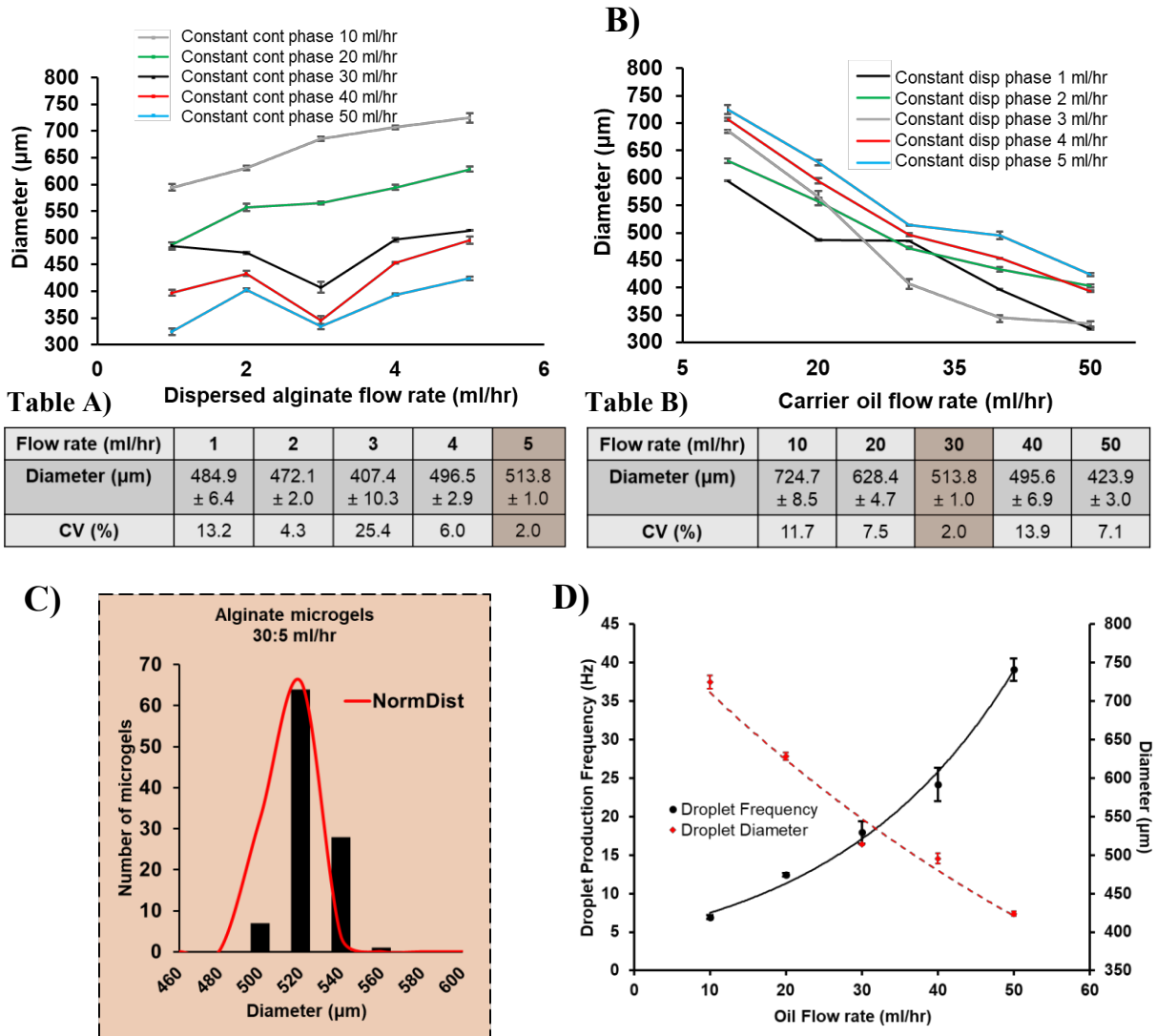


**Figure 2. 6:** The effect of various flow rate combinations on microgel production using 3D-printed SE-MD, further analysis of monodispersity and correlation between droplet frequency and diameter. **A)** Microgel diameter against the dispersed phase (ml/hr) graph, while maintaining each carrier phase constant (n=50). **Table A)** lists the diameter values (n=50) and CV (%) of the graphed black line data relating to the constant carrier flow rate of 30 ml/hr and varying alginate phase. **B)** Microgel diameter against continuous phase (ml/hr), while maintaining each dispersed phase constant (n=50). **Table B)** has the diameter values (n=50) and CV (%) of the graphed blue line data relating to the constant dispersed flow rate of 5 ml/hr and varying the carrier phase. The orange highlighted area in the tables corresponds to the flow rates used for further experiments involving cell encapsulation. **C)** Microgel diameter distribution for the flow rate ratio 30:5 ml/hr, concluding the generation of monodispersed microgels (n=100). **D)** The inversely proportional relationship between droplet frequency (n=20) and droplet diameter (n=50) against the continuous flow rate.

#### 2.4.4. Double emulsion microfluidic device (DE-MD)

The intent of this section is to understand and explore the formation of oil-core hydrogel capsules, to further utilise them for enclosing droplet interface bilayers (DIBs) (Section 2.4.5). Although, the formation of the desired single oil-core capsules was relatively easy to achieve, the control of multiple oil-core encapsulation in alginate was challenging and further investigated. Double emulsion, oil-core, alginate-shell capsules were produced using the device (DE-MD) shown in **Figure 2. 7A**. This 3D-printed microfluidic device consisted of a Nylon T-junction, [with design and dimensions same as the SE-MD (see Section 2.4.32.4.2 above)] and a 2<sup>nd</sup> COC flow-focusing junction (**Figure 2. 7B**).

##### 2.4.4.1. Single-core O/H/O

Single-core alginate-shell capsules, from **Figure 2. 7C**, were produced and gelled as described in Section 2.3.4. The inner oil phase, OP2 (3.5 ml/hr), alginate mid-phase, AP2 (17.5 ml/hr), and carrier gelling emulsion, OC2 (34 ml/hr) facilitated the production of the oil-core hydrogel-shell capsules. The diameter of the oil-core hydrogel capsules was measured on-chip during formation, and off-chip, after full gelation had occurred. On-chip diameter measurements revealed that the red oil droplets had diameter  $421.7 \mu\text{m} \pm 5.5$  and the whole capsules (i.e., alginate diameter) had diameter of  $947.9 \mu\text{m} \pm 14.3$  (**Figure 2. 7C(i)**). The double emulsion formation in **Figure 2. 7C(i)**, seemed to be governed by the dripping regime with the final capsules being relatively uniform in size (**Figure 2. 7C(ii)-(v)**). According to Utada *et. al* 2005 the dripping regime can produce droplets with diameters close to the orifice diameter (in this case diameter,  $a$ , in **Figure 2. 7B**), while during jetting, droplet break-up occurs further downstream, at a distance three times the orifice diameter<sup>37</sup>. This delayed double emulsion break-up was not observed here, hence the assumption of the dripping regime. In addition, the 2<sup>nd</sup> droplet-forming orifice ( $a$ ) in the CAD model was assigned to have diameter of  $800 \mu\text{m}$  (**Figure 2. 7B**), which was approximately  $150 \mu\text{m}$  less than the measured on-chip diameter of the eDIB capsules.

Furthermore, it was observed that off-chip diameter measurements of the alginate capsules enclosing the oil core (**Figure 2. 7C(ii-iii)**), shrank by approximately  $200 \mu\text{m}$ , due to the crosslinking of alginate in the presence of  $\text{Ca}^{2+}$  ions<sup>38</sup>. This off-chip diameter decrease could also be due to the eliminated shape restriction occurring on-chip. In the attempt to increase the number of oil cores, by increasing the inner OP2 flow rate, the formed oil droplets were dominant in size with respect to the alginate shell area, leading to merging with the carrier phase, OC2.

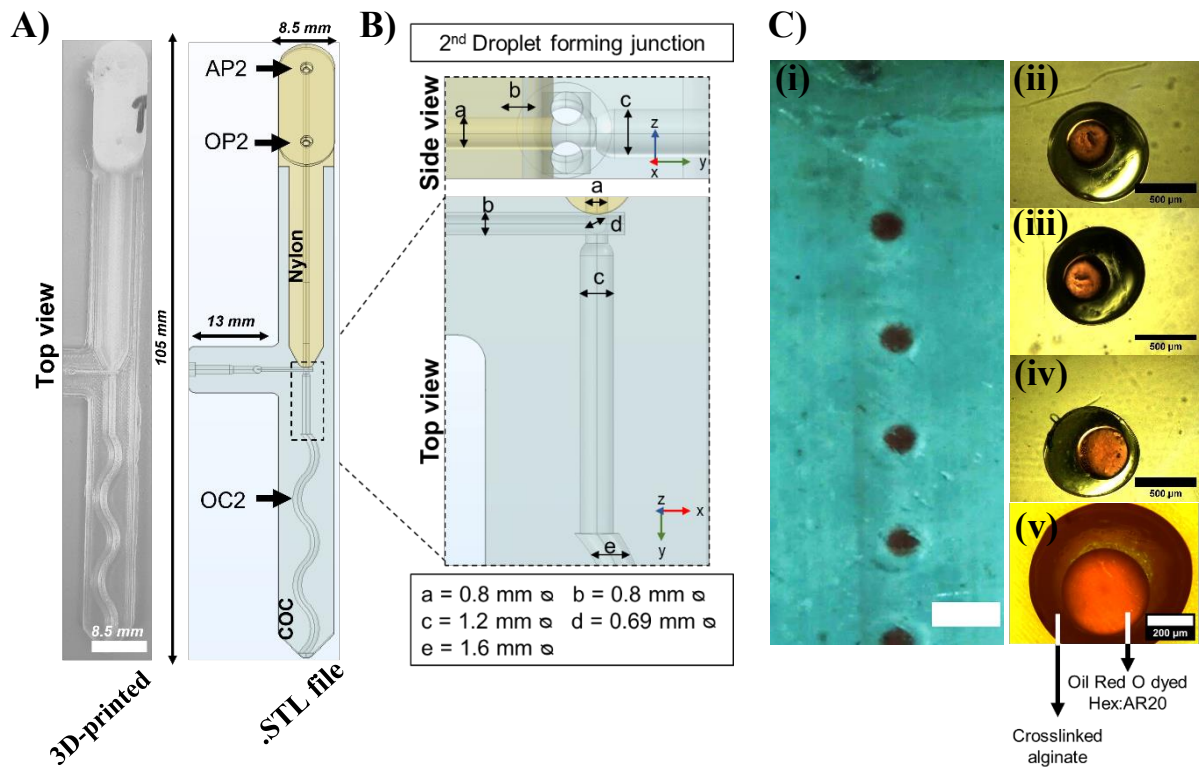


**Figure 2. 7: DE-MD experimental setup and device dimensions for single oil-core hydrogel-shell production.** *A)* Top view of the DE-MD utilised for O/H/O emulsion formation (LHS: 3D-printed device, RHS: STL file generated by COMSOL Multiphysics). *B)* Side and top view of the flow-focusing 2<sup>nd</sup> droplet-forming junction (light yellow: Nylon material, light blue: COC material), with annotated channel dimensions. *C)* Oil-core capsules produced using 3.5, 17.5 and 34 ml/hr for the inner, alginate and outer oil phase, respectively (i) Mega Speed camera image of the 2<sup>nd</sup> junction, with an array of single oil-core alginate-shell capsules (scale bar is 1 mm). (ii)-(v) Isolated single oil-core capsules in a petri dish with mineral oil, after complete gelation.

#### 2.4.4.2. Multi-core O/H/O

To understand the controlled oil core encapsulation in O/H/O emulsions, the flow rates of follow-up experiments were decreased substantially. The oil phase (OP2) ranged from 0.1 to 1 ml/hr, in increments of 0.1 ml/hr, while the alginate phase (AP2) and carrier oil phase (OC2) were kept constant at 2 ml/hr and 8 ml/hr, respectively. At every 0.1 ml/hr increment, an increase in the number of oil cores was observed as shown by the increasing size of the bubbles in the graph of **Figure 2. 8A**. Two additional observations were made when the AP2 flow rate was increased further to 3 and 4 ml/hr, while the OP2 was kept constant at 0.7 ml/hr. First, as expected, the diameter of the oil droplets had decreased, and second, the number of the encapsulated oil cores increased by a greater extent (3-4 oil cores) compared to the rest of the flow rates (orange highlighted regions in **Figure 2. 8A**). These data shows that in order to control the number of encapsulated oil cores, it is not enough to only increase the inner oil phase, but the alginate middle phase as well <sup>37</sup>.

To explore the encapsulation of more oil cores ( $\geq 3$  oil droplets per capsule), the AP2 rate was increased from 2 ml/hr to 5 ml/hr (**Figure 2. 8B**). The flow rate of 5 ml/hr reduced the inner oil cores' diameter and resulted in up to 7 oil droplets being encapsulated in the alginate shell. It is noteworthy to mention that the experiments summarised and plotted in **Figure 2. 8A&B** resulted from the droplet formation following the jetting or squeezing regime (*Appendix 2.B*). In the squeezing regime, the emerging alginate droplet that carried the oil cores, occupied the whole area of the microfluidic channel, leading to an upstream pressure build-up that broke the alginate phase into droplets <sup>39,40</sup>. These effects strongly depend on the carrier flow rate, which in this case was 10 ml/hr.

Subsequently, it was hypothesised that to achieve an incremental and consistent multi-core encapsulation, both the alginate and inner oil flow rates needed to be manipulated (**Figure 2. 8C**). Based on this hypothesis, the flow rates were increased almost equally every time, and a linear relationship was obtained between the number of oil cores and flow rate ratio  $Q_d/Q_c$  (**Figure 2. 8D**). A similar relationship and phenomena of the controlled encapsulation of inner cores, has been previously characterised by Ji, *et al.* 2018, as the synchronised regime <sup>41</sup>. Images of single and multi-core O/H/O capsules across multiple experiments are shown in **Figure 2. 9A**. Finally, **Figure 2. 9B** shows the O/H/O monodispersed capsules from the final dripping/synchronised regime experiment (**Figure 2. 8C&D**), before and after gelation. Detailed tables on the flow rates, average core number, diameter measurements and the error of mean, can be found in *Appendix 2.C*.

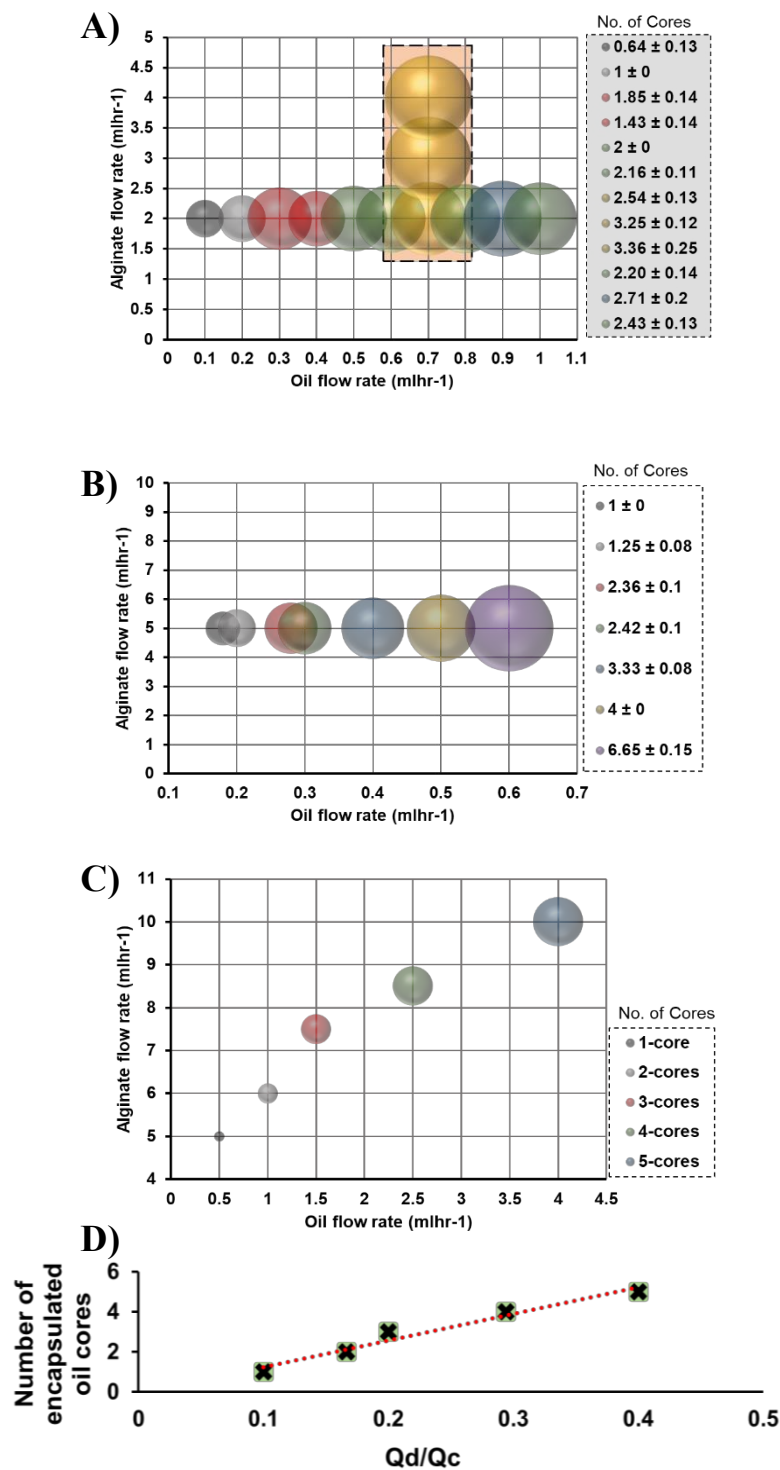


**Figure 2. 8: Production of multi-core O/H/O capsules using the DE-MD and the effect of different flow rates on the number of encapsulated cores.** *A)* The first experiment showing that a slight increase in the alginate flow rate can have a greater impact on the control over the number of encapsulated cores compared to the increase of the inner oil phase ( $n=10-14$ ). Here, the continuous carrier phase was 8 ml/hr. *B)* The second experiment establishes that the oil droplet diameter is also a significant factor for controlling the core number ( $n=21-36$  except  $4\pm 0$  with  $n=4$ ). The continuous carrier phase was 10 ml/hr. *C)* Conclusive data showing that the incremental increase of both the inner oil and alginate phase, benefitted the control over the core number ( $\pm SEM = 0$ , due to the consistent encapsulation number). In this experiment, the continuous carrier phase was 35 ml/hr. The size of the bubbles in all graphs corresponds to the oil core number. The average core number was calculated based on a 10 s video of O/H/O formation and the diameter is the average of multiple oil cores ( $n=14$ ). *D)* A linear trendline was obtained between the number of encapsulated oil cores against the  $Q_d/Q_c$ , based on data from C).

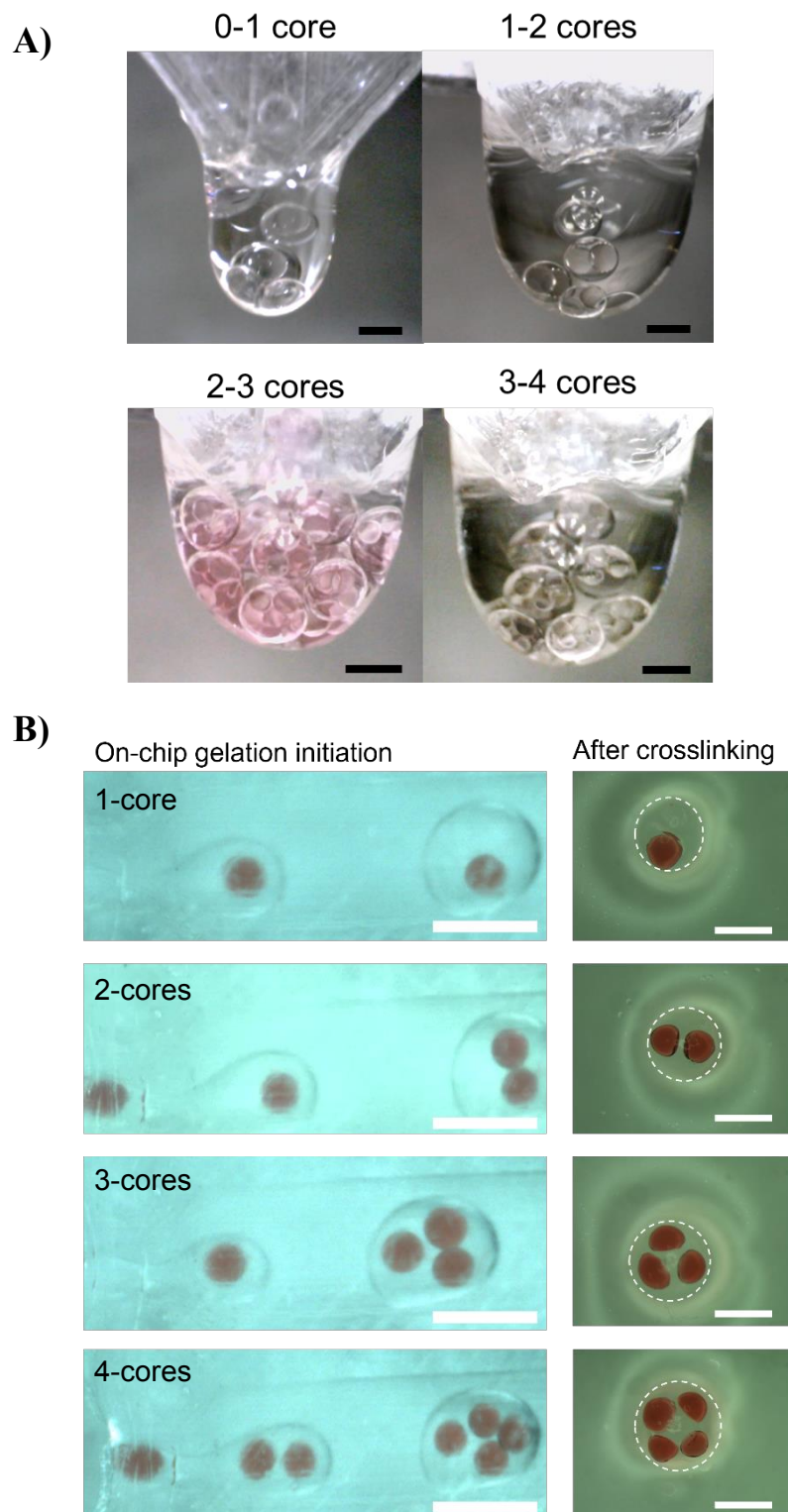


**Figure 2. 9: Images of various single and multi-core capsules produced using DE-MD. A)** Images of the outlet channel, right before the O/H/O capsules are collected in 0.2 M  $\text{CaCl}_2$  (OC2 is pure mineral oil). **B)** High speed video frames of 1-4 red oil-core hydrogel-shell capsules, before (on-chip) and after crosslinking of alginate (capsules are in a petri dish with mineral oil). OC2 is a 1:6  $\text{Ca}^{2+}$ -infused nano-emulsion. Scale bar of 1 mm included.

### 2.4.5. Triple emulsion microfluidic device (TE-MD)

Compared to the DE-MD, the TE-MD required more development time in terms of optimising the 3D-printed microfluidic channel dimensions, the encapsulated droplet interface bilayer (eDIB) material components and stability of the artificial lipid membranes. So far in this chapter, 3D FFF printed microfluidic devices produced double emulsions using two droplet-forming junctions. In this section, triple emulsion and eDIB formation is reported using a triple junction 3D-printed microfluidic device made of COC and Nylon. The TE-MD was inspired by the SE-MD and DE-MD and the development stages are presented in *Appendix 2.D*. The final 3D-printed microfluidic device employed for the formation of eDIBs is shown in **Figure 2. 10A**, along with the top and side view channel dimensions, displayed in **Figure 2. 10B** and **Figure 2. 10C**, respectively. The channel overlap, between inner water phase (WP3) and lipid-oil phase (OP3) channels shown in **Figure 2. 10C(i)** of approximately 0.06 mm along the z-axis (layer height assigned in CURA print settings), minimises the area of the 1<sup>st</sup> droplet-forming junction, compared to a planar flow focusing device (*Appendix 2.E*).

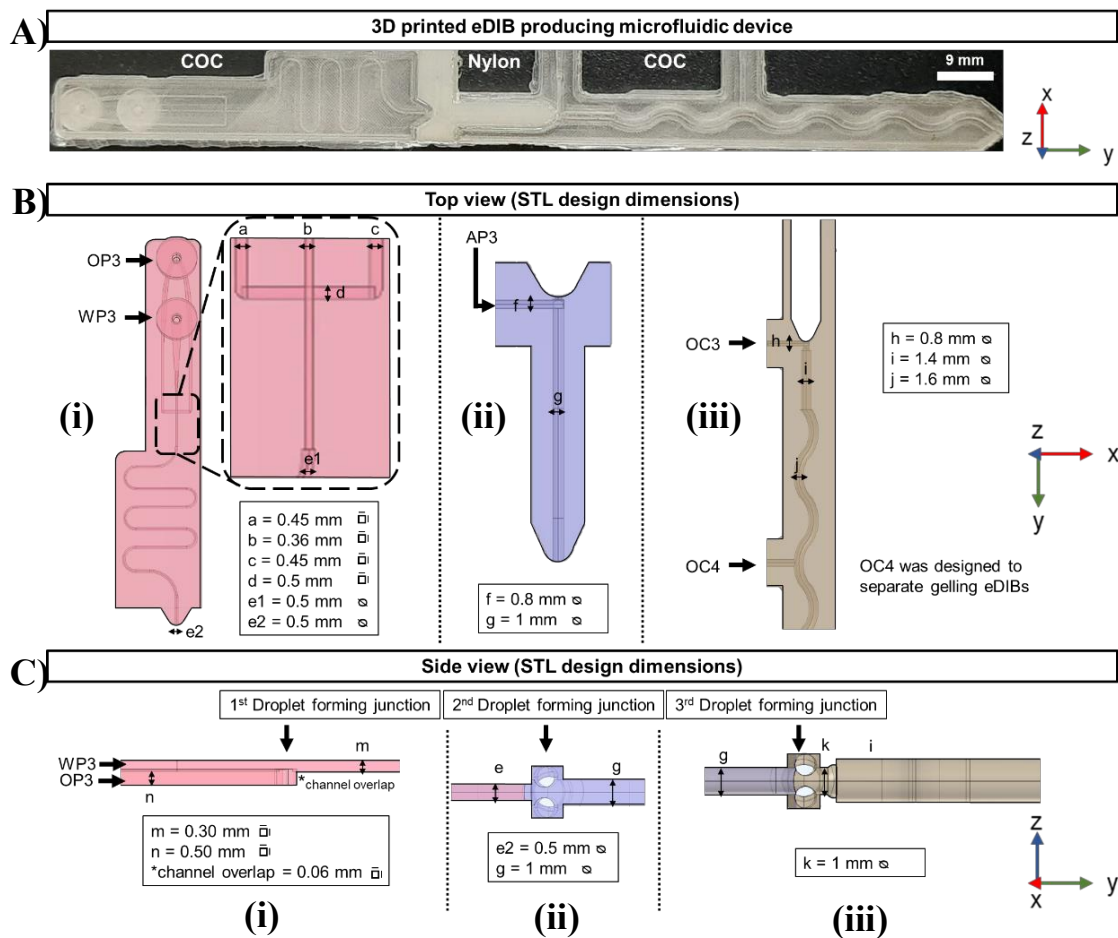


**Figure 2. 10:** The final TE-MD and its dimensions utilised for triple emulsion capsule and eDIB formation. **A)** The COC/Nylon/COC 3D-printed TE-MD after fabrication. **B)** Top and **C)** Side view CAD (STL) dimensions of the microfluidic channels that make up the microfluidic device for eDIB production. The TE-MD consists of a 1<sup>st</sup>, 2<sup>nd</sup> and 3<sup>rd</sup> droplet-forming junction, responsible for the W/O, W/O/H, W/O/H/O emulsion formation, respectively.

### 2.4.5.1. CAD geometry dimensions Vs 3D-printed dimensions

Understanding the printing capabilities of the Ultimaker S5 3D printer is crucial, therefore the STL design dimensions were compared to the dimensions of the microfluidic device after production (**Figure 2. 11**). These comparisons are also important for the practical formation of the DIB buffer droplets and the mid-oil core, with respect to the overall eDIB capsule. The comparisons were limited to the top view dimensions, given that the channels were impossible to visualise from the side, with the equipment available. In addition, due to the lack of transparency of printed Nylon, only the COC channel dimensions were analysed.

Except one (*e1*), all the microfluidic channels had decreased dimensions after fabrication compared to the designed (STL) channels. These diameter reductions ranged from 3 % to 14 % for the cylindrical channels ( $\ominus$ ) and 33 % to 40 % for the rectangular channels ( $\square$ ) (Table in **Figure 2. 11**). Similar observations were made in a different study on stereolithography (SLA) 3D-printed cylindrical and rectangular channels, where the designed cylindrical channel dimensions complemented the microscopically measured dimensions, while the rectangular dimensions not so much<sup>42</sup>. These claims were made by Wang, *et al.* 2021, who printed these geometries with the open faces along the z-axis, while the open faces of the TE-MD presented here, are along the y-axis. Only the channel *e1*, which is responsible for slowing down the water-in-oil (W/O) emulsion and incubating the droplets to form a lipid monolayer, showed a post-fabrication diameter increase of 6 %.

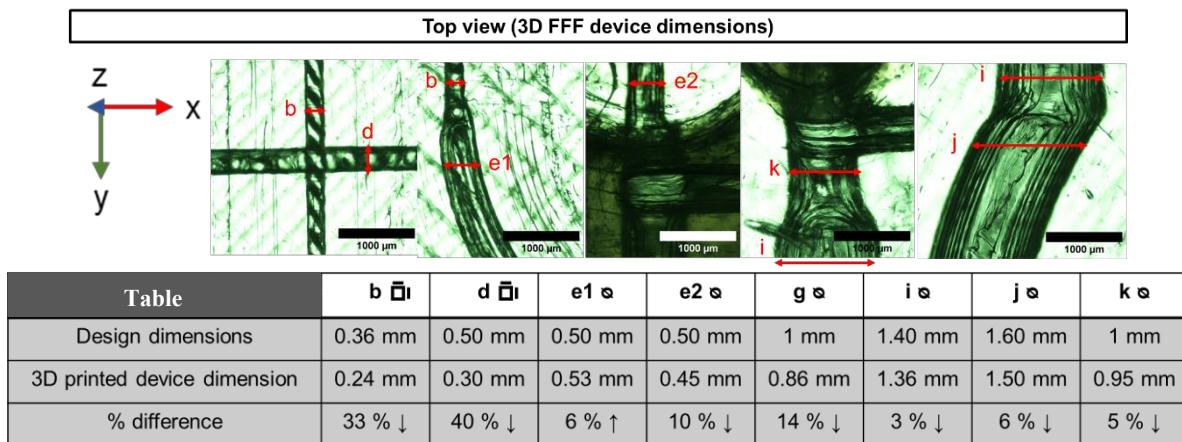


**Figure 2. 11: Microscopy images of the 3D-printed, COC, TE-MD channels and comparisons with the CAD assigned dimensions.** TOP: Images taken by the widefield microscope (MM800) of the microfluidic channels after fabrication by the Ultimaker S5 Pro Bundle. Each red letter corresponds to the same dimension as the CAD STL file from the previous figure. BOTTOM: Table summarising the design dimensions and microscopically measured dimensions of the microfluidic device. The percentage (%) difference of each dimension was calculated to show the impact of filament deposition on the designated channel sizes.

The rectangular channels ( $\bar{\square}$ ) had the largest size differences between the design and post-fabrication channel dimensions. Despite that, they are more suited for small-scale printing and droplet production, compared to the cylindrical microfluidic channels, since the area of a rectangle is smaller than the area of a circle. Moreover, it is more likely for cylindrical small-scale channels to be clogged, due to the infill pattern (Raster fill, Contour fill or a combination) and travelling of the nozzle<sup>43</sup>. **Figure 2. 12A**, shows these three infill patterns for material deposition of a closed cylinder, being printed along the z-axis. However, for open loop channels (e.g., inlets and vertical cylindrical channels), **Figure 2. 12B** provides a more accurate representation of the combination infill pattern. The circular motions and curved lines can lead to the deposition of melted plastic to the channel, leading to the clogging of the device. Therefore, care should be taken regarding the selection of the geometries that make up the microfluidic channels, their contribution on the finished device and, the post-fabrication dimensional changes.

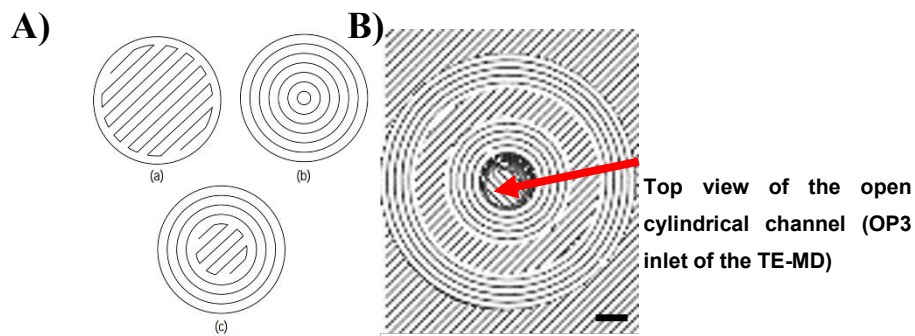


**Figure 2. 12: 3D printing infill patterns and nozzle travel of cylinder geometries.** *A) (a) Raster fill (b) Contour fill (c) Raster/Contour combination of closed-loop structures<sup>36</sup>. B) Infill pattern raster/contour combination of cylinder geometry with an open channel (OP3 inlet). Scale bar is 1 mm.*

## 2.4.5.2. eDIB formation, from the inside-out

### 2.4.5.2.1. 1<sup>st</sup> droplet-forming junction

The 1<sup>st</sup> part of the TE-MD is the hydrophobic COC droplet-forming junction, which enables the formation and long incubation (at least 10 s) of buffer droplets in dioleoyl-phosphatidylcholine (DOPC) phospholipid-containing hexadecane oil (W/O). This is a non-planar, two-layer droplet-forming junction (**Figure 2. 10C(i)**) and it is shown in **Figure 2. 13A**, during operation<sup>44</sup>. The decreased dimensions of the 3D-printed microfluidic devices, enabled the production of smaller droplets than initially planned (designed as 360  $\mu\text{m}$ , printed as 240  $\mu\text{m}$ , **Figure 2. 11-BOTTOM**), which was beneficial for faster and more complete lipid monolayer assembly and eventually stable eDIB formation. The printed COC had good transparency, supporting the visualisation of the channel and possible calculation of droplet generation (Hz), either with the use of fluorescently excited dyes (e.g., sulforhodamine B, SulfB and Calcein) or under ambient lighting (**Figure 2. 13B**).

The W/O emulsion occasionally caused clogging of the 1<sup>st</sup> droplet-forming channel, due to possible lipid aggregates in the hexadecane solution or, more likely, the softening of the materials due to hexadecane. The former phenomena can occur when an oil lipid-containing solution comes in contact with water, undesirably, forming lipid aggregates leading to clogging of the first junction. Although, the latter reasoning is more likely to be the clogging factor, due to the reported dissolution of COC in non-polar solvent, including hexadecane<sup>29</sup>.

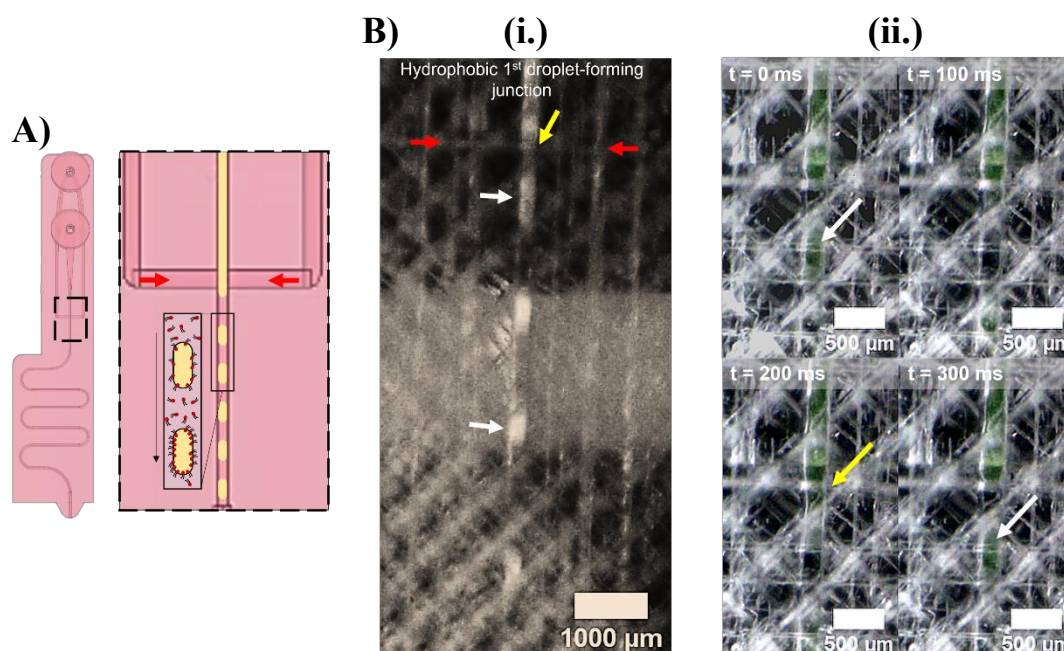


**Figure 2. 13:** Calcein/buffer droplet formation in 12.5 mg/ml DOPC/Hex (W/O) at the 1<sup>st</sup> droplet-forming junction of the TE-MD. **A)** Schematic of the 1<sup>st</sup> junction showing the water-in-oil emulsion formation. The lipid monolayer is formed around the water droplets as they flow through the central channel. **B)** Photographs of the 1<sup>st</sup> junction showing the water-in-oil emulsion. The droplet production frequency of this experiment was 3.6 Hz. The yellow arrows indicate the location of the junction, and the white arrows show the emerged droplets. (i.) The calcein droplets were excited by a UV torch of wavelength 365 nm (no filter used). Red arrows reveal the channels of the continuous lipid-containing oil. (ii.) Panel figure of the droplet pinch-off in ambient light at four consecutive timepoints. Images of this figure were acquired using Dino-Lite edge USB camera.

The serpentine channels were tailored to support the lipid monolayer formation around the W/O buffer droplets, by prolonging incubation time. However, premature bilayer formation between multiple adjacent droplets, as shown in the schematic of **Figure 2. 14** was regularly observed. This could be a result of a combination of factors, including the pressure differences between droplet aggregates and aggregates having different velocities, or due to printed artifacts around the curved fluidic channels <sup>45,46</sup>. Therefore, the design, as well as the 3D printing process, can give rise to irregularities of the flow. These irregularities are not ideal for applications that depend on droplet volume control and consistency. However, the aim of this chapter is the production of stable eDIBs, with the least possible participation of synthetic reagents (for biocompatibility reasons in Chapter IV). Thus, this final design progressed to further experimentation, despite the challenges with the uncontrolled premature bilayer formation between several buffer droplets.

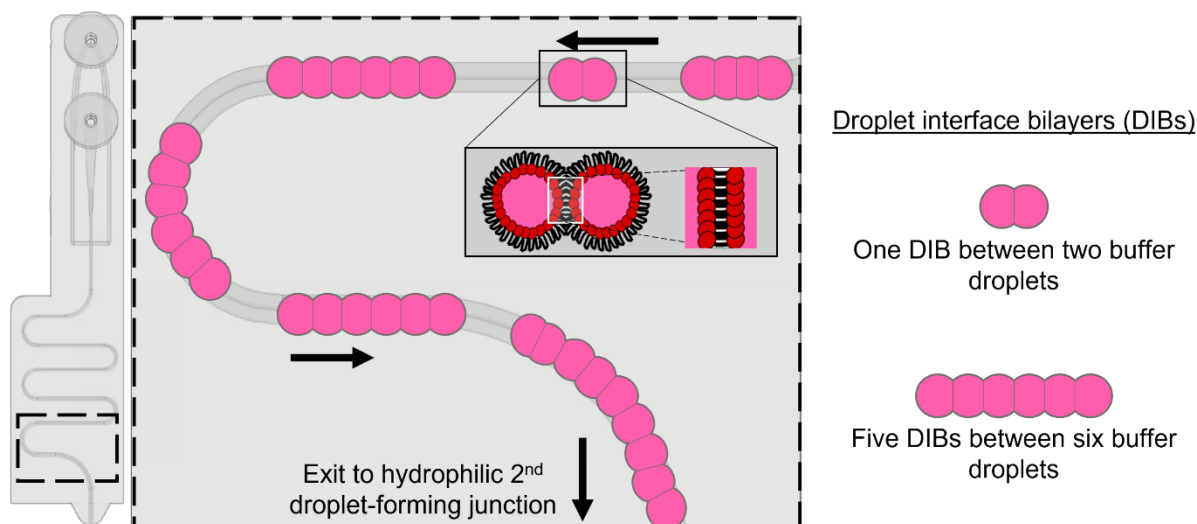


**Figure 2. 14:** From single to multiple DIB formation in the 1st COC microfluidic serpentine component of the TE-MD. DIBs are formed when two or more lipid-coated water droplets come in contact. Pressure differences along the serpentine channel causes buffer droplets to come closer to each other, forming numerous premature bilayers (ranging from 1 bilayer to many bilayers).

### 2.4.5.2.2. 2<sup>nd</sup> droplet-forming junction

The stable emulsification of the W/O by the AP3, was difficult to achieve, due to the decreased surface tension ( $\gamma$ ) of lipid-containing hexadecane oil and the presence of DIBs inside the oil<sup>47,48</sup>. The lipid-oil mixture was usually made of pure hexadecane, but oil mixtures from initial experiments consisted of silicone oil (AR20), too. Most earlier reported DIB studies, incorporate AR20 as it forms stable lipid bilayers, and is difficult to manipulate and separate<sup>49</sup>. Although, AR20 decreases the  $\gamma$  of an oil mixture further, making emulsification more challenging<sup>50,51</sup>. To increase the stability of the DIBs and evidently the formation of eDIBs, moderate DOPC concentration of 12.5 mg/ml was primarily used.

The DIBs or W/O emulsions enter the 2<sup>nd</sup> droplet-forming junction (Nylon) and are pinched-off by the AP3 with considerably higher flow rates than the earlier oil phase (OP3) (approx. 10 times higher). The 3D-printed Nylon filament is not as transparent as the COC, as it appears from **Figure 2.15**. However, some information was successfully extracted from high-speed videos relating to the W/O/H emulsion, which was satisfactory for some flow and droplet formation assumptions. During the double emulsion formation (W/O/H) and after pinch-off, the water droplets moved in a circular, vortex-like motion which has been previously described as planetary-like motion<sup>52</sup>. The water droplets appeared to be rotating along the periphery of the oil droplet.

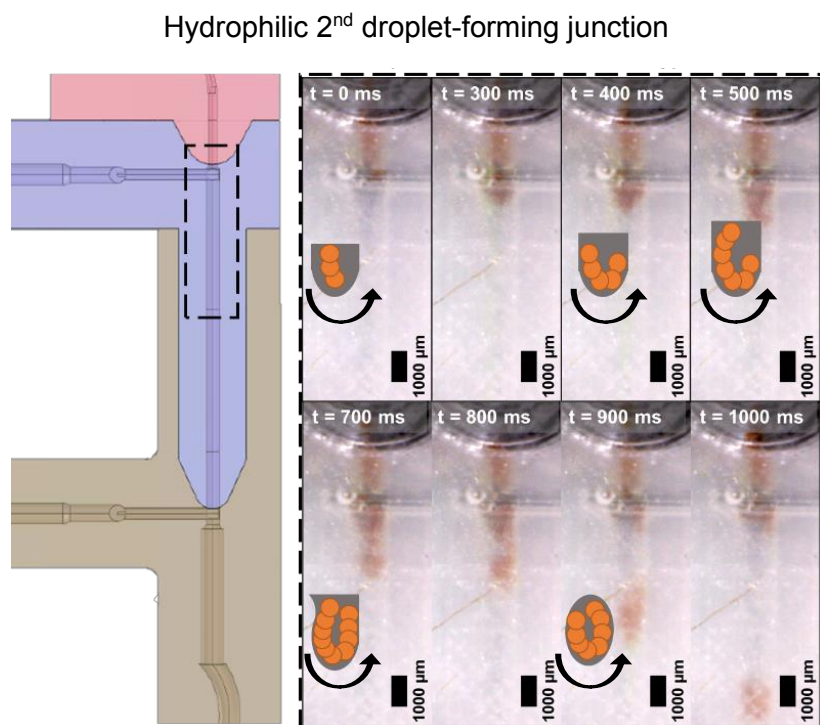


**Figure 2.15:** Nylon microfluidic component of the TE-MD responsible for enclosing the DIBs in single oil droplets, by an alginate phase. The droplets or DIBs enter the 2<sup>nd</sup> droplet-forming junction, follow a vortex-like mixing and continued to mix after the W/O/H emulsion was pinched-off. The orange cores here are 70 mM calcein buffer droplets (WP3) in 12.5 mg/ml DOPC/Hex grey droplet (OP3) and the alginate phase (AP3) consists < 1 mg/ml DPPC vesicles. Images in this figure were acquired using Dino-Lite edge USB camera.

### 2.4.5.2.3. 3<sup>rd</sup> droplet-forming junction and eDIB protocol optimisation

The eDIBs, as triple emulsion capsules, need to retain their structure and ensure minimal cytotoxicity for subsequent experiments. For the formation of eDIBs, oils of different characteristic properties were used throughout this chapter (hexadecane, silicone oil, mineral oil), to either facilitate DIB formation or ensure aqueous phase pinch-off. Their density, viscosity and surface tension can be found in the table in *Appendix 2.F*. The use of surfactants for the formation of complex emulsions is beneficial, however surfactants can injure the biological cell membrane<sup>53</sup>. During preliminary experiments, the lack of surfactants led to merging between miscible phases upon the entry into the subsequent junction or channel. This occurred between the inner water droplets (WP3) and the alginate phase (AP3) or, between the mid-oil phase (OP3) and the outer oil carrier phase (OC3). These observations related to the merging of miscible phases within the microfluidic chip in the absence of surfactants are animated in **Figure 2. 16A**. In order to minimise the effect of coalescence, lipid-vesicles were incorporated into the alginate phase (AP3) and were studied in the following paragraphs to obtain the final eDIB protocol.

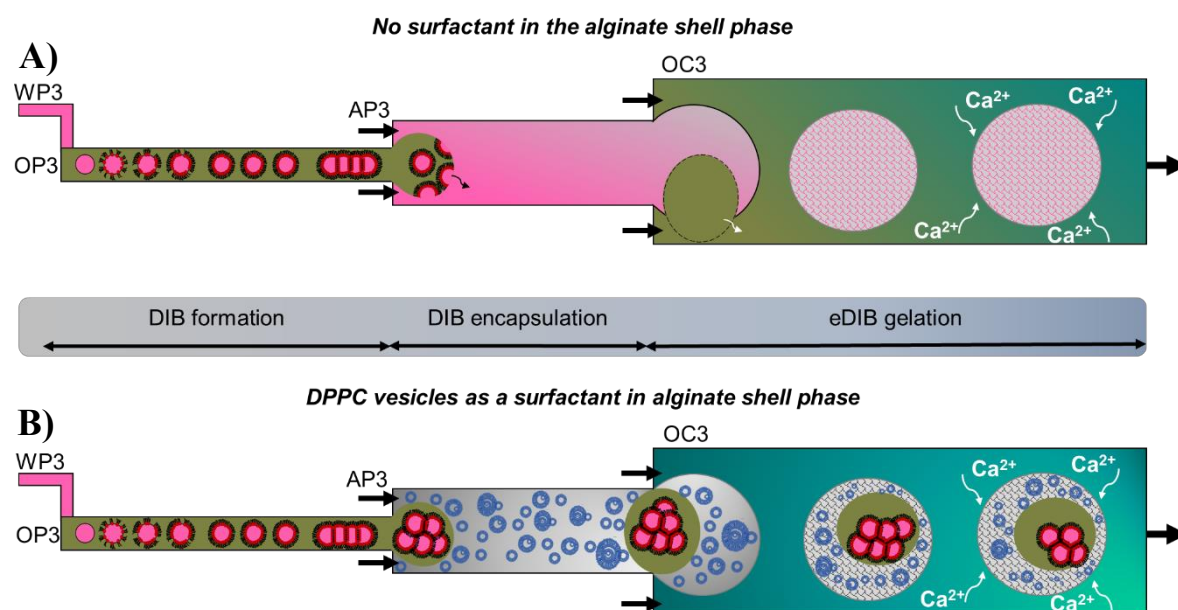


**Figure 2. 16:** Schematics of the microfluidic channel sequence without and with DPPC vesicles, starting from the lipid monolayer assembly to the DIB formation, encapsulation and eDIB production. **A)** Microfluidic phase flow setup lacking the vesicles. The pink buffer droplets (WP3) leak into the AP3 upon entering the 2<sup>nd</sup> droplet-forming junction (nylon) and the oil core (OP3) merges with the Ca<sup>2+</sup> nano emulsion (OC3). **B)** Phase flow setup with DPPC vesicles in the alginate. The vesicles prevent the water droplets and DIBs from merging with the outer alginate phase (AP3). The W/O/H emulsion enters the 3<sup>rd</sup> droplet-forming junction (COC) forming W/O/H/O, where the oil core (OP3) is stopped from merging with carrier nano emulsion (OC3), by the stabilising vesicles in the alginate.

*Dipalmitoyl-phosphatidylcholine (DPPC) vesicle addition and study*

The troubleshooting procedure for resolving the merging issue, involved the addition of surfactants to the alginate solution, starting with Tween 20. Tween 20 of 1 % final concentration in alginate was tested for eDIB formation (*Appendix 2.G*). The incorporation of 1% Tween 20 to the eDIB recipe, formed somewhat successful eDIBs, however synthetic surfactants at high concentrations can be toxic to living cells<sup>53</sup>. To combat the coalescence during on-chip microfluidic formation of eDIBs, others added CaCO<sub>3</sub> particles in the alginate phase which acted as viscosity-altering and gelling agents<sup>16</sup>. Consequently, an alternative surfactant was considered, which involved the supply of small lipid particles, DPPC vesicles, as shown in **Figure 2. 16B**. DPPC lipids reduced the  $\gamma$  of alginate<sup>54,55</sup> and acted as small particles that supported lipid bilayer formation<sup>56,57</sup>. Additionally, lipid vesicles can act as emulsion stabilising agents, by developing a barrier that mitigates merging effects between miscible phases. The stabilising property of lipid particles inspired the addition of lipid vesicles to the alginate phase, to facilitate the generation of eDIBs.

Through the process of trial and error, it was revealed that a variety of concentrations of DPPC can facilitate eDIB formation. Final DPPC concentrations in alginate for eDIB formation ranged between 0.5 and 12.5 mg/ml. However, as the vesicle concentration approached the upper limit of this concentration range, challenges emerged relating to the droplet pinch-off at the 3<sup>rd</sup> droplet-forming junction. Two concentrations of DPPC vesicles in alginate (7.3 mg/ml and 12.5 mg/ml) were investigated with similar flow rates, in order to examine the effect of the vesicle concentration on the eDIB generation. The panel images in **Figure 1. 17A&B**, indicate that higher vesicle concentration complicates the droplet break-up and introduced an unstable jetting regime. Such unstable formation of droplets and jets correlates with high Capillary number (Ca), which grows as the  $\gamma$  lowers by the increasing concentration of DPPC vesicles (inertial forces dominate interfacial forces)<sup>58,59</sup>. Additionally, the chaotic flow could be an indication of density differences within the alginate phase, due to the highly concentrated, polydisperse and multilamellar vesicles (for microscopy images of vesicle see *Appendix 2.H*)<sup>60</sup>.

Further decrease of DPPC vesicles to 6.5 mg/ml and increase of the DOPC concentration to 30 mg/ml, resulted in effective microfluidic eDIB formation (**Figure 1. 18A&B**). The diameter of the eDIBs post-gelation ( $\varnothing_{\text{eDIB}}$ ) was approximately  $1347.1 \mu\text{m} \pm 37.4$  (n=15). The internal SulfB buffer droplets ( $\varnothing_{\text{int}}$ ) were stable after production (**Figure 1. 18C**), however overnight merging caused the internal droplets to almost triple in size ( $\varnothing_{\text{int}}=460.7 \mu\text{m} \pm 16.2$ , n=25), compared to their diameter right after production ( $\varnothing_{\text{int}}=189.9 \mu\text{m} \pm 4.6$ , n=25) (**Figure 1. 18D**).

One of the concerns of the incorporation of vesicles in the aqueous alginate phase, is the formation of asymmetric lipid bilayers, instead of symmetric. From the timepoint where the oil core meets the alginate shell phase (2<sup>nd</sup> junction), up until the complete gelation of the alginate shell, DPPC vesicles can fused with the lipid bilayer, forming DOPC /DPPC asymmetric bilayers.

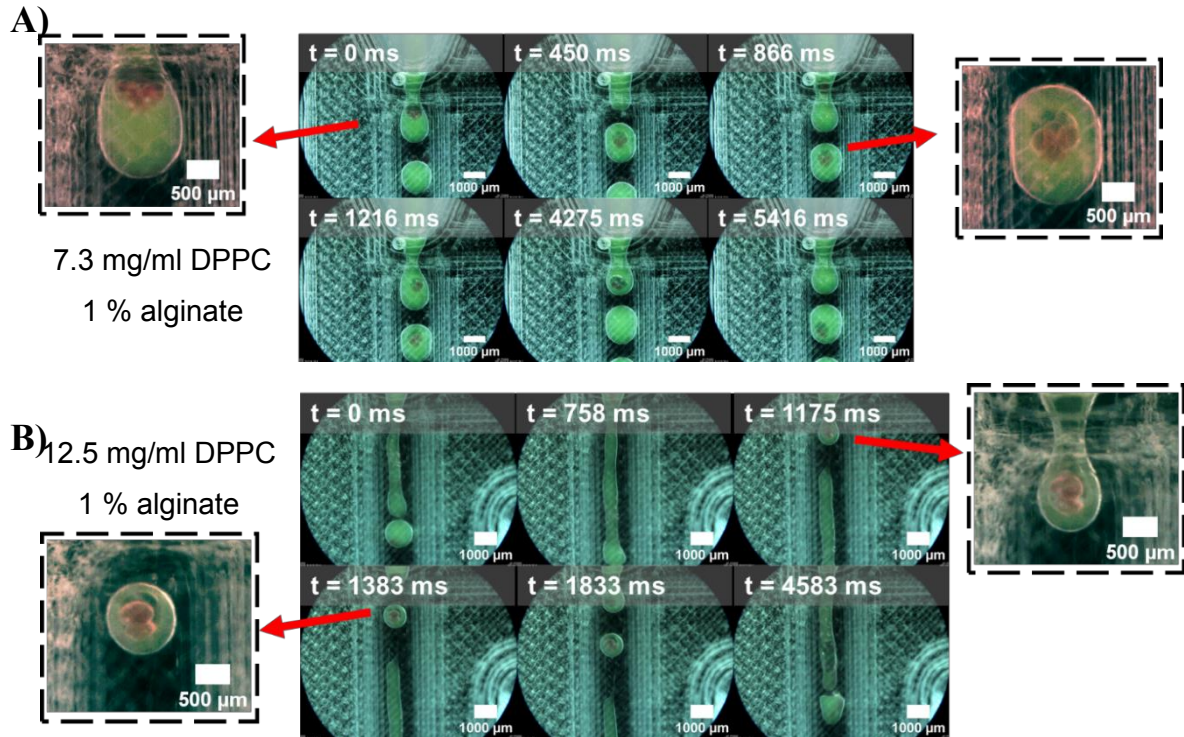


**Figure 1. 17:** Time-lapse images of *eDIB* formation with different final concentration of DPPC vesicles in the alginate phase (AP3). **A)** Lower concentration of DPPC in the alginate (7.3 mg/ml DPPC) permits more consistent *eDIB* formation. **B)** Higher DPPC vesicles concentration in alginate (12.5 mg/ml DPPC) introduces unstable jetting regime and difficulties in emulsifying the W/O/H emulsion. For this experiment, no gelation of the *eDIB*s was attempted. The rest of the phases are

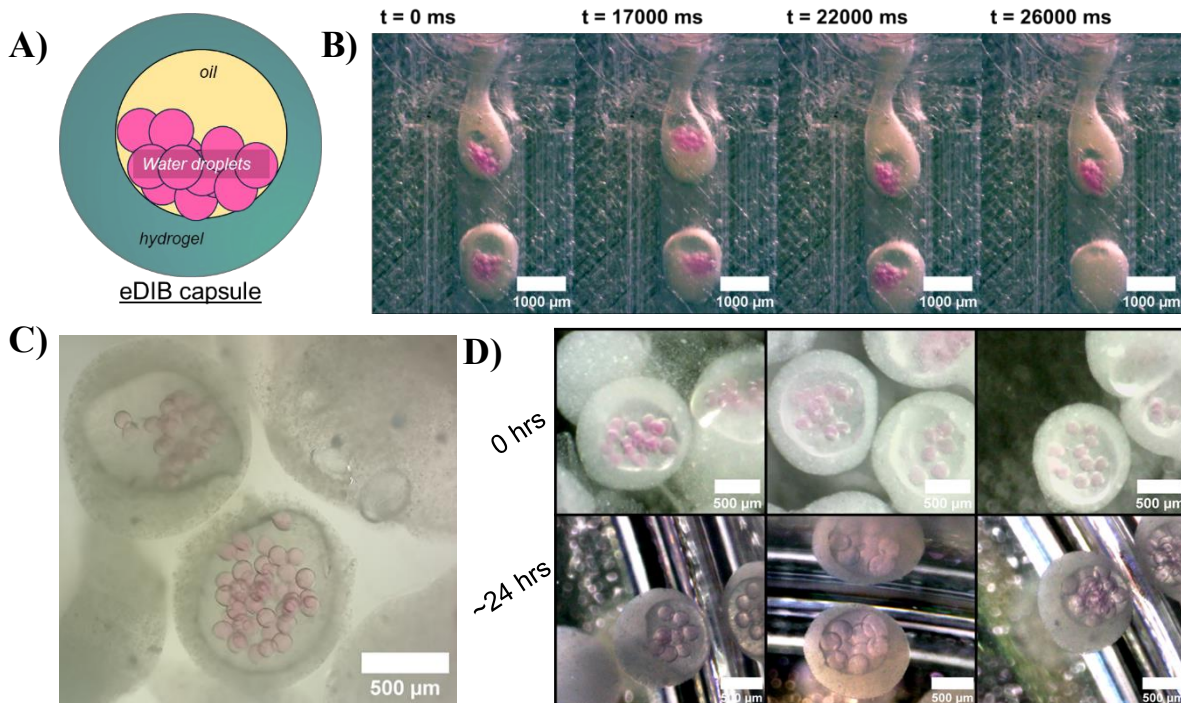


**Figure 1. 18:** Microfluidically formed *eDIB*s using 6.5 mg/ml final DPPC concentration in alginate shell and 30 mg/ml DOPC in Hex as the middle oil phase. **A)** Illustration of an *eDIB* capsule consisting of multiple water droplets encapsulated by a lipid-containing oil, surrounded by a hydrogel shell. **B)** Timepoint images of consistent *eDIB* production at the 3<sup>rd</sup> droplet-forming junction. **C)** *eDIB*s after production with  $\varrho_{eDIB} = 1128.5 \mu\text{m}$  and  $\varrho_{int} = 114.2 \mu\text{m} \pm 2.8$ . **D)** Images of *eDIB*s ( $\varrho_{eDIB} = 1347.1 \mu\text{m} \pm 37.4$ ) at  $t = 0 \text{ hrs}$  ( $\varrho_{int} = 189.9 \mu\text{m} \pm 4.6$ ) and at  $t = 24 \text{ hrs}$  ( $\varrho_{int} = 460.7 \mu\text{m} \pm 16.2$ ). The rest of the phases are WP3: Sph-B=buffer, OP3=30 mg/ml DOPC/Hex, OC3-OC4= 1:9  $\text{Ca}^{2+}$ -nano emulsion. Photographs in this figure were obtained using Dino-Lite edge USB camera.

Middle-oil phase (OP3) compositional changes and effect on surface tension ( $\gamma$ )

Changes of the phases' flow rates across the eDIB experiments, were well kept at minimum. Details on the approximate microfluidic phase flow rates applied for the eDIB formation can be found in Chapter III, Section 3.3.1. The mid-oil core droplets ( $\varnothing_{oil}$ ) of the eDIBs using 30 mg/ml DOPC, were larger ( $\varnothing_{oil} = 954.5 \mu\text{m} \pm 30.5$ ) than the 12.5 mg/ml DOPC in Hex:AR20 ( $\varnothing_{oil} = 776.9 \mu\text{m} \pm 31.7$ ). According to Yanagisawa, *et al.* 2013, the addition of DOPC to hexadecane oil reduces the interfacial tension of water-hexadecane by 95 % (air-hexadecane  $\gamma = 27.5 \text{ mN/m}$ )<sup>48,61</sup>. A later study, by Taylor, *et al.* 2015, demonstrated that the monolayer tension of diphytanoyl-phosphatidylcholine (DPhPC) in hexadecane solution decreased by 17 %, when silicone oil of equal hexadecane volume (1:1) was added<sup>51</sup>. Different concentrations, lipid compositions and oils yield a distinct  $\gamma$ , depending on their strong or weak interactions and the size differences between hydrophilic heads and hydrophobic tails<sup>48</sup>. Therefore, it was understood that the 30 mg/ml DOPC in hexadecane only, had higher  $\gamma$  than moderate DOPC concentration of 12.5 mg/ml in 1:1 Hex:AR20 mixture, resulting to larger volume oil droplets.

Final eDIB protocol

Despite the overnight merging observations in **Figure 2.18D**, it was decided to use a moderate DOPC concentration (12.5 mg/ml) in hexadecane and removed the AR20 entirely from the 'equation'. Lastly, high-levels of vesicle content caused the hydrogel shell to become opaque, due to the milk-looking solution of DPPC/buffer. Therefore, the DPPC concentration was further reduced, leading to significant transparency differences between the  $< 1 \text{ mg/ml}$  DPPC and  $12.5 \text{ mg/ml}$  DPPC eDIB (**Figure 2.19A&B**). The final eDIB formulation experiments were conducted with DPPC vesicle concentration as low as  $0.5 \text{ mg/ml}$  in  $1.5 \%$  w/v alginate. These experiments finalised the eDIB protocol, where the internal cores (WP3) consisted of SulfB buffer, the mid-oil phase (OP3) was  $12.5 \text{ mg/ml}$  DOPC in pure Hex, the  $1.5 \%$  w/v alginate phase (AP3) had  $0.5 \text{ mg/ml}$  DPPC vesicles and finally the carrier phase (OC3-OC4) consisted of 1:9  $\text{Ca}^{2+}$ -nanoemulsion. These tailored soft eDIB capsules maintained their stability and their transparency, while obtaining high contrast between each layer and compartments for further imaging and analysis (B). Such well-compartmentalised and durable 1-2 mm eDIBs can withstand external shocks, such as pipetting and washing, therefore they can be further studied and imaged using more sophisticated microscopes (confocal microscopy and light-sheet microscopy).

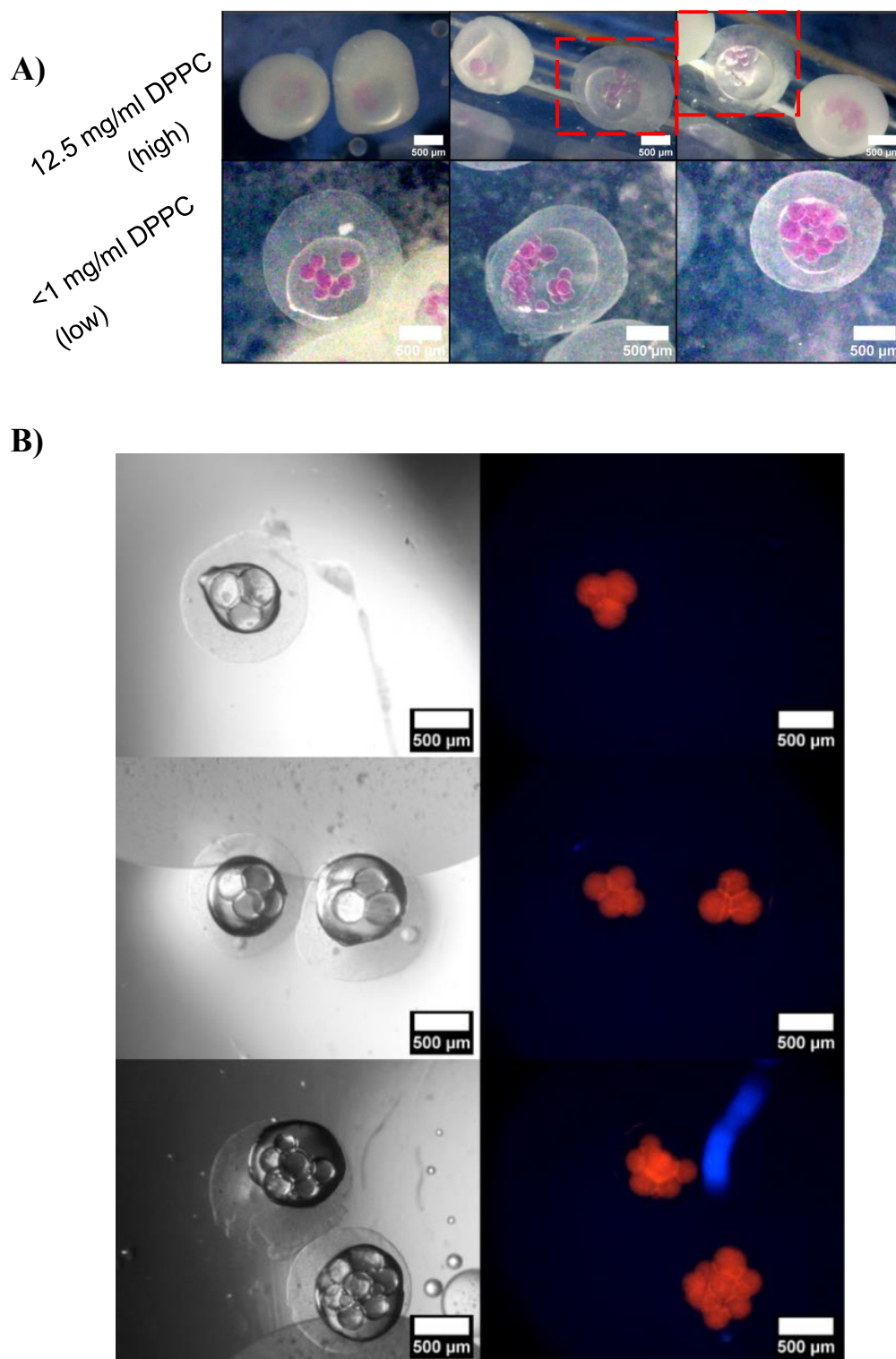


**Figure 1. 19: Images of eDIBs created using the final protocol. A)** Comparison between eDIBs with 12.5 mg/ml (high concentration) and <0.1 mg/ml (low concentration) DPPC vesicles in the alginate shell. Side to side comparison of eDIB between the high and low DPPC in alginate concentration, where the red dashed box encloses the eDIBs with low DPPC concentration. Images were obtained with the Dino-Lite edge USB camera. **B)** Bright and Dark field images of SulfB/buffer (red fluorescent droplets) encapsulated in eDIBs produced following the final protocol. The diameters of these eDIBs, oil cores and internal cores were measured approximately to be  $\varpi_{eDIB} = 1285.1 \mu\text{m} \pm 27.5$  ( $n=21$ ),  $\varpi_{oil} = 804.8 \mu\text{m} \pm 20.9$  ( $n=21$ ) and  $\varpi_{int} = 241.7 \mu\text{m} \pm 8.1$  ( $n=21$ ). Images were obtained with the GXM-XDY-2 inverted microscope.

## 2.5. Conclusion

The novelty of this thesis chapter lies within the combination of monolithic triple-junction 3D-printed microfluidic devices for encapsulated Droplet Interface Bilayer (eDIB) production. Hydrogel-in-oil (H/O), oil-in-hydrogel-in-oil (O/H/O) and water-in-oil-in-hydrogel-in-oil (W/O/H/O) emulsion microgel capsules were formed with increasingly complicated 3D-printed microfluidic devices by Fused Filament Fabrication (FFF). Using this fabrication technique monodispersed microgels, oil core-containing microgels and triple-order emulsions were formed using droplet-forming microfluidic circuits. The eDIB model is a W/O/H/O emulsion, fabricated using multi-material, multi-junction FFF microfluidic devices and very importantly, with no channel surface modifications and negligible involvement of synthetic surfactants. Therefore, this eDIB model, which is considered as being of low cytotoxicity and with effective compartmentalisation capability, can contribute to scientific accomplishments in tissue culture and engineering, drug delivery and screening, as well as synthetic biology and soft matter materials. The release of the cores encapsulated in eDIB constructs is investigated in Chapter III using artificial lipid membrane modulation, while cancer cell and spheroids culture in hydrogel microbeads, oil-core microgels and triple emulsion eDIBs are investigated in Chapter IV.

## 2.6. References

1. Seiffert, S. Functional Microgels Tailored by Droplet-Based Microfluidics. *Macromolecular Rapid Communications* **32**, 1600–1609 (2011).
2. Kanai, T., Ohtani, K., Fukuyama, M., Katakura, T. & Hayakawa, M. Preparation of monodisperse PNIPAM gel particles in a microfluidic device fabricated by stereolithography. *Polym J* **43**, 987–990 (2011).
3. Wanselius, M., Rodler, A., Searle, S. S., Abrahmsén-Alami, S. & Hansson, P. Responsive Hyaluronic Acid–Ethylacrylamide Microgels Fabricated Using Microfluidics Technique. *Gels* **8**, 588 (2022).
4. Hwang, Y.-H., Um, T., Ahn, G.-N., Kim, D.-P. & Lee, H. Robust and scalable production of emulsion-templated microparticles in 3D-printed milli-fluidic device. *Chemical Engineering Journal* **431**, 133998 (2022).
5. Mohamed, M. G. A., Ambhorkar, P., Samanipour, R., Yang, A., Ghafoor, A. & Kim, K. Microfluidics-based fabrication of cell-laden microgels. *Biomicrofluidics* **14**, 021501 (2020).
6. Nielsen, A. V., Beauchamp, M. J., Nordin, G. P. & Woolley, A. T. 3D Printed Microfluidics. *Annu Rev Anal Chem (Palo Alto Calif)* **13**, 45–65 (2020).
7. Rosales, S., Ferrándiz, S., Reig, M. J. & Seguí, J. Study of soluble supports generation in 3d printed part. *Procedia Manufacturing* **13**, 833–839 (2017).
8. Urrios, A. *et al.* 3D-printing of transparent bio-microfluidic devices in PEG-DA. *Lab Chip* **16**, 2287–2294 (2016).
9. Romanov, V., Samuel, R., Chaharlang, M., Jafek, A. R., Frost, A. & Gale, B. K. FDM 3D Printing of High-Pressure, Heat-Resistant, Transparent Microfluidic Devices. *Anal. Chem.* **90**, 10450–10456 (2018).
10. Li, J., Baxani, D. K., Jamieson, W. D., Xu, W., Rocha, V. G., Barrow, D. A. & Castell, O. K. Formation of Polarized, Functional Artificial Cells from Compartmentalized Droplet Networks and Nanomaterials, Using One-Step, Dual-Material 3D-Printed Microfluidics. *Adv Sci (Weinh)* **7**, 1901719 (2019).

11. Chan, H. F., Zhang, Y., Ho, Y.-P., Chiu, Y.-L., Jung, Y. & Leong, K. W. Rapid formation of multicellular spheroids in double-emulsion droplets with controllable microenvironment. *Sci Rep* **3**, 3462 (2013).
12. Trantidou, T., Friddin, M. S., Salehi-Reyhani, A., Ces, O. & Elani, Y. Droplet microfluidics for the construction of compartmentalised model membranes. *Lab Chip* **18**, 2488–2509 (2018).
13. Kim, J. H., Jeon, T. Y., Choi, T. M., Shim, T. S., Kim, S.-H. & Yang, S.-M. Droplet Microfluidics for Producing Functional Microparticles. *Langmuir* **30**, 1473–1488 (2014).
14. Chen, M., Bolognesi, G. & Vladisavljević, G. T. Crosslinking Strategies for the Microfluidic Production of Microgels. *Molecules* **26**, 3752 (2021).
15. Baret, J.-C. Surfactants in droplet-based microfluidics. *Lab Chip* **12**, 422–433 (2012).
16. Baxani, D. K., Morgan, A. J. L., Jamieson, W. D., Allender, C. J., Barrow, D. A. & Castell, O. K. Bilayer Networks within a Hydrogel Shell: A Robust Chassis for Artificial Cells and a Platform for Membrane Studies. *Angewandte Chemie International Edition* **55**, 14240–14245 (2016).
17. Liposome Preparation - Avanti® Polar Lipids. <https://www.sigmaaldrich.com/GB/en/technical-documents/protocol/cell-culture-and-cell-culture-analysis/transfection-and-gene-editing/liposome-preparation>.
18. Mukhopadhyay, R. When PDMS isn't the best. 3248–3253 (2007).
19. Saggiomo, V. A 3D Printer in the lab: Not only a toy. 10.
20. Lopes, L. R., Silva, A. F. & Carneiro, O. S. Multi-material 3D printing: The relevance of materials affinity on the boundary interface performance. *Additive Manufacturing* **23**, 45–52 (2018).
21. Harris, C. G., Jursik, N. J. S., Rochefort, W. E. & Walker, T. W. Additive Manufacturing With Soft TPU – Adhesion Strength in Multimaterial Flexible Joints. *Front. Mech. Eng.* **5**, 37 (2019).
22. Li, J., Dimitriou, P., Castell, O. & Barrow, D. GENERATION OF COMPLEX EMULSIONS USING MONOLITHIC, DUAL- MATERIAL 3D-PRINTED MICROFLUIDIC DEVICES. 2 (2020).
23. Mukhopadhyay, S. K. 8 - Manufacturing, properties and tensile failure of nylon fibres. in *Handbook of Tensile Properties of Textile and Technical Fibres* (ed. Bunsell, A. R.) 197–222 (Woodhead Publishing, 2009).

24. Heikkinen, I. T. S., Kauppinen, C., Liu, Z., Asikainen, S. M., Spoljaric, S., Seppälä, J. V., Savin, H. & Pearce, J. M. Chemical compatibility of fused filament fabrication-based 3-D printed components with solutions commonly used in semiconductor wet processing. *Additive Manufacturing* **23**, 99–107 (2018).
25. Mohammadzadeh, M., Gupta, A. & Fidan, I. Mechanical benchmarking of additively manufactured continuous and short carbon fiber reinforced nylon. *Journal of Composite Materials* **55**, 3629–3638 (2021).
26. Miri, V., Persyn, O., Lefebvre, J.-M. & Seguela, R. Effect of water absorption on the plastic deformation behavior of nylon 6. *European Polymer Journal* **45**, 757–762 (2009).
27. Bernard, M., Jubeli, E., Bakar, J., Tortolano, L., Saunier, J. & Yagoubi, N. Biocompatibility assessment of cyclic olefin copolymers: Impact of two additives on cytotoxicity, oxidative stress, inflammatory reactions, and hemocompatibility. *Journal of Biomedical Materials Research Part A* **105**, 3333–3349 (2017).
28. Bundgaard, F., Perozziello, G. & Geschke, O. Rapid prototyping tools and methods for all-Topas® cyclic olefin copolymer fluidic microsystems. *Proceedings of the Institution of Mechanical Engineers, Part C: Journal of Mechanical Engineering Science* **220**, 1625–1632 (2006).
29. Agha, A., Waheed, W., Alamoodi, N., Mathew, B., Alnaimat, F., Abu-Nada, E., Abderrahmane, A. & Alazzam, A. A Review of Cyclic Olefin Copolymer Applications in Microfluidics and Microdevices. *Macromolecular Materials and Engineering* **307**, 2200053 (2022).
30. Gang, M. G., Chae, K. W., Kim, W.-B., Jung, Y. H., Jun, M. B. G. & Min, B.-K. Wettability modification of cyclic olefin copolymer surface and microchannel using micromilling process. *Journal of Manufacturing Processes* **37**, 168–176 (2019).
31. Peta, K., Bartkowiak, T., Galek, P. & Mendak, M. Contact angle analysis of surface topographies created by electric discharge machining. *Tribology International* **163**, 107139 (2021).
32. Davoudinejad, A., Cai, Y., Pedersen, D. B., Luo, X. & Tosello, G. Fabrication of micro-structured surfaces by additive manufacturing, with simulation of dynamic contact angle. *Materials & Design* **176**, 107839 (2019).

33. Barrios, J. M. & Romero, P. E. Improvement of Surface Roughness and Hydrophobicity in PETG Parts Manufactured via Fused Deposition Modeling (FDM): An Application in 3D Printed Self-Cleaning Parts. *Materials* **12**, 2499 (2019).
34. Jena, R. K. & Yue, C. Y. Cyclic olefin copolymer based microfluidic devices for biochip applications: Ultraviolet surface grafting using 2-methacryloyloxyethyl phosphorylcholine. *Biomicrofluidics* **6**, 012822-012822–12 (2012).
35. Canal, C., Molina, R., Bertran, E. & Erra, P. Wettability, ageing and recovery process of plasma-treated polyamide 6. *Journal of Adhesion Science and Technology* **18**, 1077–1089 (2004).
36. Agarwal, P. *et al.* Microfluidics Enabled Bottom-Up Engineering of 3D Vascularized Tumor for Drug Discovery. *ACS Nano* **11**, 6691–6702 (2017).
37. Utada, A. S., Lorenceau, E., Link, D. R., Kaplan, P. D., Stone, H. A. & Weitz, D. A. Monodisperse Double Emulsions Generated from a Microcapillary Device. *Science* **308**, 537–541 (2005).
38. Huang, S.-L. & Lin, Y.-S. The Size Stability of Alginate Beads by Different Ionic Crosslinkers. *Advances in Materials Science and Engineering* **2017**, e9304592 (2017).
39. Li, X., He, L., He, Y., Gu, H. & Liu, M. Numerical study of droplet formation in the ordinary and modified T-junctions. *Physics of Fluids* **31**, 082101 (2019).
40. Da Ling, S., Zhang, J., Chen, Z., Ma, W., Du, Y. & Xu, J. Generation of monodisperse microdroplets within the stable narrowing jetting regime: effects of viscosity and interfacial tension. *Microfluid Nanofluid* **26**, 53 (2022).
41. Ji, Q., Zhang, J. M., Liu, Y., Li, X., Lv, P., Jin, D. & Duan, H. A Modular Microfluidic Device via Multimaterial 3D Printing for Emulsion Generation. *Sci Rep* **8**, 4791 (2018).
42. Wang, J., Liang, K., Zhang, N., Yao, H., Ho, T.-Y. & Sun, L. Automated calibration of 3D-printed microfluidic devices based on computer vision. *Biomicrofluidics* **15**, 024102 (2021).
43. Agarwala, M. K., Jamalabad, V. R., Langrana, N. A., Safari, A., Whalen, P. J. & Danforth, S. C. Structural quality of parts processed by fused deposition. *Rapid Prototyping Journal* **2**, 4–19 (1996).

44. Li, J. *et al.* Building programmable multicompartment artificial cells incorporating remotely activated protein channels using microfluidics and acoustic levitation. *Nat Commun* **13**, 4125 (2022).
45. Tao, Y., Pan, L., Liu, D. & Li, P. A case study: Mechanical modeling optimization of cellular structure fabricated using wood flour-filled polylactic acid composites with fused deposition modeling. *Composite Structures* **216**, 360–365 (2019).
46. Tao, Y., Kong, F., Li, Z., Zhang, J., Zhao, X., Yin, Q., Xing, D. & Li, P. A review on voids of 3D printed parts by fused filament fabrication. *Journal of Materials Research and Technology* **15**, 4860–4879 (2021).
47. R. Abate, A., Thiele, J. & A. Weitz, D. One-step formation of multiple emulsions in microfluidics. *Lab on a Chip* **11**, 253–258 (2011).
48. Yanagisawa, M., Yoshida, T., Furuta, M., Nakata, S. & Tokita, M. Adhesive force between paired microdroplets coated with lipid monolayers. *Soft Matter* **9**, 5891–5897 (2013).
49. Makhoul-Mansour, M. M., El-Beyrouthy, J. B., Mao, L. & Freeman, E. C. Enhancing membrane-based soft materials with magnetic reconfiguration events. *Sci Rep* **12**, 1703 (2022).
50. Wauer, T., Gerlach, H., Mantri, S., Hill, J., Bayley, H. & Sapra, K. T. Construction and Manipulation of Functional Three-Dimensional Droplet Networks. *ACS Nano* **8**, 771–779 (2014).
51. J. Taylor, G., A. Venkatesan, G., Patrick Collier, C. & A. Sarles, S. Direct in situ measurement of specific capacitance, monolayer tension, and bilayer tension in a droplet interface bilayer. *Soft Matter* **11**, 7592–7605 (2015).
52. Tiribocchi, A., Montessori, A., Lauricella, M., Bonaccorso, F., Succi, S., Aime, S., Milani, M. & Weitz, D. A. The vortex-driven dynamics of droplets within droplets. *Nat Commun* **12**, 82 (2021).
53. Jamur, M. C. & Oliver, C. Permeabilization of Cell Membranes. in *Immunocytochemical Methods and Protocols* (eds. Oliver, C. & Jamur, M. C.) 63–66 (Humana Press, 2010).
54. Barenholz, A., Barenholz, Y. & Bercovier, H. Nano-Liposomes of Crude Soy Lecithin are Effective for Cleaning Fuel-Contaminated Sands and Soils. *Expert Opinion on Environmental Biology* **2016**, (2016).

55. Bai, X., Xu, L., Tang, J., Zuo, Y. & Hu, G. Adsorption of Phospholipids at the Air-Water Surface. *Biophysical Journal* **117**, (2019).
56. Punnamaraju, S., You, H. & Steckl, A. J. Triggered Release of Molecules across Droplet Interface Bilayer Lipid Membranes Using Photopolymerizable Lipids. *Langmuir* **28**, 7657–7664 (2012).
57. Attwood, S. J., Choi, Y. & Leonenko, Z. Preparation of DOPC and DPPC Supported Planar Lipid Bilayers for Atomic Force Microscopy and Atomic Force Spectroscopy. *Int J Mol Sci* **14**, 3514–3539 (2013).
58. Mastiani, M., Mosavati, B. & Kim, M. (Mike). Numerical simulation of high inertial liquid-in-gas droplet in a T-junction microchannel. *RSC Adv.* **7**, 48512–48525 (2017).
59. Patrascu, C. & Balan, C. Dispersion relations, capillary waves, and the Rayleigh-Plateau instability. *INCAS BULLETIN* **14**, 75–85 (2022).
60. Giuliano, C. B., Cvjetan, N., Ayache, J. & Walde, P. Multivesicular Vesicles: Preparation and Applications. *ChemSystemsChem* **3**, e2000049 (2021).
61. Rolo, L. I., Caço, A. I., Queimada, A. J., Marrucho, I. M. & Coutinho, J. A. P. Surface Tension of Heptane, Decane, Hexadecane, Eicosane, and Some of Their Binary Mixtures. *J. Chem. Eng. Data* **47**, 1442–1445 (2002).

---

## ***Chapter III***

# ***Characterisation, post-processing and in-situ content release activation from encapsulated Droplet Interface Bilayer synthetic cell interiors***

---

### **3.1. Chapter summary**

This chapter focuses on the imaging, characterisation, and post-processing of encapsulated droplet interface bilayers (eDIBs). Individual or batch-produced eDIBs were analysed with respect to their stability, core size distribution and DIB liquid contact angle. EVOS and Optical Coherence Tomography (OCT) imaging provided complementary analysis of eDIBs. Further tests on eDIB stability were conducted using elevated temperatures and centrifugal force. Moreover, the release of the internal compartments of eDIBs was controlled *in-situ*, through membrane modulation by lysophosphatidylcholine (LPC). Fluorescence intensity measurements were collected throughout the incubation of eDIBs with LPC, evidencing a consistent method for eDIBs' core release. Computational simulations (2D and 3D) were performed for the diffusion of LPC and subsequent core release by varying the threshold concentration and the hydrogel parameters. The LPC effect on lipid bilayers was further supported by DIB electrophysiology studies.

### 3.2. Introduction

Droplet interface bilayers (DIBs) are models that mimic cellular membranes, fabricated using simple bottom-up reconstruction. These biomimetic systems are formed when lipid monolayer-coated aqueous droplets encounter one another, forming an artificial lipid bilayer. The coating of the droplets is achieved, by incorporating phospholipids inside the aqueous droplets, as liposomes (lipid-in) or by dispersing them in an outer oil solution (lipid-out). DIBs present a tool for engineering artificial lipid bilayers containing plasma membrane components and may be used as molecular biosensors<sup>1</sup>. Some concepts that attracted the research community into developing soft biomimicking devices, i.e. DIBs, include the understanding of the electrical potentials across cellular membranes<sup>2</sup>, toxin susceptibility and translocation in cells<sup>3</sup>, as well as contained and controlled sequential chemical reactions<sup>4</sup>.

DIBs are tailored to the application and end-goal. For example, self-supported DIB tissue-like structures, have previously been established using a thermoresponsive polymer, while maintaining the functionality of embedded transmembrane pores<sup>5</sup>. Zhou, *et al.* 2020 used DIB network bioprinting, for encapsulating living cells and maintaining their viability<sup>6</sup>. Others have utilised DIB as biodevices for in-vitro transcription / translation (IVTT) for protein production, with subsequent insertion into the lipid bilayer<sup>7</sup>. Attention is also given to explore the interactions between molecules, ion channels and pores using DIBs models or droplet-hydrogel bilayers (DHBs)<sup>8,9</sup>. DHBs provide a platform for single molecule fluorescent studies and similar to DIBs, they are usually performed by hand and manual pipetting, suggesting that the throughput of experiments may be low.

Droplet-microfluidics increase the throughput and yield to a large number of individual DIBs. Microfluidic production of DIBs can be achieved through double emulsions, or triple emulsions, with devices that are tailored to form multi-compartment systems, often termed as multisomes<sup>10,11</sup>. Before attempting to increase production rates using microfluidic technologies, it is important to understand the susceptibility of DIB systems. For example, DIBs have been reported to be sensitive to temperatures that may lead to evaporation effects<sup>12</sup>. The stability and durability of planar lipid bilayers<sup>13</sup>, and device-encapsulated DIBs, have been previously studied by exposing them to mechanical stresses<sup>14</sup>. Sarles and Leo (2010), reported that DIBs surrounded by lipid-containing oil, can maintain their stability by the continuous feeding of lipid molecules into the lipid bilayer, even under mechanical agitation<sup>14</sup>. Hence, the isolation of DIBs in oils and additional outer layers, would be beneficial. The encapsulation of DIBs in oil surrounded by a soft hydrogel, introduces new possibilities for their application and these have been previously generated using droplet-microfluidics and were termed as encapsulated droplet interface bilayers (eDIBs)<sup>15</sup>. This encapsulation process of DIB systems can allow them to be used in physiological aqueous environments<sup>4</sup>, and permit their manipulation and post-processing in various ways, including electrophysiology which is a standard operating procedure for DIB membrane studies<sup>16</sup>.

Tailored eDIB constructs can carry cellular building blocks or engineered materials responsive to external stimuli. This would lead to on-demand encapsulant release, targeting drug delivery and screening applications<sup>17</sup>. Their characterisation is important, but most of the characterisation of artificial cell membranes has been focused on DIBs, which lack the bilayer interface between the droplet and the hydrogel. The stability of DIBs and consequently, eDIBs, is highly dependent on the surrounding environment and needs to be maintained, but also understood and explored, especially when it comes to designing content release platforms. This should be considered, as eDIBs are not only, a robust artificial/synthetic cell mimicking chassis, but they also offer a biodevice skeleton for drug screening applications.

Reagent encapsulation in eDIBs could potentially offer drug transport and delivery to a diseased area, following controlled release. Usually, drugs are encapsulated in hydrogels, polymer particles or liposomes. They are designed to protect the load from the outer environment, until it reaches the designated target<sup>18</sup>. Some stimuli-responsive liposomes and microparticles are used clinically and in research, and some stimuli examples include temperature, pH, photo-activation and membrane modulation<sup>19-23</sup>. Disruption of artificial lipid bilayers has been achieved using membrane modulation by metal oxide particles<sup>24</sup>, and the use of lysolipids<sup>25</sup>. Egg lysophosphatidylcholine (LPC) are cone-shaped, single-tailed phospholipids with a headgroup larger than the tail, making up lipid structures with positive curvature<sup>26</sup>. They have been reported to activate mechanosensitive pores in DIB systems<sup>27</sup>, increase the permeability of cell membranes for drug uptake studies<sup>28</sup>, and induce cell apoptosis at various concentrations depending on the cell line (50  $\mu$ M and higher)<sup>29,30</sup>.

The molecular transport in DIB or eDIBs, in the absence of transmembrane pores, is usually dominated by slow diffusion, if possible, between the encapsulated compartments and the outer environment<sup>31</sup>. In this chapter, eDIB structures were characterised further, after executing the final eDIB protocol from Chapter II. Different imaging techniques were used to image and analyse eDIBs and their stability was assessed after experiencing high temperatures and gravitational forces. The interplay between compartments and the outer environment is dominated by diffusion, since no transmembrane pores were utilised. An active content release protocol was demonstrated, which applies *in-situ* membrane modulation, driven by the diffusion of LPC molecules through the porous hydrogel shell of eDIBs. This was further studied by 2D and 3D computational simulations governed by Fick's Law of Diffusion and Millington and Quirk model. Finally, DIB electrophysiology experiments were performed, to delve into the effect of LPC molecules on artificial lipid bilayers.

### 3.3. Materials and Methods

All the studied encapsulated droplet interface bilayers (eDIBs) were produced using the triple emulsion microfluidic device (TE-MD) (**Figure 3. 1A**) developed in Chapter II – Section 2.3.2 and formulated with materials described in Chapter II - Section 2.3.5, with a few modifications based on the final eDIB protocol (Chapter II - Section 2.4.5.2.3 - *Final eDIB protocol*). The internal compartments of eDIBs consisted of sulforhodamine B (sulfb) or calcein dye in buffer or Phosphate Buffered Saline, PBS (pH 7.4, 1 X, Gibco, UK). The buffer used throughout this thesis consisted of 0.05 M HEPES, 0.15 M KCl in deionised water. For the DIB formation, 12.5 mg/ml dioleoyl-phosphatidylcholine (DOPC) in hexadecane (Hex) was used and for comparison experiments, this was replaced with 12.5 mg/ml diphytanoyl-phosphatidylcholine (DPhPC) in Hex or 4 mg/ml DOPC in Hex with 10 % silicone oil (AR20). The shell phase of the eDIBs remained as 1.5 % alginate with 0.5 mg/ml dipalmitoyl-phosphatidylcholine (DPPC) vesicles, and was gelled by 1:9 ratio  $\text{Ca}^{2+}$ -infused nanoemulsion.

For the experiments related to the active content release from eDIBs, Egg lysophosphatidylcholine (LPC) in chloroform was purchased from Merck/Sigma-Aldrich (830071C) and prepared in buffer solution, following the thin film hydration method (same as DOPC and DPPC in Chapter II - Section 2.3.5).

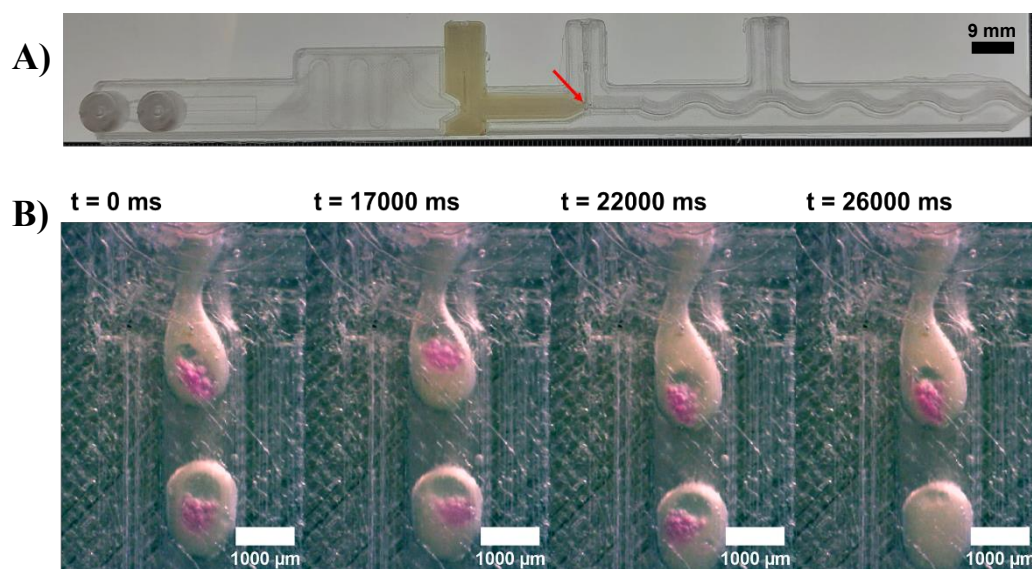


**Figure 3. 1:** Photographs of the TE-MD developed in Chapter II for triple emulsion eDIB production. **A)** FFF 3D-printed microfluidic device, made from COC/Nylon/COC filaments and droplet-forming junctions. Red arrow indicates the 3<sup>rd</sup> droplet-forming junction. **B)** Timelapse images of the eDIB formation at the 3<sup>rd</sup> junction of the TE-MD. The eDIBs showed were produced using sulfb/buffer cores in 10 mg/ml DOPC in Hex with 20 % AR20 and 6.5 mg/ml DPPC in 1 % w/v alginate.

### **3.3.1. Imaging of eDIBs**

Day-to-day microfluidic experiments and eDIB formation were monitored using the Dino-Lite Edge USB microscope (**Figure 3. 1B**). The analysis of eDIBs (contact angle, diameter, etc) was primarily based on images acquired using EVOS M7000 Imaging System (Thermofisher, UK). Contact angle (CA) measurements were also carried out using Optical Coherence Tomography (OCT). Any other means of imaging will be mentioned in the appropriate section.

#### **3.3.1.1. EVOS**

eDIBs after production were transferred from the collection dish to a well plate suitable for imaging with EVOS. Depending on the dye encapsulated in the cores of the eDIBs, the appropriate LED light cubes were used, those being Texas Red (Ex = 585/29 nm, Em= 628/32 nm) for SulFB and GFP (Ex = 470/22 nm, Em= 525/50 nm) for calcein dye. Bright-field images were also obtained. For multi-well and multi-timepoint imaging, the eDIBs were immobilised at the bottom of the well by depositing a thin layer (50-100  $\mu$ l) of 1 % w/v low temperature melting agarose (A9414, Merck) dissolved in buffer at 37 °C. For immediate imaging and quenched calcein experiments (Section **3.3.3.2**), eDIBs were placed in clear buffer. Imaging was carried out at room temperature unless otherwise stated and for prolonged imaging, the wells were sealed with microplate tape to avoid evaporation. For imaging and further manipulation or treatments, a clear buffer of 0.05 M HEPES, 0.15 M KCl was used.

#### **3.3.1.2. OCT**

Optical Coherence Tomography (OCT) (VivoSight System, Michelson Diagnostics, UK) machine was used to take axial images of eDIBs. The eDIBs were transferred onto a microscope glass slide, which was in turn placed on the imaging platform. The moving platform was adjusted to focus the microscope objective on the eDIBs by tuning its z-axis dial. An area of 6 mm<sup>2</sup> was scanned at 500 FPS with a 4  $\mu$ m step size. Image processing was carried out using ImageJ Fiji, for the visualisation of eDIBs' orthogonal views and 3D image reconstruction.

### **3.3.2. Stability of eDIBs**

eDIBs were stored in buffer solution and three days after microfluidic production their stability was assessed. To do that, they were exposed to temperatures and centrifugal forces varying from 30 to 80 °C, and 39 $\times$ g to 3913 $\times$ g, respectively. The eDIBs (n=5) were transferred to 1.5 ml Eppendorf vials with 500  $\mu$ l of mineral oil and were either placed on a heating block with the pre-set temperature for 30 minutes or centrifuged for 5 minutes. After each test, the Eppendorf was placed on a microtube rack for imaging using a custom-built fluorescent microscope. This consisted of a Nikon SMZ745T microscope,

an RGB LED light source (RS) for exciting the sulfB encapsulated in the cores, a 600 nm (for the encapsulated sulfB) bandpass filter to remove some of the excitation wavelength and a Basler Pulse pu1280-54  $\mu\text{m}$  camera<sup>32</sup>. The eDIBs were imaged with this set up and image acquisition was performed using Basler's pylon viewer software V6.2.

The performance of the eDIBs after each test was assessed based on the visualisation of the internal core fluorescence and any detected leakage was identified by adjusting the contrast of images in ImageJ, Fiji. For the centrifugation experiments, two eDIB populations were studied, one with smaller diameter internal cores ( $\varnothing < 100 \mu\text{m}$ ), and one with larger diameter internal cores ( $\varnothing > 200 \mu\text{m}$ ).

### **3.3.3. eDIB core release using LPC**

#### **3.3.3.1. Leakage assay based on fluorescence decrease**

eDIBs encapsulating sulfB were washed with buffer, immobilised with 1 % w/v low temperature melting agarose in wells of a 96-well plate and imaged using EVOS M7000 Imaging System. LPC in buffer was prepared and used appropriately, in order for each well to have final LPC concentration of 1, 10, 100 and 1000  $\mu\text{M}$ . Imaging was carried out for a minimum of 14 hours at 37 °C. The core release was evaluated by monitoring the decrease in the fluorescence of sulfB from the cores of individual eDIBs. The timepoint images were processed using ImageJ and intensity measurements were based on the fluorescent areas falling within a pre-defined threshold intensity range (*Appendix 3.A*).

#### **3.3.3.2. Leakage assay based on fluorescence increase**

Self-quenched calcein at a concentration of 70 mM was encapsulated in the aqueous cores of eDIBs, following the protocol in Section 3.3. The core release assay was similar to the fluorescent decrease assay (Section 3.3.3.1). However, the eDIBs were floating in buffer and the final LPC concentrations tested were 1, 10, 100 and 300  $\mu\text{M}$ . Image processing for each timepoint was based on the fluorescence of the whole well and not individual eDIBs, as in the earlier assay from Section 3.3.3.1.

### **3.3.4. COMSOL simulations on the LPC diffusion and core release**

Computational simulations were performed using COMSOL Multiphysics version 5.6 to investigate the LPC diffusion and concentration dependant core release rate. The 'Transport of Diluted species (TDS) in Porous medium' module was employed along with a Time-transient study, for a 2D and a 3D geometry of the eDIB structure, with an extremely fine mesh (physics-controlled mesh). For details on the dimensions of each geometrical model see *Appendix 3.B*. The 2D and 3D models are based on the reaction sequence illustrated in **Figure 3. 2**, where the LPC molecules added to the aqueous bath (light blue), diffuse through the porous alginate medium (dark blue) and reach the lipid bilayer

(yellow line), causing the release of the cores (orange domains) into the hydrogel shell through the lipid bilayers only.

For random three-dimensional  $(x,y,z)$  transport of species, Fick's first Law of Diffusion was considered in the model, (Equation 3.1) <sup>33</sup>, where the Diffusive Flux ( $J$ ,  $mol/m^2s$ ), is dependent on the Diffusion coefficient ( $D$ ,  $m^2/s$ ) and concentration of the species ( $c$ ,  $mol/m^3$ ):

$$J = -D \nabla c = \frac{\partial c_x}{\partial x} + \frac{\partial c_y}{\partial y} + \frac{\partial c_z}{\partial z} \quad (3.1)$$

The TDS model also supports the mass transport due to diffusion (Fick's Law), through porous media, by using the Millington and Quirk model <sup>34</sup>, (Equation 3.2), based on the tortuosity  $\tau_L$  or  $\tau_G$  of the porous medium:

$$\tau_L = \theta_l^{-\frac{7}{3}} \varepsilon_p^2, \quad \tau_G = \theta_g^{-\frac{7}{3}} \varepsilon_p^2, \quad (3.2)$$

where  $\varepsilon_p$  is the porosity,  $\theta_l$  is the liquid volume fraction and  $\theta_g$  is the gas volume fraction. A saturated porous medium was considered, so  $\theta_l = \varepsilon_p$ , where the pores of the medium are only filled with liquid (no gas is present), therefore Equation 3.2 becomes :

$$\tau_L = \varepsilon_p^{-\frac{1}{3}} \quad (3.3)$$

Several 2D COMSOL studies were carried out, including the effect of eDIB shell porosity (10 – 90 %), shell thickness (0.4-0.7 mm) and the threshold LPC concentration ( $1 \times 10^{-8}$ ,  $1 \times 10^{-7}$ ,  $1 \times 10^{-6}$ ,  $1 \times 10^{-5}$ ). The threshold LPC concentration was defined as the concentration of LPC that causes the breach of the lipid bilayers and subsequent core release. This was imported in the model as a contributor within a step function employed in the model, and can be found in Appendix 3.B. Similar 3D simulations were also performed. Comparisons were subsequently made between the COMSOL simulations and the practical experiments.

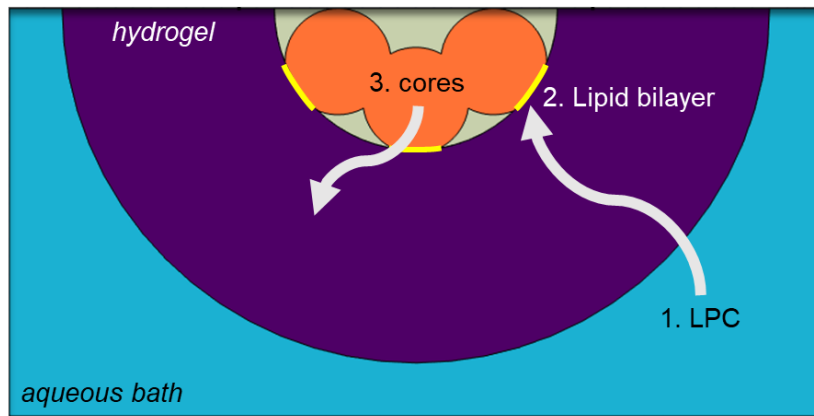


**Figure 3. 2:** COMSOL designed geometry of the 2D model explaining the rationale behind the simulations. Illustration of the sequence of actions, including the diffusion of LPC lipids (Step 1) through the hydrogel to the lipid bilayer (Step 2) and subsequent activation of the core release into the hydrogel shell (Step 3).

### 3.3.5. DIB electrophysiology

Custom made 20-30 cm electrodes were used for the DIB electrophysiology experiments. These were connected to a 203BU head stage, which was in turn connected to an Axopatch 200B amplifier (Axon Instruments, Inc). To make the electrodes, silver wires were polished with fine sandpaper and then submerged in sodium hypochlorite solution for a minimum of 30 minutes for bleaching. This creates a thin silver chloride (Ag/AgCl) layer, which allows these wires to be used as electrodes. Prior to each experiment, the tips of the Ag/AgCl electrodes were lightly coated with 1 % w/v low temperature melting agarose. Current and voltage data were obtained through the WinEDR software (University of Strathclyde), and further processing and plotting was done in MATLAB R2022a software. The voltage applied during experiments was either a +/- 23 mV triangular wave at 10 Hz, or a fixed potential of 20 mV set on the Axopatch 200B equipment (V-clamp mode and 5 kHz low pass Bessel filter). The triangular waveform of the applied voltage, induces a square wave output for the current, allowing the capacitance measurement of the lipid bilayer (not carried out).

The setup for the DIB electrophysiology execution included, two Ag/AgCl agarose coated electrodes, two micromanipulators, a polymethylmethacrylate (PMMA) milled device with 3-5 mm deep wells, a reflective surface (e.g., back of a CD) and a Dino-Lite USB microscope (**Figure 3. 20A**). The PMMA wells were cleaned with deionised water and ethanol, prior to the experiment. One well of the PMMA device, was filled with approximately 30 % of Diethyl phthalate (DEP) oil and 70 % of a lipid mixture, consisting of 8 mg/ml DOPC in 64 % Hex and 36 % AR20 (oil bath). Subsequently, one electrode at a time, was submerged into the oil bath and 0.2  $\mu$ l of each solution in test, was pipetted onto it. One droplet was deposited on the ground electrode ( $\ominus$  or *cis*) and the other droplet on the electrode through which the voltage was applied ( $V_{app}$  or *trans*). Following an incubation time of 2-3 minutes, the two electrodes were brought into close proximity using micromanipulators, and at this point data acquisition began. The droplets after the incubation time were assumed to have formed a lipid monolayer around their periphery, and when in contact with each other, the oil between the droplets will be replaced by a lipid bilayer. The control experiment consisted of two identical buffer droplets. A second droplet pair consisted of a buffer droplet on the *cis* electrode and an LPC-containing buffer droplet on the *trans* electrode. Final concentrations of LPC tested were 100  $\mu$ M, 500  $\mu$ M or 1000  $\mu$ M. For the third DIB pair test, the *cis* electrode had a droplet of 100  $\mu$ M LPC in buffer and the *trans* electrode had a gelled alginate droplet containing DPPC vesicles. This formed a DHB-like system. The gelled droplet on the electrode was prepared as follows; a clean well of the PMMA device was filled with hexadecane oil, an electrode was submerged into the oil bath, then 0.2  $\mu$ l of 1.5 % w/v alginate with 0.5 mg/ml DPPC vesicles was pipetted onto the electrode, and subsequently 50-100  $\mu$ l of 0.2 M CaCl<sub>2</sub> was pipetted above the droplet to gel it (< 30 s) (*Appendix 3.C*). The electrode with the gelled droplet was then transferred into the lipid-containing oil to begin the experiment, after attempting to form a bilayer between the gelled droplet and the 100  $\mu$ M LPC-containing buffer.

### 3.4. Results and Discussion

#### 3.4.1. Encapsulated Droplet Interface Bilayer (eDIB) characterisation

Microfluidic formation of eDIBs became a high-yield daily operation, using the triple emulsion microfluidic device (TE-MD) reported in Chapter II. The eDIBs were produced using a range of flow rates as shown in **Table 3. 1**, subsequently imaged and their overall stability assessed.

**Table 3. 1: Summarised phases and flow rate ranges used for eDIB production.**

Liquid Phase	Description	Flow rates
Aqueous inner cores with dye	Buffer or PBS with calcein or sulfB *	0.1- 0.5 ml/hr
Lipid-containing oil	12.5 mg/ml phospholipids in hexadecane	0.2-0.8 ml/hr
Hydrogel shell	1.5 % alginate, 0.5 mg/ml DPPC *	3-6 ml/hr
Nanoemulsion	1:9 Ca <sup>2+</sup> -infused mineral oil	5-12 ml/hr

\*PBS=Phosphate Buffered Saline, sulfB=sulforhodamine B, DPPC=dipalmitoyl-phosphatidylcholine

The aqueous core diameter was varied by controlling the flow rates of the inner aqueous phase and middle lipid oil phase. For reducing the diameter of the core droplets, the inner droplet phase flow rate was decreased, and the lipid-containing oil was increased, and vice versa for increasing the droplets' diameter. By doing so, the total flow rate of the system was kept approximately constant. This led to eDIBs encapsulating large cores of diameter around  $236.3 \mu\text{m} \pm 8.72$  ( $n=64$ ) (**Figure 3. 3(i-iv)**) or small cores of diameter approximately  $90 \mu\text{m} \pm 1.5$  ( $n=35$ ) (**Figure 3. 3(v-vi)**). Image analysis of the eDIBs

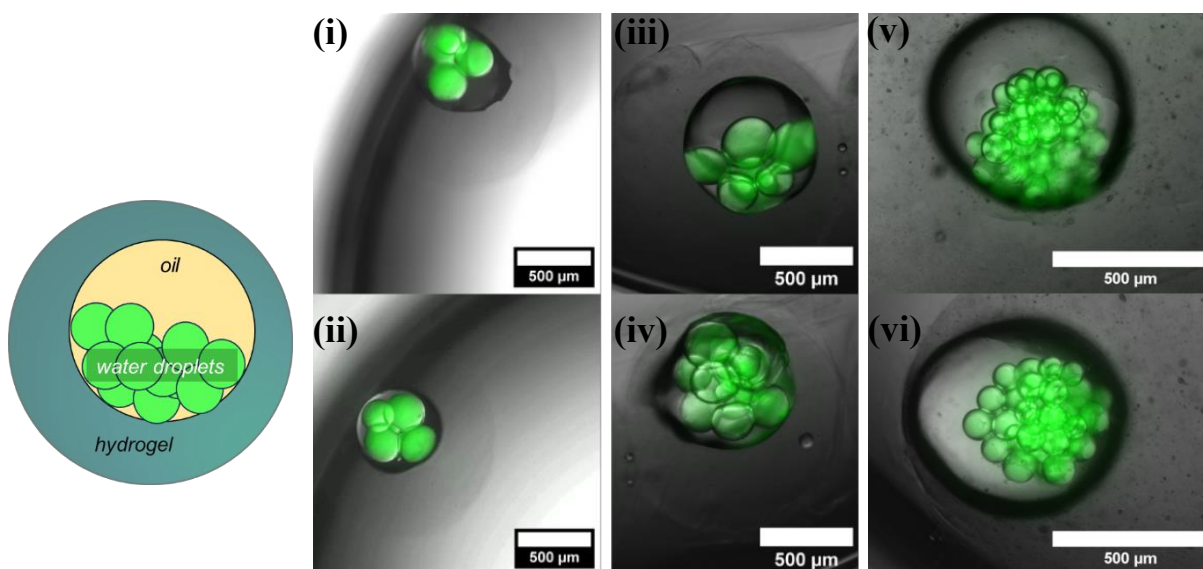


**Figure 3. 3: eDIBs with calcein/buffer inner droplets produced using dual-material 3D-printed microfluidic devices. (i)-(iv) Merged BF and GFP images of eDIBs encapsulating large ( $>200 \mu\text{m}$ ), fluorescent cores in DOPC/Hex. (v)-(vi) Merged BF and GFP channels of eDIB-containing fluorescent cores of smaller diameter ( $<100 \mu\text{m}$ ), in DPhPC/Hex. The outer shell for all these samples is 1.5 % alginate with 0.5 mg/ml DPPC vesicles.**

with large cores revealed contact angles ( $\theta$ ) of  $31.2^\circ \pm 2.1$  ( $n=10$ ) between aqueous cores and formed lipid bilayer interfaces of  $100.8 \mu\text{m} \pm 5.3$  ( $n=24$ ).

It was unclear whether the large cores were a result of merging between smaller droplets during production and settling, or whether they were generated due to the 3D-printed microfluidic junction inconsistencies and artefacts. The merging of inner cores was a frequent phenomenon, that could be a result of poor lipid monolayer and bilayer formation. **Figure 3. 4A**, shows eDIBs from the same experiment, starting from the eDIBs with the smallest measured inner cores ( $\varnothing = 65.1 \mu\text{m}$ ) to the eDIBs with the largest cores after merging ( $\varnothing > 195.2 \mu\text{m}$ ). The most frequent droplet diameter in this batch of eDIB was approximately  $100 \mu\text{m}$  (**Figure 3. 4B**). As described in Chapter II - Section 2.4.5.2.1, when approaching the exit of the COC channel, some droplets accumulate together, forming a network of DIBs, which perhaps could be the cause of merging, if the lipid bilayer was poor and unstable in the COC channel. Yet, this was a phenomenon which could have occurred off-chip as well. After repeated eDIB encapsulation experiments, it was noticed that less successful microfluidic experiments (which exhibited leaking and clogging), produced eDIBs that were often unstable, especially during the first few hours after production.

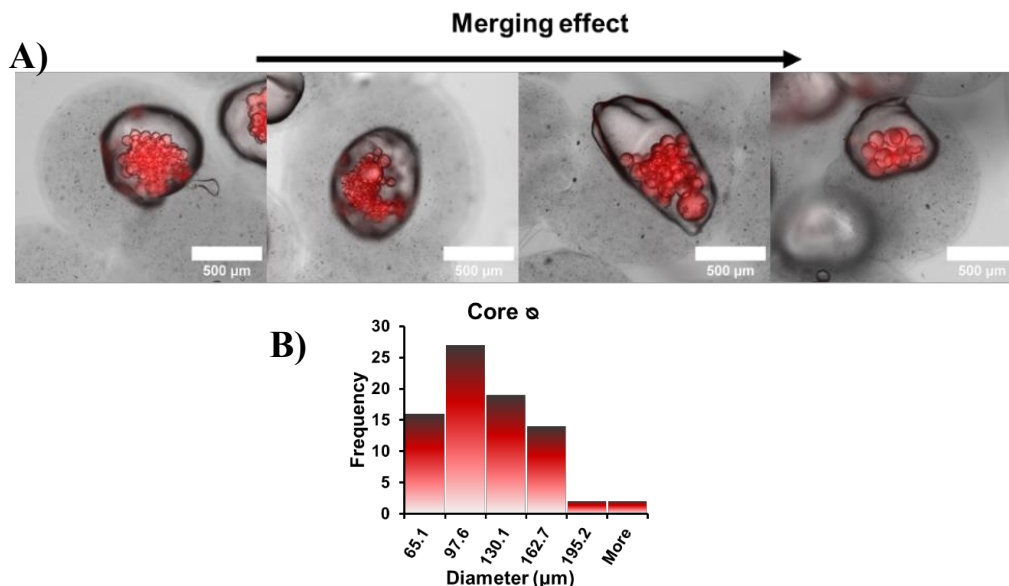


**Figure 3. 4: Merging of the inner aqueous cores encapsulated in eDIBs. A)** Cores encapsulating *suII*B/buffer undergo a degree of merging (following the direction of the arrow) after microfluidic production, as shown in the BF/Texas red fluorescence images. **B)** Histogram of the inner droplets' diameter distribution after settling of the eDIBs ( $n=80$  for inner droplets).

Most production of eDIBs throughout this thesis was completed using dioleoyl-phosphatidylcholine (DOPC) lipids. However, most DIBs and transmembrane protein studies use diphytanoyl-phosphatidylcholine (DPhPC) in hexadecane (Hex) or undecane with some fraction of silicone oil<sup>35</sup>. Hence, eDIBs were formed using 12.5 mg/ml DPhPC in Hex (**Figure 3. 5A**) or 4 mg/ml DOPC in Hex with 10 % silicone oil (AR20) (**Figure 3. 5B**). While the contact angle and lipid bilayer interface of DPhPC eDIBs did not exhibit distinct differences compared to the DOPC eDIBs, the silicone oil-containing eDIBs demonstrated an increase in the contact angle  $\theta$  ( $41.9 \pm 1.4^\circ$ ) and an obvious increase in the lipid bilayer interface ( $163.2 \pm 19.3 \mu\text{m}$ ). The addition of a small volume fraction (10 %) of silicone oil AR20 formed less spherical aqueous cores, due to the surface tension decrease of the bilayers between the aqueous droplets and the hydrogel shell and according to earlier claims in literature, such formations have been correlated with more stable and robust DIBs (**Figure 3. 5B**)<sup>31,36</sup>.

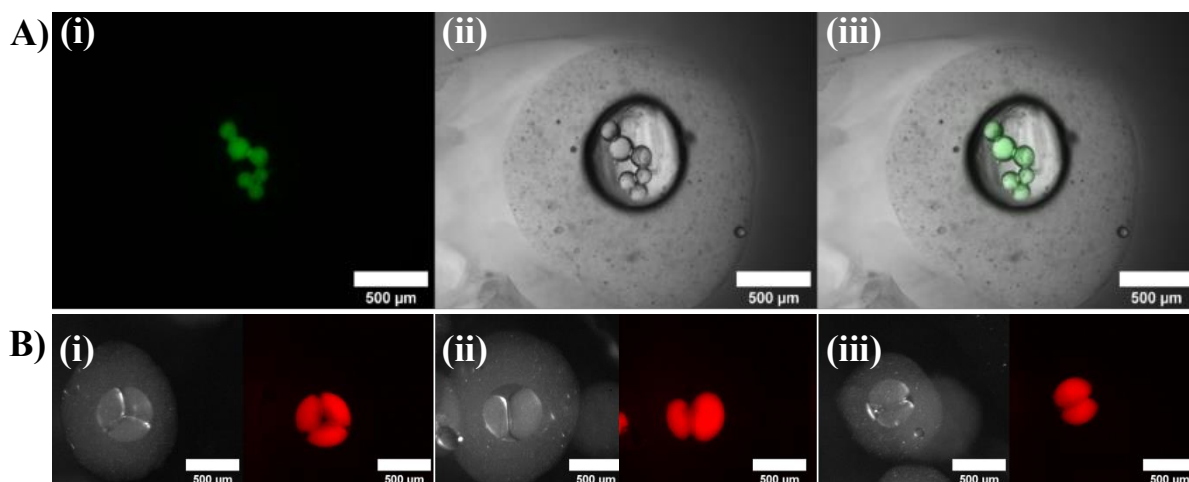


**Figure 3. 5: eDIB capsules with different lipid oil compositions exhibit distinct morphologies.** *A) eDIB with calcein/PBS fluorescent droplets produced with 12.5 mg/ml DPhPC (i) GFP, (ii) BF, and (iii) BF/GFP. Images taken with EVOS Imaging system. B) (i)-(iii) eDIBs produced using 4 mg/ml DOPC in 10 % silicon oil with sulfB cores and (BF: LHS and red LUT: RHS). Images obtained with the custom-built fluorescent microscope.*

### 3.4.2. Optical Coherence Tomography (OCT) imaging of eDIBs

OCT uses a light source of low-coherence, and the imaging process relies on light interference<sup>37</sup>. The emitted light from the optical probe penetrates the sample and is reflected along the same axis back to the detector, allowing its characterisation. This is because the layers that make up the test sample, may have different refractive indices and reflection properties, resulting to a distinct backscattered light at their interface. Depending on the material, light along the scanning axis (depth of the sample) is scattered back and received by the detector, which is then translated into a pixelated grey scale image<sup>38,39</sup>. The field of depth of OCT is usually a few millimetres, but it also depends on the light absorbance and attenuation of the sample<sup>38</sup>. The resolution of OCT is approximately 10  $\mu\text{m}$  for clinical, or less for research OCT equipment<sup>40</sup>.

By performing OCT imaging on eDIBs, it is possible to extract information, otherwise difficult to obtain using other imaging procedures. As the principle of OCT relies on the scattering and reflective properties of the sample being imaged, the contrast is enhanced at the interface of each phase or layer of the eDIB (**Figure 3. 6**). OCT imaging is usually used for the diagnosis of skin and eye pathologies<sup>41,42</sup>, although various groups have used OCT for imaging characteristic properties of capsules<sup>43,44</sup>.

By exploiting OCT's capability to image along the depth of eDIB samples and perform axial scanning with resolution of 4  $\mu\text{m}$ , it was possible to obtain the orthogonal views (**Figure 3. 6A-C**) and reconstruct 3D stacked images of eDIBs (**Figure 3. 6D**). The orthogonal views can be used to extract data like the diameter of simple oil-core capsules (**Figure 3. 6A**) and the contact angle of DIBs (**Figure 3. 7A**). From the OCT imaging of a single eDIB with three cores, at least 12 contact angles were recorded, while with conventional imaging, this would be limited to 2-4 contact angles. Additionally, the volume of each aqueous core was calculated to be between 6-8 nl, by utilizing the high contrast axial images. This was achieved by measuring the area of each core at every axial scan and multiplying the sum of the area with the step resolution (4  $\mu\text{m}$ ). The hydrogel shell of the eDIB sample shown in **Figure 3. 7A**, was also measured at two locations, the thickest and the thinnest hydrogel layer between the air and oil interface. The average thickness from all orthogonal views of the hydrogel shell was measured to be  $339.9 \mu\text{m} \pm 30.7$  for the thickest, and  $37.2 \mu\text{m} \pm 2.9$  for the thinnest.

Moreover, the capsule diameters from each orthogonal view can be measured to identify the exact location of the oil core in three dimensions (3D). The 3D central position of the oil core ( $p_{3D}$ ) was expressed as  $p_{3D(\text{centre})} = 0.62x + 0.66y + 0.42z$ , by measuring the diameter of the eDIB outer shell in every axis ( $\varpi_x = 1.135 \text{ mm}$ ,  $\varpi_y = 1.150 \text{ mm}$ ,  $\varpi_z = 1.045 \text{ mm}$ ) and considering the bottom left corner as the origin  $(x,y,z) = (0,0,0)$  (**Figure 3. 7B**). Therefore, by using this quick and cost-effective imaging technique in combination with precise image processing, equations can be generated for compartmentalised structures including, but not limited to, the central location of the oil core and quantification of the oil core's offset in all three dimensions.

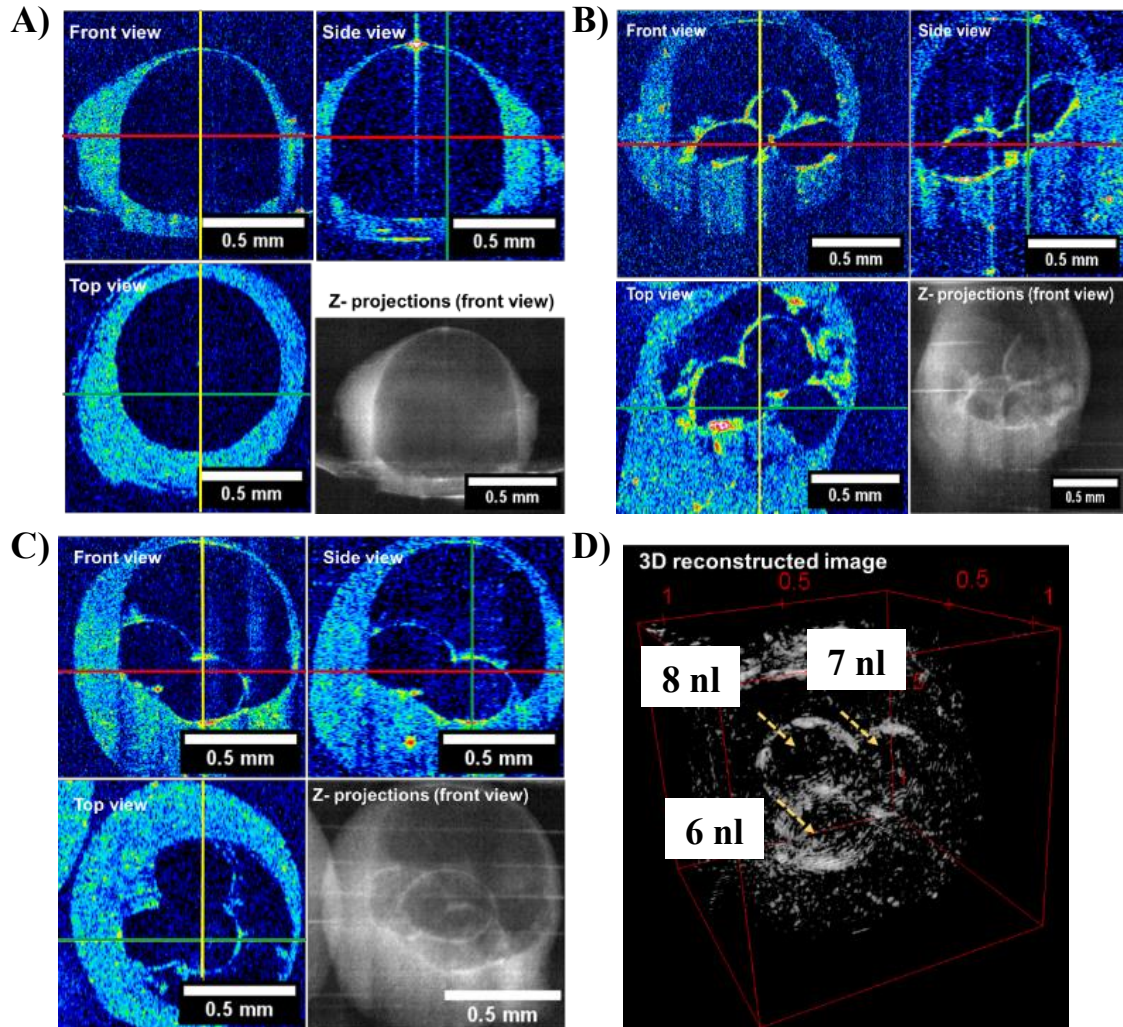


**Figure 3. 6: eDIB orthogonal views and 3D reconstructed image using OCT imaging.** *A)* Orthogonal views and z-projection of a false 16-colour LUT oil-core capsule. *B-C)* Orthogonal views and z-projection of two eDIBs (with false 16-colour LUT). *D)* 3D volume reconstructed eDIB sample with adjusted threshold for 3D visualisation of the internal core structure. The volume of the cores was accurately calculated from the slices to be 6, 7 and 8 nl (yellow arrows).

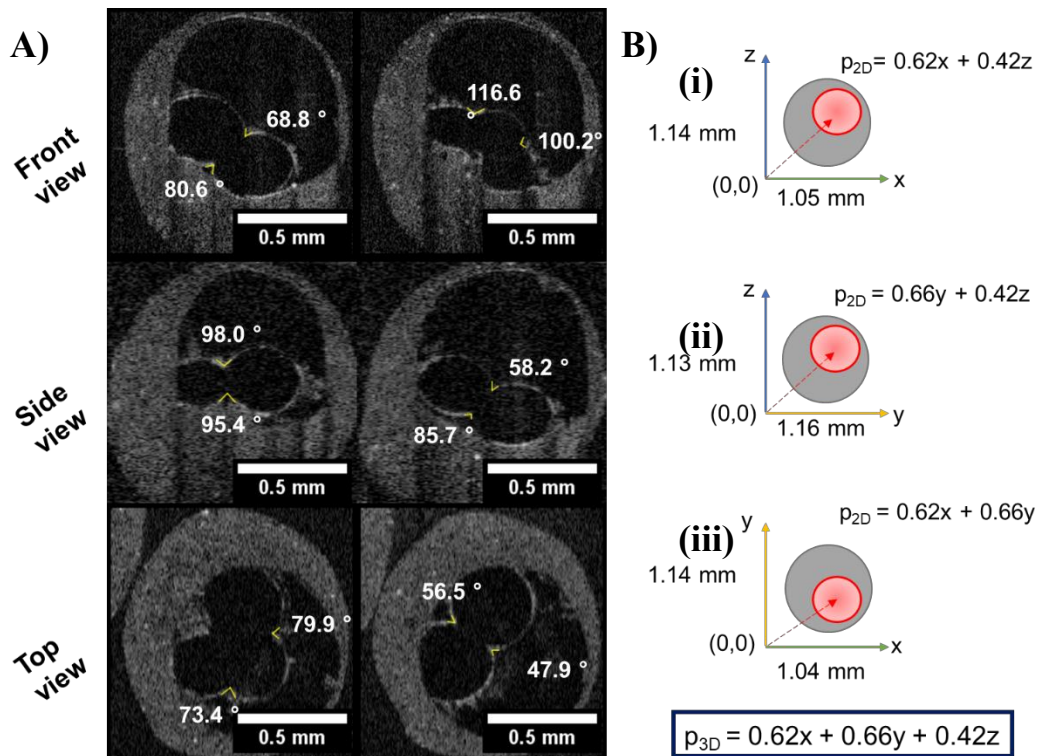


**Figure 3. 7:** Contact angles and 3D location extracted from an individual eDIB following OCT imaging and analysis. **A)** OCT orthogonal views of one eDIB with 12 annotated contact angle values. **B)** By measuring the eDIB diameter at the different planes ( $\mathcal{Q}_x$ ,  $\mathcal{Q}_y$ ,  $\mathcal{Q}_z$ ), the central position of the oil core in 3D was expressed as  $p_{3D}$ .

### 3.4.3. Centrifugation and temperature stability tests

The eDIBs which survived prolonged storage after production and maintained a degree of structure, were exposed to temperature and centrifugation tests. The samples referred to as ‘control’, were not exposed to centrifugation or elevated temperatures.

Small and large core-containing eDIBs exposed to centrifugal forces exhibited different responses. The eDIBs with the small cores were imaged after the centrifugation (0 hrs) and two days later (48 hrs), in order to report any leakage disruption of the lipid bilayer. The centrifugation process caused the small cores of eDIBs to sediment and tightly pack at the bottom of the oil core (**Figure 3. 8**). Tightly packed DIBs are associated with stability<sup>31</sup>, which could possibly explain why there was no leaking over the period of 48 hours. On the contrary, large core-containing eDIBs showed evidence of leakage 30 min after centrifugation, as shown in **Figure 3. 9B**. From this, it was evident that the leakage was induced by the centrifugation step, since the control eDIBs (non-centrifuged samples) did not show any significant fluorescent dye leakage from the cores to the hydrogel shell, when imaged five days after the experiment (**Figure 3. 9A**). Large core-containing eDIBs, were also subject to a gradual 5 min centrifugation, which caused a strong fluorescence in the hydrogel shell (**Figure 3. 9C**). Finally, an eDIB was captured after 3913×g centrifugation with leaking encapsulated cores, as pointed out in **Figure 3. 9E**.

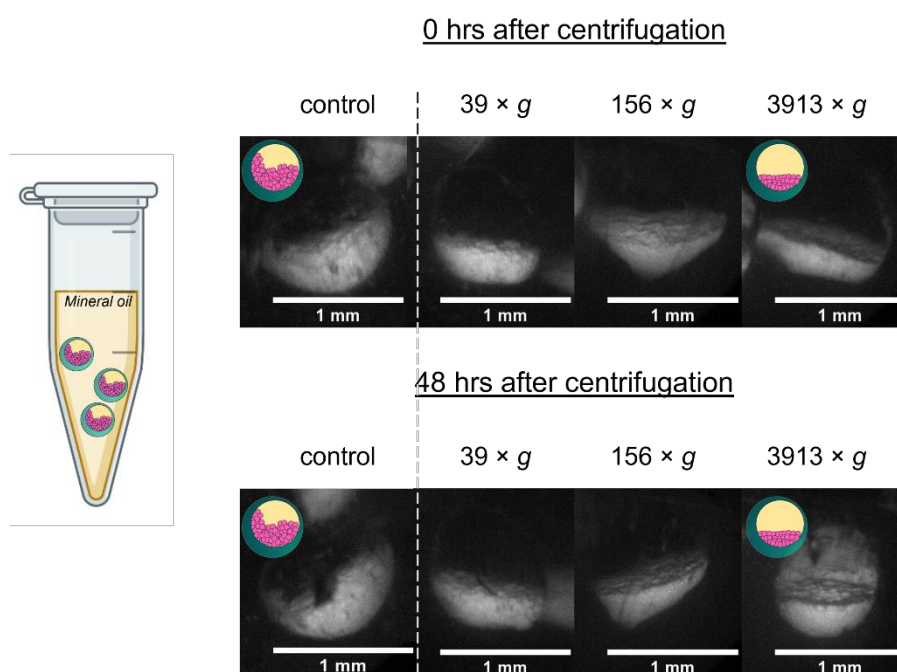


**Figure 3. 8:** eDIBs with encapsulated cores of diameters less than 100  $\mu\text{m}$ , imaged at 0 hrs and 48 hrs after centrifugation. Small cores formed tightly packed networks with no indication of leakage into the hydrogel. The eDIBs were centrifuged in mineral oil and imaged from the side of the vial.

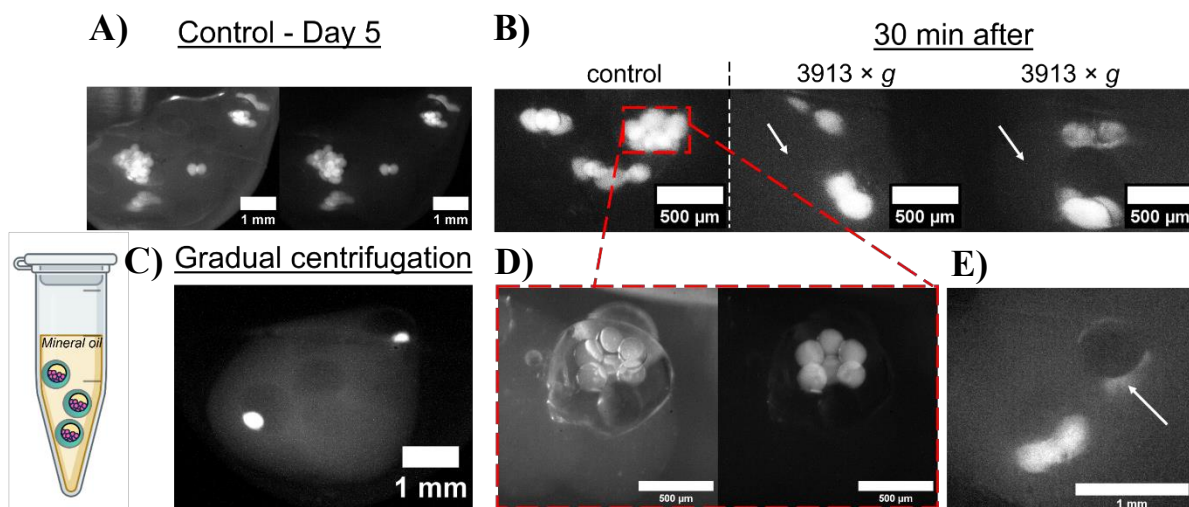


**Figure 3. 9: eDIBs with encapsulated cores of diameters greater than 200  $\mu\text{m}$ , imaged at different timepoints after centrifugation.** **A)** Control eDIBs were stable for more than 5 days (LHS: merged BF and fluorescent channel; RHS: fluorescent channel only) **B)** Centrifugation at 3913 $\times$ g showed increased fluorescence in the hydrogel shell (white arrows) after 30 min. **C)** Gradual centrifugation from 39 $\times$ g to 3913 $\times$ g, instantly showed fluorescence in the shell, with a couple of cores remaining. **D)** BF (LHS) and fluorescent (RHS) images of an individual eDIB before the experiment reveals a distinct core organisation. **E)** Captured a leaking eDIB right after centrifugation at 3913 $\times$ g (white arrow). The eDIBs were centrifuged in mineral oil and imaged from the side of the vial.

Using the same imaging setup as in the centrifugation tests, the vials with eDIBs were exposed to varying temperatures (30-80  $^{\circ}\text{C}$ ), showing changes in their arrangement. Significant changes were observed at 60  $^{\circ}\text{C}$  and higher, where the water cores started to sediment at the bottom of the oil core, similar to the centrifugation tests (**Figure 3. 10**). However, the water cores were not closely packed, since there were no strong gravitational forces acting on them. Increased temperatures reduce the surface tension of oil and water<sup>45,46</sup>. Here, the temperature of 60  $^{\circ}\text{C}$  reduced the surface tension of the oil to a degree that allowed droplets to rearrange lightly at the bottom of the oil. Their integrity at this temperature was preserved, as also shown in previously reported eDIBs exposed to 60  $^{\circ}\text{C}$  for a bioluminescent reaction assay<sup>47</sup>.

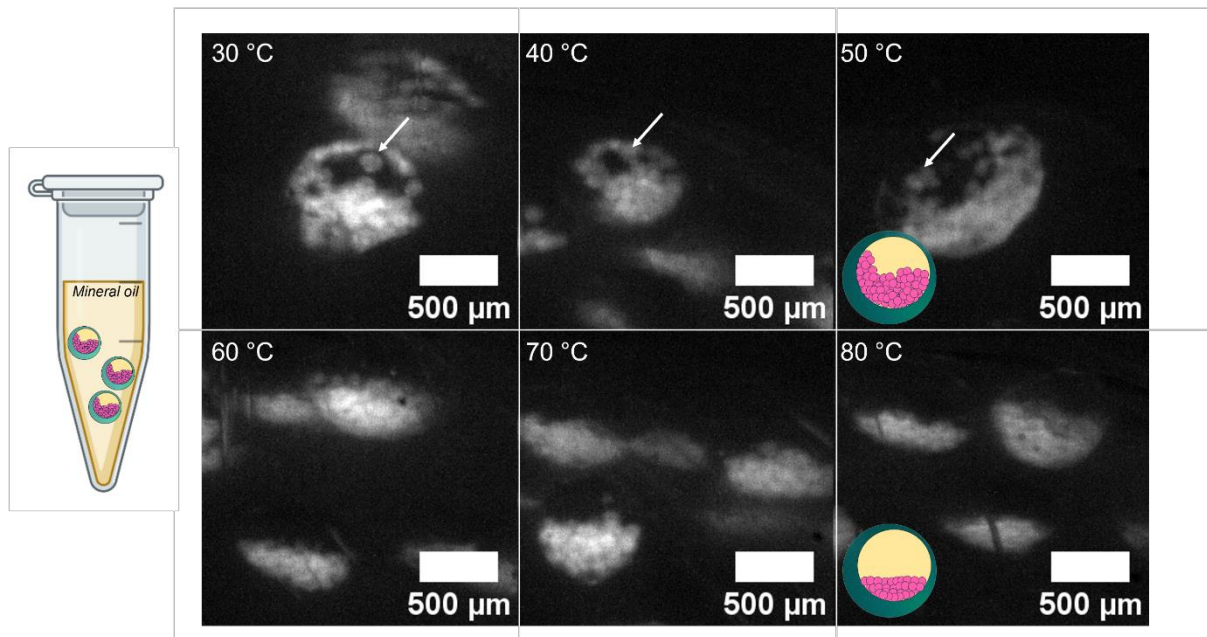


**Figure 3. 10:** Fluorescent images of eDIBs exposed to temperatures ranging from 30 to 80 °C for 30 minutes. White arrows indicate aqueous fluorescent cores, which were not influenced by the set temperature ( $\leq 40$  °C), while as the temperature increases ( $\geq 50$  °C), the cores sedimented due to surface tension changes. Above 60 °C, all the fluorescent aqueous cores are found at the bottom part of the oil core. The eDIBs were heated in mineral oil and imaged from the side of the vial.

#### 3.4.4. Active core content release assays using lysophosphatidylcholine (LPC)

Microfluidically formed eDIBs can be tailored to become responsive to external stimulus, by encapsulating key reagents and altering the environment accordingly, to actuate eDIBs, as desired<sup>32,47</sup>. For example, locomotion of eDIBs was previously demonstrated by encapsulating magnetic nanoparticles in the hydrogel shell<sup>11</sup>, demonstrating the ability to design magnetic field-responsive eDIB capsules. Light seemed an attractive and somewhat less toxic stimulus for eDIB encapsulant release, and therefore in collaboration with Oxford University, some experiments were conducted using custom-made photo-switchable lipids (Professor Matthew Langton, Oxford University)<sup>48,49</sup>. However, very little was known about the physical and chemical properties of these lab-made lipids and experiments were inconclusive. For this reason, these experiments were not included in the main thesis, but can be found in *Appendix 3.D*.

eDIB technology has the potential for reagent storage and release, by regulating the external environment. This was demonstrated in this thesis, by promoting the controlled aqueous core content release, through the *in-situ* lysolipid-induced membrane artifacts. A concentration dependant release of the cores was demonstrated, by performing two fluorescent assays. The LPC lysolipid added to the physiological aqueous environment of the eDIB would follow passive diffusion and interaction with other present lipids. These included the DPPC vesicles in the alginate shell and the DOPC lipid bilayer interfaces between the hydrogel shell and internal cores.

As shown in **Figure 3. 11A**, the two highest concentrations of 1000  $\mu\text{M}$  and 100  $\mu\text{M}$  LPC activated core release within the first 6 hours. The eDIBs exposed to 100  $\mu\text{M}$ , held on to some of the cores for longer period, while the 1000  $\mu\text{M}$  LPC emptied the fluorescent cores completely after approximately 4 hours. Small changes in the rearrangement of the cores occurred during the first few hours of eDIB incubation at 37 °C with 1  $\mu\text{M}$  and 10  $\mu\text{M}$  LPC.

The LPC effect on the core release from eDIBs, was further analysed in terms of the fluorescence decrease over time across a population of eDIB capsules ( $n=11$  (control - 0  $\mu\text{M}$ ),  $n=15$  (1  $\mu\text{M}$ ),  $n=19$  (10  $\mu\text{M}$ ),  $n=17$  (100  $\mu\text{M}$ ),  $n=16$  (1000  $\mu\text{M}$ )). The core release profile for each concentration over a period of 15 hours is shown in **Figure 3. 11B**. It was noticeable, that the control experiment (0  $\mu\text{M}$ ) had also shown unexpected intensity reduction. These reductions were justified as optical mishaps due to the core rearrangement at 37 °C and stresses exerted by the moving EVOS platform. The imaging platform and incubation temperature had caused shifting of the eDIBs' location, taking them out of focus and reducing the fluorescence. It may be that the core location shifting impacted all the eDIBs exposed to all LPC concentrations. Despite the fact that the initial timepoints of the experiments were compromised by the imaging setup, the aqueous core release profiles still indicated an LPC concentration dependence. Additionally, it should be noted that after approximately 4 hours of incubation, the intensity almost stabilised for eDIBs exposed to 0  $\mu\text{M}$  and 1  $\mu\text{M}$  LPC concentrations,

indicating that subsequent intensity reductions was only related to the effect of LPC, and that any other effects by the imaging setup were negligible.

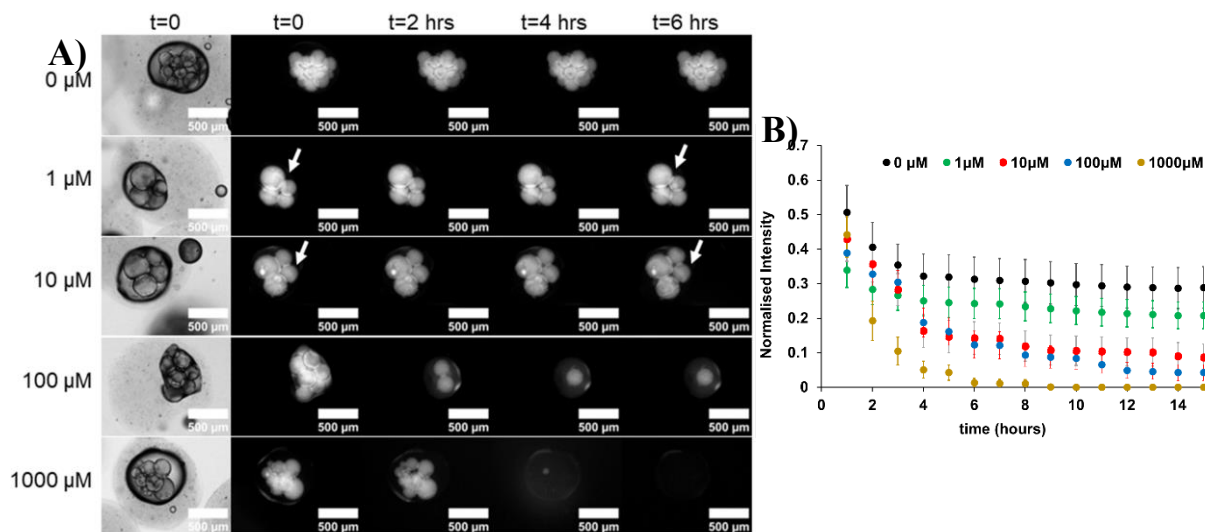


**Figure 3. 11: LPC concentration dependant release of encapsulated cores in eDIBs, according to the fluorescence decrease assay.** A) BF and fluorescent timelapse images of individual eDIBs during the initial 6 hours under the influence of different LPC concentrations. White arrows for concentrations 1  $\mu$ M and 10  $\mu$ M, indicated a degree of rearrangement of the cores. Higher concentrations induced quick bursting of the inner cores. B) Release rate profiles of the internal fluorescent cores induced by the presence of different LPC molarities. The data of the intensity measured by ImageJ, where normalised based on the overall raw recorded data and the error bars indicate the calculated  $\pm$ SEM of each data set ( $n=11$  (control - 0  $\mu$ M),  $n=15$  (1  $\mu$ M),  $n=19$  (10  $\mu$ M),  $n=17$  (100  $\mu$ M),  $n=16$  (1000  $\mu$ M)).

A similar assay was performed on eDIBs encapsulating self-quenched 70 mM calcein dye and imaged in wells with 100  $\mu$ l of clear buffer. The diameter distribution of the internal cores of an exemplar calcein-encapsulating eDIB can be found in *Appendix 3.E*. This experiment aimed to obtain a fluorescence intensity profile induced by the addition of LPC, which could give an estimated time of maximum core leakage. The bursting of the inner cores would be characterised by a signal of strong fluorescence around the shell of the eDIB. **Figure 3. 12A**, shows eDIBs treated with three LPC concentrations (0, 10 and 100  $\mu$ M). The 100  $\mu$ M caused a rapid bursting compared to both the control and 10  $\mu$ M LPC. There was a small amount of fluorescence at the periphery of the well around 7 hours after the addition of 10  $\mu$ M of LPC, which closely correlates with quantitative data in **Figure 3. 12C**.

The calcein dye was not fluorescent at a concentration of 70 mM in buffer, but it would fluoresce, once it was de-quenched by dilution. Therefore, attempts were made to encapsulate the non-fluorescent calcein in the cores of eDIBs, in order to assess their release and dilution after the external addition of LPC. It is noteworthy that during microfluidic generation of eDIBs, calcein had leaked from the cores into one of the other phases, which led to the contamination of the microfluidic channels (especially the hydrophilic Nylon channel) and unpredictable eDIB formation. This unstable and compromised eDIB formation resulted to the merging of the droplets, which in turn translated into

bright fluorescent cores captured within the eDIBs, as shown in **Figure 3. 12B** (0  $\mu\text{M}$  and 10  $\mu\text{M}$ ). Despite this slight calcein dilution in the cores, the dye was still able to give high intensity when de-quenched further, however the number of samples was reduced ( $n= 11$  (0  $\mu\text{M}$ ),  $n=5$  (1  $\mu\text{M}$ ),  $n=3$  (10  $\mu\text{M}$ ),  $n=3$  (100  $\mu\text{M}$ ),  $n=3$  (300  $\mu\text{M}$ )). The de-quenching of the calcein in the eDIBs was stimulated further by the introduction of LPC, which evidently revealed the release profiles describing the fluorescence of the well (**Figure 3. 12C**). According to the intensity profile results, maximum release or bursting for concentrations of 300  $\mu\text{M}$ , 100  $\mu\text{M}$  and 10  $\mu\text{M}$  occurred at approximately 2, 3 and 8 hours, respectively.

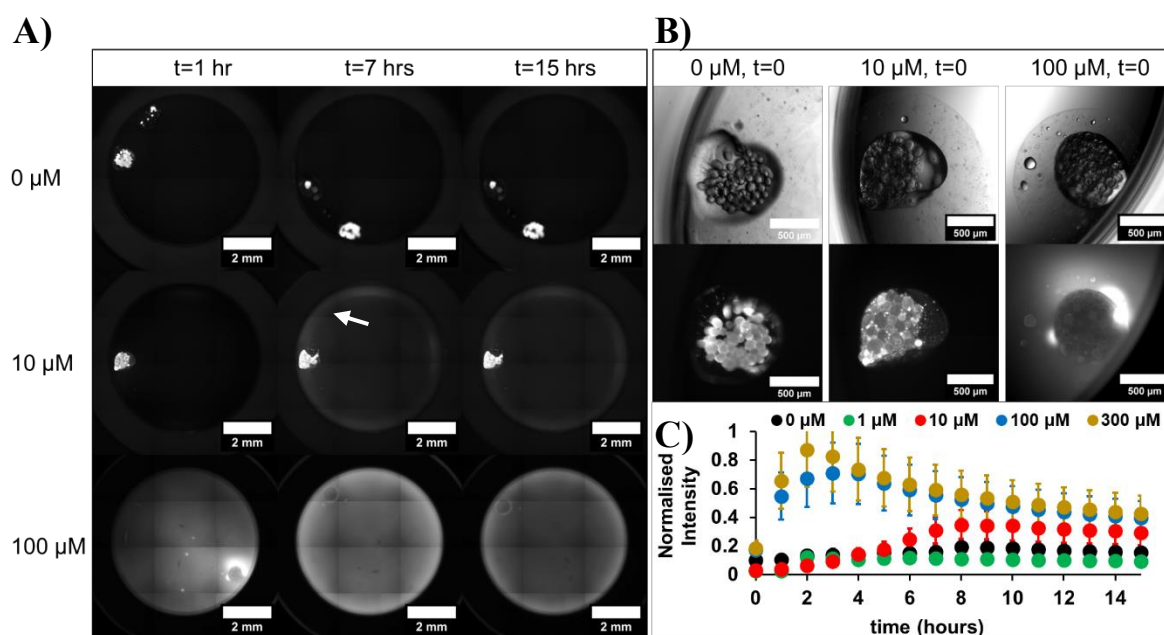


**Figure 3. 12: LPC concentration dependant release of encapsulated cores in eDIBs, according to the fluorescence increase assay.** **A)** Dark field fluorescent timelapse images of eDIBs when incubated with 0  $\mu\text{M}$  (no strong leaked fluorescence), 10  $\mu\text{M}$  (see white arrow for small fluorescence in the well periphery around 7 hours) and 100  $\mu\text{M}$  (quickly leaked and strong fluorescence) over 15 hours. **B)** eDIB BF images (top) and fluorescent images of the internal cores at  $t=0$ , which revealed dilution of the quenched dye due to strong fluorescent signal in the cores. **C)** Release rate profiles of the internal fluorescent cores induced by the presence of different LPC concentrations. Maximum fluorescence signals for 10  $\mu\text{M}$ , 100  $\mu\text{M}$  and 1000  $\mu\text{M}$  LPC were at 8, 3 and 2 hours, respectively. The data of the intensity measured by ImageJ, where normalised based on the overall raw recorded data and the error bars indicate the calculated  $\pm\text{SEM}$  of each data set ( $n= 11$  (0  $\mu\text{M}$ ),  $n=5$  (1  $\mu\text{M}$ ),  $n=3$  (10  $\mu\text{M}$ ),  $n=3$  (100  $\mu\text{M}$ ),  $n=3$  (300  $\mu\text{M}$ )).

The action of LPC within the eDIB system is certainly effected and triggered by the diffusion of LPC molecules to the lipid bilayer<sup>25</sup>. However, it is plausible that the LPC also interacts with the DPPC vesicles near the interface of the bilayer and the hydrogel, however there is no evidence to support this. Others have reported that LPC introduced to the outer leaflet of liposomes induces pressure changes to the lipid bilayer and enhances membrane permeability<sup>50</sup>. LPC lipid molecules have one hydrophobic tail, forming a cone-shaped lipid structure with positive curvature, known as micelles. According to Avanti Lipids (the manufacturer), the Egg Lyso PC composition is dominated by approximately 69 % of 16:0 Lyso PC, leading to the assumption that the critical micelle concentration (CMC) is that of 16:0 Lyso PC. This CMC value for 16:0 Lyso PC was published to be between 4  $\mu\text{M}$

and  $8.3 \mu\text{M}$  at temperatures ranging from  $4 \text{ }^\circ\text{C}$  to  $49 \text{ }^\circ\text{C}$ <sup>51</sup>. Hara, *et al.* 1960, reported a similar  $8 \mu\text{M}$  CMC of LPC in water at  $20 \text{ }^\circ\text{C}$ <sup>52</sup>. Therefore, the  $10 \mu\text{M}$  concentration used in the current practical experiments was very close to previously reported CMCs. However, the CMC value is a variable of temperature, pH and salt, which means that the form of LPC delivered to the eDIBs was uncertain. This would be, either individual LPC lipid molecules, monomers (<CMC) or micelles (>CMC). In accordance with the fluorescence assays, concentrations above  $100 \mu\text{M}$  LPC exhibited a faster release rate, as these concentrations were well above the CMC and higher concentration of LPC micelles were delivered to the targeted site. Thereby, depending on the concentration added to the external buffer bath, below or above the CMC, the LPC will diffuse to the lipid bilayer in the form of monomers or micelles. Subsequently, these lysolipids of positive curvature insert the bilayer, promote asymmetry across the leaflets and result to the release of the cores, where the release rate depends on the concentration of the added lysolipids (**Figure 3. 13**).

As briefly mentioned in Chapter II, a theoretically asymmetric bilayer could have formed between the hydrogel and water cores (i.e., asymmetric DHB), where some DPPC vesicles could have fused with the DHB. Therefore, in the instance of a DOPC/DPPC asymmetric bilayer, the addition of LPC would have promoted further asymmetry, hence fluidity changes and subsequent core release, depending on the LPC concentration (<CMC or > CMC) (*Appendix 3.F*).

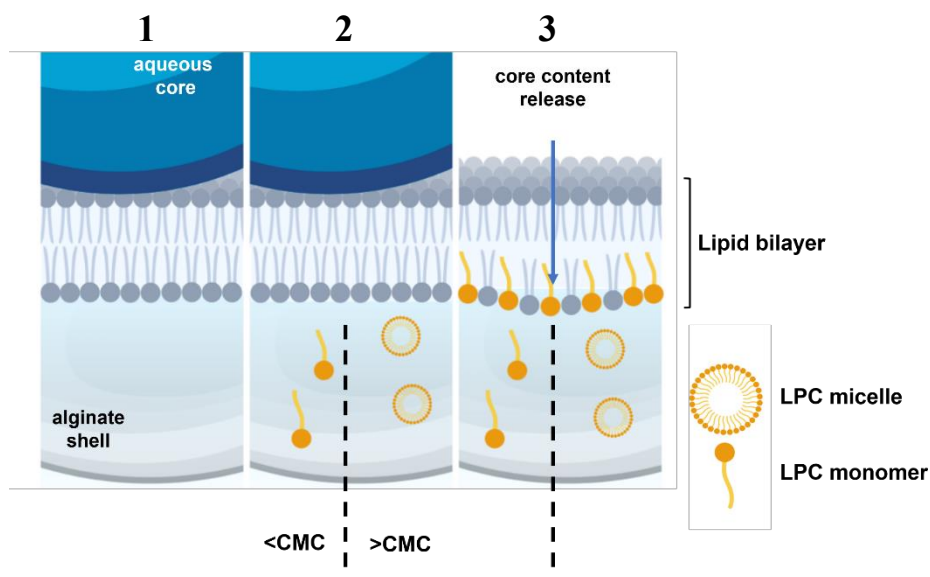


**Figure 3. 13: Schematic representation of the LPC effect on the lipid bilayer of an eDIB.** A symmetric stable bilayer between an aqueous core and the hydrogel shell or as often referred to as DHB (1). Addition of LPC lipids either as monomers (<CMC) or as micellar structures (>CMC) (2). Both LPC micelles and individual lipids, interact with the leaflet adjacent to the hydrogel, LPC molecules insert the bilayer, causing membrane pressure differences and eventual rupture of the membrane and consequently the content of the internal cores is released (3).

### 3.4.5. The effect of low LPC concentrations (1 $\mu\text{M}$ and 10 $\mu\text{M}$ ) on eDIBs

eDIBs with characteristics and structures like the one shown in **Figure 3. 14A**, were incubated with 1  $\mu\text{M}$  and 10  $\mu\text{M}$  LPC to study how the addition of LPC affects the rearrangement of the droplets. Microfluidic experiments produced eDIBs with aqueous core average diameter  $201.1 \mu\text{m} \pm 5.3$  (**Figure 3. 14B**,  $t=0$ ) and a contact angle  $\theta$  of approximately  $36.6^\circ \pm 0.6$ . After introducing the LPC of 1  $\mu\text{M}$  and 10  $\mu\text{M}$ , droplets started to rearrange, while merging occurred approximately 10 hours later, in cores exposed to 10  $\mu\text{M}$  (**Figure 3. 14B**,  $t=600$  min). This was revealed by a drop in the core number with diameters around 210  $\mu\text{m}$  (indicated by the yellow and red stars in **Figure 3. 14B**). The addition of 1  $\mu\text{M}$  LPC induced similar merging of the aqueous cores, but not as substantially observed with 10  $\mu\text{M}$  LPC. It should be noted that due to the merging of the cores in the presence of 10  $\mu\text{M}$  of LPC, the number of samples measured 16 hours later, was reduced by 7 ( $n=21 \rightarrow 14$ ), while the measured samples for 1  $\mu\text{M}$  reduce by 2 ( $n=23 \rightarrow 21$ ). The considerable drop in the core number caused by 10  $\mu\text{M}$  LPC, within a single eDIB, is evidence that merger occurs between cores and that core release into the hydrogel was very likely (missing yellow line trace of 10  $\mu\text{M}$  treated eDIB at 650 min in **Figure 3. 14C**). eDIB samples were monitored over 10 hours and every 5 minutes the position of the cores was recorded using a tracking tool on ImageJ. It is clear from **Figure 3. 14C** (only shows 5 timepoints), that there was significant movement and merging action in the cores of eDIBs treated with 10  $\mu\text{M}$  LPC, compared to the control and 1  $\mu\text{M}$  LPC.

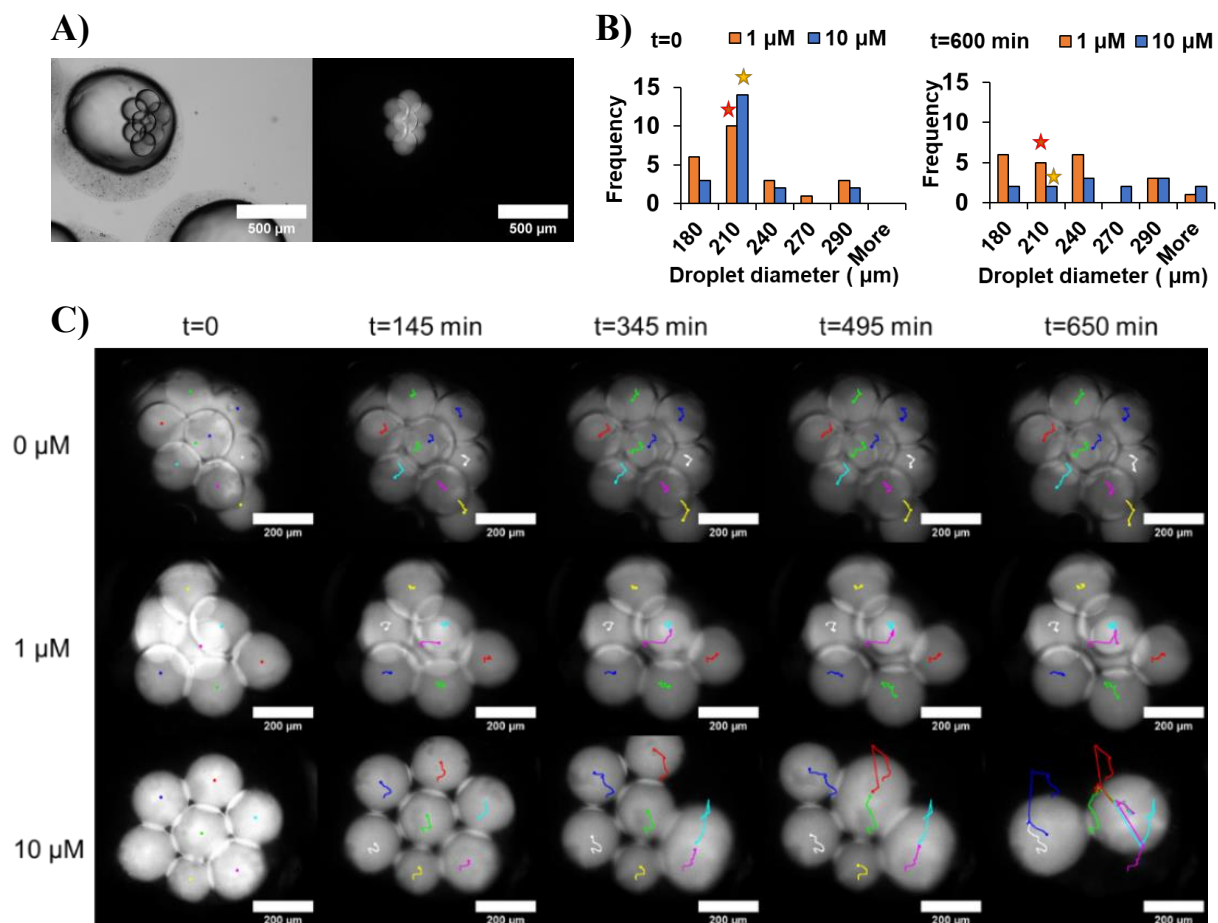


**Figure 3. 14: Effects of 1  $\mu\text{M}$  and 10  $\mu\text{M}$  LPC on the internal cores of eDIB.** *A)* Untreated eDIB with 7 cores of diameter 172  $\mu\text{m}$  (BF (LHS) and dark field fluorescence image (RHS)). *B)* eDIBs treated with 10  $\mu\text{M}$  LPC for 600 min (10 hours), undertook significant merging between internal cores or they were released into the hydrogel, compared to the ones treated with 1  $\mu\text{M}$  (see red and yellow stars) (for 1  $\mu\text{M}$ ,  $n=23$  ( $t=0$ ),  $n=21$  ( $t=600$  min) and for 10  $\mu\text{M}$ ,  $n=21$  ( $t=0$ ),  $n=14$  ( $t=600$  min)). *C)* Tracking of inner cores stimulated by 0, 1 and 10  $\mu\text{M}$  LPC in buffer. The dots indicate the position of the cores, starting at  $t=0$ , while the coloured lines indicate their locomotory movement from the starting point ( $t=0$ ) to each timepoint shown. Scale bar in A) indicates 500  $\mu\text{m}$  and in C) 200  $\mu\text{m}$ .

### 3.4.6. COMSOL simulations on the LPC transport and core release in an eDIB-like design

For simulating the diffusion of LPC through the eDIB hydrogel shell and subsequent core release, the parameters listed in **Table 3. 2** were employed to the COMSOL TDS module:

*Table 3. 2: Expressions, descriptions and units of parameters used within COMSOL Multiphysics for 2D and 3D computational simulation.*

Parameters	Description	Value
$D_{F,LPC}$	Diffusion coef. of the LPC through the hydrogel	$1 \times 10^{-11} \text{ m}^2/\text{s}$
$D_{F,c}$	Diffusion coef. of the core contents (C) through the hydrogel	$1 \times 10^{-11} \text{ m}^2/\text{s}$
$D_{s,LPC}$	Diffusion coef. of the LPC through the lipid bilayer	$1 \times 10^{-26} \text{ m}^2/\text{s}$
$d_s$	Thin diffusion barrier, i.e., lipid bilayer thickness	$7 \times 10^{-9} \text{ m}$
$C$	Inner droplet concentration	$0.002 \text{ mol}/\text{m}^3$
$D_c$	Diffusion coef. of C within the water domains	$2 \times 10^{-9} \text{ m}^2/\text{s}$
$D_{LPC}$	Diffusion coef. of LPC within the water domains	$2 \times 10^{-9} \text{ m}^2/\text{s}$
$LPC$	LPC concentration introduced outside the hydrogel shell	1, 10, 100, 1000 $\mu\text{M}$
$porH$	Hydrogel porosity	0.7 (dimensionless)

The molecular weight of LPC and SulfB is 503.334 g/mol and 580.65 g/mol, respectively. Due to the relatively similar molecular weights of LPC and SulfB, their diffusion coefficients through the hydrogel were set to  $1 \times 10^{-11} \text{ m}^2/\text{s}$ . This order of magnitude was selected according to a previously published COMSOL simulations of diffusion of species through hydrogel media<sup>53,54</sup>. The parameter of the thin diffusion barrier described the thickness of the lipid bilayer, which was set to be 7 nm, slightly higher than reported artificial lipid bilayer thicknesses (2-5 nm) and slightly lower than that of eukaryotic cell membranes (8-10 nm)<sup>55,56</sup>. The LPC molecules diffuse through the hydrogel and subsequently reach and disrupt the lipid bilayer, but do not diffuse through it. Therefore, the diffusion coefficient of the lipid bilayer was set to  $1 \times 10^{-26} \text{ m}^2/\text{s}$ , considering it negligible during the study. The LPC and SulfB diffusion through the water domains was set to  $2 \times 10^{-9} \text{ m}^2/\text{s}$ <sup>57</sup>. The hydrogel porosity of the shell was kept at 0.7 for all the simulations apart from the porosity study in Section 3.4.6.2, and similarly the hydrogel thickness was kept at 0.6 mm, excluding the study in Section 3.4.6.3.

### 3.4.6.1. Threshold concentration for core release activation (2D)

According to the experimental results from Section 3.4.4, the addition of LPC to eDIBs constructs, induced the release of the encapsulated content (**Figure 3. 11**). This led to the indication that there is a threshold concentration of LPC, which activates the release from the internal cores. This was further explored by employing a threshold concentration of LPC into the computational models, which would trigger the release from the cores.

The release of the cores' contents in the model, occurred only when the boundary at the thin diffusion barrier, i.e., the lipid bilayer, reached the pre-set LPC molar concentration threshold. Increasing this threshold value by a 10-fold, the initial concentration drop followed a delay, as computed in **Figure 3. 15**. The threshold values tested were  $1 \times 10^{-8}$  mol/m<sup>3</sup>,  $1 \times 10^{-7}$  mol/m<sup>3</sup>,  $1 \times 10^{-6}$  mol/m<sup>3</sup>,  $1 \times 10^{-5}$  mol/m<sup>3</sup>. Each highlighted region indicates a group of data sets corresponding to the introduced LPC concentration. It should be noted that 1  $\mu$ M LPC data, did not show any concentration decrease throughout the simulation period, a phenomenon which was usually observed in the practical experiments. The three lowest threshold concentrations tested with 1000  $\mu$ M LPC, exhibited minimal differences in the inner droplet concentration reduction profiles (overlapping data points in yellow highlighted region). Similar minor differences in the release were also shown by the 100  $\mu$ M LPC concentration (overlapping data points for the three lowest thresholds in the intersection of the yellow/blue highlighted regions). When the 2D model was treated with 10  $\mu$ M LPC, the thresholds were met, and the cores released the encapsulant analogue after 4-6 hours. For subsequent computational simulations, the threshold concentration of LPC at the lipid bilayer was set to  $1 \times 10^{-6}$  mol/m<sup>3</sup>, while the concentration of the introduced LPC in subsequent models was 100  $\mu$ M.

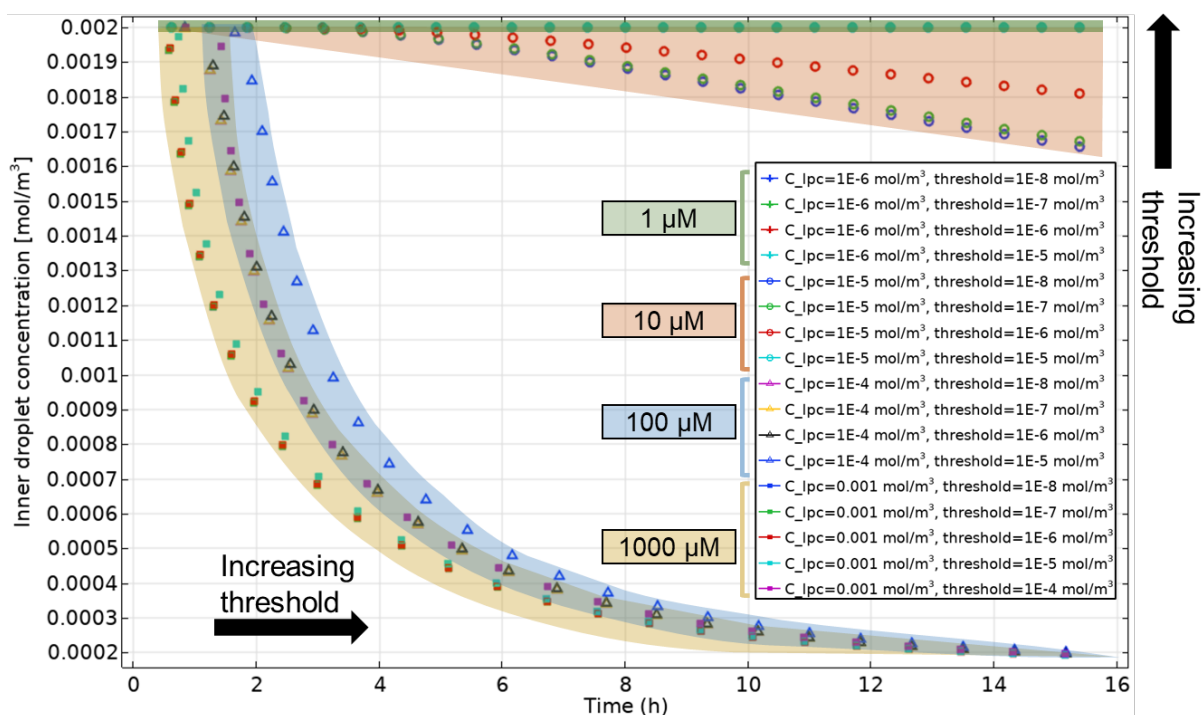


**Figure 3. 15:** The effect of the LPC concentration (1, 10, 100, 1000  $\mu\text{M}$ ) on the inner droplet intensity decrease, depending on the LPC threshold value, defined within the model. Data are grouped according to the concentration of LPC introduced to the model (colour highlighted regions), and each profile within each region, corresponds to a pre-set threshold concentration (as categorised in the legend). By increasing the threshold value, the initial core release was hindered, due to the insufficient accumulation of LPC at the bilayer. The lowest concentration of LPC, 1  $\mu\text{M}$ , (green region) was unable to activate the release at these threshold values.

### 3.4.6.2. Porosity of the hydrogel shell (2D)

One of the required parameters for simulating the mass transport through porous medium, is the porosity of the hydrogel material. Alginate hydrogel has been reported to obtain very high porosity, which can vary depending on the viscosity, origin, concentration and crosslinking method<sup>58–60</sup>. According to the published work by Ceccaldi, *et al.* 2017 and others, the porosity of  $\text{CaCl}_2$  crosslinked alginate is quite high and can span between 60-95 %<sup>59,61–63</sup>. Moreover, the lipid vesicles in the alginate hydrogel shell of the eDIBs, could potentially reduce the porosity, as vesicles may fill the voids of the porous material. This has been attributed, by earlier works, to the diffusion resistance of drug-laden liposomes entrapped in alginate microbeads<sup>64</sup>. Equally, the liposomes present in the hydrogel shell of the eDIB model, may be hypothesised to affect the diffusion of a substance through the material. By changing the porosity of the porous medium in the model, the diffusive flux of LPC through the hydrogel was computed. This was plotted over time for a region of interest on the lipid bilayer, indicating that, as the porosity tends to one ( $\epsilon_p$  or  $porH = 1$ ), i.e. high porosity, the mass transport over an area is higher as it appears in **Figure 3. 16A**. As the LPC concentration increases at the lipid bilayer, the concentration gradient between the LPC bath and the lipid bilayer weakens and the diffusive flux decays.

### 3.4.6.3. Hydrogel shell thickness ( $t_H$ ) (2D)

Similar to the porosity, the hydrogel shell thickness ( $t_H$ ) was also studied to show this parameter's effect on the diffusion of LPC. The hydrogel porosity and diffusion coefficient of the LPC were kept at 0.7 and  $1 \times 10^{-11}$  m<sup>2</sup>/s, respectively. In practise, the hydrogel shell thickness can be controlled by altering the microfluidic flow rates of the alginate and carrier phase that produce the eDIBs. Moreover, as presented by the OCT data and  $p_{3D}$  equation in Section 3.4.2, the oil core's location was not centred, leading to the hydrogel thickness to be varied around the eDIBs. **Figure 3. 16B** shows that by increasing the thickness of the hydrogel within the simulation's geometry, the time to reach a plateau of the LPC concentration at the lipid bilayer is extended. This implies that the threshold concentration at the thin diffusion barrier (lipid bilayer) is met at a later timepoint, directly affecting and delaying the initial core release. As an example, **Figure 3. 17** illustrates the contour plots for the LPC and core concentration distribution at  $t=180$  min for  $t_H=0.4$  mm and  $t_H=0.7$  mm. At this timepoint, the threshold was met and core release was already triggered. These graphic plots show that increasing the shell thickness to 0.7 mm, caused a delay to the uniform distribution and delivery of LPC to the lipid bilayer, which in turn affected the contour of the core intensity.

The last two computational studies, determine that the diffusion and subsequent effect of LPC on the eDIBs and internal cores, can be controlled by manipulating the structural characteristics of the hydrogel. The porosity has a direct effect on the diffusion coefficient, while the shell thickness affects the distance travelled by the LPC source to the targeted area (lipid bilayer). Both of these parameters are involved in Fick's Law of the diffusive flux and are factors that influence the core release profile, hence their control can give rise to a programmed release system.

In practice, the eDIBs did not always obtain a concentric oil core, hence the diffusion of the LPC was not symmetric or uniform. Hence, eDIBs with offset mid-oil cores, would lead to inconsistent results during LPC diffusion and activation of the drug release system. The inhomogeneities of the hydrogel shell thickness around the oil core occur during the emulsification process and as the alginate shell crosslinks by the carrier phase in the downstream channel. To overcome this problems and achieved concentric emulsions, many have employed density matching of phases or by applying electric fields on double emulsion droplets with different dielectric properties<sup>65,66</sup>. Other parameters that may influence the concentricity of multiple emulsions are the carrier phase velocity and viscosity, the core to shell diameter ratio, while larger capillaries may also minimise the non-uniformity of emulsions<sup>67</sup>.

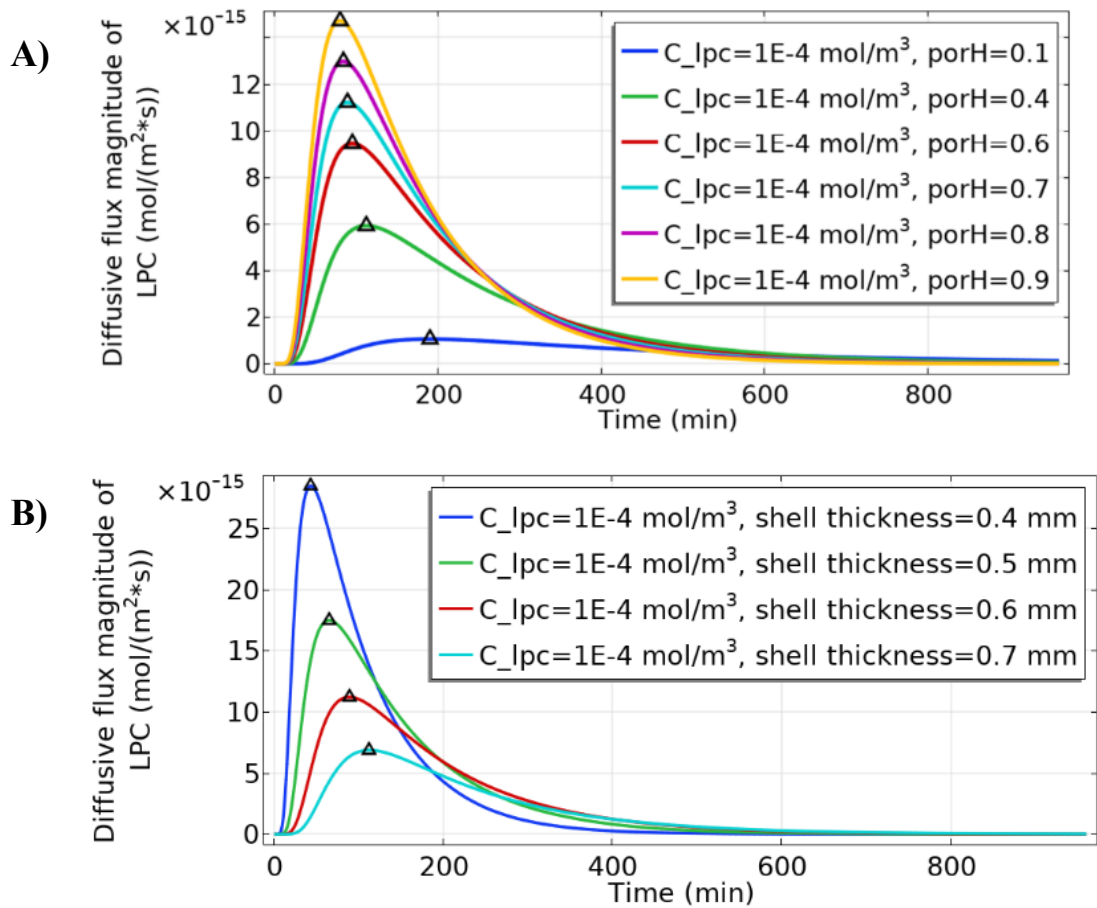


**Figure 3.16: Diffusive flux of LPC (100  $\mu\text{M}$ ) at a point near the lipid bilayer, where the decrease of the porosity and increase of the shell thickness exhibits delayed LPC concentration build-up at the lipid bilayer. A) The porosity is a characteristic of the porous material, and it is required to solve the model. Increasing the porosity ( $\text{porH}$ ), yields a faster travel of the LPC substance to the lipid bilayer. B) The shell thickness of the eDIB model can be controlled during the microfluidic experiment. While the diffusion coefficient and porosity are kept the same, the increase of the porous shell material delays the build-up of the LPC concentration at the lipid bilayer. The triangles indicate the timepoints at which the LPC concentration at the lipid bilayer region of interest matches the LPC concentration in the surroundings (equilibrium), which was interpreted as a drop of the diffusive flux magnitude.**

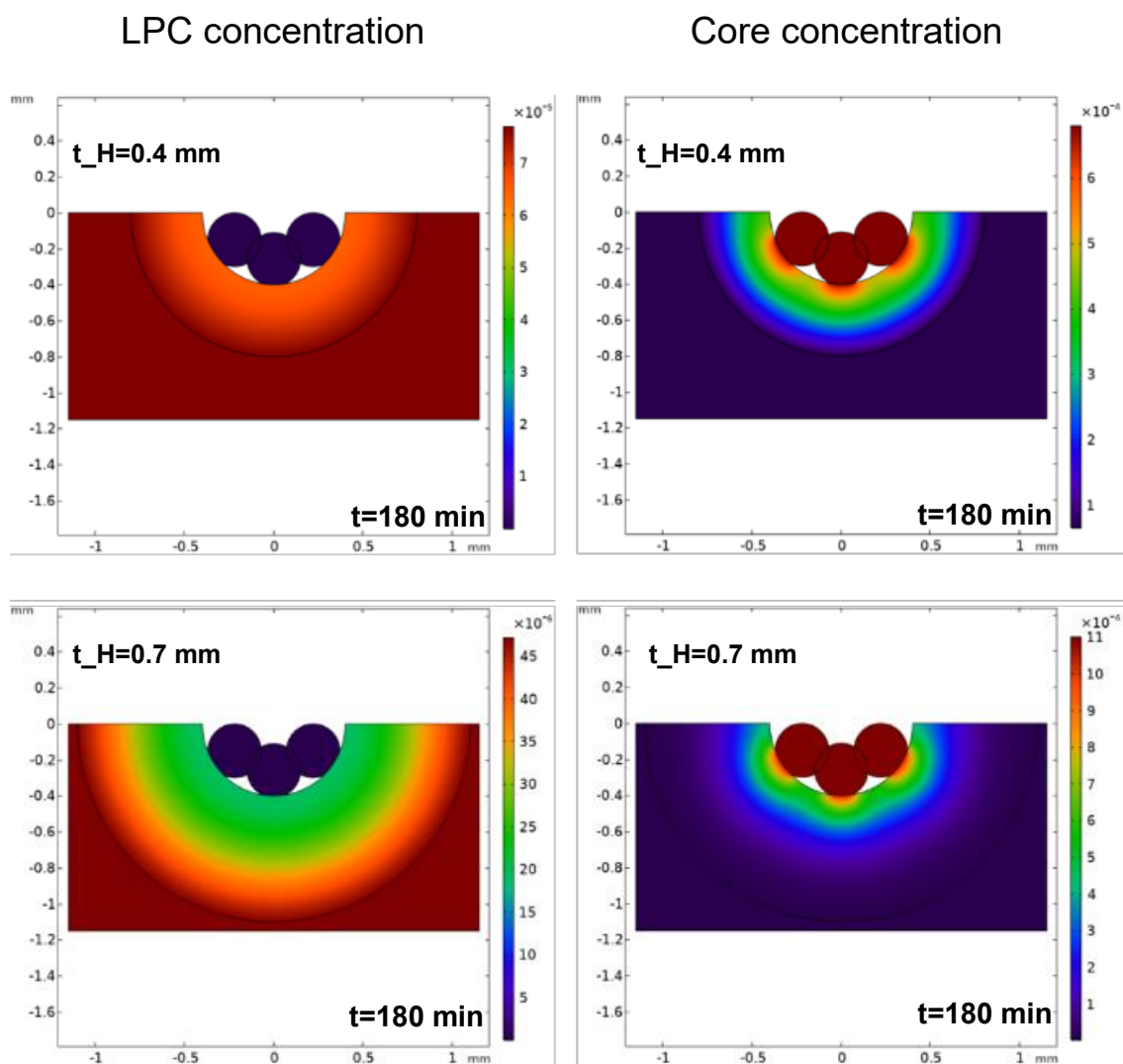


**Figure 3. 17:** 2D concentration contour plots at  $t = 180$  min for the LPC and internal cores, resulting from different hydrogel shell thicknesses ( $t_H$ ). These contour plots show the release of the cores after the LPC had met the threshold value at the bilayer barrier (prior to 180 min). As the  $t_H$  increases from 0.4 mm to 0.7 mm, the LPC concentration at the lipid bilayers turns from a red contour colour to green. The red contour is attributed to high LPC concentration at this timepoint, while green attributed to a lower concentration. This reduction is due to the larger distance travelled. With the smaller shell thickness (0.4 mm), the LPC reached the lipid bilayer faster, hence the content of the cores was released and dissipated all over the porous shell, in contrast to the 0.7 mm thickness.

### 3.4.6.4. 3D simulation

Totally realistic computational simulations using this module, are difficult to achieve, since there are elements from the practical experiments which were not included in the simulation. For example, the eDIBs carry multilamellar and polydisperse DPPC vesicles in the hydrogel shell. The degree of interaction between the DPPC and the introduced LPC, such as adsorption was not included in the simulation. Other environmental factors such as salt concentration and temperature were not included in the simulation either. To improve the simulation results and predictions, a 3D eDIB model was built to perform simulation with enhanced dimensional accuracy. The 3D model utilised porH = 0.7, threshold concentration =  $1 \times 10^{-6}$  mol/m<sup>3</sup> and shell thickness of 0.6 mm. **Figure 3. 18A&B** show the LPC and inner droplet concentration contour plots at t=180 min, respectively for both the 2D and 3D computational models. Both of these concentration profiles were compared between the 2D and 3D models over a 16-hour period study, indicating a faster diffusion of LPC to the lipid bilayer and consequently a faster release of the cores within the 3D model (**Figure 3. 18C**).

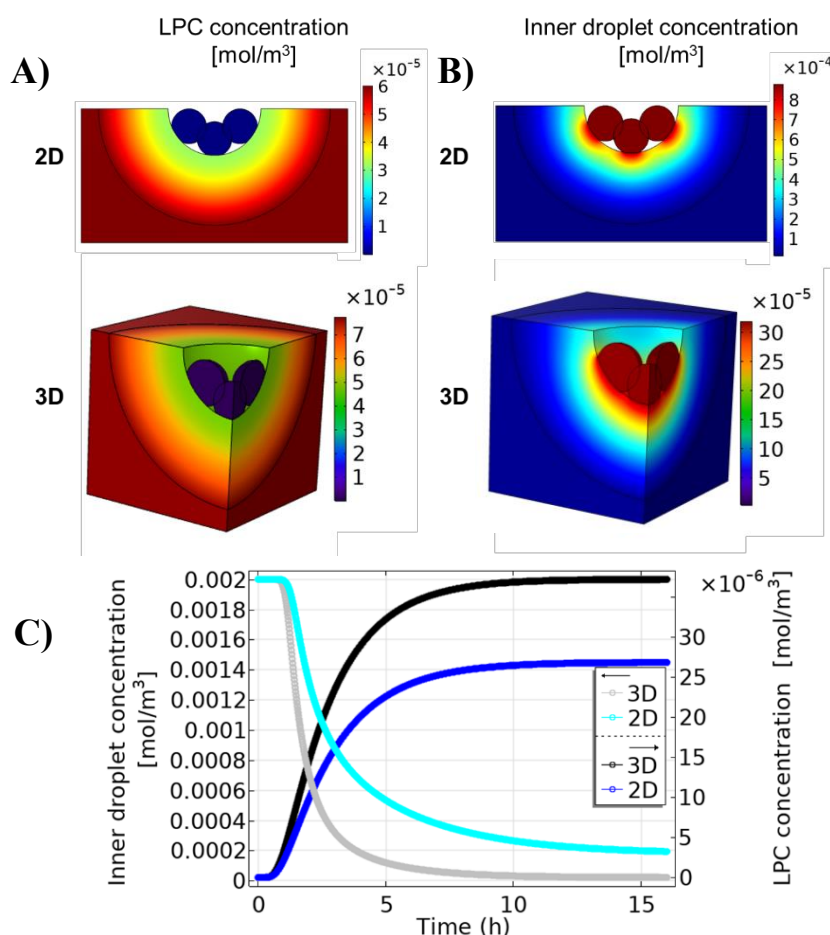


**Figure 3. 18: 2D and 3D simulation comparisons focusing on the LPC and inner core concentrations. A)** LPC concentration contour plots at t=180 min. The LPC concentration near the cores is higher in the 3D model than in the 2D model (see colour scale bars). **B)** Core concentration contour plots at t=180 min. The inner core concentration leaving the lipid bilayer is lower at this timepoint in the 3D model than in the 2D model (see colour scale bars), because of the faster. **C)** Two y-axis data plot of core and LPC concentrations exported from the 2D and 3D models. Each data point of the line graph represents a computed value (in total 960 datapoints).

### 3.4.6.5. Practical versus computational results

The 2D and 3D simulation results were compared to the practical experiments related to the core content release activated by LPC, from Section 3.4.4. First, the data points from the 2D simulated threshold concentration of  $1 \times 10^{-6}$  M LPC from Section 3.4.6.1, were exported and normalised, for subsequent plotting with the practical data. Both practical and computational normalised data (intensities) were plotted as  $I/I_{\max}$ . The only significant correlation observed here, is the closely matched reduction profile caused by 100  $\mu\text{M}$  LPC, in both the 2D COMSOL and practical experiments (**Figure 3. 19A(i)**). The 100  $\mu\text{M}$  LPC from the practical experiment also overlaps with the 1000  $\mu\text{M}$  LPC COMSOL simulation. The linear trendline of the concentration release profiles, were also plotted in **Figure 3. 19A(ii)** (with intercept set to 1).

The same analysis was carried out for the 3D COMSOL simulation. Even though the earlier comparison showed well matched datapoints for the 100  $\mu\text{M}$  data, this was not conveyed in the 3D simulation. **Figure 3. 19B(i)**, reveals a fairly balanced release profile under the influence of 1000  $\mu\text{M}$  LPC in both 3D simulations and in practice. Additionally, the 10  $\mu\text{M}$  endpoints of the 3D simulation and practical experiments are in closer proximity than in 2D. As mentioned earlier, there are a few additional parameters which were not considered in the computational simulations, including also the CMC of LPC (4-8.3  $\mu\text{M}$ )<sup>51,52</sup>. The COMSOL model assumes the diffusion of diluted species and does not utilise the CMC of LPC, which, depending on the structure of the lipid (monomers or micelles), it could affect the diffusion of the species through the porous medium. Hence, the exclusion of the CMC values from the computational model, could justify the divergence of the data regarding the 10  $\mu\text{M}$  LPC.

The laboratory (wet) and computational (dry) tests varied largely in theory and in practice, which explains the large differences between data. Despite that, it was possible to obtain some satisfactory results after the comparison of the experiments, such as the similarity between release profiles. However, the higher concentrations of LPC (1000  $\mu\text{M}$  and 100  $\mu\text{M}$ ) in the practical experiments induced bursting of the cores, due to the extreme and abundant concentration of LPC presented to the lipid bilayers. At lower concentrations, the bursting effect was reduced but still apparent in some cases (e.g. 10  $\mu\text{M}$ ). On the contrary the computational simulations performed precise constant core release, guided by leaking effects and not abrupt bursting effects as seen in the practical experiments from Sections 3.4.4.

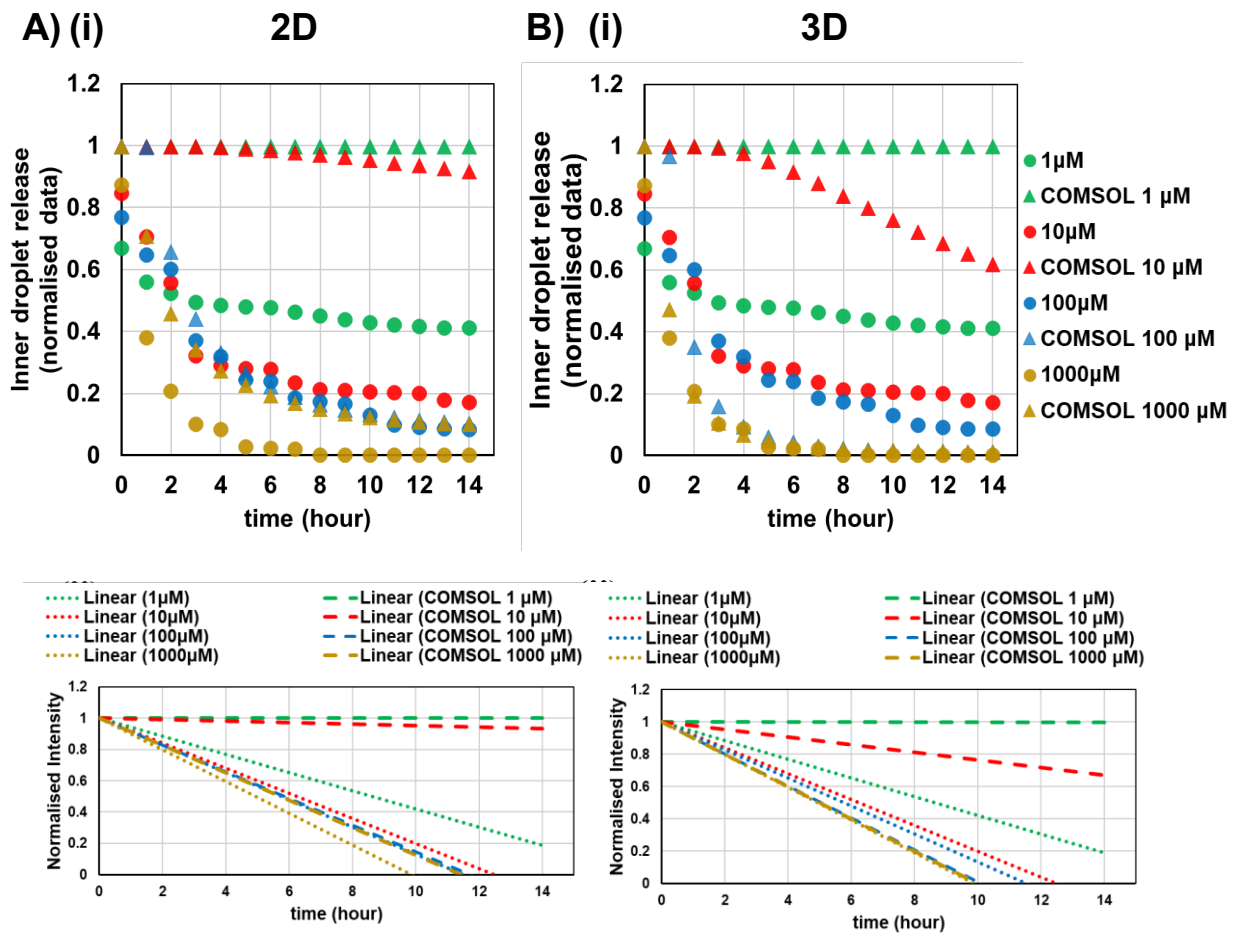


**Figure 3.19: Plotted wet (practical) and dry (computational) laboratory data for the LPC triggered core release over 14 hours.** **A)** The 2D computed inner droplet concentration reduction data points were exported every 60 min and (i) plotted with experimental data against time. The trendlines of all release profiles from (i) were plotted in (ii), with 1 set as the intercept. Overlap between computational and non-computational data resulted from the cores treated with 100  $\mu\text{M}$  LPC. **B)** The 3D computed inner droplet intensity release data points were exported every 60 min and (i) plotted with experimental data versus time. The trendlines of all release profiles from (i) were plotted in (ii), with 1 set as the intercept. Well match data points between computational and non-computational data resulted from the cores treated with 1000  $\mu\text{M}$  LPC.

### 3.4.7. DIB electrophysiology

The DIB electrophysiology experiments were conducted following the setup in **Figure 3. 20A**, in order to obtain any further information on the impact of LPC molecules on artificial lipid bilayers. The DIB acts as a capacitor and can store charge when a voltage is applied (**Figure 3. 20B**). This enables the investigation of any interactions between the droplets and the formed DIB artificial membrane, by recording current traces under an applied voltage. For initial indication of the bilayer formation, the voltage applied to a buffer-buffer DIB setup was +/- 23 mV triangular wave (10 Hz). As the two conductive droplets slowly touch and rearrange their lipid monolayer into a bilayer (**Figure 3. 20C**), the peak-to-peak current changed from 40 pA to approximately 180 pA, displaying a characteristic current trace as shown in **Figure 3. 20D**. During bilayer stabilisation, the amplitude increased up to 200 pA and eventually stabilised at approximately 160 pA (current trace not shown). The bilayer of the control buffer-buffer DIB became stable after 1-2 min.

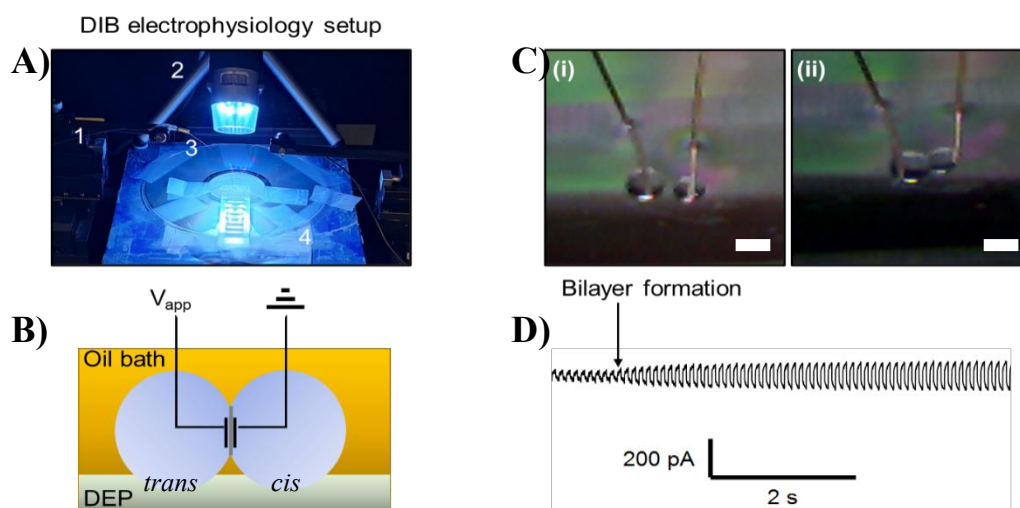


**Figure 3. 20: DIB electrophysiology setup and control bilayer formation.** **A)** DIB experimental setup included one micromanipulator (1) on each side of the platform, a fixed handheld camera with a light source (2), a platform with a reflective surface for contrast reasons (3) and a PMMA device with milled wells (4). **B)** Schematic representation of the DIB, acting as a capacitor in a closed circuit. **C)** In a PMMA well filled with lipid-oil mixture, the electrodes were deposited with two identical buffer droplets, which are shown before they come in contact (i) and after (ii), leading to the DIB formation. Scale bar: 500  $\mu\text{m}$ . **D)** Capacitive current trace indicating the formation of a lipid bilayer between two buffer droplets, by the current amplification from 40 pA to 180 pA.

In contrast to the buffer-buffer pairs, when LPC was introduced at a concentration of  $100\ \mu\text{M}$  in the *trans* droplet, under the same applied voltage ( $\pm 23\ \text{mV}$  triangular voltage at  $10\ \text{Hz}$ ), the bilayer kept growing even after  $8\ \text{min}$ , reaching peak-to-peak currents of almost  $6000\ \text{pA}$  (**Figure 3. 21A&B**). At a concentration of  $100\ \mu\text{M}$  of LPC, means that the LPC molecules encapsulated in the *trans* buffer droplet, are in the form of micelles and the expansion of the lipid bilayer could be an indication of the steady fusion of micelles with the lipid bilayer.

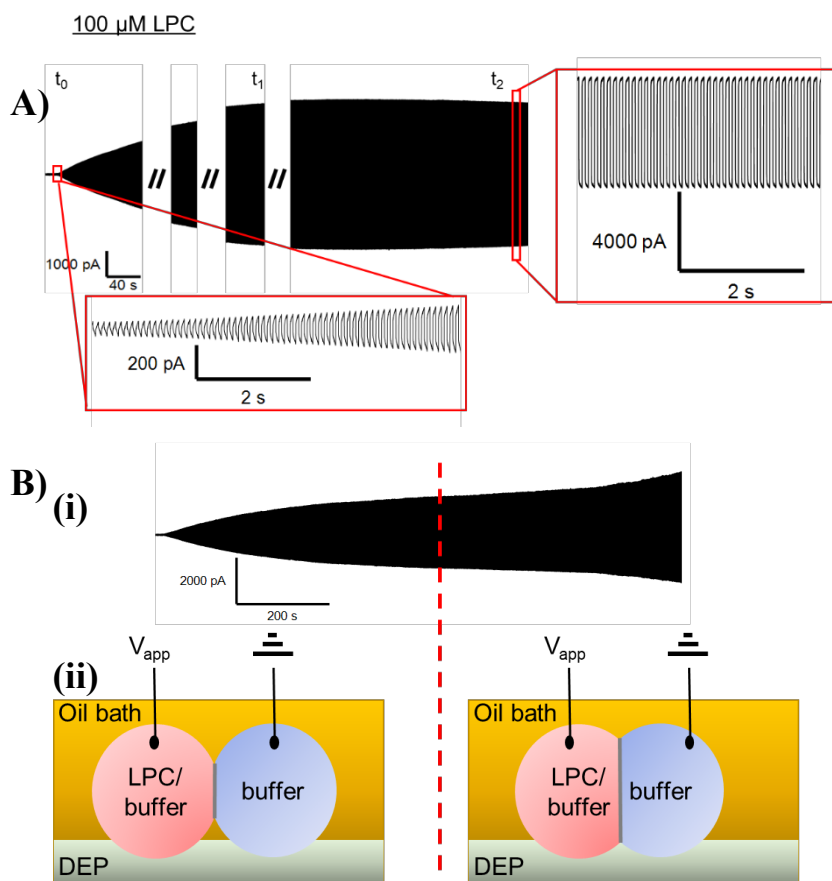


**Figure 3. 21: Lipid bilayer amplification and expansion in the presence of  $100\ \mu\text{M}$  LPC in the *trans* droplet of the DIB electrophysiology setup. A) DIB experiment, showing the lipid bilayer formation ( $t_0$ ), growth ( $t_1$ ) and stabilisation ( $t_2$ ). B) (i) Bilayer capacitive current trace expansion in an experiment carried out for longer than 15 minutes (ii) Schematic of the DIB before (LHS) and after (RHS) obvious lipid bilayer area increase and current amplification.**

However, as the concentration of LPC in the *trans* droplet was increased to 500  $\mu\text{M}$  and 1000  $\mu\text{M}$ , the bilayer became unstable or failed to form. The electrophysiology traces evidenced bilayer formation for approximately 20 s, between a 500  $\mu\text{M}$  LPC *trans* droplet and a *cis* buffer droplet. The LPC caused the formation of a considerably leaky bilayer, while the area of the DIB increased over time and eventually the bilayer failed, as shown in **Figure 3. 22A**. By increasing the LPC concentration further to 1000  $\mu\text{M}$ , the DIB was difficult to form. This could be due to the substantial reduction of the droplet's surface tension carrying the highly concentrated LPC micelles. In fact, it was observed that the 1000  $\mu\text{M}$  *trans* droplet engulfed the *cis* buffer droplet of significantly higher surface tension<sup>68</sup>, leading to the instant failure of the lipid bilayer, as revealed in **Figure 3. 22B**.

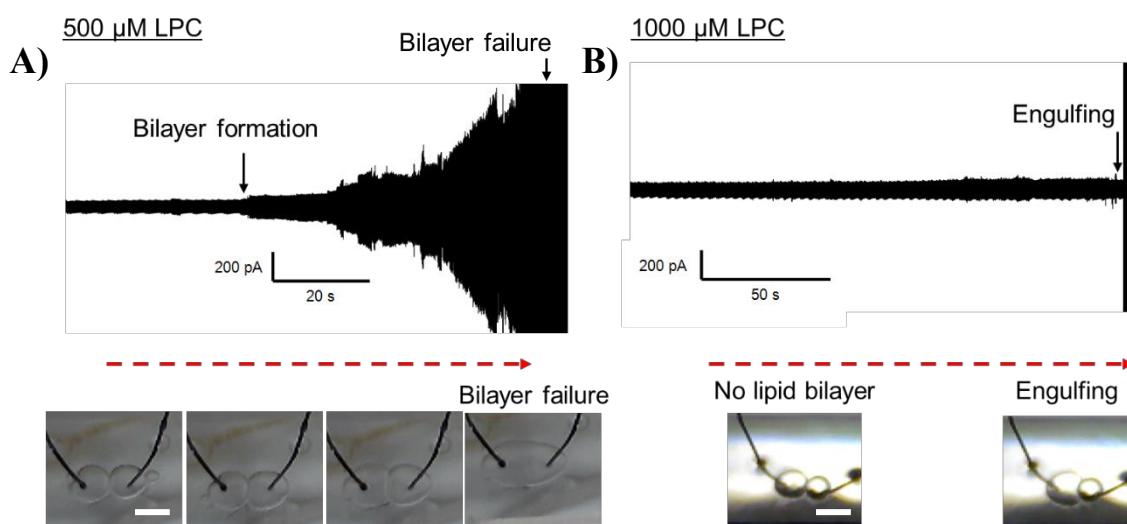


**Figure 3. 22: DIB electrophysiology experiments with 500  $\mu\text{M}$  and 1000  $\mu\text{M}$  of LPC in the *trans* droplet, resulted in bilayer failure. A) 500  $\mu\text{M}$  LPC in one DIB droplet formed unstable lipid bilayers, leading to merging and failure of the lipid bilayer. B) A DIB system with 1000  $\mu\text{M}$  LPC in one of the buffer droplets never attained bilayer formation and an engulfing behavior was expressed by the highly concentrated LPC droplet. Scale bar is 500  $\mu\text{m}$ .**

To explore the hypothesis regarding the fusion effect of LPC micelles with the lipid bilayer (**Figure 3. 23**), the voltage was switched to a constant and continuous +/- 20 mV voltage, after stable bilayer formation. The applied voltage to a buffer-buffer DIB (**Figure 3. 24A a-(i)**), induced a steady reoccurring current of approximately 10 pA, as plotted in **Figure 3. 24A a-(ii)**. Then, the introduction of LPC to the *trans* droplet, gave rise to a noisy current trace (**Figure 3. 24B b-(i)**), which corresponded to approximately 40-60 pA according to the histogram analysis, as illustrated in **Figure 3. 24B b-(ii)**. The 40 pA and 60 pA capacitances shown under positive and negative potentials ( $t_1 = 440$  s), were assumed to be an indication of noise (**Figure 3. 24B(b-(ii))**). A similar observation was made at later timepoint  $t_2 = 750$  s, with currents around 95 pA and 115 pA (**Figure 3. 24C(c-(ii))**). To obtain accurate capacitive current values, these set of data were filtered using the Chung-Kennedy filtration, developed by another researcher (*Appendix 3.G*)<sup>69,70</sup>. The data filtration revealed current occurrences for timepoints  $t_1$  and  $t_2$ , at 50 pA and 105 pA, respectively (**Figure 3. 24B(b-(iii))&C(c-(iii))**).

The continuous amplification of the current traces throughout the lifetime of a single experiment, was due to the increasing area of the bilayer, caused by LPC micelle fusion with the DIB. Interestingly, Strutt, et al. 2021 reported no such effects when they introduced vesicles with 15 % LPC to an asymmetric, lipid-in, micelle-free DIB system<sup>27</sup>. Thus, to conclude on the experimental results presented in **Figure 3. 24**, the buffer-buffer DIBs, produced a stable current flow across the lipid bilayer. When the 100  $\mu$ M LPC was introduced to one of the droplets of the DIB system, the bilayer became leakier, and it is possible that over time pores were formed due to the fusion of micelles, as indicated by the small sudden current steps at  $t_2 = 750$  s. A recent study by El-Beyrouthy, *et al.* 2022 studied DIBs and their surface interactions with membrane disrupting agents, i.e. surfactants, where they correlated unexpected jumps in the current to the membrane permeabilisation, due to the formation of pores by the flip-flop nature of the surfactants to the second leaflet<sup>71</sup>. These abrupt current changes induced extreme noise to their system. Their evidence validates the results in **Figure 3. 24B(b-(ii))&C(c-(ii))** where the noisy current traces only arose when the LPC was present in the system.

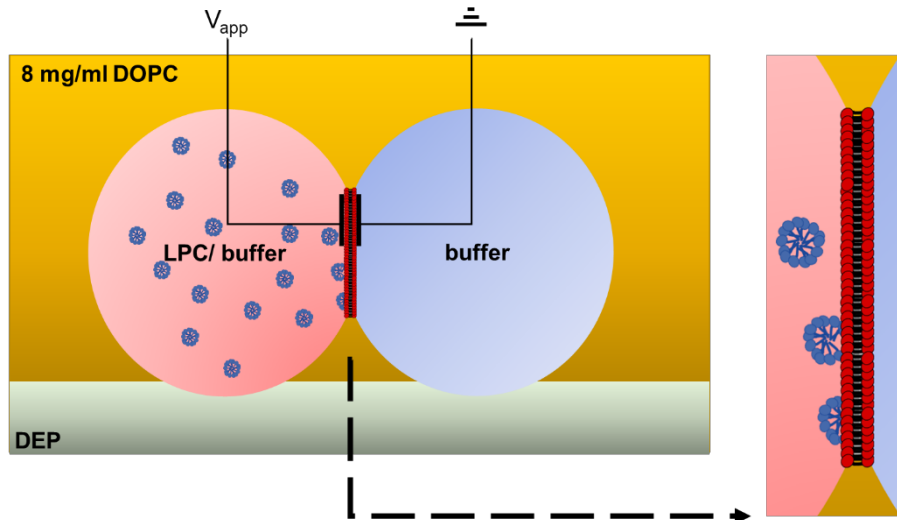


**Figure 3. 23:** Illustration of the hypothesis related to the fusion of LPC micelles with the lipid bilayer of the DIB during electrophysiology experiments.

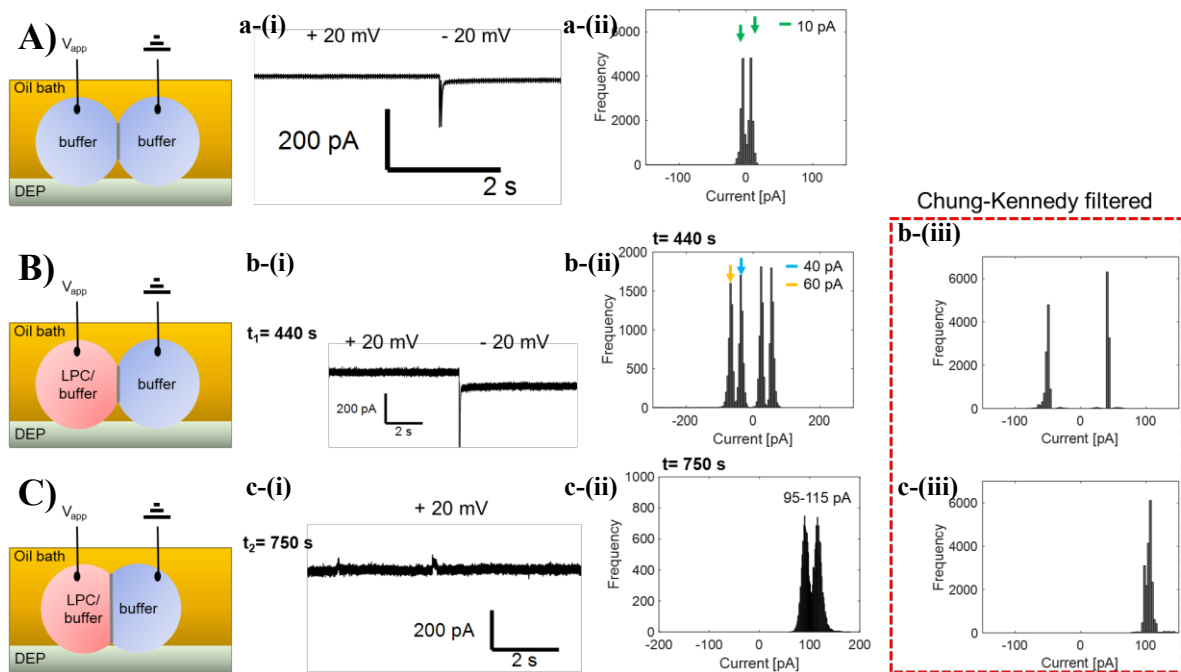


**Figure 3. 24:** DIB electrophysiology current traces and occurrences under applied potential of  $\pm 20$  mV in buffer-buffer and buffer-100  $\mu$ M LPC. **A)** Buffer-buffer droplet pair under an applied  $\pm 20$  mV, showed stable current trace (a-(i)). Histogram with most frequent current approximately at 10 pA (a-(ii)). **B)** A DIB of 100  $\mu$ M LPC and buffer droplets at  $t_1 = 440$  s, under applied  $\pm 20$  mV recorded a noisy trace (b-(i)), accompanied by a histogram analysis with positive and negative peaks at 40 and 60 pA (b-(ii)). The Chung Kennedy filtration of the data revealed 50 pA at  $t_1$  (b-(iii)). **C)** The same droplet pair at a later timepoint,  $t_2 = 750$  s, under +20 mV (c-(i)), held the noisy trace at higher current due to the bilayer area increase (95-115 pA), as evidenced by the histogram analysis (c-(ii)). The Chung Kennedy filtration of the data revealed current occurrences of 100 pA (c-(iii)).

For subsequent experiments,  $\pm 20$  mV voltage was applied through a supposed DHB consisting of a DPPC-containing gelled alginate droplet (*trans*) and an LPC buffer droplet (*cis*) (Figure 3. 25(i)). The most frequent current across the lipid bilayer was approximately 160 pA under positive and negative voltages, as uncovered by the current distribution histogram analysis in **Figure 3. 25(ii)**. Although, under positive potential, the current distribution was broader (80 – 240 pA), compared to the negative potential. The electrophysiology trace showed irregular and inconsistent current steps and peaks, which have been previously correlated to bursting or negligible noisy effects<sup>72,73</sup>. However, the reason for this directionality preference of the current occurrences in **Figure 3. 25**, was unclear and not further explored. The setup of this DHB droplet pair was quite complex and perhaps simpler experiments could provide more insight. However, one assumption for these events is the interaction or fusion of LPC micelles with an unstable lipid bilayer formed between the liquid droplet and the semi-solid droplet of the system. Another hypothesis is the interaction of the positive  $V_{app}$  with the negatively charged alginate<sup>74</sup>, perhaps pulling the alginate away from the lipid bilayer. Other hypotheses include, the fusion of DPPC vesicles with the bilayer, if they are in close proximity or if they disassociated from the hydrogel<sup>75</sup>, and the electroporation of DPPC vesicles by the applied voltage<sup>76,77</sup>, releasing their buffer content. The third hypothesis is less likely to occur because electroporation of vesicles usually takes place at higher applied voltages ( $> 200$  mV)<sup>78</sup>.

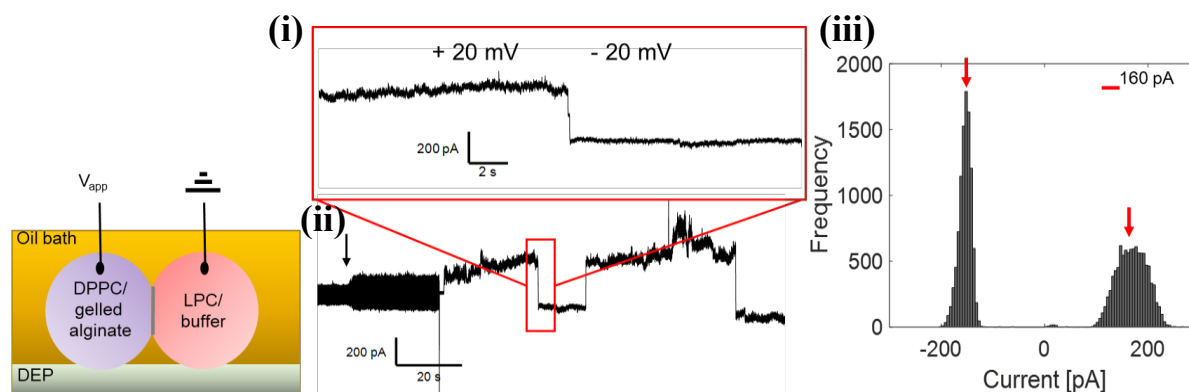


**Figure 3. 25: Electrophysiology experiment on a bilayer formed between a DPPC-containing gelled alginate droplet (*trans*) and a 100  $\mu$ M LPC buffer droplet (*cis*).** (i) Current trace of the applied  $\pm 20$  mV voltage through the DIB. (ii) Electrophysiology traces of applied  $\pm 23$  mV triangular wave for 40 s to indicated bilayer formation (black arrow) and then alternative between +20 mV and  $-20$  mV. (iii) Histogram analysis of  $\pm 20$  mV in the red box, shows frequent current around 160 pA, but narrower distribution under negative potential and broader under positive.

Overall, the electrophysiology experiments established the affinity of LPC and their considerable impact on the lipid bilayer. Finally, these results suggest that the durability and fate of the DIB, highly depend on the concentration of the LPC present in the system, which agrees with the fluorescent intensity data obtained from the eDIB triggered core content release.

### 3.5. Conclusion

This chapter focused on the familiarisation with important parameters, characteristics and capabilities of soft matter encapsulated Droplet Interface Bilayer (eDIB) devices. Their microfluidic production uses complex emulsion 3D-printed microfluidic devices, which is a process easily repeated and adjusted. The eDIB formula is robust and flexible permitting their use in operating protocols, involving centrifugation and elevated temperatures. Various imaging techniques can be used to further analyse these capsules, including clinical Optical Coherence Tomography (OCT) imaging, a quick approach for obtaining information regarding the internal structures of the capsules.

eDIBs, present platforms for drug encapsulation, are capable for prolonged reagent storage, and can be designed to be reactive to external stimuli, leading to a programmable, controlled and on-demand encapsulant release. Part of this chapter focused on the specific sensitivity of the lipid bilayers assembled at the interface of the internal compartments and hydrogel shell of eDIBs. This sensitivity was explored by introducing surfactant-like, single-tailed lysophosphatidylcholine (LPC) lysolipids, with great affinity to the lipid bilayer. Fluorescence increase and fluorescence decrease assays demonstrated an LPC concentration dependent core release. Concentration release profiles were supported by 2D and 3D computational simulations, with which correlations were mostly established at the highest concentrations of LPC. On the contrary, the concentrations of LPC closer to the critical micelle concentration (CMC), did not demonstrate significant correlations with practical experiments. Finally, the LPC introduction to the eDIB system was then explored with DIB electrophysiology experiments. These tests showed that LPC micelles have a significant influence on the lipid bilayer area and current flow, while also demonstrating, once again, an LPC concentration dependent bilayer stability.

### 3.6. References

1. Villar, G. & Bayley, H. Functional Droplet Interface Bilayers. in *Encyclopedia of Biophysics* (ed. Roberts, G. C. K.) 861–868 (Springer, 2013).
2. Taylor, G., Nguyen, M.-A., Koner, S., Freeman, E., Collier, C. P. & Sarles, S. A. Electrophysiological interrogation of asymmetric droplet interface bilayers reveals surface-bound alamethicin induces lipid flip-flop. *Biochimica et Biophysica Acta (BBA) - Biomembranes* **1861**, 335–343 (2019).
3. Lee, S. & Bayley, H. Reconstruction of the Gram-Negative Bacterial Outer-Membrane Bilayer. *Small* **18**, 2200007 (2022).
4. Elani, Y., Solvas, X. C. I., Edel, J. B., Law, R. V. & Ces, O. Microfluidic generation of encapsulated droplet interface bilayer networks (multisomes) and their use as cell-like reactors. *Chem. Commun.* **52**, 5961–5964 (2016).
5. Challita, E. J., Najem, J. S., Monroe, R., Leo, D. J. & Freeman, E. C. Encapsulating Networks of Droplet Interface Bilayers in a Thermoreversible Organogel. *Sci Rep* **8**, (2018).
6. Zhou, L., Wolfes, A. C., Li, Y., Chan, D. C. W., Ko, H., Szele, F. G. & Bayley, H. Lipid-Bilayer-Supported 3D Printing of Human Cerebral Cortex Cells Reveals Developmental Interactions. *Advanced Materials* **32**, 2002183 (2020).
7. Booth, M. J., Schild, V. R., Graham, A. D., Olof, S. N. & Bayley, H. Light-activated communication in synthetic tissues. *Science Advances* **2**, e1600056 (2016).
8. Manafirad, A. Single Ion-Channel Analysis in Droplet Interface Bilayer. in *Nanopore Technology: Methods and Protocols* (ed. Fahie, M. A. V.) 187–195 (Springer US, 2021).
9. Senior, M. J. T., Monico, C., Weatherill, E. E., Gilbert, R. J., Heuck, A. P. & Wallace, M. I. Single-molecule tracking of perfringolysin O assembly and membrane insertion uncoupling. *The FEBS Journal* **290**, 428–441 (2023).
10. Trantidou, T., Friddin, M. S., Salehi-Reyhani, A., Ces, O. & Elani, Y. Droplet microfluidics for the construction of compartmentalised model membranes. *Lab Chip* **18**, 2488–2509 (2018).

11. Li, J., Baxani, D. K., Jamieson, W. D., Xu, W., Rocha, V. G., Barrow, D. A. & Castell, O. K. Formation of Polarized, Functional Artificial Cells from Compartmentalized Droplet Networks and Nanomaterials, Using One-Step, Dual-Material 3D-Printed Microfluidics. *Adv Sci (Weinh)* **7**, 1901719 (2019).
12. Boreyko, J. B., Mruetusatorn, P., Sarles, S. A., Retterer, S. T. & Collier, C. P. Evaporation-Induced Buckling and Fission of Microscale Droplet Interface Bilayers. *J. Am. Chem. Soc.* **135**, 5545–5548 (2013).
13. Kang, X., Cheley, S., Rice-Ficht, A. C. & Bayley, H. A Storable Encapsulated Bilayer Chip Containing a Single Protein Nanopore. *J. Am. Chem. Soc.* **129**, 4701–4705 (2007).
14. Sarles, S. A. & Leo, D. J. Physical encapsulation of droplet interface bilayers for durable, portable biomolecular networks. *Lab Chip* **10**, 710–717 (2010).
15. Baxani, D. K., Morgan, A. J. L., Jamieson, W. D., Allender, C. J., Barrow, D. A. & Castell, O. K. Bilayer Networks within a Hydrogel Shell: A Robust Chassis for Artificial Cells and a Platform for Membrane Studies. *Angewandte Chemie International Edition* **55**, 14240–14245 (2016).
16. Baxani, D. K., Jamieson, W. D., Barrow, D. A. & Castell, O. K. Encapsulated droplet interface bilayers as a platform for high-throughput membrane studies. *Soft Matter* **18**, 5089–5096 (2022).
17. Dimitriou, P., Li, J., Tornillo, G., McCloy, T. & Barrow, D. Droplet Microfluidics for Tumor Drug-Related Studies and Programmable Artificial Cells. *Global Challenges* **5**, 2000123 (2021).
18. Gautam, L., Shrivastava, P., Yadav, B., Jain, A., Sharma, R., Vyas, S. & Vyas, S. P. Multicompartment systems: A putative carrier for combined drug delivery and targeting. *Drug Discovery Today* **27**, 1184–1195 (2022).
19. Cao, Z.-Q. & Wang, G.-J. Multi-Stimuli-Responsive Polymer Materials: Particles, Films, and Bulk Gels. *The Chemical Record* **16**, 1398–1435 (2016).
20. Bozzuto, G. & Molinari, A. Liposomes as nanomedical devices. *Int J Nanomedicine* **10**, 975–999 (2015).
21. Kaddah, S., Khreich, N., Kaddah, F., Charcosset, C. & Greige-Gerges, H. Cholesterol modulates the liposome membrane fluidity and permeability for a hydrophilic molecule. *Food and Chemical Toxicology* **113**, 40–48 (2018).

22. Jensen, G. M. & Hodgson, D. F. Opportunities and challenges in commercial pharmaceutical liposome applications. *Advanced Drug Delivery Reviews* **154–155**, 2–12 (2020).
23. López Ruiz, A., Ramirez, A. & McEnnis, K. Single and Multiple Stimuli-Responsive Polymer Particles for Controlled Drug Delivery. *Pharmaceutics* **14**, 421 (2022).
24. Acharya, S., Lu, B., Edwards, S., Toh, C., Petersen, A., Yong, C., Lyu, P., Huang, A. & Schmidt, J. Disruption of artificial lipid bilayers in the presence of transition metal oxide and rare earth metal oxide nanoparticles. *J. Phys. D: Appl. Phys.* **52**, 044002 (2018).
25. Disalvo, E. A., Viera, L. I., Bakas, L. S. & Senisterra, G. A. Lysophospholipids as Natural Molecular Harpoons Sensing Defects at Lipid Membranes. *Journal of Colloid and Interface Science* **178**, 417–425 (1996).
26. Zalba, S. & ten Hagen, T. L. M. Cell membrane modulation as adjuvant in cancer therapy. *Cancer Treatment Reviews* **52**, 48–57 (2017).
27. Strutt, R., Hindley, J. W., Gregg, J., Booth, P. J., Harling, J. D., Law, R. V., Friddin, M. S. & Ces, O. Activating mechanosensitive channels embedded in droplet interface bilayers using membrane asymmetry. *Chem Sci* **12**, 2138–2145 (2021).
28. Rasmussen, N., Andersen, J. H., Jespersen, H., Mouritsen, O. G. & Ditzel, H. J. Effect of free fatty acids and lysolipids on cellular uptake of doxorubicin in human breast cancer cell lines. *Anti-Cancer Drugs* **21**, 674–677 (2010).
29. Kakisaka, K., Cazanave, S. C., Fingas, C. D., Guicciardi, M. E., Bronk, S. F., Werneburg, N. W., Mott, J. L. & Gores, G. J. Mechanisms of lysophosphatidylcholine-induced hepatocyte lipoapoptosis. *American Journal of Physiology-Gastrointestinal and Liver Physiology* **302**, G77–G84 (2012).
30. Chang, M.-C. *et al.* Lysophosphatidylcholine induces cytotoxicity/apoptosis and IL-8 production of human endothelial cells: Related mechanisms. *Oncotarget* **8**, 106177–106189 (2017).
31. Makhoul-Mansour, M. M. & Freeman, E. C. Droplet-Based Membranous Soft Materials. *Langmuir* **37**, 3231–3247 (2021).

32. Li, J. *et al.* Building programmable multicompartment artificial cells incorporating remotely activated protein channels using microfluidics and acoustic levitation. *Nat Commun* **13**, 4125 (2022).
33. Civetti, E. M., Khaimov, V. & de Guzman, R. C. Keratin biomaterial diffusivity determination in a 1D-like channel using COMSOL and MATLAB. *2* (2019).
34. Millington, R. J. & Quirk, J. P. Permeability of porous solids. *Trans. Faraday Soc.* **57**, 1200 (1961).
35. Graham, A. D. *et al.* High-Resolution Patterned Cellular Constructs by Droplet-Based 3D Printing. *Sci Rep* **7**, 7004 (2017).
36. El-Beyrouthy, J., Makhoul-Mansour, M. M., Taylor, G., Sarles, S. A. & Freeman, E. C. A new approach for investigating the response of lipid membranes to electrocompression by coupling droplet mechanics and membrane biophysics. *J. R. Soc. Interface.* **16**, 20190652 (2019).
37. Song, G., Jelly, E. T., Chu, K. K., Kendall, W. Y. & Wax, A. A review of low-cost and portable optical coherence tomography. *Prog. Biomed. Eng.* **3**, 032002 (2021).
38. Fujimoto, J. G., Pitris, C., Boppart, S. A. & Brezinski, M. E. Optical Coherence Tomography: An Emerging Technology for Biomedical Imaging and Optical Biopsy. *Neoplasia* **2**, 9–25 (2000).
39. Kaivosoja, T. P., Liu, S., Dijkstra, J., Huhtala, H., Sheth, T. & Kajander, O. A. Comparison of visual assessment and computer image analysis of intracoronary thrombus type by optical coherence tomography. *PLoS One* **13**, e0209110 (2018).
40. Popescu, D. P., Choo-Smith, L.-P., Flueraru, C., Mao, Y., Chang, S., Disano, J., Sherif, S. & Sowa, M. G. Optical coherence tomography: fundamental principles, instrumental designs and biomedical applications. *Biophys Rev* **3**, 155 (2011).
41. Ferrante di Ruffano, L. *et al.* Optical coherence tomography for diagnosing skin cancer in adults. *Cochrane Database Syst Rev* **12**, CD013189 (2018).
42. Viedma, I. A., Alonso-Caneiro, D., Read, S. A. & Collins, M. J. Deep learning in retinal optical coherence tomography (OCT): A comprehensive survey. *Neurocomputing* **507**, 247–264 (2022).
43. Chen, C.-W., Betz, M. W., Fisher, J. P., Paek, A. & Chen, Y. Macroporous Hydrogel Scaffolds and Their Characterization By Optical Coherence Tomography. <https://home.liebertpub.com/tec>  
<https://www.liebertpub.com/doi/10.1089/ten.tec.2010.0072> (2010)

44. Parker, S., Coulman, S. & Birchall, J. CHARACTERISING THE WALL THICKNESS OF QUALI-V®-I CAPSULES. *6* (2021).
45. Palmer, S. J. The effect of temperature on surface tension. *Phys. Educ.* **11**, 119 (1976).
46. Bui, T., Frampton, H., Huang, S., R. Collins, I., Striolo, A. & Michaelides, A. Water/oil interfacial tension reduction – an interfacial entropy driven process. *Physical Chemistry Chemical Physics* **23**, 25075–25085 (2021).
47. Hardinge, P., Baxani, D. K., McCloy, T., Murray, J. A. H. & Castell, O. K. Bioluminescent detection of isothermal DNA amplification in microfluidic generated droplets and artificial cells. *Sci Rep* **10**, 21886 (2020).
48. Kerckhoffs, A., Bo, Z., Penty, S. E., Duarte, F. & Langton, M. J. Red-shifted tetra-ortho-haloazobenzenes for photo-regulated transmembrane anion transport. *Org. Biomol. Chem.* **19**, 9058–9067 (2021).
49. Chander, N., Morstein, J., Bolten, J. S., Shemet, A., Cullis, P. R., Trauner, D. & Witzigmann, D. Optimized Photoactivatable Lipid Nanoparticles Enable Red Light Triggered Drug Release. *Small* **17**, 2008198 (2021).
50. Hindley, J. W., Zheleva, D. G., Elani, Y., Charalambous, K., Barter, L. M. C., Booth, P. J., Bevan, C. L., Law, R. V. & Ces, O. Building a synthetic mechanosensitive signaling pathway in compartmentalized artificial cells. *Proc. Natl. Acad. Sci. U.S.A.* **116**, 16711–16716 (2019).
51. Marsh, D. *Handbook of Lipid Bilayers, Second Edition*. (CRC Press, 2013).
52. Hara, I., Kaneko, H. & Kato, A. The Critical Micelle Concentration of Phospholipids. *Journal of Japan Oil Chemists' Society* **9**, 407–409 (1960).
53. Truong, D., Puleo, J., Llave, A., Mouneimne, G., Kamm, R. & Nikkhah, M. Breast Cancer Cell Invasion into a Three Dimensional Tumor-Stroma Microenvironment. *Scientific Reports* **6**, (2016).
54. Hao, J., Zhao, W., Oh, J. M. & Shen, K. A Pillar-Free Diffusion Device for Studying Chemotaxis on Supported Lipid Bilayers. *Micromachines* **12**, 1254 (2021).
55. Freeman, E. C., Farimani, A. B., Aluru, N. R. & Philen, M. K. Multiscale modeling of droplet interface bilayer membrane networks. *Biomicrofluidics* **9**, 064101 (2015).

56. Rideau, E., Dimova, R., Schwille, P., R. Wurm, F. & Landfester, K. Liposomes and polymersomes: a comparative review towards cell mimicking. *Chemical Society Reviews* **47**, 8572–8610 (2018).
57. Inglesby, M. K. & Zeronian, S. H. Diffusion coefficients for direct dyes in aqueous and polar aprotic solvents by the NMR pulsed-field gradient technique. *Dyes and Pigments* **50**, 3–11 (2001).
58. Simpliciano, C., Clark, L., Asi, B., Chu, N., Mercado, M., Diaz, S., Goedert, M. & Mobed-Miremadi, M. Cross-Linked Alginate Film Pore Size Determination Using Atomic Force Microscopy and Validation Using Diffusivity Determinations. *JSEMAT* **03**, 1–12 (2013).
59. Reed, S. & Wu, B. M. Biological and mechanical characterization of chitosan-alginate scaffolds for growth factor delivery and chondrogenesis. *Journal of Biomedical Materials Research Part B: Applied Biomaterials* **105**, 272–282 (2017).
60. Wen, H., Xiao, W., Biswas, S., Cong, Z.-Q., Liu, X.-M., Lam, K. S., Liao, Y.-H. & Deng, W. Alginate Hydrogel Modified with a Ligand Interacting with  $\alpha 3\beta 1$  Integrin Receptor Promotes the Differentiation of 3D Neural Spheroids toward Oligodendrocytes in Vitro. *ACS Appl. Mater. Interfaces* **11**, 5821–5833 (2019).
61. Dvir-Ginzberg, M., Elkayam, T. & Cohen, S. Induced differentiation and maturation of newborn liver cells into functional hepatic tissue in macroporous alginate scaffolds. *FASEB j.* **22**, 1440–1449 (2008).
62. Mohandas, A., PT, S. K., Raja, B., Lakshmanan, V.-K. & Jayakumar, R. Exploration of alginate hydrogel/nano zinc oxide composite bandages for infected wounds. *Int J Nanomedicine* **10**, 53–66 (2015).
63. Ceccaldi, C., Bushkalova, R., Cussac, D., Duployer, B., Tenailleau, C., Bourin, P., Parini, A., Sallerin, B. & Girod Fullana, S. Elaboration and evaluation of alginate foam scaffolds for soft tissue engineering. *International Journal of Pharmaceutics* **524**, 433–442 (2017).
64. Balanč, B., Trifković, K., Đorđević, V., Marković, S., Pjanović, R., Nedović, V. & Bugarski, B. Novel resveratrol delivery systems based on alginate-sucrose and alginate-chitosan microbeads containing liposomes. *Food Hydrocolloids* **61**, 832–842 (2016).

65. Liu, M., Chen, S., Qi, X. bo, Li, B., Shi, R., Liu, Y., Chen, Y. & Zhang, Z. Improvement of wall thickness uniformity of thick-walled polystyrene shells by density matching. *Chemical Engineering Journal* **241**, 466–476 (2014).
66. Bei, Z., Jones, T. B. & Harding, D. R. Electric field centering of double-emulsion droplets suspended in a density gradient. *Soft Matter* **6**, 2312–2320 (2010).
67. Li, J., Lindley-Start, J., Porch, A. & Barrow, D. Continuous and scalable polymer capsule processing for inertial fusion energy target shell fabrication using droplet microfluidics. *Sci Rep* **7**, 6302 (2017).
68. Barlow, N. E., Kusumaatmaja, H., Salehi-Reyhani, A., Brooks, N., Barter, L. M. C., Flemming, A. J. & Ces, O. Measuring bilayer surface energy and curvature in asymmetric droplet interface bilayers. *Journal of The Royal Society Interface* **15**, 20180610 (2018).
69. Chung, S. H. & Kennedy, R. A. Forward-backward non-linear filtering technique for extracting small biological signals from noise. *J Neurosci Methods* **40**, 71–86 (1991).
70. Little, M. A., Steel, B. C., Bai, F., Sowa, Y., Bilyard, T., Mueller, D. M., Berry, R. M. & Jones, N. S. Steps and Bumps: Precision Extraction of Discrete States of Molecular Machines. *Biophysical Journal* **101**, 477–485 (2011).
71. El-Beyrouthy, J., Makhoul-Mansour, M. M. & Freeman, E. C. Studying the Mechanics of Membrane Permeabilization through Mechanoelectricity. *ACS Applied Materials & Interfaces* (2022)
72. Riquelme, G., Stutzin, A., Barros, L. F. & Liberona, J. A chloride channel from human placenta reconstituted into giant liposomes. *American Journal of Obstetrics & Gynecology* **173**, 733–738 (1995).
73. Haylock, S., Friddin, M. S., Hindley, J. W., Rodriguez, E., Charalambous, K., Booth, P. J., Barter, L. M. C. & Ces, O. Membrane protein mediated bilayer communication in networks of droplet interface bilayers. *Commun Chem* **3**, 1–8 (2020).
74. Sabet, S., Rashidinejad, A., Melton, L. D., Zujovic, Z., Akbarinejad, A., Nieuwoudt, M., Seal, C. K. & McGillivray, D. J. The interactions between the two negatively charged polysaccharides: Gum Arabic and alginate. *Food Hydrocolloids* **112**, 106343 (2021).

75. Thompson, B. R., Zarket, B. C., Lauten, E. H., Amin, S., Muthukrishnan, S. & Raghavan, S. R. Liposomes Entrapped in Biopolymer Hydrogels Can Spontaneously Release into the External Solution. *Langmuir* **36**, 7268–7276 (2020).
76. DeBruin, K. A. & Krassowska, W. Modeling electroporation in a single cell. I. Effects Of field strength and rest potential. *Biophys J* **77**, 1213–1224 (1999).
77. Jara-Quijada, E., Pérez-Won, M., Tabilo-Munizaga, G., González-Cavieres, L. & Lemus-Mondaca, R. An Overview Focusing on Food Liposomes and Their Stability to Electric Fields. *Food Eng Rev* **14**, 292–306 (2022).
78. Retelj, L., Pucihar, G. & Miklavcic, D. Electroporation of intracellular liposomes using nanosecond electric pulses--a theoretical study. *IEEE Trans Biomed Eng* **60**, 2624–2635 (2013).

---

## *Chapter IV*

# *From primary to tertiary emulsion microcapsules for tumour-related studies and potential compartmentalised drug screening capsules*

---

### **4.1. Chapter summary**

This chapter employs the work completed in Chapter II, towards the encapsulation of breast cancer cells using single emulsion microfluidic devices (SE-MDs), double emulsion microfluidic devices (DE-MDs) and triple emulsion microfluidic devices (TE-MDs). MCF-7 breast cancer cells demonstrated tumour formation in alginate and alginate-collagen type I capsules, as well as in the shell of oil-core capsules (OCCs) and encapsulated droplet interface bilayers (eDIBs). The applied methods and protocols including gelation, encapsulation, and capsule formulation and structure, provided a robust and well-preserved environment for 3D multicellular tumour spheroid (MCTS) growth. This was established by monitoring the proliferation of a model cell line (MCF-7) encapsulated in microgel beads and OCCs, through live/dead cell staining and a metabolic assay. The 3D cultures in OCCs were not influenced by the tested doxorubicin concentrations, while they proliferated in the presence of lysophosphatidylcholine (LPC) and also showed transferrin receptor expression. These capsules were presented as a simplified form of the proposed Droplet Incubator (DI) technology. The DI was introduced as a biocompatible eDIB screening capsule, which can potentially host interactions between living cells and artificial cell membranes. Finally, the progressive tumour growth within eDIB constructs and the preservation of enclosed DIBs was monitored and discussed.

## 4.2. Introduction

*In-vitro* monolayer (2D) cell cultures lack the *in-vivo* mimicking arrangement of cells that is evident in 3D cell culture models, and which is a determining factor of drug potency<sup>1</sup>. This is of significant importance in cancer research, due to the drug resistance adopted by cells when cultured as 3D multicellular tumour spheroids (MCTSs)<sup>2,3</sup>. Common 3D culture models for MCTSs include hanging drop<sup>4</sup>, low-attachment substrates<sup>5</sup>, spinning-cell cultures<sup>6</sup>, scaffolds<sup>7</sup>, hydrogels<sup>8</sup> and tumour-on-a-chip devices<sup>9,10</sup>. Droplet microfluidics is an alternative approach for producing cell-laden confined environments made of soft materials to host and assist the development of MCTSs<sup>11-13</sup>. Usually, this involves the encapsulation of single or multiple cells in an extracellular matrix (ECM), which supports cell-substrate interactions, in addition to cell-cell interactions. Alginate and collagen type I are natural polymers, which provide structural support and binding sites for cells, respectively, and are widely used as the ECM for the development of 3D cultures and MCTSs<sup>14,15</sup>. Droplet microfluidics and cell encapsulation have shown to partner well together, giving rise to high-throughput drug screening studies<sup>11,12,16</sup>. This is due to the reproducibility, precise volume control and adaptability of microfluidic platforms, to meet the experimental outcome.

Microfluidics also offers a controlled way to produce cell friendly complex architectures, including multilayer capsules<sup>17</sup> and multiple emulsions<sup>18</sup>. Multiple emulsion products from microfluidic technologies have applications in areas such as cell biology *in-vitro* systems<sup>18,19</sup>, synthetic biology<sup>20</sup>, and drug delivery<sup>21,22</sup>. The combination of droplet microfluidics and multiple emulsions has achieved the production of capsules with high-order architectures, utilised as bottom-up constructs for artificial cells<sup>23,24</sup>. Droplet interface bilayers (DIBs) are an easy and productive technique for bottom-up artificial cell membrane studies, since they model a critical element of a living cell, that being the phospholipid bilayer membrane<sup>25</sup>.

Protocells are usually built as enclosed environments capable to execute chemical reactions *in-situ*, although these systems are unable to be activated (energised) alone<sup>26</sup>. This was an appealing fact, that led researchers to develop hybrid models of artificial and living cells. Such hybrid model developed by Elani, *et al.* 2018, consisted of an encapsulated living cell within an artificial cell-like construct (vesicle) and demonstrated a synergistic enzymatic reaction, initiated by the cell's ability to hydrolyse lactose<sup>27</sup>. An earlier study by Godoy-Gallardo, *et al.* 2017, encapsulated functional liposomes within biological cells and demonstrated their ability to replace dysfunctional organelles<sup>28</sup>. Both aforementioned studies, are characterised as 'embedded hybridisation' methods, where either living or artificial entities are encapsulated inside the other<sup>29</sup>. Elani, *et al.* 2021, presented two additional categories of hybrid models, including 'population hybridisation' and 'network hybridisation'<sup>29</sup>. The former hybridisation approach involves separate populations of artificial and living cells, able to communicate through information exchange, while the latter utilises a network which hosts artificial cells and living cells capable of physically interacting with each other. With the combination of

‘network hybridisation’ and 3D bioprinting of DIBs, Bayley and colleagues have shown the significance of tissue-like artificial networks, with potential applications in protein synthesis<sup>30</sup>, communication with the environment through protein pores<sup>31</sup>, and the formation of biological tissues<sup>32</sup>.

Other bottom-up multiple emulsion models have been developed as artificial cell chassis by integrating DIB and hydrogels<sup>23</sup>. By entrapping DIBs within hydrogels (i.e., encapsulated droplet interface bilayers or eDIBs), a complex can be established for hosting artificial membranes and an ECM hydrogel that supports 3D cell culture. Tailored and programmable entities like microfluidically formed eDIBs may have applications in organoid formation, drug screening, as well as potential hybrid models for interplay between live cells and artificial cells or membranes, though their co-culture.

This chapter initially reports the encapsulation and proliferation of a model cell line (MCF-7 breast cancer cells) in single and double emulsion, alginate-collagen type I hydrogel capsules, generated using 3D-printed microfluidic devices. Additionally, MCTSs formed in oil-core capsules (OCCs) were treated with doxorubicin, egg lysophosphatidylcholine (LPC) and transferrin conjugates, to assess the anticancer drug response, micellar susceptibility and transferrin receptor availability, respectively. Finally, a unique cell culture approach was explored, involving the formation of triple emulsion, biocompatible eDIB capsules to facilitate tumour spheroid growth. This hybrid model is envisioned to be utilised as a platform for investigating the communication of living cells and artificial cells, and potentially be used as a drug screening 3D culture model, which is defined here as the ‘Droplet Incubator’.

## **4.3. Materials and Methods**

### **4.3.1. Cell Culture**

Epithelial human breast cancer cells, MCF-7, were obtained from American Type Culture Collection (ATCC-HTB-22). Cells were maintained in Roswell Park Memorial Institute (RPMI) 1640 (Thermofisher) medium, including 10 % fetal bovine serum (FBS) (Thermofisher) and 1 % Penicillin-Streptomycin (100 X, 50 mg/ml). Prior to any experiments, MCF-7 cells were grown in tissue culture treated flasks. The cell culture media was exchanged every 2-3 days and when the culture reached 80-90 % confluency, cells were trypsinised using Trypsin-Ethylenediaminetetraacetic acid (EDTA, 0.25 %) (Thermofisher) for further culture or use in experiments. MCF-7 cells used for the experiments had passage numbers between 19 and 23. In the following sections, RPMI is defined as the RPMI culture medium including additives (10 % FBS and 1 % P/S).

### **4.3.2. Microfluidic device fabrication**

The 3D FFF-printed microfluidic devices utilised for cell encapsulation experiments, included the single emulsion microfluidic device (SE-MD), double emulsion microfluidic device (DE-MD) and triple emulsion microfluidic device (TE-MD), which were developed in Chapter II - Sections 2.3. & 2.3.2.

### **4.3.3. Reagent preparation for microfluidic experiments**

All materials were purchased from Merck/Sigma-Aldrich, unless otherwise stated. Alginic acid from brown seaweed was dissolved overnight using magnetic stirring in phosphate buffered saline (PBS) or 0.9 % w/v NaCl, at a concentration of 2.5 % w/v (stock alginate solution). The alginate solution was autoclaved prior to the experiment and was used within a week, if kept sterile. Rat-tail type I Collagen of concentration 5 mg/ml and 10 X Minimum Essential Medium (MEM) were purchased from First Link, UK. Collagen neutralisation was achieved using 10 X MEM and sterile filtered 0.1 M NaOH (according to supplier instructions), prior to microfluidic reagent loading.

Mineral oil suitable for embryo culture was used as purchased in sterile condition or filtered using vacuum filters. Partial on-chip gelation was achieved using the Ca<sup>2+</sup>-infused nanoemulsion as described in Chapter II - Section 2.3.3. Hexadecane (Hex), silicon oil (AR20), SPAN 80, CaCl<sub>2</sub>, NaCl and NaOH solutions were sterile filtered using 0.2 µm filters. Dioleoyl-phosphatidylcholine (DOPC)-containing hexadecane oil phase (12.5 mg/ml) and dipalmitoyl-phosphatidylcholine (DPPC) vesicles in alginate, were prepared as described in Chapter II - Section 2.3.5., although the buffer was replaced with PBS. The inner aqueous cores of the cell-laden encapsulated droplet interface bilayers (eDIBs) consisted of 200 µM sulforhodamine B (sulfb) in PBS, which was filtered through a 0.2 µm filter.

Transferrin-alexa488 (Tf-488), epidermal growth factor-alexa488 (EGF-488) and Doxorubicin hydrochloride ( $M_w=543.52$  g/mol) were purchased from Fisher Scientific. Tf-488 and EGF-488 were supplied by a collaborator (Pharmacy Department). Doxorubicin (DOX) powder was dissolved with deionised water to a stock concentration of 10 mg/ml. Stock concentration of 4.96 mM lysophosphatidylcholine (LPC) was prepared in PBS as described in Chapter II - Section 3.3.

#### 4.3.4. Microfluidic setup and production of cell-laden capsules

The operation of the microfluidic setup was described in Chapter II - Sections 2.3.2. and the operation of each microfluidic devices (SE-MD, DE-MD, TE-MD), is described in Sections 2.3.3., 2.3.4., 2.3.5., of the same chapter. The operation of these devices was modified to suit cell encapsulation, meaning that, aseptic techniques were followed. To sterilise the devices and eliminate possible contamination, the tubing and microfluidic devices were overflowed using 70 % ethanol for a minimum of 10 minutes, which was washed off thoroughly with sterile PBS.

#### 4.3.5. Cell counting and encapsulation matrix preparation

Once the cell culture had reached 80-90 % confluency, cells were trypsinised, centrifuged and resuspended in fresh culture media (cell suspension). Subsequently, 100  $\mu$ l from the cell suspension was transferred to an empty 1 ml vial. Then, a Via1-cassette (Thermofisher) was used immediately to aspirate the volume of cell suspension required for cell counting test with the NucleoCounter NC-200 (Thermofisher). After cell counting, an appropriate volume from the cell suspension was transferred and mixed with the cell encapsulation matrix, to obtain a final cell density of  $1 \times 10^6$  viable cells/ml.

**Table 4. 1** the encapsulation matrices and the corresponding microfluidic device utilised for each experiment. SE-MDs were utilised to produce 1 % alginate (ALG) and 1 % alginate, ~ 1 mg/ml collagen type I (ALGCOL) cell-laden microbeads. The DE-MDs generated alginate-collagen type I (ALGCOL) oil-core capsules (OCCs), with the inner oil phase consisting of 2:1 Hex:AR20. The cell-containing shell of ALGCOL OCCs consisted of 1 % alginate and ~ 1 mg/ml collagen. Finally, TE-MDs were utilised to encapsulate cells in the shell of eDIBs using the *Final eDIB protocol*, from Chapter II - Section 2.4.5.2.3.. Briefly, the inner aqueous cores of the eDIBs consisted of 200  $\mu$ M sulfB in PBS, which in turn were encapsulated in a 12.5 mg/ml DOPC in 100 % Hex and this was emulsified by a mixture of 1.5 % alginate, ~ 1 mg/ml collagen type I and 0.5 mg/ml DPPC vesicles (vesALGCOL eDIBs). In the attempt to produce cell-laden eDIBs, OCCs were also produced using the TE-MDs. These OCCs and eDIBs with no clear aqueous cores (after possible merging with hydrogel shell), were utilised for subsequent drug treatments and referred to as vesALGCOL OCCs.

ALG and ALGCOL capsules were produced using flow rates of 30 ml/hr and 5 ml/hr for the gelling nanoemulsion and the cell encapsulation matrix phase, respectively. The flow rates for DE-MDs were approximately 0.2 ml/hr, 5 ml/hr and 15 ml/hr, for the oil mixture, hydrogel phase and gelling

emulsion, respectively. Finally, the cell-laden eDIBs and OCCs were produced by TE-MDs with flow rates shown in **Table 3.1** from Chapter III - Section 3.4.1..

**Table 4. 1: Encapsulation matrices (including polymer and cell density) and the corresponding microfluidic device utilised for the experiment.**

	Encapsulation matrix	Microfluidic device
<b>ALG</b>	1 % alginate	SE-MD
	$1 \times 10^6$ cell/ml	
<b>ALGCOL</b>	1 % alginate	SE-MD
	1 mg/ml collagen	DE-MD (OCCs)
	$1 \times 10^6$ cell/ml	
<b>vesALGCOL</b>	1.5 % alginate	TE-MD (OCCs and eDIBs)
	1 mg/ml collagen	
	0.5 mg/ml DPPC vesicles	
	$1 \times 10^6$ cell/ml	

#### 4.3.6. Culturing the cell-laden capsules

All types of capsules produced and collected in the CaCl<sub>2</sub> bath, were carefully pipetted into a cell strainer and washed thoroughly with PBS. Subsequently, the capsules were transferred into a sterile petri dish using pre-warmed RPMI culture media. ALG, ALGCOL capsules and ALGCOL OCCs were cultured in separate T-75 tissue culture flasks. The flasks were incubated at 37 °C, 5% CO<sub>2</sub> and the culture medium was replaced every 2-3 days. Cell-laden vesALGCOL OCCs and eDIB capsules were cultured in petri dishes or tissue culture 6-well plates. Bright field images throughout their culture were captured using conventional inverted microscopes (Olympus or GXM-XDY-2).

#### 4.3.7. Cell proliferation assays and drug treatments

##### 4.3.7.1. MCF-7 culture in ALG, ALGCOL and ALGCOL OCCs

The proliferation of cells in ALG, ALGCOL and ALGCOL OCCs was assessed using the CellTiter Blue (CTB) assay (Promega) on Days 1, 4, 8 and 11. On Day 0 (encapsulation day), the cell-laden capsules were transferred into a 24-well plate with three replicates for each timepoint and 1 ml final volume of culture media. The test began by adding 100 µl of the blue reagent to each well with the cell-laden microgels, including the blanks (no cells, only RPMI). The blue reagent was incubated with the microgels at 37 °C, 5% CO<sub>2</sub> for 1.5 hours. After incubation, three replicates were prepared by transferring 100 µl of the incubated media under test, to three wells of a 96-well plate (n=3 per one incubated well). The CTB assay is based on the conversion of resazurin by viable cells into fluorescent

resorufin, whose fluorescence was recorded (Ex = 545 nm, Em = 600 nm, Gain 1000) using the microplate reader (Clariostar).

#### **4.3.7.2. DOX<sub>IC50</sub> and LPC<sub>IC50</sub> determination of MCF-7 2D cultures**

The CTB assay was used to determine the half maximal inhibition concentrations (IC<sub>50</sub>) of MCF-7 breast cancer cells exposed to DOX and LPC. To do this, MCF-7 cells were cultured in a 96-well plate, with seeding density of  $5 \times 10^3$  viable cells/well and final RPMI volume of 200  $\mu$ l. Cells were incubated for 24-36 hours, or until confluency reached approximately 20 %. After removing the culture media, cells were washed with PBS and treated with 200  $\mu$ l of LPC in RPMI at final concentrations of 1  $\mu$ M, 10  $\mu$ M, 100  $\mu$ M, 300  $\mu$ M and 1000  $\mu$ M, while other cells were treated with 200  $\mu$ l of DOX in RPMI at final concentrations of 0.01  $\mu$ M, 0.05  $\mu$ M, 0.21  $\mu$ M, 0.96  $\mu$ M, 4.37  $\mu$ M and 20  $\mu$ M. Cells were incubated with LPC or DOX concentrations for 72 hours. The control of these experiments consisted of MCF-7 cultured cells in RPMI only. For the CTB assay here, 40  $\mu$ l of the blue reagent was added to each well containing 200  $\mu$ l of treated and untreated culture media. The plate was incubated for 1.5 hours at 37 °C, 5% CO<sub>2</sub>, and then the cell proliferation was recorded using the microplate reader.

#### **4.3.7.3. DOX and LPC treated 3D cultures in vesALGCOL OCCs**

On the 15<sup>th</sup> day of MCF-7 3D culture in vesALGCOL OCCs, the capsules were washed with PBS and transferred to a new well plate, with 1 ml final volume of culture media. On this day, the OCCs were treated with LPC and DOX using the materials and concentrations described in Section 4.3.7.2.. Cell proliferation of treated and untreated OCCs (control) was assessed on Days 1, 3 and 5, after the addition of the drug (Day 0, DOX or LPC), by following the same CTB protocol from Section 4.3.7.1..

### **4.3.8. Tf-488 ligand treated MCF-7 cultures**

#### **4.3.8.1. 2D culture**

MCF-7 cells were monolayer cultured in a 24-well plate, with seeding density of  $40 \times 10^3$  viable cells/well, for 48 hours. Then, the 2D cell cultures were washed with PBS and incubated for 30 minutes with serum free RPMI media (no FBS, no P/S), also referred to as SFM. This incubation period in SFM, was defined as the starvation period. Subsequently, the well plate was placed on ice for 5 minutes, and then the SFM media was replaced with 1 ml of 25  $\mu$ g/ml Tf-488 in SFM. The cells were incubated for 30 minutes with Tf-488, then washed with PBS and imaged in phenol red-free RPMI, using the EVOS system (with the GFP cube). For comparison, 1 ml of 500 ng/ml EGF-488 in SFM, was also added after the starvation period, and as a control cells were incubated with RPMI containing additives.

#### **4.3.8.2. 3D culture in OCCs**

On Day 21 of culture, vesALGCOL OCCs were washed with PBS and transferred to a new well plate with SFM. The OCCs were incubated at 37 °C, 5% CO<sub>2</sub> for either 30 minutes or 90 minutes with SFM. After each starvation duration, the well plates were placed on ice for 2-3 minutes. Then, the SFM was replaced by 25 µg/ml Tf-488 in SFM. OCCs were incubated with the transferrin solution for 15 minutes and then washed thoroughly with PBS. Imaging of the vesALGCOL OCCs was performed using the EVOS system, while keeping them in phenol red-free RPMI.

#### **4.3.9. Live/dead Cytotoxicity Assay**

Live and dead cells were stained using fluorescent Calcein-acetoxymethylester (calcein-AM) and Ethidium Homodimer-1 (EthD-1), respectively, which are the components of the LIVE/DEAD™ Viability/Cytotoxicity Kit, for mammalian cells (ThermoFisher). A staining stock solution was prepared by adding 5 µl of Calcein-AM and 20 µl of EthD-1 to 10 ml PBS. Cell-laden capsules were washed with PBS and incubated with 200-300 µl of staining solution at room temperature for minimum of 25 minutes before imaging. Cell and spheroid staining were imaged using a fluorescent inverted microscope (Olympus or GXM-XDY-2), with either a mercury lamp or a CoolLED illumination system. Additional imaging of stained cells was performed using Light Sheet Fluorescent Microscopy (LSFM) (Zeiss Lightsheet Z.1).

#### **4.3.10. Light Sheet Fluorescent microscopy (LSFM)**

For LSFM, all capsules were embedded in 1 % low temperature melting agarose in PBS. All equipment and agarose solutions were kept at 37 °C, to avoid unwanted gelation. Cell and spheroid-laden capsules were stained as mentioned in Section 4.3.9. After incubation of the capsules with the live/dead staining solutions, the excess PBS was removed and replaced with 500-1000 µl of 1% warm agarose solution. Glass capillaries of the appropriate inner diameter and plungers with Teflon tips were used to aspirate capsules in the agarose solution. Prior to use, the capillaries were sterilised with 70 % ethanol and washed with PBS. The microscope's chamber in **Figure 4. 1** was filled with PBS, prior to loading the capillary with the sample. Z-stack images (slices) were obtained for the green and red fluorescence using 488 nm and 561 nm lasers respectively, accompanied by the Laser Blocking filter (LBF) 405/488/561/640. The filters used for the emission selection were BP 505-545 for the green channel and BP 575-615 for the red channel. Bright field images were also recorded.

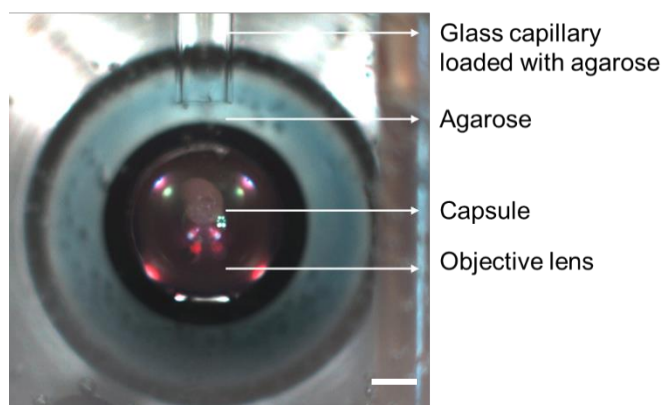


**Figure 4. 1: Light sheet fluorescent microscope sample chamber.** The camera's perspective for positioning the sample capillary within the PBS filled chamber. The glass capillary holds the agarose with the sample (capsule) in front of the objective lens. Scale bar: 2 mm.

#### 4.3.11. EVOS fluorescent imaging

eDIBs with cultured MCTSs were stained using the live/dead assay (Section 4.3.9) and followed fluorescent imaging using EVOS M7000 Cell Imaging System. The eDIBs were imaged in a dish with a small volume of PBS. The sulfB cores were imaged using Texas Red light cube (Ex = 585/29 nm, Em= 628/32 nm). Live cells were imaged with the GFP light cube (Ex = 470/22 nm, Em= 525/50 nm), but no imaging of red cells was performed (RFP light cube was not supplied). Bright field images were also captured.

#### 4.3.12. Statistical Analysis

All microscopic images were analysed using ImageJ (Fiji). Any green fluorescence analysis was conducted based on the thresholding method provided by ImageJ. When suitable, two-way ANOVA test was performed to obtain the significance of results. The statistical analysis was carried out in Microsoft Excel or GraphPad Prism 9. Uncertainties and error bars are described by the standard error of mean (SEM), unless otherwise stated and  $p$ -values (significance) was presented as  $*p \leq 0.05$ ,  $**p \leq 0.005$ ,  $***p \leq 0.0005$ .

## 4.4. Results and Discussion

Often, cell-laden alginate capsules involving chelating agents (e.g. Ethylenediaminetetraacetic acid, EDTA or calcium carbonate,  $\text{CaCO}_3$  particles) are gelled in acidic pH<sup>33,34</sup>. To avoid the introduction of such potentially cytotoxic agents and operation at low pH, an alternative gelation method was employed as part of this thesis. The nanoemulsion gelation method in this thesis was influenced by Agarwal, *et al.* 2017, who utilised  $\text{Ca}^{2+}$ -infused mineral oil for the gelation of collagen-alginate, core-shell capsules encapsulating breast cancer cells<sup>16</sup>. This gelation method, requires the addition of emulsion stabilising surfactants (SPAN 80), which can directly affect the shape of the alginate microbeads, as demonstrated by Liu, *et al.* 2017<sup>35</sup>. The crosslinking of the alginate and collagen, facilitated the immobilisation of MCF-7 breast cancer cells in single, double, and triple emulsion soft hydrogel capsules, leading to 3D multicellular tumour spheroid (MCTS) formation. MCF-7 breast cancer cells constitute a robust cell line with no special culturing requirements, and it is widely used in cancer related studies, hence its selection as an exemplar model cell line in this chapter.

### 4.4.1. Microfluidically produced cell-laden single emulsion microgels

As presented in Chapter II, Section 2.4.3.2., the flow rate ratio of 30:5 ml/hr, produced cell-free microgels of diameter  $\sim 513 \mu\text{m}$ . By introducing the dense cell suspension ( $1 \times 10^6$  cells/ml) to the same single emulsion microfluidic device (SE-MD) regime, cell-laden capsules of alginate (ALG) (**Figure 4. 2A(i)**) and alginate-collagen type I (ALGCOL) (**Figure 4. 2A(ii)**) were generated with diameters approximately  $476.9 \mu\text{m} \pm 2.6$  and  $492.1 \pm 2.9 \mu\text{m}$ , respectively. This diameter reduction compared to the cell-free system, was attributed to three factors, including, the changes in the surface tension and viscosity of the dispersed fluid phase and the possible size reduction of the 3D-printed droplet-forming junction<sup>36,37</sup>. The cell suspension may increase the viscosity ( $\mu$ ) of the dispersed phase<sup>38,39</sup>, and according to Nekouei and Vanapalli, 2017, reported reduced droplet diameter with high capillary numbers ( $C_a = \frac{\mu U}{\gamma}$ ), due to the high viscosity,  $\mu$ <sup>36</sup>.

Also, the cell suspension introduced some flow irregularities, as determined by plotting and comparing the diameter distribution of cell-laden to the cell-free microgels. According to Kalantarifard, *et al.* 2021, pressure variations at the inlet phases and droplet-forming junctions, will influence the flow rate ratio and hence the monodispersity<sup>37</sup>. The diameter distribution of ALG and ALGCOL capsules, shown in **Figure 4. 2B(i)-(ii)**, was broader than cell-free ALG capsules from Chapter II, Section 2.4.3.2.. The broad diameter distribution and  $\text{CV} > 3 \%$  indicated that the SE-MD produced polydisperse cell-laden ALG and ALGCOL microcapsules. The variance between cell-laden ALG and ALGCOL microcapsule populations appeared to be insignificant **Figure 4. 2C**, although, when compared to the cell-free ALG microcapsules the variance was significant (\* $p < 0.05$ ).

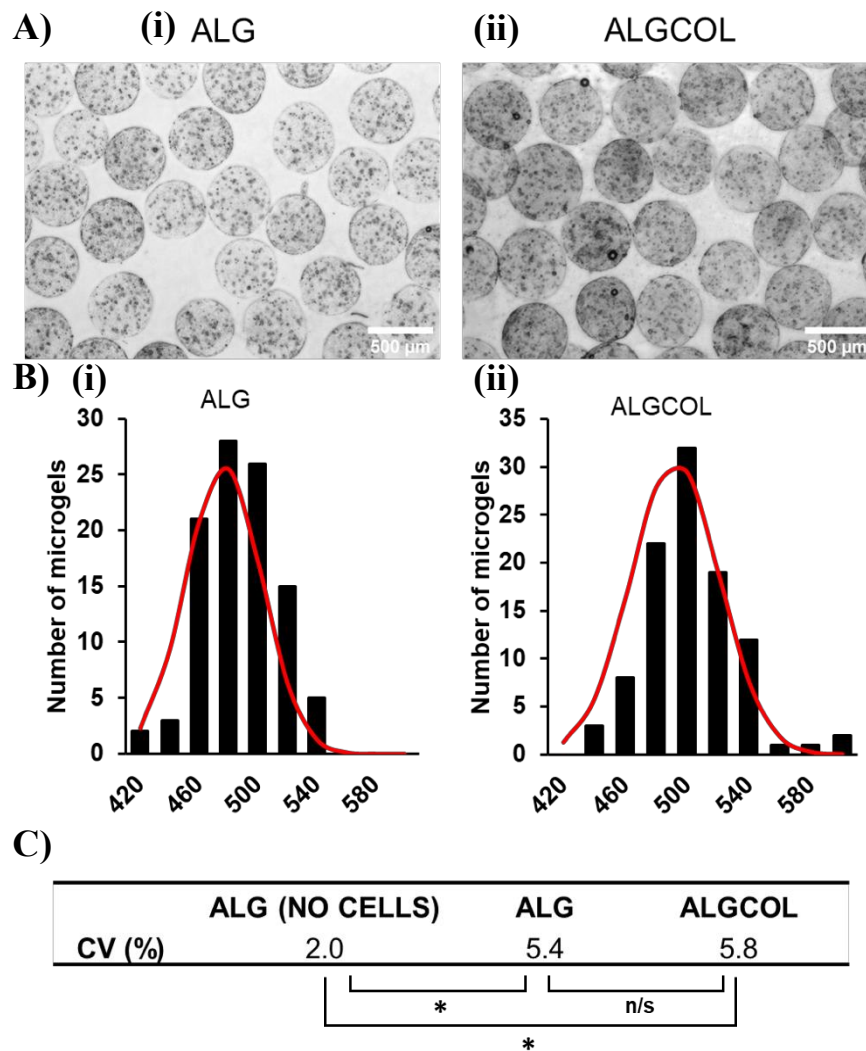


**Figure 4. 2: Analysis of the polydisperse cell-laden ALG and ALGCOL microgels.** A) Bright-field images of (i) ALG and (ii) ALGCOL microgels encapsulating MCF-7 breast cancer cells (scale bar is 500  $\mu\text{m}$ ). B) The diameter distribution of ( $n=100$ ) (i) ALG and (ii) ALGCOL microgels. The red line shows the normal distribution for each population. C) Comparison of the coefficient of variation (CV) % between cell-free ALG microgels, and cell-laden ALG and ALGCOL microgels, showing the loss of the monodispersity when cells were introduced to the dispersed phase. Statistical analysis for the diameter distribution was performed using the F-test and showed significant variations between the cell-laden and the cell-free populations.

#### 4.4.2. ALG, ALGCOL and ALGCOL OCCs

##### 3.3.1.3. MCF-7 culture and spheroid formation in ALG, ALGCOL and ALGCOL OCCs

The MCF-7 breast cancer cells in ALG, ALGCOL and ALGCOL oil-core capsules (OCCs), were cultured up to 19 days, as shown by the bright field images in **Figure 4. 3**. The diameter of MCF-7 cells before encapsulation, was approximately 14-16  $\mu\text{m}$ . The biobank from which the MCF-7 cells were supplied from, and other reports claim a doubling time between 24-29 hours for 2D cultured MCF-7 cells<sup>40,41</sup>, although Lovitt, *et al.* 2018, reported a doubling time reduction in 3D cultured MCF-7 cells<sup>42</sup>. Such proliferation rate hindering was also noticed here, since by day 4, the cells only formed clusters of 2-3 cells across all capsules. The MCF-7 cells eventually formed tumour spheroids attaining diameters as large as 200  $\mu\text{m}$  longitudinal diameter (day 19); however, the spheroid size was variable across the different types of capsules.

The MCTSs throughout the culture period, appeared to have broad size distribution in all types of capsules. This was a reoccurring phenomenon, which was attributed to the low initial cell density with respect to the hydrogel area and possible encapsulation of cell clusters instead of single cells, which would proliferate faster into clusters, than single cells<sup>3,43,44</sup>. Subsequently, the tumour area of MCF-7 spheroids was measured throughout the culture period. It was preferred to measure the area of the spheroids instead of the diameter, due to the variable shapes and sizes of the developed tumours (spherical or oblate). Oblate tumour spheroids were reported to be formed due to mechanical stresses by the surrounding hydrogel<sup>45</sup>, but generally different culture conditions (culture medium, cell density, cell type) and techniques for MCTS formation, yield different spheroid morphologies<sup>3</sup>.

The area of 50 spheroids per capsule type, was measured on day 6, 8, 11 and 18 (**Figure 4. 4A&B**). From **Figure 4. 4A** and accompanied statistical analysis, it was clear that the proliferation of MCF-7 cells into spheroids, benefited by the presence of collagen, either in single emulsion hydrogel beads or double emulsion OCCs. By day 6, ALGCOL OCCs, displayed significant differences indicating that the cells were growing slower than in ALG and ALGCOL capsules (**Figure 4. 4A&C**). Moreover, all the hydrogel capsules facilitated MCF-7 proliferation over the first 8 days, but after this period, the tumour spheroids in ALG and ALGCOL capsules proliferated insignificantly. ALGCOL OCCs proliferated less than the single emulsion capsules by day 8, but their proliferation was remarkably higher significantly ( $p < 0.0001$ ) from day 11 onwards. **Figure 4. 4B**, reveals that the area distribution of the MCTSs increased over time, which profile was consistent with other cell lines too<sup>46</sup>. By day 18, the MCTSs of areas approximately 6700  $\mu\text{m}^2$ , 8100  $\mu\text{m}^2$  and 15300  $\mu\text{m}^2$ , had developed in ALG, ALGCOL and ALGCOL OCCs, respectively.

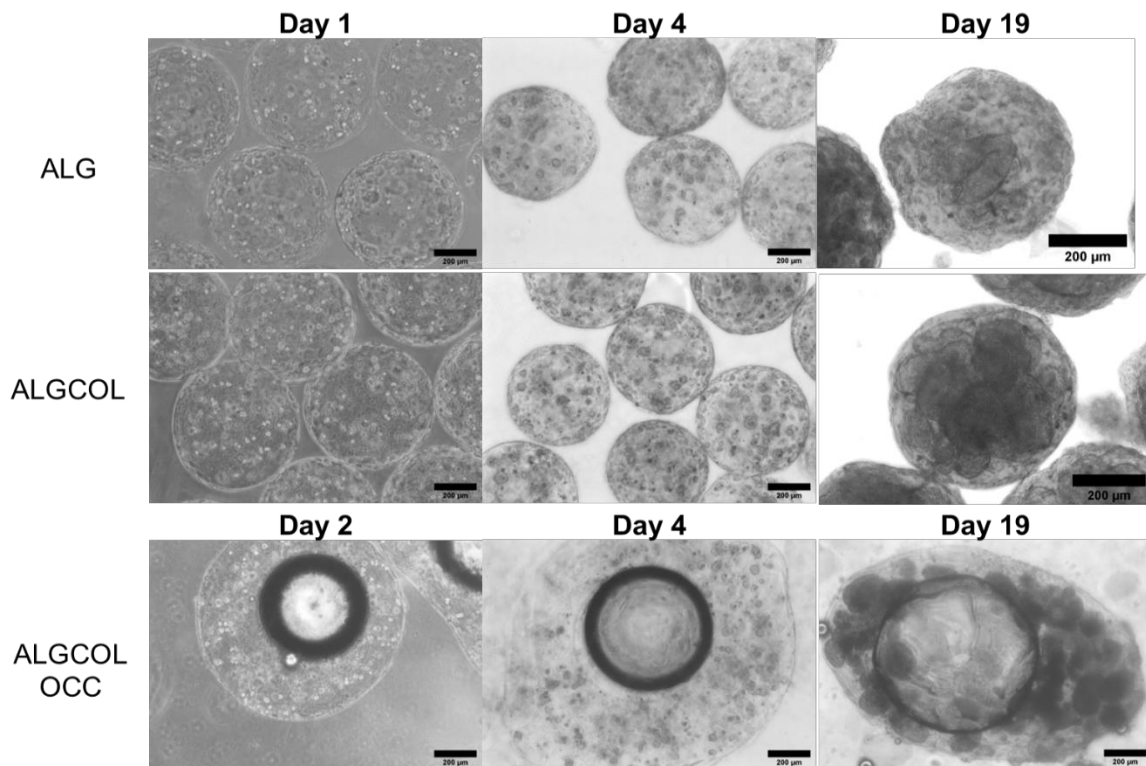


**Figure 4. 3: Bright Field images of MCF-7 cells in ALG, ALGCOL and ALGCOL OCC at different timepoints, leading to tumour spheroid formation.** MCF-7 cells show no clear differences in their proliferation in the first 4 days of culture in the microgel capsules, irrespective of the emulsion order (single or double emulsion) and hydrogel composition. However, the area covered by the MCTSs formed by Day 19, is considerably higher in collagen capsules (ALGCOL and ALGCOL OCCs), than alginate only (ALG). All scale bars indicate 200 µm.

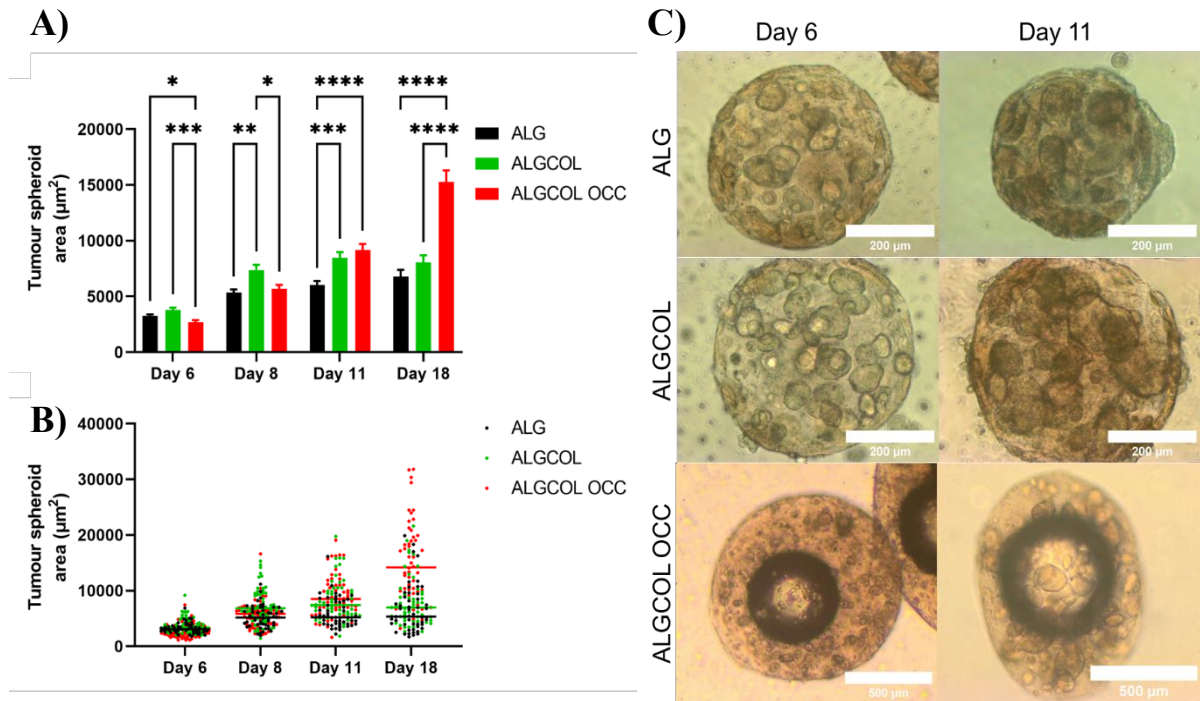


**Figure 4. 4: MCF-7 tumour spheroid area over time starting from the 6th day of culture in ALG, ALGCOL and ALGCOL OCCs. A)** Average tumour area over time across the three types of capsules. On Day 6, cells are still slow growing and adapting to the environment. MCF-7 cells proliferated more over time in ALGCOL than ALG capsules, as shown by the increasing significant values; however, no significant changes were shown on Day 18. The average area of the MCTSs in ALGCOL OCCs on Day 18 appeared to be approximately twice the area of MCTSs in single emulsion microgels ( $n=50$  per timepoint and capsule type). Data shown as mean  $\pm$  SEM. Two-way ANOVA test was performed where,  $*p \leq 0.05$ ,  $**p \leq 0.005$ ,  $***p \leq 0.0005$ ,  $****p \leq 0.00001$ . **B)** Scatter plot with measured tumour spheroid areas across all timepoints and microgels ( $n=50$  per timepoint and capsule type). Over time, the data spread out across the y-axis, than the earlier timepoint, with ALGCOL OCCs showing the most broad MCTS area distribution by Day 18. The horizontal lines note the median of each population. **C)** Bright field images of ALG, ALGCOL and ALGCOL OCC capsules showing MCF-7 tumour spheroids on days 6 and 11. ALG and ALGCOL images have scale bars of 200  $\mu\text{m}$  and ALGCOL OCC images have scale bars of 500  $\mu\text{m}$ .

### 3.3.1.4. CellTiter Blue (CTB) Metabolic Assay of MCF-7 cells

The CTB assay detects the fluorescent resorufin, which was produced by the conversion of the resazurin in the assay's agent by viable cells. The average number of plated capsules per well of ALG, ALGCOL and ALGCOL OCCs were 67, 44 and 4, respectively. **Figure 4. 5A** displays the proliferation profile over time, for ALG (n=67), ALGCOL (n=44) and ALGCOL OCCs (n=4). The number of samples (n) indicates the average number of capsules in a single well. It appeared that the MCF-7 proliferation expressed in ALG and ALGCOL matrices was similar, with the lag (Day 1-4) and log (Day 4-8) phases of the cells lasting approximately the same time. The lag phase of MCF-7 cells in a 2D culture lasts for approximately 2 days, where the cells adapt in the culturing conditions, but do not divide<sup>40</sup>. Although in the current 3D culture work, the lag phase lasted for 4 days. During the log phase, the MCF-7 cells proliferated exponentially and reached a plateau after approximately 4 days (stationary phase). Towards the late log phase (Day 8), the assay revealed an increased proliferation by the cells in ALGCOL capsules, which confirms the benefits of collagen type I in the extracellular matrix (ECM). These proliferation profiles were in agreement with other literature that reported mathematical models for MCTS growth kinetics<sup>3,47</sup>, and with earlier spheroid area measurements (**Figure 4. 4**).

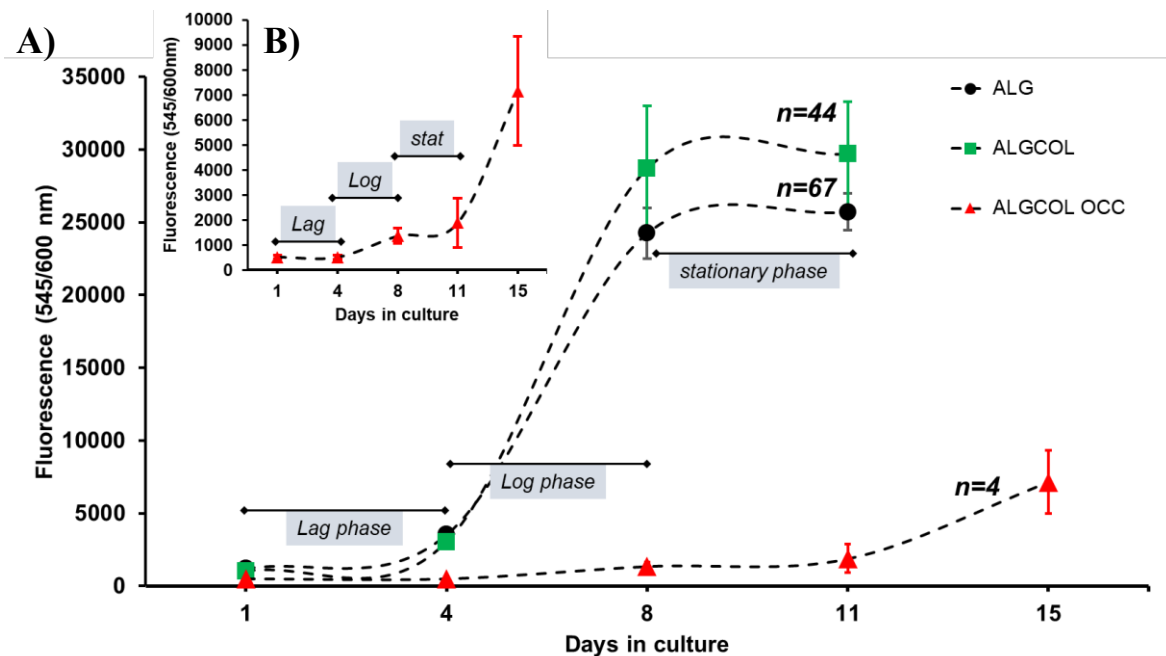


**Figure 4. 5: Graphs of the proliferation profiles of MCF-7 in ALG, ALGCOL and ALGCOL OCCs determined by the CTB metabolic assay. A)** The proliferation of tested samples over 11 days (ALG (n=67),ALGCOL (n=44)) or 15 days (ALGCOL OCC (n=4)). Cell growth phases (lag, log and stationary) were noted on the graph. MCF-7 show similar proliferation in ALG and ALGCOL capsules, with cells reaching an equilibrium around Day 11. ALGCOL OCC profile was similar, but with significantly lower fluorescence output, due to the considerably lower number of samples tested (n) per timepoint. The floating ability of OCCs allowed the assay to be extended minimum of four more days. **B)** A more detailed inspection of the proliferation profile of the MCF-7 cells cultured in ALGCOL OCCs (up to Day 11), with lag, log and stationary phases noted. OCCs continued to proliferate after Day 11 (stationary phase). Error bars indicate the  $\pm$ SEM.

It is likely that the low fluorescence signal detected in ALGCOL OCCs, was due to the small sample number ( $n=4$ ), however this was inconclusive. The subplot in **Figure 4. 5B**, shows the cell growth profile of MCF-7 cells with a clear lag, log and stationary phase. It appears that the cells continued to proliferate, after the 11<sup>th</sup> day of culture, which was the end of the stationary phase. This permitted for the prolonged metabolic assay for MCF-7 in ALGCOL OCCs, unlike the ALG and ALGCOL capsules, which migrated at the bottom of the culture plate, after the 11<sup>th</sup> day of culture (*Appendix 4.A*). This occurred because the OCCs were floating in the culture media, keeping any cells from migrating and proliferating on the culture plate, while the ALG and ALGCOL microbeads were in contact with the bottom of the plate. Therefore, the CTB assay was not performed for cell-laden ALG and ALGCOL capsules, after this undesired migration had occurred.

### **3.3.1.5. LSFM live/dead cell staining and intensity quantification**

Calcein-AM permeates the plasma membrane of viable cells, where esterase activity converts it to fluorescent calcein. EthD-1 penetrates mammalian cells with membranes of reduced integrity, binds to free DNA fragment, and when excited, it emits red fluorescence. Light Sheet Fluorescence Microscopy (LSFM) was performed on days 1 and 15 of culture, to assess the MCF-7 cell viability and tumour growth in ALG, ALGCOL and ALGCOL OCCs (**Figure 4. 6A**). One day after encapsulation (Day 1), green fluorescence emitted by viable cells was dominant in the capsules, but a small number of dead cells was indicative of possible overnight cell death. This negligible degree of cell death was not quantified in any way and was associated to stresses exerted during cell suspension handling or encapsulation, or due to prolonged imaging in non-cell culture conditions<sup>48</sup>.

After two weeks of culture, the hydrogel capsules were stained and imaged, showing formed tumours of various sizes and morphologies. The green fluorescence intensity from Day 1 and 15 was quantified across the capsules, using the thresholding method in ImageJ (**Figure 4. 6B**). According to the statistical analysis, there were no significant differences between the two timepoints for the viable cells in ALG and ALGCOL capsules. On the contrary, ALGCOL OCCs had significantly higher fluorescence on Day 15 compared to Day 1, as well as compared to Day 15 ALG and ALGCOL capsules. The 3D MCTS formation in ALG and ALGCOL microgels by Day 15 was clear; however, according to the intensity measurement, this was insignificant when compared to Day 1.

MCF-7 cells are human mammary epithelial cells and present a model cell line widely used to study luminal breast cancer and drug responses<sup>49,50</sup>. The 3D culture of these cells in ALG, ALGCOL and ALGCOL OCCs, formed MCTSs with a hollow lumen, as indicated in **Figure 4. 7A**. The fact that the lumen was not stained suggests that no live or dead cells were present, but only a hollow space. The formation of a hollow lumen in MCF-7 spheroids, was previously demonstrated in alginate-collagen hydrogels<sup>51</sup>, and scaffold-free systems<sup>52,53</sup>. Swaminathan, *et al.* 2019, showed that different cell lines and compositions of hydrogels exhibited different MCTS morphology, with MCF-7 cells in alginate-

collagen type I capsules forming irregular sized tumours after 5-6 days<sup>51</sup>. The fluorescent signals of cross-sectional slices near the middle of the tumour spheroids, as show in **Figure 4. 7A(i)**, were processed along the longitudinal diameter (**Figure 4. 7A(ii)**). The signal plots for each spheroid, displayed the measured intensity being higher at the edges of the tumour and lowest in the middle, confirming the central hollow lumen. The close-up analysis of the MCF-7 MCTS and the z-projection images in **Figure 4. 7B**, reveal strong cell-cell adhesion and compact spheroids, which is consistent with other studies<sup>3,54</sup>. Especially, a closer look on the ALG capsules, the morphology of the spheroid and cell-cell junctions differ from the ones cultured in collagen-containing ECM, although in all cases the adhesion between cells appears robust.

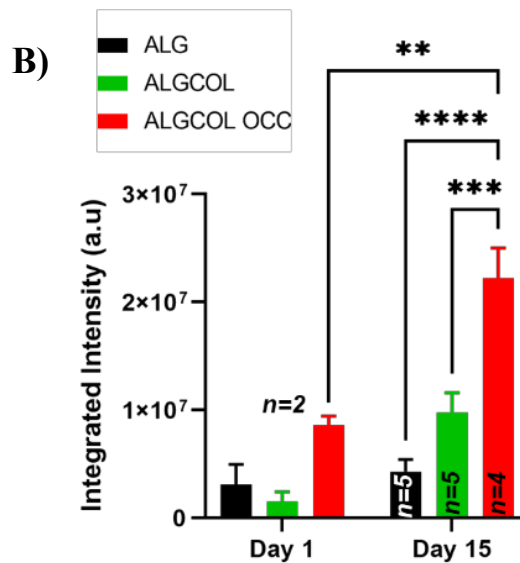
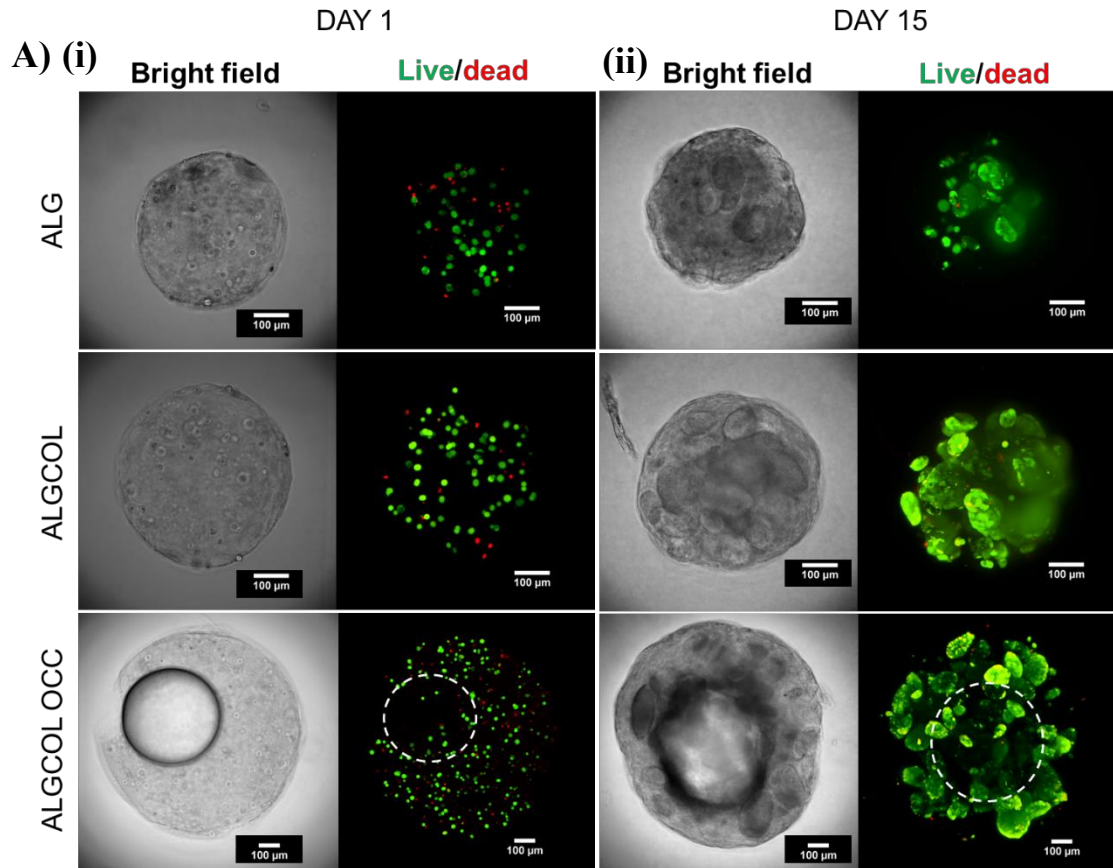


**Figure 4. 6: LSFM images and intensity analysis relating to MCTS formation (Day 1 and 15).** **A)** Bright field (LHS) and dark field (RHS) LSFM images of ALG, ALGCOL and ALGCOL OCC on (i) Day 1 and (ii) Day 15. The bright field images show a single slice, while the fluorescent images shown the projection of the maximum intensity of the slices (z-projection). The dashed white lines indicate the oil core of the ALGCOL OCCs. All scale bars are 100  $\mu\text{m}$  **B)** Analysis of green fluorescence integrated intensity of LSFM images of ALG, ALGCOL and ALGCOL OCC capsules. Significant increase in the fluorescence, i.e. viable MCTSs, was obtained by ALGCOL OCCs on Day 15 compared to ALG and ALGCOL of the same timepoint. The samples (n) utilised for the green fluorescence analysis were as follows; for Day 1: ALG (n=2), ALGCOL (n=2), ALGCOL OCCs (n=2), and for Day 15: ALG (n=5) and ALGCOL (n=5), ALGCOL OCCs (n=4). Data shown as mean  $\pm$  SEM. Two-way ANOVA test was performed where, \* $p \leq 0.05$ , \*\* $p \leq 0.005$ , \*\*\* $p \leq 0.0005$ .

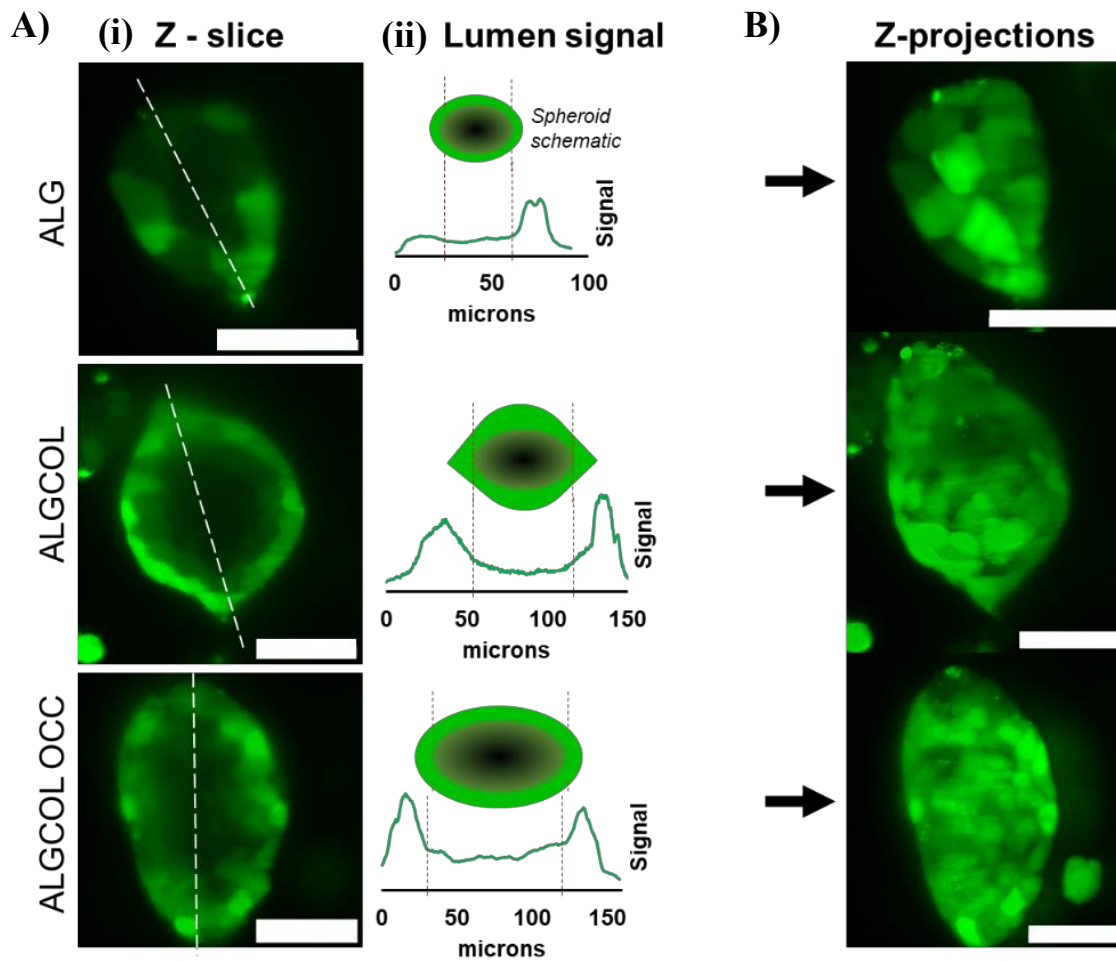


**Figure 4. 7:** LSFM images of individual MCF-7 MCTSs formed after 15 days of culture in ALG, ALGCOL and ALGCOL OCCs. **A)** (i) Z-slices of individual MCTSs near the middle of the spheroids, showing the hollow space. The white dashed line notes the longitudinal distance along the MCTSs, from which the signal of the lumen was measured and plotted in (ii). **B)** Z-projections of each MCTS, revealing compact spheroids and strong cell-cell adhesion. All the scale bars are 50  $\mu\text{m}$ .

### 4.4.3. Oil-core capsules (OCCs) as a novel 3D culture model

Single (ALG, ALGCOL) and double emulsion hydrogel capsules (ALGCOL OCCs) were generated using 3D-printed single or dual-material microfluidic devices and established the formation of spheroids, with a clearly discernible lumen. Their proliferation was benefited by the culture conditions and ECM materials (alginate and collagen), which are widely used in tissue engineering<sup>15</sup>. The ALGCOL OCCs demonstrated the most significant spheroid growth. The enhanced proliferation of cells and enlarged tumour spheroids in OCCs, compared to ALG and ALGCOL capsules, could be a result of the higher number of cells initially encapsulated in the hydrogel shell. The core-to-shell ratio of OCCs can be controlled by manipulating the flow rates of the double emulsion microfluidic device (DE-MD). By doing so, OCCs with thin alginate shell and large oil core and vice versa.

The encapsulation of an oil core, which is less dense than the hydrogel shell, led to floating ALGCOL OCCs in the cell culture medium. Another hypothesis for the formation of larger MCF-7 MCTSs in these OCCs, was the plausible exposure to higher oxygen levels during the cell culture. However, no gas related studies were conducted in this thesis, and this can only be supported by limited literature. MCF-7 cells cultured *in-vitro* under elevated oxygen levels, a study conducted by Crowley, *et al.* 2017, showed improved migration and upregulation of proliferating genes<sup>55</sup>. Therefore, the presumably elevated oxygen levels could have potentially improved the proliferation of the cells in OCCs, compared to ALG and ALGCOL sunk capsules.

Place, *et al.* 2017 argued that cell culture plates do not represent the *in-vivo* oxygen diffusion rates, due to the unrealistic distance from the oxygen source, and they proposed alternative *in-vitro* 3D models, in order to recapitulate oxygen levels in the body (bioreactors, roller bottle, oxygen permeable plates)<sup>56</sup>. Moreover, the diffusion of oxygen through the cell culture medium was previously described by Fick's Law ( $F = -D \nabla c = -D \frac{\Delta c}{\Delta h}$ )<sup>56,57</sup>, which assumed similar oxygen transport in lung capillaries<sup>58</sup>. By considering the culture medium with a diffusivity D, **Figure 4. 8** schematically presents Fick's Law and implies that the oxygen diffusive flux would be higher for floating OCCs than sunk ALG and ALGCOL microgel beads. This is due to the position of the floating OCCs being closer to the air-liquid interface ( $h_a, c_a$ ), hence translates to higher oxygen concentrations. The oxygen gradient highly depends upon the volume of culture medium, which is why this volume was kept the same during culture, across all capsules cultured in T-75 flasks. On the other hand, slow proliferation rates of tumour cells have been correlated to hyperoxic conditions, which could explain the non-significant proliferation during the first week of culture in ALGCOL OCCs<sup>57</sup>.

The most comparable 3D culture model to OCCs, is the hanging-drop method, which faces challenges such as imaging, culture medium exchange and susceptibility to sudden shocks<sup>59</sup>. Leshner-Perez, *et al.* 2017, conducted an oxygenation study on 3D spheroid cultures and reported that, the oxygen levels in hanging-drop spheroids, were higher compared to the oxygen levels of spheroids cultured in round bottom wells<sup>60</sup>. This was attributed to the null distance between the air-liquid interface

and the spheroids in the hanging-drop<sup>60</sup>. Therefore, the enhanced proliferation of the cells in the floating OCCs, may be due to the smaller distance between the spheroids and the air-culture medium interface, encouraging these microfluidically formed double emulsion capsules, as a novel technology for *in-vitro* 3D culture oxygenation studies.

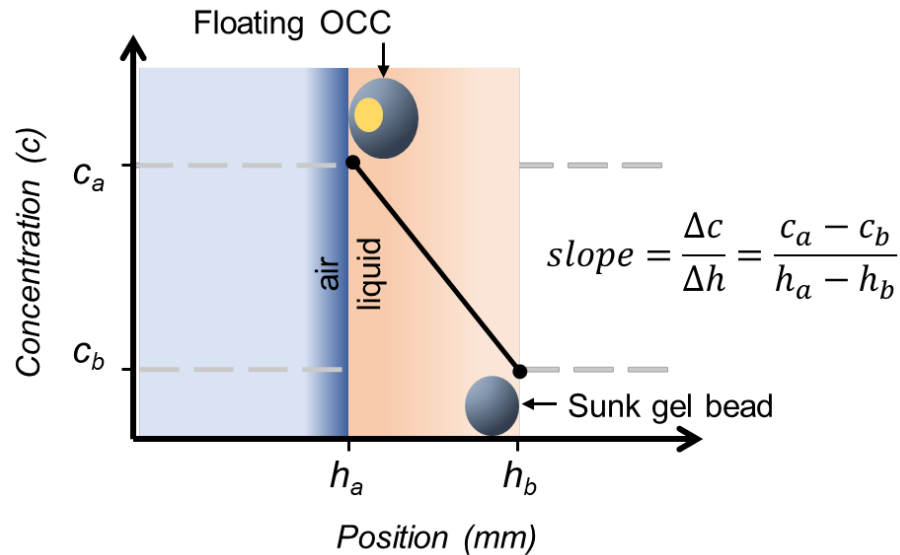


**Figure 4. 8:** Model graph showing the higher oxygen concentration closer to the surface of the culture medium. The slope equation describes the concentration gradient along the depth ( $h$ ) of the culture medium, with a floating OCC exposed to higher oxygen levels ( $C_a$ ) and a sunk single emulsion microbead exposed to lower oxygen levels ( $C_b$ ).

#### 4.4.4. Vesicle-containing, alginate-collagen type I oil-core capsules (vesALGCOL OCCs)

The following subsections utilised double emulsion OCCs to evaluate the proliferation and receptor expression of MCF-7 microtumours, when exposed under certain drugs and ligands. More specifically, vesicle-containing ALGCOL OCCs (vesALGCOL OCCs) were treated externally with DOX, LPC and Tf-488. **Figure 4. 9** shows bright field images of vesALGCOL OCCs before (Day 1) and after (Day 15) MCTS formation. Some OCCs, untreated, were also imaged using OCT equipment to possibly visualise any MCTSs within the hydrogel shell after 28 days of culture (*Appendix 4.B*). On the 15<sup>th</sup> day of culture, vesALGCOL OCCs were treated with DOX and LPC, externally, and cell proliferation was assessed. Tf-488 ligands was introduced to vesALGCOL OCCs, towards the end of 3D MCTS culture (Day 21).

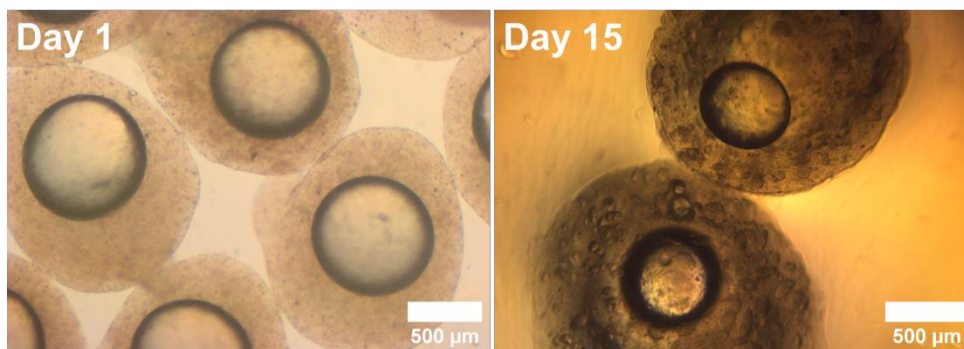


**Figure 4. 9: Bright field images of vesALGCOL OCCs, before and after MCTS formation.** Day 1 capsules have similar morphology and oil core diameter (not quantified) and were stored and imaged in a petri dish containing cell culture medium. Capsules imaged on day 15 originate from a different encapsulation experiment, which explains the difference in oil-core to hydrogel-shell volume ratio. These vesALGCOL OCCs were imaged in a petri dish with a small volume of PBS.

#### 4.4.4.1. Doxorubicin treatment

Doxorubicin (DOX) is a widely used anticancer drug, which binds and intercalates between DNA bases, preventing cells from dividing<sup>61</sup>. 2D cultured MCF-7 cells were treated with DOX for three days to obtain the half maximal inhibition concentration  $IC_{50}$  ( $DOX_{IC_{50}}$ ), which is the value defined as the concentration to inhibit 50 % of cell proliferation. The calculated  $DOX_{IC_{50}}$  yielded to be  $0.84 \mu M \pm 0.18$ , as shown in **Figure 4. 10A**, which value was perfectly matched with the  $DOX_{IC_{50}}$  reported by Gong, *et al.* 2015 ( $0.46 \mu g/ml$ ). Others have reported the  $DOX_{IC_{50}}$  of 2D cultured MCF-7 cells to be approximately  $0.1 \mu M$ <sup>62,63</sup>, and that of drug-resistant MCF-7 cells to be approximately  $1-1.9 \mu M$ <sup>63,64</sup>. The  $IC_{50}$  of any drug depends on many cell culture and assay variables, including cell density, treatment periods, cell line and others<sup>3,65</sup>.

Subsequently, three concentrations of DOX ( $0.96 \mu M$ ,  $4.37 \mu M$  and  $20 \mu M$ ) were used to treat MCTSs in vesALGCOL OCCs on Day 15 of culture. According to the CTB metabolic output in **Figure 4. 10B** and accompanied statistical analysis, none of the tested concentrations was able to show any evidence of significant cell growth or death over the incubation period with the drug. Essentially, DOX treated MCF-7 spheroids, seemed to have entered a dormant phase, in which they did not proliferate further, while the MCF-7 cells in control ( $0 \mu M$ ), continued to proliferate. Hence, this proliferation inhibition agrees with the DOX's action relating to the cell cycle arrest, by intercalating the DNA and preventing cell growth and mitosis<sup>66</sup>. The slight increase in  $4.37 \mu M$  DOX treated MCTSs on Day 3 and 5 could be a result of handling errors, but according to the statistical analysis this was insignificant. The  $DOX_{IC_{50}}$  of a 3D culture, has been reported to be approximately 30-50 times higher than the  $DOX_{IC_{50}}$  of 2D cultured MCF-7 cells<sup>3,11,16,67,68</sup>. Others have established differential  $DOX_{IC_{50}}$  between MCTSs in soft ( $104.5 \mu M$ ) and stiff ( $57.4 \mu M$ ) alginate-collagen type I hydrogels after two weeks of culture<sup>69</sup>. Hence, the  $DOX_{IC_{50}}$  of the 3D culture could not have been estimated, because the concentrations tested were not considerably higher than the DOX concentrations tested in 2D cultures (at least 30 times higher).

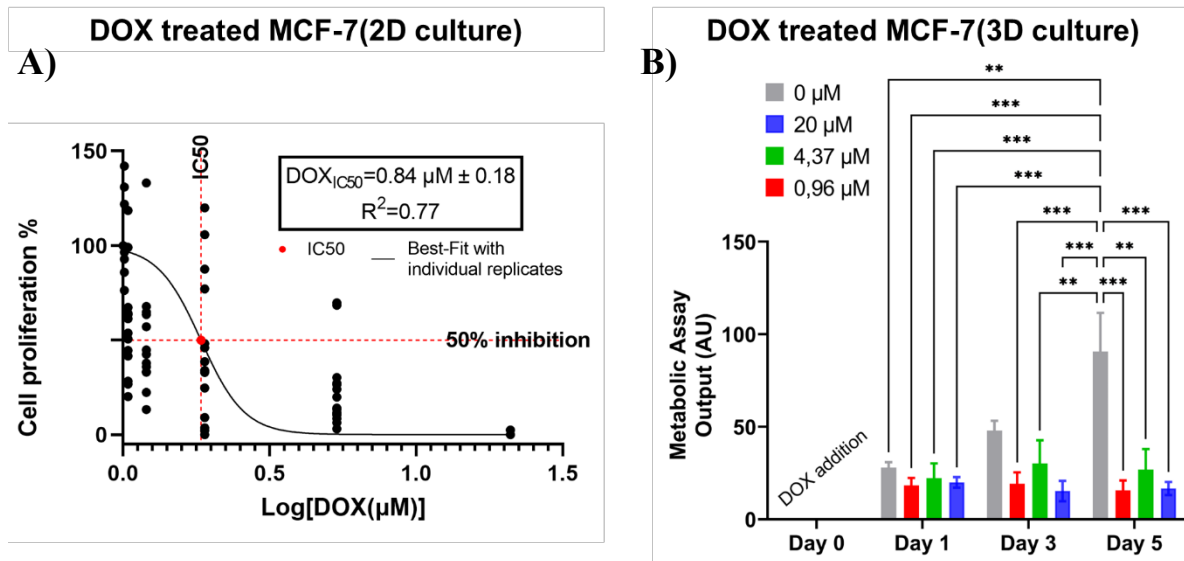


**Figure 4. 10: Doxorubicin response of a 2D culture and 3D cultured MCF-7 MCTSs in vesALGCOL OCCs.** **A)** Percentage of cell proliferation against  $\log[\text{DOX concentration}]$ , with data points corresponding to individual replicates. Non-linear regression curve fitting determined the  $\text{DOX}_{\text{IC50}}$  (red dotted lines) of MCF-7 2D cultured cells, when treated with 0.01, 0.05, 0.21, 0.96, 4.37, 20  $\mu\text{M}$  DOX ( $n=17$  across three experiments). The curve fitting showed  $\text{DOX}_{\text{IC50}}=0.84 \mu\text{M}$  with  $R^2=0.77$  ( $R^2 > 0.7$  well fitted curve). **B)** MCF-7 MCTSs in vesALGCOL OCCs treated with DOX concentrations for 5 days (DOX added on day 15 of culture). No significant differences observed between DOX concentrations, due to increased drug resistance of 3D cultures, while the control MCTSs, continued to proliferate. Data shown as mean  $\pm$  SEM ( $n=3$ ). Two-way ANOVA test was performed where,  $*p \leq 0.05$ ,  $**p \leq 0.005$ ,  $***p \leq 0.0005$ .

After the 5-day treatment, vesALGCOL OCCs were washed with phosphate buffered saline (PBS) and MCTSs were stained using the calcein AM and EthD-1 (live/dead assay). The fluorescence microscopy in **Figure 4. 11**, revealed live and dead cells, as well as the DOX accumulated around the MCTSs (4.37  $\mu\text{M}$  DOX). The red channel of accumulated DOX fluorescence was obtained using the same excitation wavelength as the excitation wavelength used to image the viable cells ( $\sim 470 \text{ nm}$ )<sup>70</sup>. Furthermore, no clear spheroid deterioration was observed after DOX treatment, a phenomenon which was detected by Lovitt, *et al.* 2018, in MCF-7 spheroid-laden gels<sup>42</sup>. Although, from the merged channels (calcein AM/EthD-1) in **Figure 4. 11**, the cell-cell contact exhibited some differences after the DOX treatment, where the control tumours maintained compact spheroids with strong cell-cell adhesions, while DOX treated MCTSs seemed to have formed loose aggregates<sup>3,42</sup>. This phenomenon would be clearer with more elegant microscopy, such as LSM or confocal laser microscopy (laser confocal microscopy image of non-DOX treated 3D cultures can be found in *Appendix 4.C*).

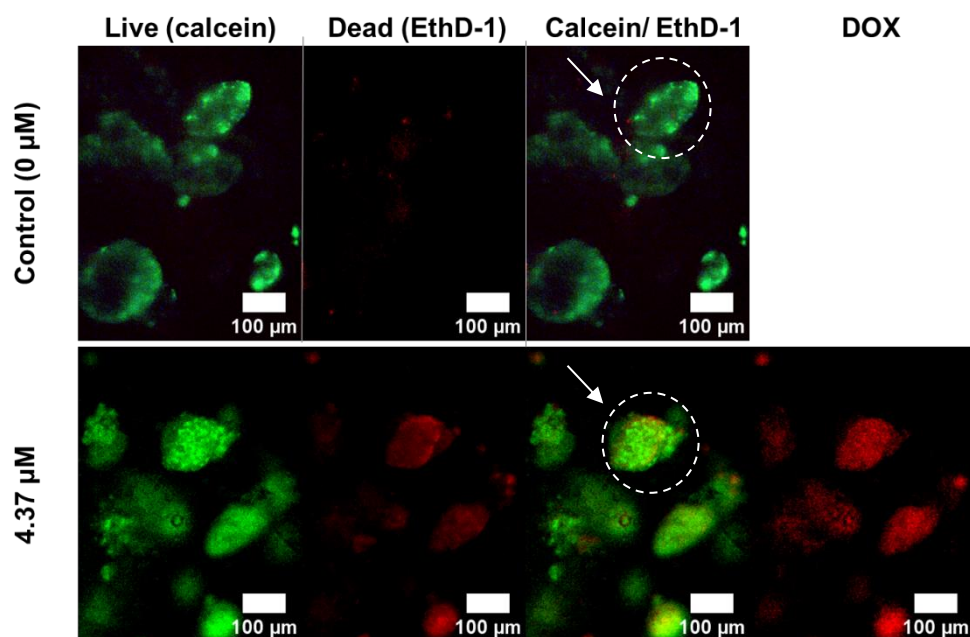


**Figure 4. 11:** Fluorescent images of control (0  $\mu\text{M}$ ) and 5 day DOX treated (4.37  $\mu\text{M}$ ) MCTSs in vesALGCOL OCCs. Live and dead cells appear green and red, due to the calcein and EthD-1, respectively. Accumulated DOX appears red under blue light ( $\sim 470\text{ nm}$ ) in 4.37  $\mu\text{M}$  treated MCTSs. Considerably fewer dead cells appear in the control condition than in DOX treated spheroids. White dashed circles noted on the merged channel images (calcein/EthD-1), show spheroids with morphological variabilities in their cellular arrangement. Images were obtained using a conventional fluorescent inverted microscope.

#### 4.4.4.2. Lysophosphatidylcholine treatment

Initial LPC experiments involved the calculation of the  $\text{IC}_{50}$  ( $\text{LPC}_{\text{IC}_{50}}$ ) of treated 2D cultured MCF-7 cells. The estimated  $\text{LPC}_{\text{IC}_{50}}$  was approximately  $86.42\ \mu\text{M} \pm 0.44$  (**Figure 4. 12A**). The  $\text{LPC}_{\text{IC}_{50}}$  was ten-fold higher than the CMC of LPC reported in literature (4-8.3  $\mu\text{M}$ )<sup>71</sup>. The  $\text{LPC}_{\text{IC}_{50}}$  and CMC values are important, in order to understand the interaction of cancer cells with either single LPC molecules or LPC micelles. Reported  $\text{LPC}_{\text{IC}_{50}}$  of LPC with longer fatty acid chains (LPC(18:0)) on cancer cells ranged between 120 and 180  $\mu\text{M}$ <sup>72</sup>, while in another study cancer cells were treated with 450  $\mu\text{M}$  LPC(16:0) and did not exhibit any significant toxicity<sup>73</sup>. Weltzien, 1979, suggested a few modes of interaction of LPC molecules with phospholipid membranes, including the insertion of LPC molecules into the outer leaflet and ‘flip-flop’ to the inner leaflet, at low concentrations<sup>74</sup>. On the other hand, at high concentrations, the membrane fluidity may change, micelles may form within the phospholipid membrane, or the membrane may be solubilised; all three cases lead to pore formation and evidently cell lysis<sup>74</sup>.

Similar to the DOX treatment, LPC concentrations were added to MCTSs in vesALGCOL OCCS on the 15<sup>th</sup> day of culture (**Figure 4. 12B**). The control group and the 10  $\mu\text{M}$  LPC treated MCF-7 cells, exhibited similar proliferation profiles, while the concentrations much higher than the CMC of LPC (100  $\mu\text{M}$ , 300  $\mu\text{M}$ , 1000  $\mu\text{M}$ ), affected the cells differently. The impact on the cell proliferation took place within the first 24 hours of incubation with LPC, especially with 100  $\mu\text{M}$  and above. No

proliferation occurred during the 5-day incubation with 1000  $\mu\text{M}$  LPC, but cell death was apparent. The form of cell death was assumed to be cell lysis, due to the drastic increase of the plasma membrane permeability under the influence of highly concentrated LPC micelles<sup>74,75</sup>. Interestingly, the 100  $\mu\text{M}$  LPC treated tumours, underwent significant proliferation compared to the control. This enhanced proliferation was an interesting result, which was attributed to the fusion of LPC molecules with the cell membrane and possibly their metabolism<sup>76</sup>. These assumptions were based on the reported work by Raynor, *et al.* 2015, who associated LPC reduction in the supernatant of 2D cultured MCF-7 cells, with the extracellular degradation of LPC molecules, subsequent cellular uptake of free fatty acids and their re-acylation to phosphatidylcholine<sup>76</sup>. Bao, *et al.*, 2016, reported this degradation (or cleavage) of LPC, to occur due to an enzyme highly expressed by cancer cells (lysophosphatidylcholine acyltransferase 1 - LPCAT1), which led to the drop of LPC levels and increase of phosphatidylcholine concentrations in the membrane of cancer cells, resulting in enhanced cell proliferation through membrane remodelling<sup>77,78</sup>.

Proliferation of the cells plunged on Day 3 for 100  $\mu\text{M}$  and 300  $\mu\text{M}$  LPC. However, the cause was unclear, and therefore this decrease was assumed to be related to environmental adaptations of MCF-7 cells in the presence of LPC. According to the proliferation tests, the 3D cultures in vesALGCOL OCCs were favoured by the presence of 100  $\mu\text{M}$  LPC, which concentration is above the estimated  $\text{LPC}_{\text{IC50}}$  (86.42  $\mu\text{M}$ ) of the 2D MCF-7 culture. Finally, the 3D culture of MCF-7, showed an increased resistance to the cytolytic properties of high LPC micellar concentrations, compared to the 2D culture<sup>71,79</sup>.

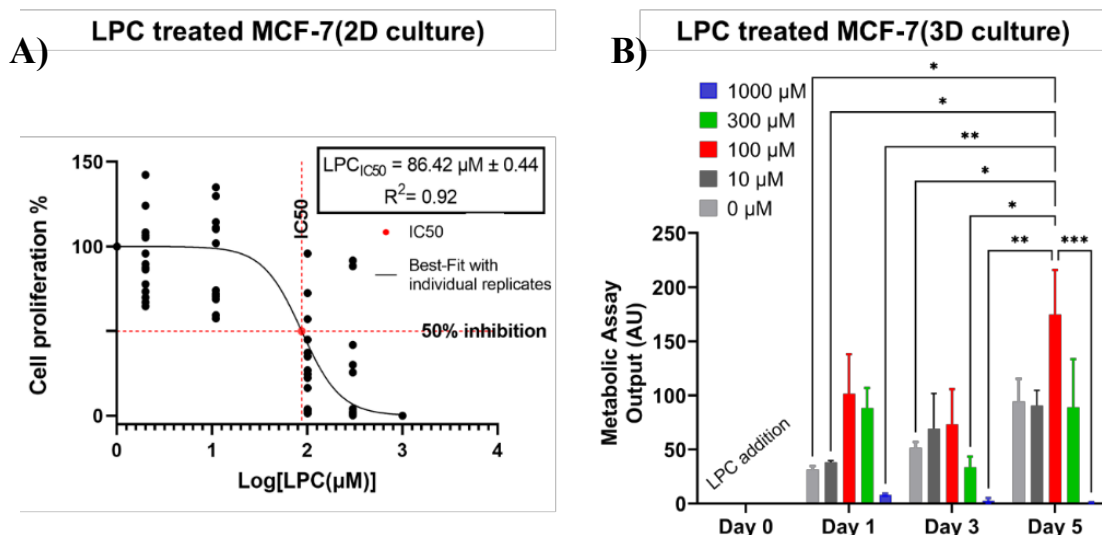


**Figure 4. 12: LPC response of a 2D culture and 3D cultured MCF-7 MCTSs in vesALGCOL OCCs.** A) Percentage of cell proliferation against  $\log[\text{LPC concentration}]$ , with data points corresponding to individual replicates. Non-linear regression curve fitting determined the  $\text{LPC}_{\text{IC50}}$  (red dotted lines) of MCF-7 2D cultured cells, when treated with 1, 10, 100, 300 and 1000  $\mu\text{M}$  LPC ( $n=16$  across three experiments). Curve fitting showed  $\text{LPC}_{\text{IC50}}=86.42 \mu\text{M}$  with  $R^2=0.92$  ( $R^2 > 0.7$  well fitted curve). B) MCF-7 MCTSs in vesALGCOL OCCs treated with LPC concentrations for 5 days (LPC added on day 15 of MCTS culture). Cell proliferation was favoured by 100  $\mu\text{M}$  LPC and increased over time, whilst 1000  $\mu\text{M}$  induced cell death. Changes in the cellular proliferation were observed within the first 24 hours and all tested LPC concentrations became diverse over time. Data shown as mean  $\pm$  SEM ( $n=3$ ). Two-way ANOVA test was performed where, \* $p \leq 0.05$ , \*\* $p \leq 0.005$ , \*\*\* $p \leq 0.0005$ .

#### 4.4.4.3. Transferrin-488 (Tf-488) labelling of 2D and 3D cultures

All mammalian cells that require iron for cellular functions, including MCF-7 breast cancer cells, express the transferrin receptor, which regulates iron transport<sup>80</sup>. Therefore, MCF-7 MCTSs cultured in vesALGCOL were assessed in terms of the transferrin receptor expression, by introducing the Tf-488 ligand.

Before doing so, epidermal growth factor-alexa488 (EGF-488) and Tf-488 were used to fluorescently label MCF-7 2D cultures, as shown in **Figure 4. 13A**, to ascertain the ligand more likely to label the specific cells used for the 3D MCTS formation. The Tf-488 conjugate bound to the MCF-7 cells, as demonstrated by the fluorescent signal, while EGF-488 did not stain any cells, following this protocol. This is due to the fact that EGFR is not highly expressed on the surface of MCF-7 cells, as demonstrated by Wymant, *et al.* 2016<sup>81</sup>. On the other hand, Tf-488 is abundantly expressed<sup>82,83</sup>, as shown by the green fluorescence emitted by the 2D culture and for this reason, Tf-488 ligand proceeded to the staining of 3D cultured cells in vesALGCOL OCCs. **Figure 4. 13A** also shows background fluorescence by MCF-7 cultured cells in FBS containing media, due to the presence of phenol red. The transferrin receptor expression can be seen as the green fluorescence in the 3D MCTS cultures in **Figure 4. 13B**, due to the binding and endocytosis of Tf-488, following 30- and 90-minutes starvation periods. Small fluorescent intensity differences were observed in MCTSs between the two starvation periods, with 90 min starved spheroids to appear slightly brighter. However, it would be naïve to assume that there was a starvation period dependence on the binding and uptake of Tf-488, because the experiment was only carried out once (with n=3 OCCs per starvation period). Most importantly, the Tf-488 diffused through the hydrogel ECM, reached the MCTSs and was recognised by the MCF-7 cells quite strongly, irrespective of the starvation period.

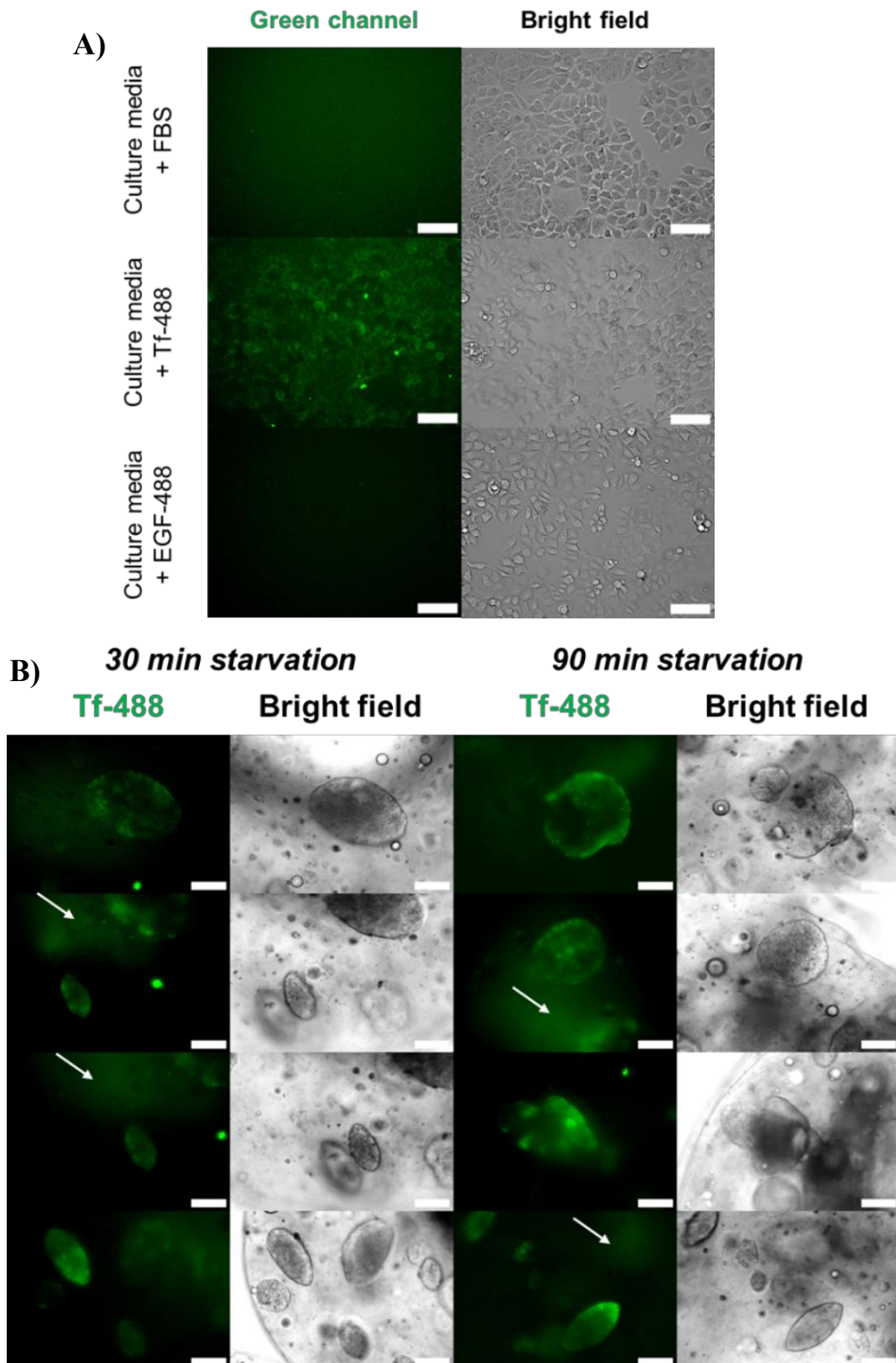


**Figure 4. 13:** Green fluorescent channel (LHS) and bright field images (RHS) of MCF-7 cells in 2D and 3D MCTS cultures, after the uptake of Tf-488. **A)** Starved 2D cultured MCF-7 cells expressed strong fluorescence only in the presence of Tf-488. No expression of EGFR was shown, and background fluorescence appeared in + FBS cell culture, due to the phenol red in the culture medium. **B)** Tf-488 labelling of MCF-7 MCTS cultures in vesALGCOL OCCs, following either 30 minutes or 90 minutes starvation period (incubation in serum-free media). White arrows note the fluorescence emitted by neighbouring, Tf-488 labelled spheroids.

#### 4.4.5. Cell and Droplet Interface Bilayer (DIB) fate in eDIBs capsules

Cell encapsulation in encapsulated droplet interface bilayers (eDIBs) using triple emulsion microfluidic devices (TE-MDs) was quite challenging and the preservation of the DIBs was particularly tricky. The main concern and constant variable component for the cell encapsulation in eDIBs experiments was the 3D-printed microfluidic device. The formation and stability of the eDIB capsules relied largely on the dimensions of the 1<sup>st</sup> cyclic olefin copolymer (COC) droplet-forming junction (Chapter II, Section 2.4.5.2.1.). More specifically, this droplet-forming junction, would determine the diameter of the encapsulated aqueous cores. In addition, the continuous phase flow rate, and the droplet-to-channel aspect ratio, influence the lipid monolayer incubation around the droplets, frankly affecting the stability of the formed DIBs<sup>84</sup>. Unstable DIBs, are more susceptible to environmental stresses, leading to merging with the hydrogel shell, leaving an eDIB without internal aqueous compartments (i.e., OCC).

The 3D printing of a TE-MD with a dimensionally accurate 1<sup>st</sup> COC droplet-forming junction, allowed successful capture of MCF-7 cells in the hydrogel shell of eDIBs, as well as improved degree of DIB stability. The incubation period after production was a crucial stage, which would determine the fate of the eDIB structure. Merging of the aqueous cores with the hydrogel shell, most likely occurred during the first hour of incubation at 37 °C and 5 % CO<sub>2</sub>. This was because the captured DIBs in dioleoyl-phosphatidylcholine (DOPC)-containing oil were still settling and adjusting within the new environment. Similar observations, were reported by Barriga, *et al.* 2014, who used a DOPC DIB system, which was stabilised after 1 hour, indicating that during the lead time, the DIB was still susceptible to merging<sup>85</sup>. DOPC are unsaturated phospholipids, while diphytanoyl-phosphatidylcholine (DPhPC) phospholipids, extensively used in DIB membrane models are saturated. Compared to DPhPC, DOPC phospholipids have bent fatty acyl chains, which influences membrane fluidity and stability. As a matter of fact, a study by Strutt, *et al.* 2022, showed that all of the tested substances (e.g. paracetamol, caffeine) were approximately 40 % more permeable through a DOPC DIB, than a DPhPC DIB<sup>86</sup>. Therefore, DPhPC could enhance the stability of the cell-laden eDIBs, which is particularly important during the initial incubation period.

Cell-laden vesALGCOL eDIBs, which survived the initial incubation period are shown in **Figure 4. 14A&B**. From these figures, it was understood that merging of aqueous cores was apparent, resulting in their variable diameters. The vesALGCOL eDIB in **Figure 4. 14A(iv)** encapsulated considerably small cores in a dumbbell-shaped oil core, that resulted by the coalescence of two eDIBs during gelation. The formation of these microscopic aqueous droplets were believed to have emerged due to artefacts at the droplet-forming junction either during fabrication, or due to the softening of COC by hexadecane<sup>87</sup>. The sulforhodamine B (sulFB) internal cores of the cell-containing eDIB in **Figure 4. 14B**, were extremely polydisperse (not quantified), although they survived the initial incubation

period post-encapsulation. Following 10 days of cell culture, MCTS formation was established in the shell of the eDIB in **Figure 4. 14C**, and the majority of the DIB network was preserved.

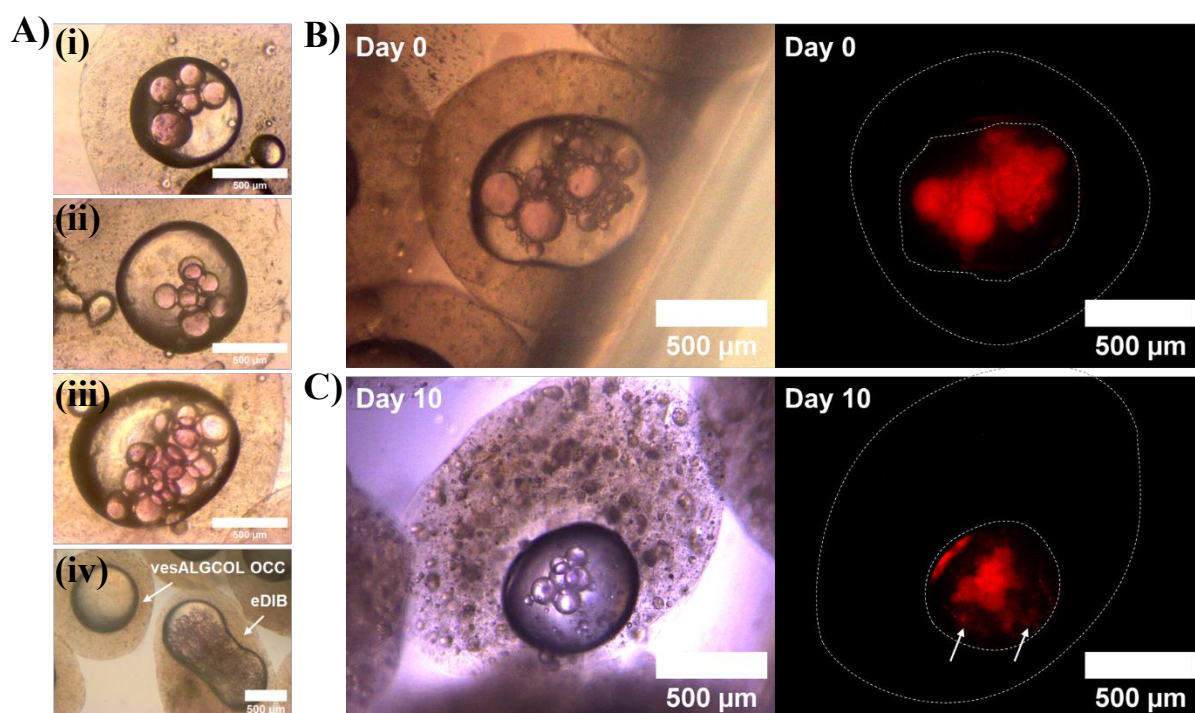


**Figure 4. 14: Bright field and dark field images of cell-laden eDIB capsules before and after MCTS formation.** *A) (i)-(iii) Bright field images of individual eDIBs with encapsulated MCF-7 cells, which survived the initial incubation period (1-2 hours) post-encapsulation experiments. B) Post-encapsulation preserved eDIB (day 0) imaged under the bright field (LHS) and dark field (RHS-green light excited), where red fluorescence was emitted by sulfB DIB network. C) eDIB cultured for 10 days, formed MCTSs in the hydrogel shell and maintained some degree of the encapsulated DIB network. White arrows indicate residue dye from merged cores with the hydrogel shell. The discrete dotted lines in the dark field images show the edges of the middle oil core and outer hydrogel shell. All the scale bars indicate 500  $\mu\text{m}$ .*

#### 4.4.5.1. Live/dead staining of MCF-7-laden eDIBs

The culture of MCF-7 breast cancer cells in eDIBs appeared to be straight forward, but most challenges were related to the prolonged preservation of the complex-emulsion structure, while in culture. The biocompatibility of OCCs was established in earlier sections, through metabolic assays (Section 3.3.1.4) and live/dead imaging (Section 3.3.1.5). The same live/dead staining protocol was performed to assess the viability of MCF-7 cells in eDIB capsules. Staining of cells in eDIBs, 24 hours after microfluidic experiments (Day 1), indicated increased viability, as shown in **Figure 4. 15A**. The cell density used for all experiments, was  $1 \times 10^6$  viable cells/ml, however **Figure 4. 15B** shows an eDIB produced with considerably lower cell density, after experiment troubleshooting. The eDIB with lower cell density, exhibited higher cell death and according to Lin and Anseth, 2011, cell packing density impacts greatly the cell viability, with low cell packing densities exhibiting poor cell proliferation<sup>88</sup>.

Furthermore, LSFM imaged eDIB in **Figure 4. 16A**, revealed approximately 18 % of red fluorescence (dead cells) of the total fluorescence emitted by MCF-7 stained cells, which was attributed to the prolonged LSFM imaging. The LSFM image slices were processed to obtain the orthographic projections of the survived DIB, as illustrated in **Figure 4. 16B**. The distance between the slices of imaged eDIB samples during LSFM, ranged between 3.50-6.09  $\mu\text{m}$ , enabling good resolution imaging of the cores<sup>89</sup>. The side view projection revealed the slightly flattened aqueous cores with a lipid bilayer less visible than other projections. In contrast, the DIB and its distinct compartments were readily visible in the front and top view projections.

Clusters of cells started forming small spheroids of longitudinal diameter between 65  $\mu\text{m}$  and 100  $\mu\text{m}$  on days 5 and 6 as shown in **Figure 4. 17A&B**, while maintaining the DIB structure. The LSFM image of the two-core eDIB on Day 5, clearly displays the lipid bilayer formed between the aqueous cores, while the eDIB imaged on Day 6 (using an inverted microscope) shows a well organised and preserved DIB network comprised of more than 15 aqueous cores of approximate diameter  $167.2 \mu\text{m} \pm 2.8$ .

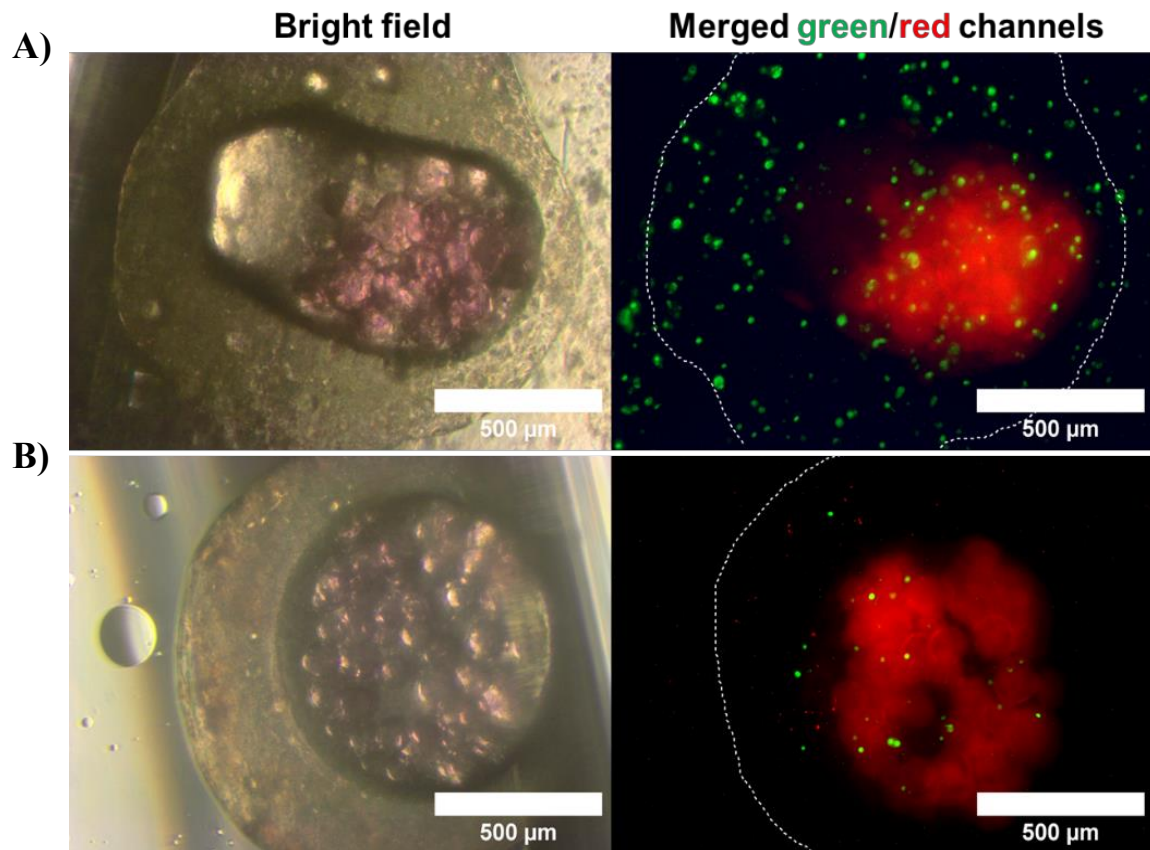


**Figure 4. 15: Live/dead staining of MCF-7 cells in eDIBs cultured for 24 hours after encapsulation (day 1), at two different cell densities. A) eDIB formed with cell density of  $1 \times 10^6$  viable cells/ml in the shell phase during microfluidic encapsulation. Viable cells were stained as green and dead cells as red (not visible). B) eDIB with considerably lower cell density (due to experiment inconveniences the exact cell density is unknown). In this example, red fluorescence emitted by dead cells is higher compared to A). In both eDIBs, the DIB network encapsulating *sulB* appears red. The red fluorescence emitted by the *sulB* cores was obtained under green excitation wavelength. The discrete dotted lines show the edges of hydrogel shell.**

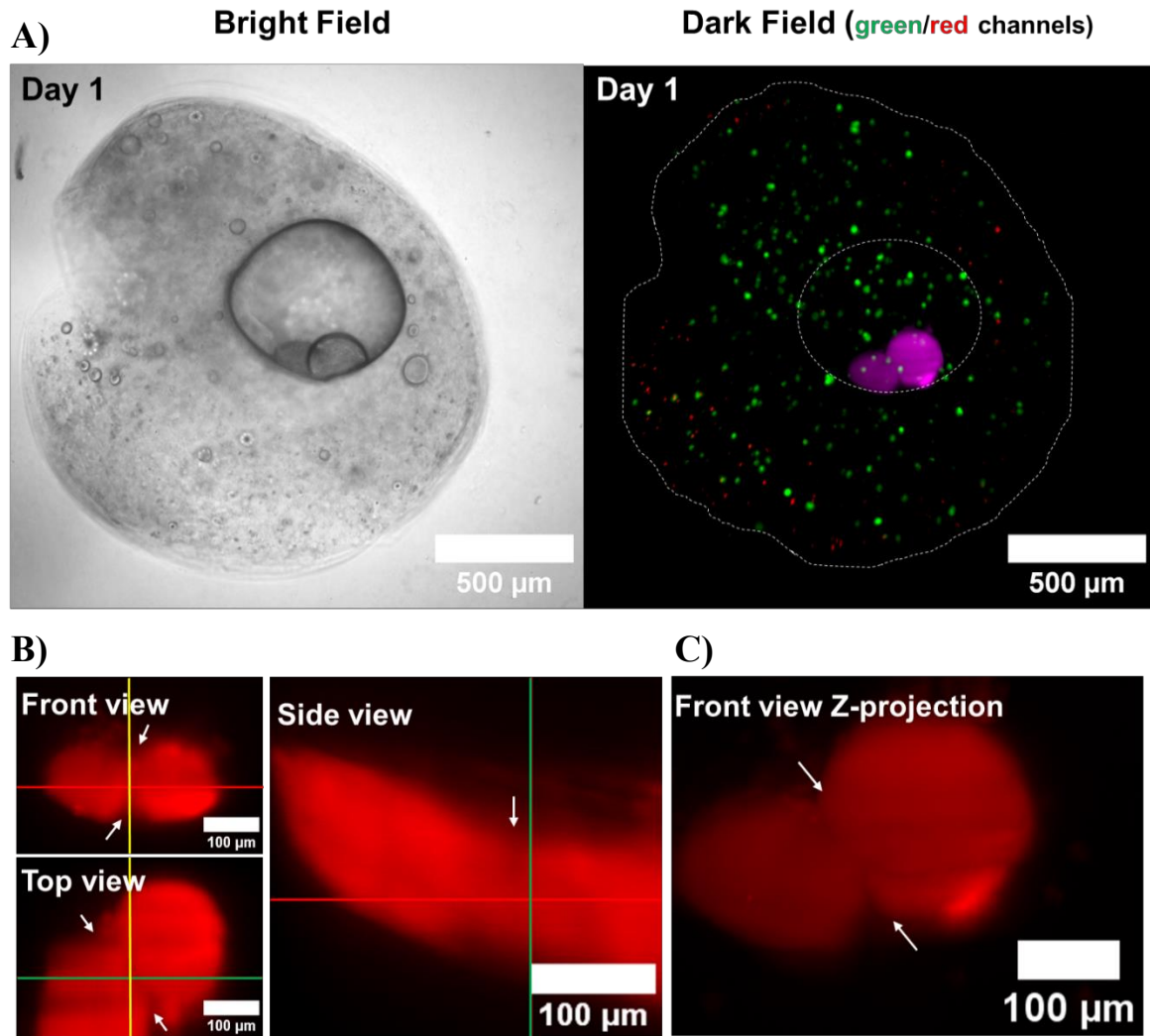


**Figure 4. 16: Multiple views of a two-core eDIB, with live/dead stained MCF-7 cells (day 1), imaged using LSM (eDIB is embedded in agarose). A)** Bright field and dark field images indicating the live cells (green), dead cells (red) and sulfB cores (magenta false colour). The discrete dotted lines were drawn around the edges of the middle oil core and outer hydrogel shell. **B)** Z-slices of three different view planes of the sulfB DIB (captured within the eDIB in A). The DIB can be easily identified (white arrows) in the front and top view, but more difficult to be seen from the side view plane. **C)** Z-projection of the DIB slices (front view) revealed a high contrast DIB. White arrows indicate the bilayer formed between the two aqueous sulfB cores.

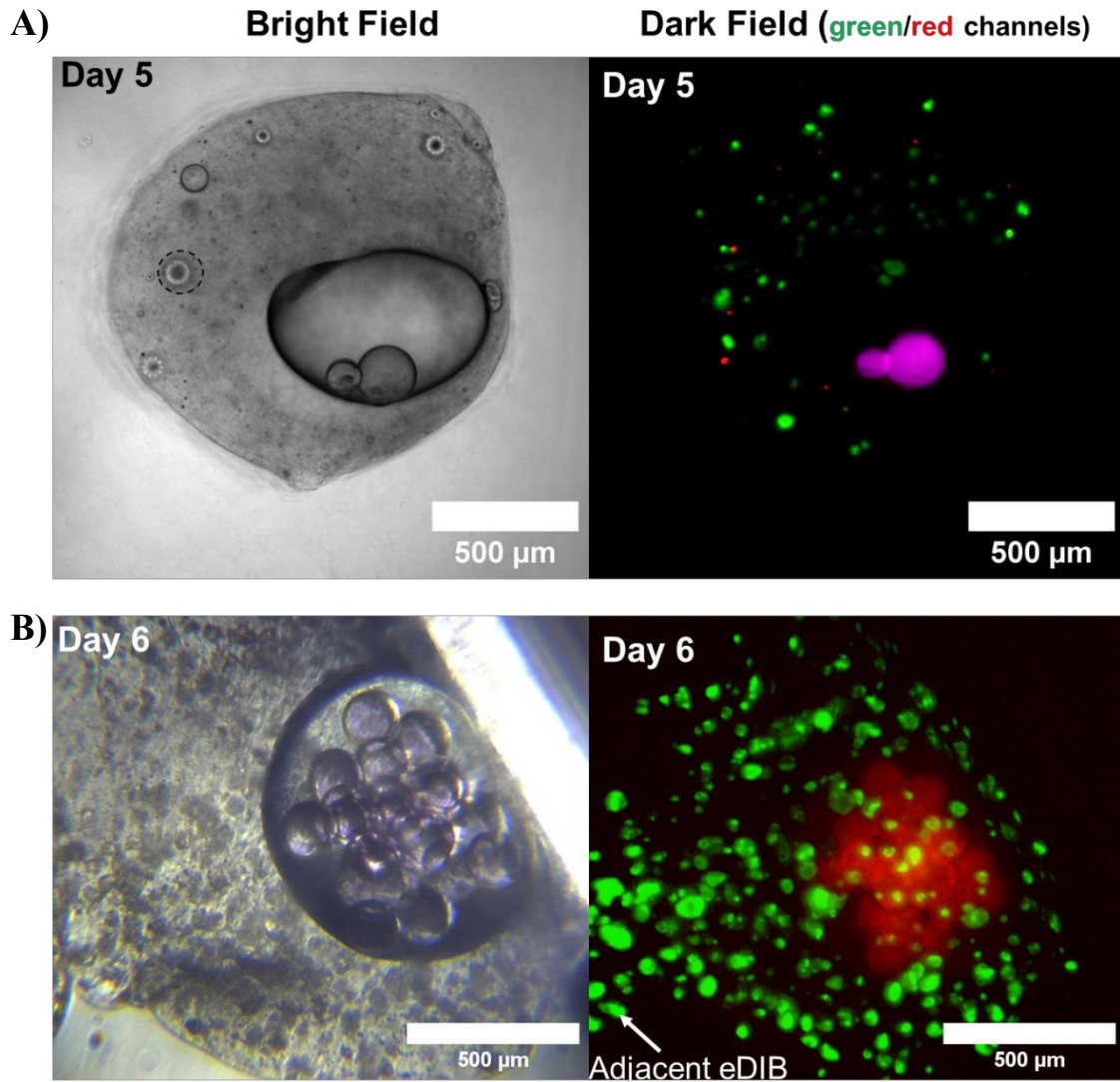


**Figure 4. 17:** Live (green) and dead (red) stained clusters and MCTSs developed in eDIBs on day 5 and 6 of culture. **A)** LSFM image of an eDIB embedded in agarose (day 5), shows small cell cluster formation and a high contrast DIB between two fluorescent sulFB cores (magenta false colour). The dashed circle in the bright field image indicates an illumination artefact example. **B)** Image obtained using a conventional inverted fluorescence microscope (day 6) uncovered highly organised and well preserved eDIB with viable MCTSs and red fluorescent sulFB cores. White arrow notes fluorescent MCTSs of a neighbouring capsule.

A less organised and distinct eDIB is shown in **Figure 4. 18A**, capturing formed tumours in eDIBs on the 8<sup>th</sup> day of culture. The dark field image in **Figure 4. 18A**, unveils the merged fluorescent channels of viable MCF-7 cells and MCTSs (green), as well as the dead cells and the sulfB cores (red). The EthD-1, which stained the dead cells, has quite a broad excitation (528 nm) and emission (617 nm) spectra, whereas the sulfB excitation (565 nm) and emission (586 nm) are narrower. The emission filter used for the red channel acquisition in LSFM (BP 575-615), picked up both light emissions of sulfB and EthD-1, hence dead cells and sulfB aqueous cores appeared red. A comparative overlap of the excitation and emission spectra of SulfB and EthD-1, using this filter can be found in *Appendix 4.D*<sup>90</sup>. Therefore, fluorophores near the oil core of the eDIB appearing red could lead to misinterpretation of the magnitude of cell death.

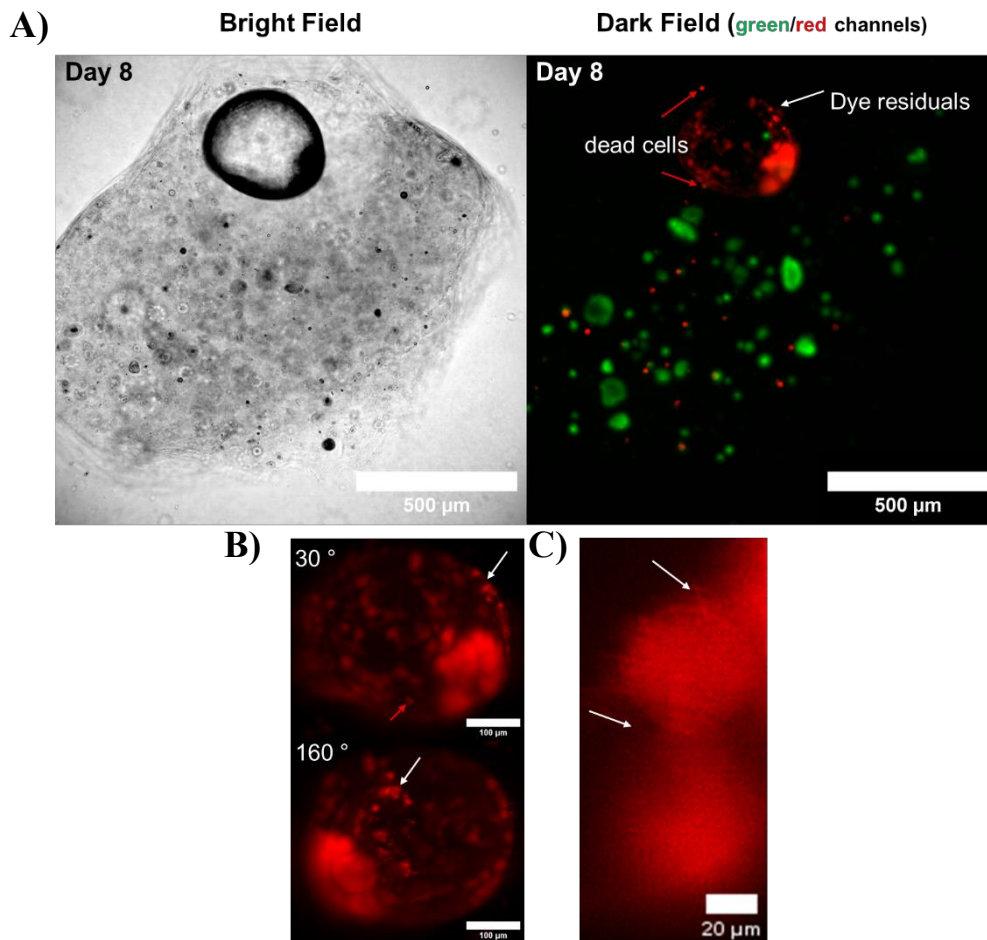


**Figure 4. 18: eDIB imaged using LSFM with live(green) and dead(red) stained MCF-7 cells and MCTSs on the 8<sup>th</sup> day of culture.** **A)** Bright field and dark field images of a quite randomly shaped (non-spherical) eDIB with stained cells and fluorescent cores. Dead cells and sulfB core emitted the red fluorescence, which could be confusing, hence the dead cells around the oil core are shown by red arrows. Only two dead cells were observed close to the outside of the oil core, whereas the remaining red dots (inside the oil core boundary) are assumed to be dye residuals (white arrow shows some dye residuals). **B)** Z-stack projection of the oil core's red channel rotated from 30° to 160°, to reveal the position and morphology of the same red dye residuals (white arrows) and red dead cell (red arrow). Scale bars indicates 100 μm. **C)** A closer look on the fluorescent sulfB cores uncovers some degree of lipid bilayer survival (white arrows).

Damaged cells appeared as red dots, but it may also be hypothesised that these red pigments are residual particles from the sulfB dye, left behind when merging occurred. Hence, during image analysis, the stained dead cells were distinguished from the fluorescent residual dye, by reconstructing a 3D image from the slice images and identifying the position of the red particle (inside or outside the oil core). **Figure 4. 18B**, shows the 3D projection of the oil core vicinity rotated by 130 °, noting a dead cell and presumable residual dye. Red dots present outside the oil core are more likely to be dead cells, while the red dots found inside the oil core are probable to be residual sulfB dye particles, perhaps trapped in the oil. This particular eDIB, retained some of the internal DIB structures, as noted in **Figure 4. 18C**.

MCTSs cultured in eDIBs, overall exhibited continuous proliferation and viability. In fact, some maintained the internal DIB compartmentalisation, however this requires further stability optimisation. **Figure 4. 19A**, shows an eDIB on the 15<sup>th</sup> day of culture, with viable tumour spheroids and preserved DIB network. Due to the image acquisition setup and possible artefacts, the resolution of the DIB network is not clear, although a rough architecture of the DIB network is visible indeed.

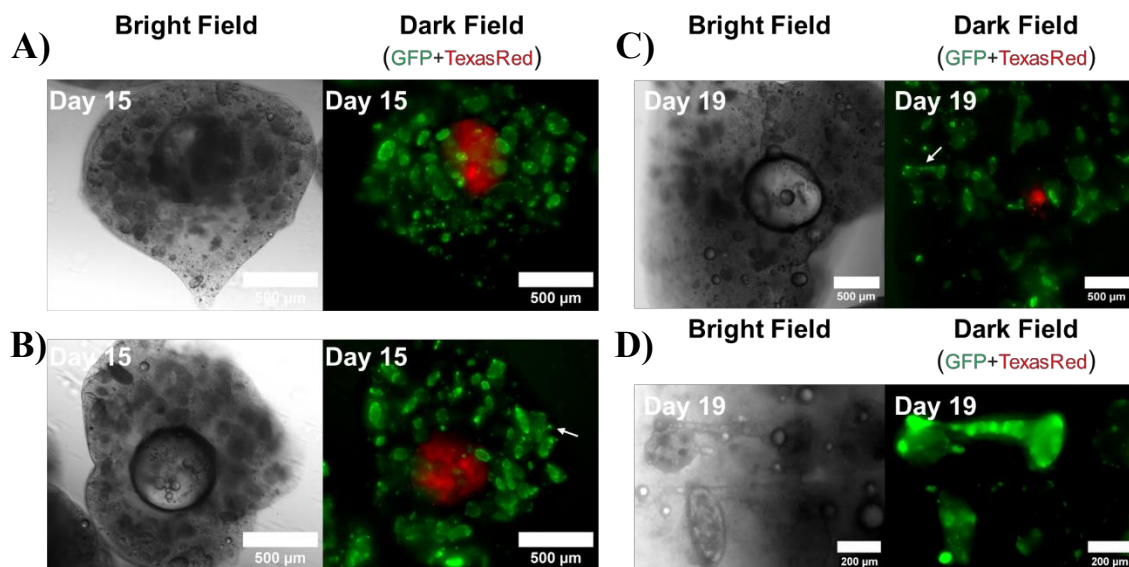


**Figure 4. 19: Bright field and dark field images (GFP(calcein)+Texas Red(sulfB) obtained using EVOS imaging setup. A)** Day 15 of culture of an eDIB with viable MCTSs, which maintained the DIB network (blurred red fluorescent cores) **B)** Another eDIB with viable MCTS, but most of the cores burst, leaving residual dye behind. The white arrow shows a small protrusion between a cell cluster and MCTS. **C)** Day 19 of eDIB culture, where only one sulfB core was preserved and some MCTSs showed more developed protrusions (white arrow). **D)** Day 19 protrusions seemed to have formed a bridge between two cell clusters in vesALGCOL eDIB. The scale bar in A-C is 500 µm and scale bar in D is 200 µm).

The ECM of vesALGCOL eDIB constructs, allowed cell-ECM interactions, which led to the proliferation of cells into MCTSs. Interestingly, in some instances, protrusion from spheroids started to form around Day 15, as indicated in **Figure 4. 19B**, which developed into full bridges between MCTSs by Day 19 (**Figure 4. 19C**). Usually, invasive behaviour is elicited by supplements, co-cultures and environmental changes in the culture medium or ECM <sup>16,91-93</sup>. Caballero, *et al.* 2021 studied protrusion formations in stimuli-free 3D MCF-7 cultures in collagen, and resulted in the dynamic formation of small protrusions away from the spheroids after 3 days of culture <sup>94</sup>. Benton, *et al.* 2015 reported substantial invasion of MCF-7 spheroids embedded in collagen-basement membrane extract (BME) gels, cultured in media with 10 % FBS, low pH and low levels of glucose <sup>95</sup>. In fact, low glucose levels have been associated with high glycolysis activity by drug-resistant and invasive tumours <sup>96</sup>. Since the invasive behaviour, can be controlled by molecular and biophysical cues <sup>94</sup>, it was believed that the alginate and collagen type I offered the mechanical support for cell migration and subsequent protrusion formation. This is supported by a recent study conducted by Peng, *et al.* 2022, who formed liver tumour spheroids in alginate capsules <sup>13</sup>, of similar morphology to the MCTSs in **Figure 4. 19D**. After 12 days of culture, they described this eventual morphology, as a ‘tadpole shaped’ cluster and attributed the formation of the shaft-like part to the hydrogel’s ECM inhomogeneities and existence of cell anchoring molecules <sup>13</sup>. In the work presented in this chapter, these anchoring molecules are the collagen type I fibres, which support migration and invasion of tumour spheroids <sup>97</sup>.

Epithelial-to-mesenchymal transition (EMT) refers to the transition of epithelial cells to mesenchymal cells by adopting mesenchymal cells characteristics, including invasive ability, enhanced migration and drug resistance <sup>98</sup>. Han, *et al.* 2022 and earlier studies by Chen, *et al.* 2012, showed MCF-7 spheroid invasion in collagen/polysaccharide complexes, by studying the biomarkers expressed in the instance of EMT. Others have reported that increasing the stiffness of the ECM, for example by increasing the concentration of alginate, also increases the gene expression by EMT <sup>16</sup>. Therefore, the cell-ECM interactions are vital regulators for the growth and fate of cells, including cell morphology and migratory behaviour, which have not been analysed here, but are worth for further investigation.

#### 4.4.6. The ‘Droplet Incubator’ and its applications

eDIB production using 3D-printed microfluidic devices was demonstrated by forming triple emulsion W/O/H/O capsules, aided by the contribution of phospholipid molecules (Chapter II). Part of this thesis aimed to explore the ability to culture breast cancer cells in the hydrogel shell of eDIBs (objective 1), encapsulate a pharmaceutical analogue in the cores (objective 2) and trigger drug release through external means (objective 3). This would essentially formulate a drug screening capsule, termed as “Droplet Incubator (DI)”. The prototype of the DI technology would require a demonstration of all three mentioned objectives in a sequence, but unfortunately this was not completed during the period of this thesis study.

**Figure 4. 20** illustrates the possible stages of an experiment utilising the DI platform in drug screening applications. Firstly, the complex architecture of free-standing DI capsules can be fabricated using droplet-microfluidics technology, which enables high-order emulsion formation and production of eDIBs. The designed DI capsule consists of two distinct parts: the ECM component and the synthetic cell component. For *in-vitro* drug screening applications, the former ensures the survival and perhaps proliferation of living cells in the hydrogel shell of eDIBs, while the latter provides drug encapsulation sites in the form of DIBs. In a cancer cell-containing eDIB/DI capsule, the controlled core release mechanism (LPC protocol from Chapter III) may facilitate the delivery of drug candidates (e.g., anticancer drugs, stimulating growth factors, receptor ligands) to the living cells, and provide post-treatment feedback for further evaluation.

OCCs were earlier studied in the presence of DOX and Tf-488. In a fully formulated eDIB/DI construct, the DOX (anticancer drug) or Tf-488 (ligand) would be encapsulated inside the aqueous cores. At a preferred timepoint of culture (e.g., Day 6 timepoint in **Figure 4. 20**), the LPC would be added externally, triggering the release of the encapsulated DOX or Tf-488. The outcome would constitute of DOX killing or influencing cell proliferation (red fluorescence read-out), while Tf-488 would bind to the transferrin receptors of cancer cells (MCF-7), emitting a green fluorescent signal.

Doxorubicin was initially planned to be utilised as the pharmaceutical analogue to demonstrate the drug screening application of the DI technology. However, the claims by Stephenson and Elvira, 2021, regarding the fast DOX leakage through symmetric and asymmetric DIBs (< 5 min), led to the abandonment of free-DOX encapsulation<sup>99</sup>. During initial timepoints of cell culture, any leaked out concentration of DOX would kill the cells or induce drug resistance<sup>61,70</sup>, which would lead to inconsistent data. Nevertheless, doxorubicin, can be delivered to a diseased tissue in different forms, including lipid or polymer nanocarriers, and not as free-DOX<sup>100</sup>. Therefore, it is hypothesised that larger doxorubicin-laden particles can be encapsulated within the DI synthetic cell component. Unlike the passive diffusion of free-DOX through the membrane of a cell, transferrin ligand uptake depends on receptor-mediated endocytosis<sup>101,102</sup>. Due to this selective recognition and high molecular weight of transferrin ligands (80 kDa), it is unlikely for it to leak through the artificial lipid bilayer, if incorporated

as the aqueous compartment in the eDIB/DI platform<sup>103</sup>. Furthermore, a complete demonstration of the DI capsule, according to this thesis, would require the extracapsular addition of LPC, which would trigger the release of the cores (i.e., drug). The LPC at high concentrations has detergent-like behaviour and can interact with the cell membrane of living cells and cause cell lysis<sup>74</sup>. For this reason, the MCTSs in vesALGCOL OCCs were treated with LPC (Section 4.4.4.2), which would give a perspective of the susceptibility and toxicity induced by LPC concentrations, for future experiments.

The DI capsule presents an interesting, yet underdeveloped technology for drug delivery and screening. The majority of the earlier discussion focused on the DI technology as a drug screening capsule; however, its applications are vast and need to be explored. For example, in artificial cell studies, the ECM and synthetic cell components can allow encapsulation of cell lines and reactions or cell membrane components, respectively. This would convey a programmable capsule which allows co-culture of artificial cell and living cell for studies related to their interactions<sup>29</sup>.

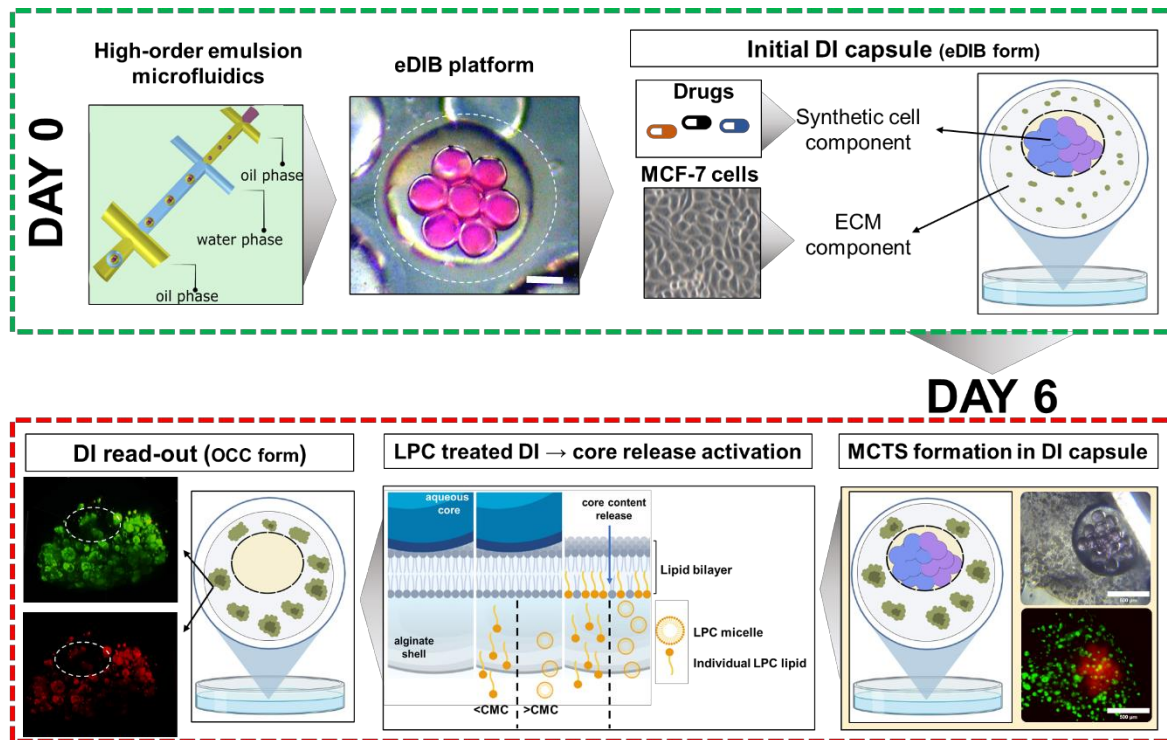


**Figure 4. 20 : Droplet incubator (DI) technology experimental design, summarising cell encapsulation in eDIBs (day 0), cell culture up to a desired timepoint (day 6) and subsequent activation of aqueous core release and subsequent DI readout.** Top: The combination of high-order droplet-microfluidics to produce complex emulsion eDIB capsules, while encapsulating drug candidates in the synthetic cell component and breast cancer cells (green dots) in the ECM component. This generates the initial phase of the DI capsule on day 0. From this point and forward, the stability of the synthetic component is crucial and mandatory. Bottom: At the desired timepoint, for example after multicellular tumour spheroid (MCTSs) formation (light/dark green clusters) in the ECM component, the core release (i.e., treatment initialisation) can be commenced via LPC membrane modulation (core release activation investigated in Chapter III). The experiment comes to an end when the drug is released, leaving behind an empty oil core (dashed-line circles in the DI read-out box) and once the treatment can provide a feedback (readout) in the form of fluorescence (live/dead assays) or culture medium extract traces.

#### 4.5. Conclusion

Single and dual-material 3D Fused Filament Fabrication (FFF) printed microfluidic devices produced single, double (OCCs) and triple emulsion capsules for MCF-7 cell encapsulation. The production and gelation method of the capsules did not induce any noticeable toxicity to the MCF-7 cells. The multicellular tumour spheroids (MCTSs) were favoured by the presence of collagen type I, which was usually observed around the 6<sup>th</sup> day of culture, based on the metabolic assay and tumour area results and analysis. Additionally, cell proliferation and cellular arrangement, indicated a luminal structure in the core of the MCTSs, which recapitulates *in-vivo* growth. The OCCs revealed MCTS with negligible responses to doxorubicin, making them an interesting and attractive model for *in-vitro* 3D culture drug resistance studies. MCTS proliferation in OCCs was enhanced by 100  $\mu$ M lysophosphatidylcholine concentrations, while transferrin ligands were recognised by such spheroids. Furthermore, MCTSs were formed in the hydrogel shell of microfluidically produced encapsulated droplet interface bilayer (eDIB) complex-emulsion capsules. Although, the preservation of the captured DIB throughout the cell culture was challenging. Finally, the Droplet Incubator (DI) model was introduced, which consists of the synthetic cell component for drug analogue entrapment, and the extracellular matrix component for encapsulation and proliferation of living cells. From the discussion of this chapter, the DI technology holds the potential for applications in pharmaceutical delivery and screening, organoid formation, as well as in synthetic biology and artificial cell-living cell interaction studies.

#### 4.6. References

1. Edmondson, R., Broglie, J. J., Adcock, A. F. & Yang, L. Three-Dimensional Cell Culture Systems and Their Applications in Drug Discovery and Cell-Based Biosensors. *Assay and Drug Development Technologies* 12, 207 (2014).
2. Law, A. M. K., Rodriguez de la Fuente, L., Grundy, T. J., Fang, G., Valdes-Mora, F. & Gallego-Ortega, D. Advancements in 3D Cell Culture Systems for Personalizing Anti-Cancer Therapies. *Frontiers in Oncology* 11, (2021).
3. Han, S. J., Kwon, S. & Kim, K. S. Challenges of applying multicellular tumor spheroids in preclinical phase. *Cancer Cell Int* 21, 152 (2021).
4. Rodoplu, D., Sierra Matahum, J. & Hsu, C.-H. A microfluidic hanging drop-based spheroid co-culture platform for probing tumor angiogenesis. *Lab on a Chip* 22, 1275–1285 (2022).
5. Ferreira, L. P., Gaspar, V. M., Mendes, L., Duarte, I. F. & Mano, J. F. Organotypic 3D decellularized matrix tumor spheroids for high-throughput drug screening. *Biomaterials* 275, 120983 (2021).
6. Islas, J. F., Abbasgholizadeh, R., Dacso, C., Potaman, V. N., Navran, S., Bond, R. A., Iyer, D., Birla, R. & Schwartz, R. J.  $\beta$ -Adrenergic stimuli and rotating suspension culture enhance conversion of human adipogenic mesenchymal stem cells into highly conductive cardiac progenitors. *Journal of Tissue Engineering and Regenerative Medicine* 14, 306–318 (2020).
7. Herreros-Pomares, A. et al. 3D printing novel in vitro cancer cell culture model systems for lung cancer stem cell study. *Materials Science and Engineering: C* 122, 111914 (2021).
8. Osuna de la Peña, D. et al. Bioengineered 3D models of human pancreatic cancer recapitulate in vivo tumour biology. *Nat Commun* 12, 5623 (2021).
9. Del Piccolo, N., Shirure, V. S., Bi, Y., Goedegebuure, S. P., Gholami, S., Hughes, C. C. W., Fields, R. C. & George, S. C. Tumor-on-chip modeling of organ-specific cancer and metastasis. *Advanced Drug Delivery Reviews* 175, 113798 (2021).

10. Dornhof, J., Kieninger, J., Muralidharan, H., Maurer, J., Urban, G. A. & Weltin, A. Microfluidic organ-on-chip system for multi-analyte monitoring of metabolites in 3D cell cultures. *Lab Chip* 22, 225–239 (2022).
11. Yu, L., W. Chen, M. C. & C. Cheung, K. Droplet-based microfluidic system for multicellular tumor spheroid formation and anticancer drug testing. *Lab on a Chip* 10, 2424–2432 (2010).
12. Dimitriou, P., Li, J., Tornillo, G., McCloy, T. & Barrow, D. Droplet Microfluidics for Tumor Drug-Related Studies and Programmable Artificial Cells. *Global Challenges* 5, 2000123 (2021).
13. Peng, X., Janicijevic, Z., Lemm, S., Laube, M., Pietzsch, J., Bachmann, M. & Baraban, L. Shell engineering in soft alginate-based capsules for culturing liver tumoroids. Preprint at <https://doi.org/10.22541/au.165830418.86011497/v1> (2022).
14. Liu, C., Lewin Mejia, D., Chiang, B., Luker, K. E. & Luker, G. D. Hybrid collagen alginate hydrogel as a platform for 3D tumor spheroid invasion. *Acta Biomaterialia* 75, 213–225 (2018).
15. Hu, T. & Lo, A. C. Y. Collagen–Alginate Composite Hydrogel: Application in Tissue Engineering and Biomedical Sciences. *Polymers* 13, 1852 (2021).
16. Agarwal, P. et al. Microfluidics Enabled Bottom-Up Engineering of 3D Vascularized Tumor for Drug Discovery. *ACS Nano* 11, 6691–6702 (2017).
17. Chen, Q., Utech, S., Chen, D., Prodanovic, R., Lin, J.-M. & Weitz, D. A. Controlled assembly of heterotypic cells in a core–shell scaffold: organ in a droplet. *Lab Chip* 16, 1346–1349 (2016).
18. Samandari, M., Alipanah, F., Haghjooy Javanmard, S. & Sanati-Nezhad, A. One-step wettability patterning of PDMS microchannels for generation of monodisperse alginate microbeads by in Situ external gelation in double emulsion microdroplets. *Sensors and Actuators B: Chemical* 291, 418–425 (2019).
19. Brower, K. K., Khariton, M., Suzuki, P. H., Still, C., Kim, G., Calhoun, S. G. K., Qi, L. S., Wang, B. & Fordyce, P. M. Double Emulsion Picoreactors for High-Throughput Single-Cell Encapsulation and Phenotyping via FACS. *Anal. Chem.* 92, 13262–13270 (2020).
20. Li, J. et al. Building programmable multicompartment artificial cells incorporating remotely activated protein channels using microfluidics and acoustic levitation. *Nat Commun* 13, 4125 (2022).

21. Zhao, C.-X. Multiphase flow microfluidics for the production of single or multiple emulsions for drug delivery. *Advanced Drug Delivery Reviews* 65, 1420–1446 (2013).
22. Hao, X., Du, T., He, H., Yang, F., Wang, Y., Liu, G. & Wang, Y. Microfluidic Particle Reactors: From Interface Characteristics to Cells and Drugs Related Biomedical Applications. *Advanced Materials Interfaces* 9, 2102184 (2022).
23. Baxani, D. K., Morgan, A. J. L., Jamieson, W. D., Allender, C. J., Barrow, D. A. & Castell, O. K. Bilayer Networks within a Hydrogel Shell: A Robust Chassis for Artificial Cells and a Platform for Membrane Studies. *Angewandte Chemie International Edition* 55, 14240–14245 (2016).
24. Bayoumi, M., Bayley, H., Maglia, G. & Sapra, K. T. Multi-compartment encapsulation of communicating droplets and droplet networks in hydrogel as a model for artificial cells. *Sci Rep* 7, 45167 (2017).
25. Bayley, H., Cronin, B., Heron, A., Holden, M. A., Hwang, W., Syeda, R., Thompson, J. & Wallace, M. Droplet interface bilayers. *Mol Biosyst* 4, 1191–1208 (2008).
26. Martin, N., Douliez, J.-P., Qiao, Y., Booth, R., Li, M. & Mann, S. Antagonistic chemical coupling in self-reconfigurable host–guest protocells. *Nature Communications* 9, 3652 (2018).
27. Elani, Y., Trantidou, T., Wylie, D., Dekker, L., Polizzi, K., Law, R. V. & Ces, O. Constructing vesicle-based artificial cells with embedded living cells as organelle-like modules. *Scientific Reports* 8, 4564 (2018).
28. Godoy-Gallardo, M., Labay, C., Trikalitis, V. D., Kempen, P. J., Larsen, J. B., Andresen, T. L. & Hosta-Rigau, L. Multicompartment Artificial Organelles Conducting Enzymatic Cascade Reactions inside Cells. *ACS Appl. Mater. Interfaces* 9, 15907–15921 (2017).
29. Elani, Y. Interfacing Living and Synthetic Cells as an Emerging Frontier in Synthetic Biology. *Angew Chem Int Ed Engl* 60, 5602–5611 (2021).
30. Alcinesio, A., Krishna Kumar, R. & Bayley, H. Functional Multivesicular Structures with Controlled Architecture from 3D-Printed Droplet Networks. *ChemSystemsChem* 4, e202100036 (2022).
31. Villar, G., Graham, A. D. & Bayley, H. A Tissue-Like Printed Material. *Science* 340, 48–52 (2013).

32. Graham, A. D. et al. High-Resolution Patterned Cellular Constructs by Droplet-Based 3D Printing. *Sci Rep* 7, 7004 (2017).
33. Shao, F., Yu, L., Zhang, Y., An, C., Zhang, H., Zhang, Y., Xiong, Y. & Wang, H. Microfluidic Encapsulation of Single Cells by Alginate Microgels Using a Trigger-Gellified Strategy. *Frontiers in Bioengineering and Biotechnology* 8, (2020).
34. Chen, M., Bolognesi, G. & Vladisavljević, G. T. Crosslinking Strategies for the Microfluidic Production of Microgels. *Molecules* 26, 3752 (2021).
35. Liu, Y., Tottori, N. & Nisisako, T. Microfluidic synthesis of highly spherical calcium alginate hydrogels based on external gelation using an emulsion reactant. *Sensors and Actuators B: Chemical* 283, 802–809 (2019).
36. Nekouei, M. & Vanapalli, S. A. Volume-of-fluid simulations in microfluidic T-junction devices: Influence of viscosity ratio on droplet size. *Physics of Fluids* 29, 032007 (2017).
37. Kalantarifard, A., Alizadeh-Haghighi, E., Saateh, A. & Elbuken, C. Theoretical and experimental limits of monodisperse droplet generation. *Chemical Engineering Science* 229, 116093 (2021).
38. Shi, Y., Ryu, D. D. Y. & Ballica, R. Rheological properties of mammalian cell culture suspensions: Hybridoma and HeLa cell lines. *Biotechnology and Bioengineering* 41, 745–754 (1993).
39. Wahlberg, B., Ghuman, H., Liu, J. R. & Modo, M. Ex vivo biomechanical characterization of syringe-needle ejections for intracerebral cell delivery. *Sci Rep* 8, 9194 (2018).
40. Sutherland, R. L., Hall, R. E. & Taylor, I. W. Cell proliferation kinetics of MCF-7 human mammary carcinoma cells in culture and effects of tamoxifen on exponentially growing and plateau-phase cells. *Cancer Res* 43, 3998–4006 (1983).
41. MCF7 - HTB-22 | ATCC. <https://www.atcc.org/products/htb-22>.
42. Lovitt, C. J., Shelper, T. B. & Avery, V. M. Doxorubicin resistance in breast cancer cells is mediated by extracellular matrix proteins. *BMC Cancer* 18, 41 (2018).
43. Shi, W., Kwon, J., Huang, Y., Tan, J., Uhl, C. G., He, R., Zhou, C. & Liu, Y. Facile Tumor Spheroids Formation in Large Quantity with Controllable Size and High Uniformity. *Sci Rep* 8, 6837 (2018).

44. An, C. et al. Continuous microfluidic encapsulation of single mesenchymal stem cells using alginate microgels as injectable fillers for bone regeneration. *Acta Biomater* 111, 181–196 (2020).
45. Cheng, G., Tse, J., Jain, R. K. & Munn, L. L. Micro-Environmental Mechanical Stress Controls Tumor Spheroid Size and Morphology by Suppressing Proliferation and Inducing Apoptosis in Cancer Cells. *PLOS ONE* 4, e4632 (2009).
46. Zhang, T. et al. One-Step Generation and Purification of Cell-Encapsulated Hydrogel Microsphere With an Easily Assembled Microfluidic Device. *Frontiers in Bioengineering and Biotechnology* 9, (2022).
47. Chignola, R., Schenetti, A., Andrighetto, G., Chiesa, E., Foroni, R., Sartoris, S., Tridente, G. & Liberati, D. Forecasting the growth of multicell tumour spheroids: implications for the dynamic growth of solid tumours. *Cell Proliferation* 33, 219–229 (2000).
48. Wang, E., Wang, D., Geng, A., Seo, R. & Gong, X. Growth of hollow cell spheroids in microbead templated chambers. *Biomaterials* 143, 57–64 (2017).
49. Messier, T. L., Gordon, J. A. R., Boyd, J. R., Tye, C. E., Browne, G., Stein, J. L., Lian, J. B. & Stein, G. S. Histone H3 lysine 4 acetylation and methylation dynamics define breast cancer subtypes. *Oncotarget* 7, 5094–5109 (2016).
50. Teixeira, F. C., Chaves, S., Torres, A. L., Barrias, C. C. & Bidarra, S. J. Engineering a Vascularized 3D Hybrid System to Model Tumor-Stroma Interactions in Breast Cancer. *Frontiers in Bioengineering and Biotechnology* 9, (2021).
51. Swaminathan, S., Hamid, Q., Sun, W. & Clyne, A. M. Bioprinting of 3D breast epithelial spheroids for human cancer models. *Biofabrication* 11, 025003 (2019).
52. Vantangoli, M. M., Madnick, S. J., Huse, S. M., Weston, P. & Boekelheide, K. MCF-7 Human Breast Cancer Cells Form Differentiated Microtissues in Scaffold-Free Hydrogels. *PLoS One* 10, e0135426 (2015).
53. Smart, C. E. et al. In Vitro Analysis of Breast Cancer Cell Line Tumourspheres and Primary Human Breast Epithelia Mammospheres Demonstrates Inter- and Intrasphere Heterogeneity. *PLoS One* 8, e64388 (2013).

54. Kenny, P. A. et al. The morphologies of breast cancer cell lines in three-dimensional assays correlate with their profiles of gene expression. *Mol Oncol* 1, 84–96 (2007).
55. Crowley, P., Stuttgen, V., O’Carroll, E., Ash, S., Buggy, D. & Gallagher, H. Exposure to 60% oxygen promotes migration and upregulates angiogenesis factor secretion in breast cancer cells. *Med Gas Res* 7, 226 (2017).
56. Place, T. L., Domann, F. E. & Case, A. J. Limitations of oxygen delivery to cells in culture: An underappreciated problem in basic and translational research. *Free Radical Biology and Medicine* 113, 311–322 (2017).
57. Al-Ani, A., Toms, D., Kondro, D., Thundathil, J., Yu, Y. & Ungrin, M. Oxygenation in cell culture: Critical parameters for reproducibility are routinely not reported. *PLoS One* 13, e0204269 (2018).
58. Kety, S. S. The theory and applications of the exchange of inert gas at the lungs and tissues. *Pharmacol Rev* 3, 1–41 (1951).
59. Joshi, P. & Lee, M.-Y. High Content Imaging (HCI) on Miniaturized Three-Dimensional (3D) Cell Cultures. *Biosensors* 5, 768–790 (2015).
60. Leshner-Perez, S. C. et al. Dispersible oxygen microsensors map oxygen gradients in three-dimensional cell cultures. *Biomater Sci* 5, 2106–2113 (2017).
61. Czczuga-Semeniuk, E., Wołczyński, S., Dabrowska, M., Dziecioł, J. & Anchim, T. The effect of doxorubicin and retinoids on proliferation, necrosis and apoptosis in MCF-7 breast cancer cells. *Folia Histochemica et Cytobiologica* 42, 221–227 (2004).
62. Fornari, F. A., Randolph, J. K., Yalowich, J. C., Ritke, M. K. & Gewirtz, D. A. Interference by doxorubicin with DNA unwinding in MCF-7 breast tumor cells. *Mol Pharmacol* 45, 649–656 (1994).
63. Lou, P.-J., Lai, P.-S., Shieh, M.-J., MacRobert, A. J., Berg, K. & Bown, S. G. Reversal of doxorubicin resistance in breast cancer cells by photochemical internalization. *International Journal of Cancer* 119, 2692–2698 (2006).
64. Panasci, L. et al. Sensitization to doxorubicin resistance in breast cancer cell lines by tamoxifen and megestrol acetate. *Biochemical Pharmacology* 52, 1097–1102 (1996).

65. Chen, M. C. W., Gupta, M. & Cheung, K. C. Alginate-based microfluidic system for tumor spheroid formation and anticancer agent screening. *Biomed Microdevices* 12, 647–654 (2010).
66. Kim, H.-S., Lee, Y.-S. & Kim, D.-K. Doxorubicin Exerts Cytotoxic Effects through Cell Cycle Arrest and Fas-Mediated Cell Death. *Pharmacology* 84, 300–309 (2009).
67. Gong, X., Lin, C., Cheng, J., Su, J., Zhao, H., Liu, T., Wen, X. & Zhao, P. Generation of Multicellular Tumor Spheroids with Microwell-Based Agarose Scaffolds for Drug Testing. *PLoS ONE* 10, e0130348 (2015).
68. Triantafyllu, U. L., Park, S. & Kim, Y. Fluid Shear Stress Induces Drug Resistance to Doxorubicin and Paclitaxel in the Breast Cancer Cell Line MCF7. *Advanced Therapeutics* 2, 1800112 (2019).
69. Li, Y., Khuu, N., Prince, E., Tao, H., Zhang, N., Chen, Z., Gevorkian, A., McGuigan, A. P. & Kumacheva, E. Matrix Stiffness-Regulated Growth of Breast Tumor Spheroids and Their Response to Chemotherapy. *Biomacromolecules* 22, 419–429 (2021).
70. Nunes, A. S., Costa, E. C., Barros, A. S., de Melo-Diogo, D. & Correia, I. J. Establishment of 2D Cell Cultures Derived From 3D MCF-7 Spheroids Displaying a Doxorubicin Resistant Profile. *Biotechnology Journal* 14, 1800268 (2019).
71. Høyrup, P., Davidsen, J. & Jørgensen, K. Lipid Membrane Partitioning of Lysolipids and Fatty Acids: Effects of Membrane Phase Structure and Detergent Chain Length. *J. Phys. Chem. B* 105, 2649–2657 (2001).
72. Jung, J. H. et al. Inactivation of HDAC3 and STAT3 is Critically Involved in 1-Stearoyl-sn-Glycero-3-Phosphocholine-Induced Apoptosis in Chronic Myelogenous Leukemia K562 Cells. *Cell Biochem Biophys* 67, 1379–1389 (2013).
73. Jantschkeff, P., Schlesinger, M., Fritzsche, J., Taylor, L. A., Graeser, R., Kirfel, G., Fürst, D. O., Massing, U. & Bendas, G. Lysophosphatidylcholine Pretreatment Reduces VLA-4 and P-Selectin-Mediated B16.F10 Melanoma Cell Adhesion In vitro and Inhibits Metastasis-Like Lung Invasion In vivo. *Molecular Cancer Therapeutics* 10, 186–197 (2011).
74. Weltzien, H. U. Cytolytic and membrane-perturbing properties of lysophosphatidylcholine. *Biochimica et Biophysica Acta (BBA) - Reviews on Biomembranes* 559, 259–287 (1979).

75. Colles, S. M. & Chisolm, G. M. Lysophosphatidylcholine-induced cellular injury in cultured fibroblasts involves oxidative events. *Journal of Lipid Research* 41, 1188–1198 (2000).
76. Raynor, A., Jantscheff, P., Ross, T., Schlesinger, M., Wilde, M., Haasis, S., Dreckmann, T., Bendas, G. & Massing, U. Saturated and mono-unsaturated lysophosphatidylcholine metabolism in tumour cells: a potential therapeutic target for preventing metastases. *Lipids Health Dis* 14, 69 (2015).
77. Bao, J. et al. Anti-melanoma activity of *Forsythiae Fructus* aqueous extract in mice involves regulation of glycerophospholipid metabolisms by UPLC/Q-TOF MS-based metabolomics study. *Sci Rep* 6, 39415 (2016).
78. Bi, J. et al. Oncogene Amplification in Growth Factor Signaling Pathways Renders Cancers Dependent on Membrane Lipid Remodeling. *Cell Metabolism* 30, 525-538.e8 (2019).
79. Henriksen, J. R., Andresen, T. L., Feldborg, L. N., Duelund, L. & Ipsen, J. H. Understanding Detergent Effects on Lipid Membranes: A Model Study of Lysolipids. *Biophysical Journal* 98, 2199–2205 (2010).
80. Du, W. et al. Bionano Interactions of MCF-7 Breast Tumor Cells with a Transferrin Receptor Targeted Nanoparticle. *Mol. Pharmaceutics* 12, 1467–1476 (2015).
81. Wymant, J. M., Hiscox, S., Westwell, A. D., Urbé, S., Clague, M. J. & Jones, A. T. The Role of BCA2 in the Endocytic Trafficking of EGFR and Significance as a Prognostic Biomarker in Cancer. *Journal of Cancer* 7, 2388 (2016).
82. Habashy, H. O. et al. Transferrin receptor (CD71) is a marker of poor prognosis in breast cancer and can predict response to tamoxifen. *Breast Cancer Res Treat* 119, 283–293 (2010).
83. Bajbouj, K., Shafarin, J. & Hamad, M. High-Dose Deferoxamine Treatment Disrupts Intracellular Iron Homeostasis, Reduces Growth, and Induces Apoptosis in Metastatic and Nonmetastatic Breast Cancer Cell Lines. *Technol Cancer Res Treat* 17, 1533033818764470 (2018).
84. Elani, Y., Solvas, X. C. I., Edel, J. B., Law, R. V. & Ces, O. Microfluidic generation of encapsulated droplet interface bilayer networks (multisomes) and their use as cell-like reactors. *Chem. Commun.* 52, 5961–5964 (2016).

85. Barriga, H. M. G., Booth, P., Haylock, S., Bazin, R., Templer, R. H. & Ces, O. Droplet interface bilayer reconstitution and activity measurement of the mechanosensitive channel of large conductance from *Escherichia coli*. *J. R. Soc. Interface*. 11, 20140404 (2014).
86. Strutt, R., Sheffield, F., E. Barlow, N., J. Flemming, A., D. Harling, J., V. Law, R., J. Brooks, N., C. Barter, L. M. & Ces, O. UV-DIB: label-free permeability determination using droplet interface bilayers. *Lab on a Chip* 22, 972–985 (2022).
87. Agha, A., Waheed, W., Alamoodi, N., Mathew, B., Alnaimat, F., Abu-Nada, E., Abderrahmane, A. & Alazzam, A. A Review of Cyclic Olefin Copolymer Applications in Microfluidics and Microdevices. *Macromolecular Materials and Engineering* 307, 2200053 (2022).
88. Lin, C.-C. & Anseth, K. S. Cell–cell communication mimicry with poly(ethylene glycol) hydrogels for enhancing  $\beta$ -cell function. *Proc. Natl. Acad. Sci. U.S.A.* 108, 6380–6385 (2011).
89. Reynaud, E. G., Kržič, U., Greger, K. & Stelzer, E. H. K. Light sheet-based fluorescence microscopy: More dimensions, more photons, and less photodamage. *HFSP Journal* 2, 266–275 (2008).
90. SearchLight Spectra Viewer from Semrock. <https://searchlight.semrock.com/?sid=fb57073f-1b45-4517-b25b-2e50432f4db9#>.
91. Ziegler, E., Hansen, M.-T., Haase, M., Emons, G. & Gründker, C. Generation of MCF-7 cells with aggressive metastatic potential in vitro and in vivo. *Breast Cancer Res Treat* 148, 269–277 (2014).
92. Tavianatou, A.-G. et al. Molecular size-dependent specificity of hyaluronan on functional properties, morphology and matrix composition of mammary cancer cells. *Matrix Biology Plus* 3, 100008 (2019).
93. Pal, A. et al. A 3D Heterotypic Breast Cancer Model Demonstrates a Role for Mesenchymal Stem Cells in Driving a Proliferative and Invasive Phenotype. *Cancers (Basel)* 12, 2290 (2020).
94. Caballero, D., Brancato, V., Lima, A. C., Abreu, C. M., Neves, N. M., Correlo, V. M., Oliveira, J. M., Reis, R. L. & Kundu, S. C. Tumor-Associated Protrusion Fluctuations as a Signature of Cancer Invasiveness. *Advanced Biology* 5, 2101019 (2021).

95. Benton, G., DeGray, G., Kleinman, H. K., George, J. & Arnaoutova, I. In Vitro Microtumors Provide a Physiologically Predictive Tool for Breast Cancer Therapeutic Screening. *PLoS ONE* 10, e0123312 (2015).
96. Chong, K.-H., Chang, Y.-J., Hsu, W.-H., Tu, Y.-T., Chen, Y.-R., Lee, M.-C. & Tsai, K.-W. Breast Cancer with Increased Drug Resistance, Invasion Ability, and Cancer Stem Cell Properties through Metabolism Reprogramming. *Int J Mol Sci* 23, 12875 (2022).
97. Brassard-Jollive, N., Monnot, C., Muller, L. & Germain, S. In vitro 3D Systems to Model Tumor Angiogenesis and Interactions With Stromal Cells. *Frontiers in Cell and Developmental Biology* 8, (2020).
98. Kalluri, R. & Weinberg, R. A. The basics of epithelial-mesenchymal transition. *J Clin Invest* 119, 1420–1428 (2009).
99. B. Stephenson, E. & S. Elvira, K. Biomimetic artificial cells to model the effect of membrane asymmetry on chemoresistance. *Chemical Communications* 57, 6534–6537 (2021).
100. Tacar, O., Sriamornsak, P. & Dass, C. R. Doxorubicin: an update on anticancer molecular action, toxicity and novel drug delivery systems. *Journal of Pharmacy and Pharmacology* 65, 157–170 (2013).
101. Aminipour, Z., Khorshid, M., Keshvari, H., Bonakdar, S., Wagner, P. & Van der Bruggen, B. Passive permeability assay of doxorubicin through model cell membranes under cancerous and normal membrane potential conditions. *European Journal of Pharmaceutics and Biopharmaceutics* 146, 133–142 (2020).
102. Ponka, P. & Lok, C. N. The transferrin receptor: role in health and disease. *The International Journal of Biochemistry & Cell Biology* 31, 1111–1137 (1999).
103. Singh, M. Transferrin As A targeting ligand for liposomes and anticancer drugs. *Curr Pharm Des* 5, 443–451 (1999).

## *Chapter V*

### *Concluding remarks*

---

The union of diverse research fields gives birth to novel techniques and applications with increased complexity. As shown in this thesis, my work combines multiple technologies, to devise constructs that incorporate encapsulated Droplet Interface Bilayers (eDIBs)<sup>1,2</sup>, and living cells for applications in drug screening and artificial cell membrane studies. These constructs were formulated using biocompatible compositions and affordable 3D-printed microfluidic fabrication methodologies. This chapter summarises the key research findings towards the development of a hybrid model for co-culturing synthetic cells and living cells, and discusses future work.

#### **5.1. Summary of findings**

##### **5.1.1. Fused Filament Fabricated (FFF) microfluidic devices for single, double, and triple emulsion hydrogel capsules**

Conventional microfluidic device fabrication usually requires a series of assembling steps and surface treatments, particularly for the formation of multiple emulsions<sup>3</sup>. In Chapter II of this thesis, dual-material 3D-printed microfluidic devices were fabricated using two commercially available filaments. Printed blocks of cyclic olefin copolymer (COC) and Nylon exhibited contact angles of 78 ° and 46 °, respectively, supporting the formation of single and multiple emulsions. Initially, single emulsion monodispersed hydrogel capsules of mean diameter 513 µm and a CV of 2 % were produced using a T-junction made of COC and an on-chip gelation method, inspired by the referenced literature<sup>4</sup>. Subsequently, double emulsion microgels with single and multiple oil cores were produced by a double emulsion microfluidic device consisting of a Nylon T-junction and a COC flow-focusing junction. The formation of multi-core, hydrogel-shell capsules using this microfluidic design was achieved by incrementally increasing both the inner oil and alginate flow rates. Following this method, 1-5 oil cores of diameter 340 µm were accurately and reproducibly encapsulated within 1 mm hydrogel capsules.

Chapter II also presents a novel monolithic 3D-printed FFF microfluidic device for the formation of triple emulsion hydrogel capsules without the need for device post-processing. These triple emulsion microfluidic devices (TE-MDs) were used for the generation of gel encapsulated Droplet Interface Bilayers (eDIBs). The eDIB hydrogel constructs of diameter 1-2 mm consisted of a mid-oil droplet (with phospholipids) with inner aqueous cores segregated by a lipid membrane (i.e. droplet interface bilayers, DIBs). The formed oil cores and the inner aqueous cores often had diameters of

approximately 800  $\mu\text{m}$  and 200  $\mu\text{m}$ , respectively. The key challenge that emerged from these triple emulsions during preliminary experiments was the coalescence of the mid-oil phase with the carrier oil phase. This was rectified by using an alginate-liposome mixture, where the liposomes acted as viscosity and surface tension-altering agents <sup>5</sup>.

All the microfluidic devices used here required no post-processing and were ready to use immediately after fabrication. The formation of high-order emulsion hydrogel capsules presents promising results and thus renders dual-material FFF printing as a powerful method for microfluidic device fabrication towards rapid prototype demonstrations. In fact, the successful triple emulsification by FFF 3D-printed microfluidic devices is reported for the first time here. Therefore, the significant and pioneering achievements of Chapter II can be summarized as:

- Dual-material 3D printing of COC and Nylon filaments.
- 3D-printed COC microfluidic devices with improved transparency that enabled in-flow characterisation of droplet formation.
- Double and triple emulsion formation using 3D-printed microfluidic devices without post-fabrication surface treatment.
- Control over the number of oil cores contained within double emulsion hydrogel capsules was achieved.
- Successful encapsulation of droplet interface bilayers (eDIBs) within a gel matrix using triple emulsion microfluidic devices (< 2 mm eDIB capsules).
- Microfluidic on-chip generation of eDIBs was demonstrated using liposomes as an alternative to synthetic surfactants.

### **5.1.2. Characterisation, post-processing and in-situ content release activation from encapsulated Droplet Interface Bilayer synthetic cell interiors**

DIBs present artificial membrane models for the study of cell membrane components, however they are assembled and operated in an oil environment. Further encapsulation of DIBs within a hydrogel material yields compartmentalised constructs, enabling their operation in an aqueous environment. This was demonstrated in Chapter II using the TE-MDs, which devices were also used in Chapter III. Aqueous inner core encapsulation and organisation varied depending on the flow rates, lipid-oil composition and the susceptibility to droplet coalescence, which was either in the form of multiple cores (> 10 cores) of diameter less than 100  $\mu\text{m}$ , or a few cores (< 10 cores) of diameter greater than 200  $\mu\text{m}$ .

Soft, free-standing eDIB constructs were compatible with Optical Coherence Tomography (OCT), which revealed their internal organisation and structure. These eDIB characteristics obtained by the OCT provided insights on the contact angle of the DIBs from different orthogonal views at once, unlike conventional imaging. OCT's capacity to obtain axial images of the samples for 3D image reconstruction offers a fast and attractive method for extracting information towards volumetric imaging

and 3D domain positioning. Therefore, OCT imaging would allow easy and fast image acquisition of multiple eDIBs at once, and when combined with software automated analysis, information could be extracted related to their spatial arrangement.

The stability of eDIBs was tested using centrifugal forces and elevated temperatures. According to the centrifugation experiments ( $39 \times g$  to  $3913 \times g$ ) larger cores were released, while smaller cores in eDIBs remained intact. In fact, the small cores formed very compact DIBs after centrifugation. Insignificant sedimentation of the inner aqueous cores was observed in eDIBs exposed to temperatures above  $50\text{ }^{\circ}\text{C}$ . Temperature and centrifugation offer possible routes to induce release from the interior of eDIBs to the external environment. The key to a programmable drug screening eDIB capsule, includes the control of the encapsulants through microfluidic means, their predictable arrangement within the capsule, as well as the use of an external stimulus that induces content release <sup>6</sup>. This may be investigated by translating the suggestions made by Villar, *et al.* 2013 on their stimuli-responsive multisome model <sup>7</sup>, to the eDIBs.

Chapter III also investigates the susceptibility of eDIBs to lysophosphatidylcholine (LPC) lysolipids that promote surface tension instabilities across the leaflets of a lipid bilayer. Different concentrations ( $1\text{ }\mu\text{M}$ ,  $10\text{ }\mu\text{M}$ ,  $100\text{ }\mu\text{M}$ ,  $300\text{ }\mu\text{M}$ ,  $1000\text{ }\mu\text{M}$ ) were tested to cause the modulation of the phospholipid bilayer and eventual core release. The fluidity of the lipid bilayers, or droplet-hydrogel bilayers (DHBs), was altered by LPC lysolipids presented in the external environment at different rates. The use of LPC for the core release assays was inspired by Strutt, *et al.* 2021, who activated the mechanosensitive channels embedded in asymmetric DIBs using LPC <sup>8</sup>. During the active core content release experiments by lysolipids, it was revealed that the introduction of highly concentrated LPC micelles ( $> 100\text{ }\mu\text{M}$ ) to the surrounding medium of the eDIB, led to the rapid merging of the cores with the hydrogel matrix. Instead, at concentrations close to the critical micelle concentration or CMC ( $10\text{ }\mu\text{M}$ ), the core release was delayed and less apparent, whilst at concentrations much lower than the CMC ( $1\text{ }\mu\text{M}$ ), the cores were sustained within the eDIBs over the study period (10-16 hours). In fact, at  $10\text{ }\mu\text{M}$  LPC the cores of eDIBs endured significant organizational changes, which evidently lead to internal core merging. The practical lysolipid-induced core release experiments were compared to 2D and 3D COMSOL simulations revealing similar core release profiles. Lastly, electrophysiology experiments were conducted on planar LPC-containing DIBs to confirm bilayer modulation occurring within eDIBs, which showed lipid bilayer expansion and possible micelle insertion by the increasing capacitive current and spikes in the current trace, respectively.

In Chapter III, eDIBs were exposed to various environmental conditions, in order to capture their versatility and susceptibility. The main achievements of this chapter are hence summarised below:

- eDIBs are stable for prolonged periods (weeks).
- The internal organisation of eDIBs can be varied from a few large aqueous cores to several small cores.

- OCT can successfully extract information on the internal structure of eDIBs (core number, diameter, contact angle, volume and position).
- eDIBs with small inner aqueous core diameter can withstand strong centrifugal forces and elevated temperatures.
- Aqueous cores release rate from eDIBs was shown to be dependent on the externally introduced LPC concentration and molecular structure.
- LPC promotes membrane expansion at the droplet-hydrogel bilayer (DHB) interface of eDIBs, as confirmed by electrophysiology experiments.

### **5.1.3. From primary to tertiary emulsion microcapsules for tumour-related studies and potential compartmentalised drug screening capsules**

Cell encapsulation and Multicellular Tumour Spheroid (MCTS) formation in alginate-collagen type I microgels has been widely studied by other groups in relation to tumour biology<sup>9</sup>. In Chapter IV, MCF-7 breast cancer cells were encapsulated in the gel phase of single, double and triple emulsion capsules, following the calcium infused-nanoemulsion gelation method<sup>4</sup>. These capsules were fabricated using the FFF-printed dual-material devices developed in Chapter II. It should be noted that, Agarwal, *et al.*, 2017 utilised a gelling nanoemulsion with higher CaCl<sub>2</sub> concentration (20 %) and a microfluidic design with on-chip capsule washing. However, because the devices in this thesis did not integrate a washing step, the final concentration of CaCl<sub>2</sub> was reduced to approximately 10 %, for cell viability reasons<sup>4</sup>. MCF-7 cells exhibited mostly increased viability within these structures.

From the diameter analysis of the single emulsion microgels, it was noticeable that the viscous cell suspension influenced the diameter of the beads and coefficient of variance, which were decreased (approximately to 480 µm) and increased (5.4-5.8 %), respectively, when compared to cell-free capsules. In addition, cell proliferation studies showed that the MCF-7 MCTS formation was favoured by the presence of collagen type I in the alginate matrix and the oil core in double emulsion hydrogel capsules. Light sheet fluorescence microscopy images of the *in-vitro* tumour spheroids exposed their hollow lumen in all compositions and structures, demonstrating *in-vivo* mimicking tumour morphology<sup>10</sup>. An interesting characteristic of oil-core capsules (OCCs) was their floating behaviour, due to the lighter density of the oil-core, suggesting a compelling method towards oxygenation studies of encapsulated cells within OCCs.

Doxorubicin anticancer drug susceptibility differed considerably between the 2D cultures and OCC 3D cultures. The doxorubicin half maximal inhibition concentration (DOX<sub>IC50</sub>) of 2D MCF-7 cultures was 0.84 µM, while no cell death was confirmed on 15-day cultured MCTSs in OCCs, treated with doxorubicin concentrations between 0.01 µM and 20 µM. Furthermore, the lysophosphatidylcholine half maximal inhibition concentration (LPC<sub>IC50</sub>) of 2D MCF-7 cultures was found to be 86.42 µM, but remarkably the MCTSs in OCCs endured different proliferation effects at

various concentrations. Briefly, no metabolic activity was observed after 24 hours with 1000  $\mu\text{M}$  LPC, whilst 100  $\mu\text{M}$  LPC promoted proliferation after 5 days of incubation. Other tested concentrations had no significant effects compared to untreated MCTSs. Increased LPC concentrations usually destabilise the cellular membranes causing cell death, while steady fusion of LPC molecules with the cell surface evidently facilitate cellular proliferation<sup>11</sup>. Mature MCTS in OCCs were also stained with fluorescent transferrin ligands, showing that ligands can diffuse through the hydrogel shell of OCCs and bind to cellular receptors.

Gel encapsulated DIBs can host living cells in the hydrogel shell and artificial membranes in the interior. Sulforhodamine B (sulFB) is a compound used in cell culture colorimetric assays<sup>12</sup>, and was encapsulated in the cores of cell-laden eDIBs. Breast cancer cell (MCF-7) encapsulation in the shell of triple emulsion eDIBs was successful and resulted to the eventual formation of MCTSs. The cores encapsulating sulFB resemble the site for potential anticancer drug (e.g. DOX) encapsulation, hence exploring the eDIB as a drug screening model, or as the introduced ‘Droplet Incubator (DI)’ technology<sup>6</sup>. The DI technology enables the compartmentalisation of multiple entities, including living cells, artificial cell membranes and pharmaceuticals within free-standing microgel capsules.

The DI technology envisions a versatile hybrid platform consisting of a synthetic cell component (interior) and an extracellular matrix (ECM) component (exterior), for studying interactions between encapsulants and living cells. These interactions within the DI model, could facilitate not only *in-vitro* anticancer drug studies, but also cellular differentiation and tumour invasion. This could be achieved by encapsulating growth factors in the aqueous cores, that would change the morphology of the cells<sup>13,14</sup>, after release by external stimulus (e.g. lysolipids). To conclude, the key methods and finding demonstrated in Chapter IV are:

- Cell encapsulation and tumour spheroid formation in single, double and triple emulsion hydrogel capsules generated by monolithic 3D-printed microfluidic devices.
- Alginate-collagen type I and oil-core capsules was shown to give rise to larger spheroids.
- The formulated hydrogel matrices promoted the formation of *in-vivo* mimicking tumour spheroids with hollow lumen.
- Floating oil-core hydrogel capsules offer a unique tissue culture model towards oxygenation studies (hypoxia, normoxia, hyperoxia).
- MCF-7 2D tissue cultures were more susceptible to doxorubicin and lysolipid treatments than 3D cultures in OCCs.
- Cell-laden encapsulated eDIBs as a proposed novel model for drug screening and artificial cell membrane studies, also defined as the ‘Droplet incubator’.

## 5.2. Future work

The following sections discuss short and long term future work. Short-term work can be achieved following methods and protocols described in this thesis along with some optimisation steps. Long-term future work focuses on the incorporation of tools or components, which were not studied in-depth in this thesis and also suggests some end-user applications.

### 5.2.1. Short-term future work

**3D printing using Fused Filament Fabrication (FFF):** Often 3D FFF introduced variability between prints <sup>15</sup>, especially with smaller channel dimensions. This could be minimised by replacing the 0.25 mm nozzle with a smaller printing nozzle (e.g. commercially available 0.1 mm). To demonstrate the flexibility of 3D printing, other filament materials could be used in combination with the print setting of this thesis, to develop microfluidic channels of comparable or enhanced resolution.

**Microfluidically-formed asymmetric phospholipid bilayers:** Throughout this thesis, the lipid bilayer formation between the aqueous cores and the hydrogel shell of eDIBs were assumed to be symmetric, comprising only of DOPC phospholipid molecules, produced by the ‘lipid-out’ approach. Yet, this lipid bilayer could be asymmetric, due to the presence of DPPC lipid vesicles in the aqueous hydrogel phase, therefore a partial ‘lipid-in’ bilayer formation may have occurred during the on-chip emulsification process. However, no evidence was found in this thesis to support such a claim. To determine whether the bilayer is asymmetric or not, the phospholipids within the system may be tagged with fluorescent conjugates <sup>16,17</sup>, to provide visible representation of any possible bilayer asymmetry <sup>18</sup>. Phospholipid bilayer asymmetry is crucial when studying transmembrane pores, pore gating and molecular translocation <sup>19,20</sup>. If future research is able to validate any degree of asymmetry within the formulated eDIBs of this thesis, it may present a new method for the formation of asymmetric encapsulated membrane models using droplet-microfluidics. The eDIB emulsification and asymmetric bilayer formation could also benefit from unilamellar and monodispersed DPPC vesicles, which can be achieved via extrusion methods <sup>21</sup>.

**Controlling the inner aqueous core number and undesired merging within eDIBs:** The number of the encapsulated water cores within the studied eDIBs was not monitored. Artefacts within the first COC component of the triple emulsion microfluidic device led to pressure differences along the fluidic channel, resulting to inconsistent formation of droplet aggregates. Despite this, earlier works have indeed demonstrated to some extent the control of the oil and water cores within larger eDIB capsules <sup>1,2</sup>. Thus, further optimisation of the component responsible for producing the inner aqueous cores, would be beneficial towards controlling the number of encapsulated cores (e.g., maintain one channel diameter dimension or use a straight channel). Following this optimisation step, additional core populations (e.g. other pharmaceutical compounds), can be introduced to the interior (multi-reagent encapsulation). To minimise the merging effect between the aqueous cores, increasing the contact angle

of DIBs and enhancing the energy of adhesion by using certain oils (e.g. silicone oil), could yield more stable and robust eDIBs<sup>22</sup>. Most of the published work on DIB studies, involve silicone oil, however, this thesis focused on the generation of eDIBs using purely hexadecane. The incorporation of silicone oil to the lipid-oil mixture could facilitate faster monolayer formation around water cores and enhance the DIB adhesion forces<sup>7</sup>. In addition to the silicone oil, the success rate of DIBs has been reported to be influenced by the participating synthetic phospholipids, as well as the approach of the DIB formation, whether that is ‘lipid-in’ or ‘lipid-out’<sup>23</sup>. Hence, eDIB stability could be advanced by further exploration of possible compositional routes of the lipid-containing oil.

**Lysolipid-induced core release at room temperature:** All LPC triggered core release protocols from the eDIBs were conducted at 37 °C. It has been reported that lysolipids reduce the phase transition temperature ( $T_m$ ) of phospholipids, such as DPPC below 40 °C<sup>24</sup>. If the DHB was in fact asymmetric as earlier discussed, this would suggest that core release was not solely activated by the fusion of LPC with the lipid bilayer and changes in the membrane tension, but also by the leaky nature of DPPC bilayers (in the presence of LPC) at temperatures close to the  $T_m$ . Hence, it would be wise to validate the LPC experiments with the assay performed at room temperatures.

**Lysolipid-induced core release from cell-laden eDIBs:** Assuming that the inner aqueous core of the eDIBs can be sustained during cell culture, the lysolipids can be introduced to the system to induce the release of the encapsulants (anticancer drugs, growth factors, fluorescent probes). However, the living cells can metabolise the externally introduced lysolipids<sup>25</sup>, hence reducing the concentration of lysolipids that diffuses to the bilayer to promote core release. Experiments are in need to obtain an optimised lysolipid concentration that would activate the encapsulant release, while maintaining cell viability and taking into consideration the consumption of lysolipids by the cells during the incubation period.

### 5.2.2. Long-term future work

**Microfluidics and emulsion formation:** Interesting studies may arise from the controlled encapsulation of water cores and oil cores. For example, Tiribocchi, *et al.* 2021, conducted simulation studies and claimed that increasing the number of inner drops in double emulsions, yields a chaotic droplet arrangement, while at low number of cores (<5), the arrangement of the cores is more predictable<sup>26</sup>. Hence, the microfluidic formation of multiple emulsions is governed by dynamics, which are worth exploring towards functionalised materials with predictable and programmable internal compartment arrangement.

**Scaling down the eDIB construct size:** Further size reduction of the eDIBs closer to the cellular scale (10-100  $\mu\text{m}$ ) could benefit artificial cell studies, due to the more realistic interpretation of the scale. Nevertheless, this would require more sophisticated and high-resolution microfluidic device fabrication methods (e.g. soft lithography using a silicon mask)<sup>3</sup>, than FFF 3D printing<sup>27</sup>. Perhaps a

hybrid approach could be envisaged, where soft lithography is integrated with 3D-printed devices for multiple emulsion production. Alternately, elastomeric microfluidic devices may be fabricated using a negative 3D-printed mask (3D-printed channels can map out the channels of the elastomer), instead of a silicon mask<sup>28</sup>.

**Controlled release from eDIBs:** Other than centrifugation and lipid bilayer instabilities (via lysolipid molecules), temperature, pH and light offer supplementary and attractive methods to induce core release from eDIBs. Attempts were made for integrating photo-switchable lipids with the eDIB system. Although these phospholipids were claimed to be sensitive to red light, they were also sensitive to other wavelengths which contradicted the specificity of the core release. Hence, due to the limited knowledge relating to their properties, they were not further explored. Through the encapsulation of well characterised (from literature) stimuli-responsive agents or phospholipids<sup>29-31</sup>, it is possible to discover new soft matter, smart multisome capsules, as similarly demonstrated in DIBs and DIB networks<sup>32,33</sup>.

**Transmembrane proteins within eDIB capsules:** One of the ambitious plans of this thesis, was the incorporation of mechanosensitive channels (MScL) into eDIBs, which would be activated using low concentrations of LPC. Unlike other widely used protein channels and pores in artificial cell studies (e.g. alpha-hemolysin,  $\alpha$ HL), MScL has a 'closed' and an 'open' state, which would be advantageous for the controlled release of the encapsulants<sup>20</sup>. However, this was not achieved during the given time, but could be further explored.

**Chemically accurate simulation studies:** The transport of diluted LPC species was studied using COMSOL 2D and 3D computation models. Compared to practical experiments, the computational simulations ensured a steady LPC diffusion and release of the cores. However, this was not the case during laboratory practical experiments. In order to develop more realistic computational models, it would be wise to incorporate critical parameters and environmental characteristics, such as the CMC of LPC and adsorption of species and particles to the porous hydrogel<sup>34</sup>. The former could give insights on the rate of LPC fusion down to the bilayer level, while the latter could simulate possible adsorption of LPC to vesicles in the alginate shell. Moreover, the characteristics of the modelled eDIB, such as the shell porosity and thickness, influenced the rate of LPC diffusion quite markedly. Hence, the spatial arrangement of the hydrogel shell and internal cores, as well as the hydrogel porosity, are vital for future eDIB molecular diffusion and kinetic studies and their reproducibility.

**Simplified droplet-hydrogel bilayer electrophysiology experiments:** While the electrophysiology results showed how the LPC amplifies the bilayer area and the current flow, the attempted reconstruction of a DHB in the form of two droplets (gelled DPPC-alginate and LPC micelles), needs to be revisited and simplified. Previously reported eDIB artificial cell chassis models, of approximate diameter 4 mm, have been used in combination with electrophysiology for monitoring transmembrane pores<sup>1</sup>. This suggests that the formulated eDIB of this thesis may also be used to obtain electrical recordings and perhaps study the effect of LPC on the artificial phospholipid membranes

between a hydrogel and a liquid. Moreover, electrophysiology experiments may be conducted on eDIBs with embedded transmembrane pores or channels, towards single molecule artificial cell studies.

**eDIBs as an artificial cell chassis:** Transmembrane pores have been previously embedded in eDIB hydrogel capsules between DIB compartments and the hydrogel shell <sup>1</sup>. Others presented eDIBs in aqueous environments as multisomes, and attained communicating compartments through pore activation <sup>3,35</sup>. Either by passive or active diffusion of molecules, communication routes may be established between the interior and exterior compartments of the eDIB system, aiming to mimic the complex communication routes of natural, living cells. The encapsulation of multiple cellular functionalities within the DIB compartments (e.g. protein expression, biochemical reactions) <sup>3,32</sup>, the incorporation of transmembrane pores for selective diffusion <sup>20</sup>, and participation of sensory probes <sup>36</sup>, gives rise to complex and multi-functional artificial cell models.

**Floating oil-core capsules towards *in-vitro* studies:** *In-vitro* oxygenation studies are often considered unreliable, due to the exposure of cells to unrealistic oxygen levels <sup>37</sup>. A versatile model such as the oil-core capsules investigated in this thesis, offers a hydrogel-based *in-vitro* tumour model that can be employed in a series of oxygenation studies by simply varying the density of the oil, hence controlling the distance of the cells from the air-liquid interface (highly oxygenated region). Therefore, with such floating models it is possible to mimic the *in-vivo* extracellular matrix using certain hydrogels, as well as manipulate oxygen levels, hence moving a step closer to the replacement, reduction and refinement (3Rs) of animal studies <sup>38</sup>.

**Artificial cell and living cell hybridisation studies:** The architecture of the ‘Droplet Incubator’ capsule relies on the eDIB format, which has been described as an artificial cell chassis, since it encloses multiple DIB artificial membranes. The ECM and synthetic cell components of the DI technology are physically connected, hence capable to direct *in-situ* communication between artificial cells of the interior and living cells in the exterior ECM component. It may be argued that the eDIB/DI describes a ‘population hybridisation’ method for artificial cell-living cell communications <sup>39</sup>. However, if the hydrogel shell thickness is minimised (ultrathin shell) <sup>40</sup>, this could immobilise living cells adjacent to the phospholipid membrane, hence interactions between the living cells and artificial cell membranes would be mediated by physical contact, i.e. ‘network hybridisation’. Therefore, the eDIB/DI platforms offer an adjustable hybrid model for the co-culture and possible interface between growing living cells and protocells. Moreover, the DI may be tailored to obtain particular global or local sensitivities (pH, light, temperature, membrane fluidity) to trigger the encapsulant release <sup>41</sup>, but care must be taken in maintaining a robust system and not compromising the DIB stability.

**Tissue culture and engineering applications of the eDIB/DI technology:** Improving the performance and stability of eDIBs would be of great importance with regard to the co-encapsulation of drugs and living cells within the eDIB/DI system. Cell biologists could benefit from the eDIB/DI technology, as it combines biocompatible environments for tissue culture and provides sites for the encapsulation of multiple drugs at once, using microfluidic technologies. In addition, through the

appropriate selection of cell lines, hydrogels and microfluidically-assisted spatial arrangement, the DI may offer a platform for the creation of an organ-in-a-capsule towards tissue engineering applications and implantation in animal studies<sup>42</sup>. Lastly, such constructs can be rendered susceptible and selective to the environment for advanced studies on anticancer drug resistance and antimicrobial resistance. Synthetic tissue-like network construction has also been an approach that groups investigate by combining DIB networks, bioprinting and living cells<sup>43</sup>. For example, Zhou *et al.*, 2020, documented interactions between cerebral cortex cells encapsulated in 3D-bioprinted DIB networks<sup>44</sup>. Finally, recently reported custom-made bioprinting equipment in combination with 3D-printed microfluidic devices<sup>45</sup>, offer the possibility of producing cell-laden eDIB/DI bioprinted proto-tissues.

### 5.3. Concluding statement

To conclude, this thesis studied the formation of simple and multiple emulsion microgels using complex 3D-printed multi-junction microfluidic devices. The encapsulation of living cells in the formulated biocompatible and multiphase encapsulated Droplet Interface Bilayers (eDIBs), offers vast opportunities to exercise in biological applications. These opportunities can range from cancer cells treated with anticancer drugs, to bacteria treated with antibiotics. Encapsulated pharmaceuticals within the interior of eDIB capsules, can be *in-situ* directed and released by environmental stimuli and provide feedback, such as cell death or proliferation. Some end-user applications of the proposed ‘Droplet Incubator’ (DI) technology, but not limited to, are illustrated in **Figure 5. 1**. These include drug delivery and screening, platforms for building bottom-up artificial cells, engineering synthetic tissues for organoid and organ development and finally investigating interactions between artificial and living cells, as a new hybrid approach. Such novel microfluidically-aided technologies adopt increased complexity and precision, which paves the way to mimicking complex living systems and environments using bottom-up design and (bio)engineering.

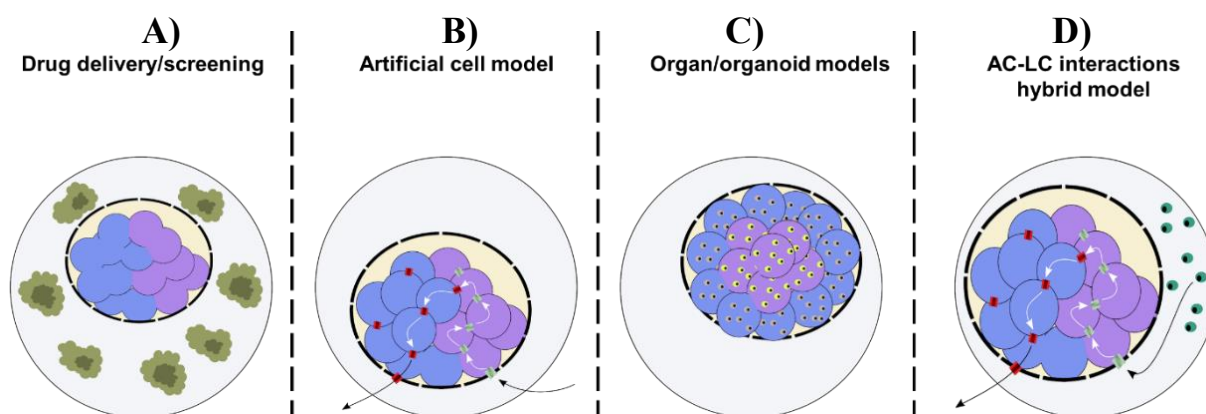


**Figure 5. 1:** Application examples for the ‘Droplet Incubator’ (DI) capsule, where the synthetic cell component (purple and blue cores represent two different populations) and ECM component serve diverse roles. **A)** Cultured tumours in the shell and drug encapsulated in the cores. The drug is released under an external stimulus, serving a drug delivery and screening capsule. **B)** Bottom-up artificial cell chassis, where artificial membranes are embedded with pores creating selective pathways between the exterior environment and the interior. **C)** Organ and organoid tissue engineering by multi-cell line encapsulation within the synthetic cell component (the blue and purple cores resemble two cell lines) or the ECM component (cells in the hydrogel not shown). **D)** A unique hybrid model for artificial cell (AC) and living cell (LC) studies (living cells appear in the ECM hydrogel component).

#### 5.4. References

1. Baxani, D. K. et al. Bilayer Networks within a Hydrogel Shell: A Robust Chassis for Artificial Cells and a Platform for Membrane Studies. *Angewandte Chemie International Edition* 55, 14240–14245 (2016).
2. Li, J. et al. Formation of Polarized, Functional Artificial Cells from Compartmentalized Droplet Networks and Nanomaterials, Using One-Step, Dual-Material 3D-Printed Microfluidics. *Adv Sci (Weinh)* 7, 1901719 (2019).
3. Elani, Y., Solvas, X. C. I., Edel, J. B., Law, R. V. & Ces, O. Microfluidic generation of encapsulated droplet interface bilayer networks (multisomes) and their use as cell-like reactors. *Chem. Commun.* 52, 5961–5964 (2016).
4. Agarwal, P. et al. Microfluidics Enabled Bottom-Up Engineering of 3D Vascularized Tumor for Drug Discovery. *ACS Nano* 11, 6691–6702 (2017).
5. Budai, L. et al. Liposomes for Topical Use: A Physico-Chemical Comparison of Vesicles Prepared from Egg or Soy Lecithin. *Scientia Pharmaceutica* 81, 1151–1166 (2013).
6. Dimitriou, P., Li, J., Tornillo, G., McCloy, T. & Barrow, D. Droplet Microfluidics for Tumor Drug-Related Studies and Programmable Artificial Cells. *Global Challenges* 5, 2000123 (2021).
7. Villar, G. & Bayley, H. Functional Droplet Interface Bilayers. in *Encyclopedia of Biophysics* (ed. Roberts, G. C. K.) 861–868 (Springer, 2013). doi:10.1007/978-3-642-16712-6\_567.
8. Strutt, R. et al. Activating mechanosensitive channels embedded in droplet interface bilayers using membrane asymmetry. *Chem. Sci.* 12, 2138–2145 (2021).
9. Karamikamkar, S., Behzadfar, E. & Cheung, K. C. A novel approach to producing uniform 3-D tumor spheroid constructs using ultrasound treatment. *Biomed Microdevices* 20, 27 (2018).
10. Swaminathan, S., Hamid, Q., Sun, W. & Clyne, A. M. Bioprinting of 3D breast epithelial spheroids for human cancer models. *Biofabrication* 11, 025003 (2019).
11. Margolis, L. B. et al. Lipid-cell interactions: Liposome adsorption and cell-to-liposome lipid transfer are mediated by the same cell-surface sites. *Biochimica et Biophysica Acta (BBA) - Molecular Cell Research* 804, 23–30 (1984).

12. Orellana, E. A. & Kasinski, A. L. Sulforhodamine B (SRB) Assay in Cell Culture to Investigate Cell Proliferation. *Bio Protoc* 6, e1984 (2016).
13. Ruohola, J. K. et al. Enhanced Invasion and Tumor Growth of Fibroblast Growth Factor 8b-overexpressing MCF-7 Human Breast Cancer Cells. *Cancer Research* 61, 4229–4237 (2001).
14. Mehta, P., Rahman, Z., Dijke, P. ten & Boukany, P. E. Microfluidics meets 3D cancer cell migration. *Trends in Cancer* 8, 683–697 (2022).
15. Oropallo, W. & Piegl, L. A. Ten challenges in 3D printing. *Engineering with Computers* 32, 135–148 (2016).
16. Hadorn, M. et al. Specific and reversible DNA-directed self-assembly of oil-in-water emulsion droplets. *Proceedings of the National Academy of Sciences* 109, 20320–20325 (2012).
17. Campàs, O. et al. Quantifying cell-generated mechanical forces within living embryonic tissues. *Nature Methods* 11, 183–189 (2014).
18. Kiessling, V., Wan, C. & Tamm, L. K. Domain coupling in asymmetric lipid bilayers. *Biochimica et Biophysica Acta (BBA) - Biomembranes* 1788, 64–71 (2009).
19. Lee, S. & Bayley, H. Reconstruction of the Gram-Negative Bacterial Outer-Membrane Bilayer. *Small* 18, 2200007 (2022).
20. Li, J. et al. Building programmable multicompartiment artificial cells incorporating remotely activated protein channels using microfluidics and acoustic levitation. *Nat Commun* 13, 4125 (2022).
21. Carroll, J. et al. Liposome Synthesis Protocol: Synthesis of anionic and cationic unilamellar liposome nanoparticles using a thin film dispersed hydration and extrusion method. (2023).
22. Makhoul-Mansour, M. M. & Freeman, E. C. Droplet-Based Membranous Soft Materials. *Langmuir* 37, 3231–3247 (2021).
23. Venkatesan, G. A. et al. Adsorption Kinetics Dictate Monolayer Self-Assembly for Both Lipid-In and Lipid-Out Approaches to Droplet Interface Bilayer Formation. *Langmuir* 31, 12883–12893 (2015).
24. Lu, J., Xu, Y., Chen, J. & Huang, F. Effect of lysophosphatidylcholine on behavior and structure of phosphatidylcholine liposomes. *Sci China C Life Sci* 40, 622–629 (1997).

25. Chai, Y.-C., Binion, D. G. & Chisolm, G. M. Relationship of molecular structure to the mechanism of lysophospholipid-induced smooth muscle cell proliferation. *American Journal of Physiology-Heart and Circulatory Physiology* 279, H1830–H1838 (2000).
26. Tiribocchi, A. et al. The vortex-driven dynamics of droplets within droplets. *Nat Commun* 12, 82 (2021).
27. Mao, M. et al. The Emerging Frontiers and Applications of High-Resolution 3D Printing. *Micromachines* 8, 113 (2017).
28. Mehta, V. & Rath, S. N. 3D printed microfluidic devices: a review focused on four fundamental manufacturing approaches and implications on the field of healthcare. *Bio-des. Manuf.* 4, 311–343 (2021).
29. Lee, Y. & Thompson, D. H. Stimuli-responsive liposomes for drug delivery. *WIREs Nanomed Nanobiotechnol* 9, e1450 (2017).
30. Doroudgar, M., Morstein, J., Becker-Baldus, J., Trauner, D. & Glaubitz, C. How Photoswitchable Lipids Affect the Order and Dynamics of Lipid Bilayers and Embedded Proteins. *J. Am. Chem. Soc.* 143, 9515–9528 (2021).
31. Gispert, I. et al. Stimuli-responsive vesicles as distributed artificial organelles for bacterial activation. *Proc. Natl. Acad. Sci. U.S.A.* 119, e2206563119 (2022).
32. Booth, M. J., Schild, V. R., Graham, A. D., Olof, S. N. & Bayley, H. Light-activated communication in synthetic tissues. *Science Advances* 2, e1600056 (2016).
33. Downs, F. G. et al. Multi-responsive hydrogel structures from patterned droplet networks. *Nat. Chem.* 12, 363–371 (2020).
34. Amin Arefi, S. M., Tony Yang, C. W., Sin, D. D. & Feng, J. J. Simulation of nanoparticle transport and adsorption in a microfluidic lung-on-a-chip device. *Biomicrofluidics* 14, 044117 (2020).
35. Booth, M. J., Cazimoglu, I. & Bayley, H. Controlled deprotection and release of a small molecule from a compartmented synthetic tissue module. *Commun Chem* 2, 1–8 (2019).
36. Cazimoglu, I., Booth, M. J. & Bayley, H. A Lipid-Based Droplet Processor for Parallel Chemical Signals. *ACS Nano* 15, 20214–20224 (2021).

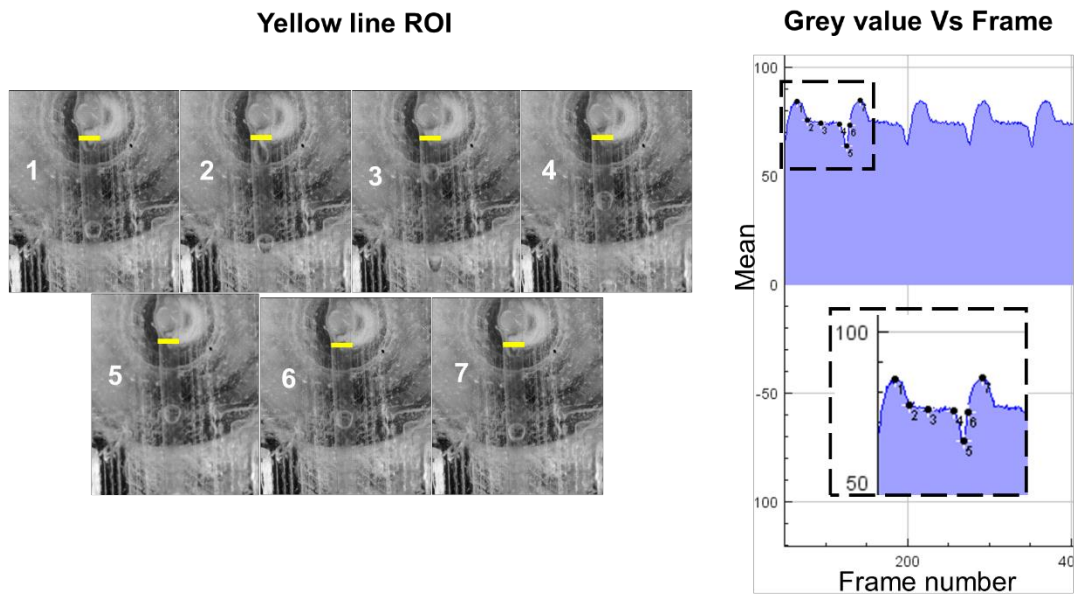
37. Place, T. L., Domann, F. E. & Case, A. J. Limitations of oxygen delivery to cells in culture: An underappreciated problem in basic and translational research. *Free Radical Biology and Medicine* 113, 311–322 (2017).
38. Rao, S. R., Edwards, C. M. & Edwards, J. R. Modeling the Human Bone–Tumor Niche: Reducing and Replacing the Need for Animal Data. *JBMR Plus* 4, e10356 (2020).
39. Elani, Y. Interfacing Living and Synthetic Cells as an Emerging Frontier in Synthetic Biology. *Angew Chem Int Ed Engl* 60, 5602–5611 (2021).
40. Ge, X. et al. Double emulsions with ultrathin shell by microfluidic step-emulsification. *Lab Chip* 21, 1613–1622 (2021).
41. Hindley, J. W., Law, R. V. & Ces, O. Membrane functionalization in artificial cell engineering. *SN Appl. Sci.* 2, 593 (2020).
42. Chen, Q. et al. Controlled assembly of heterotypic cells in a core–shell scaffold: organ in a droplet. *Lab Chip* 16, 1346–1349 (2016).
43. Krishna Kumar, R. et al. Droplet printing reveals the importance of micron-scale structure for bacterial ecology. *Nat Commun* 12, 857 (2021).
44. Zhou, L. et al. Lipid-Bilayer-Supported 3D Printing of Human Cerebral Cortex Cells Reveals Developmental Interactions. *Advanced Materials* 32, 2002183 (2020).
45. Moukachar, A. et al. Development and Evaluation of a Low-Cost LEGO 3D Bioprinter: From Building-Blocks to Building Blocks of Life. *Advanced Materials Technologies* n/a, 2100868 (2023).

---

## *Appendices*

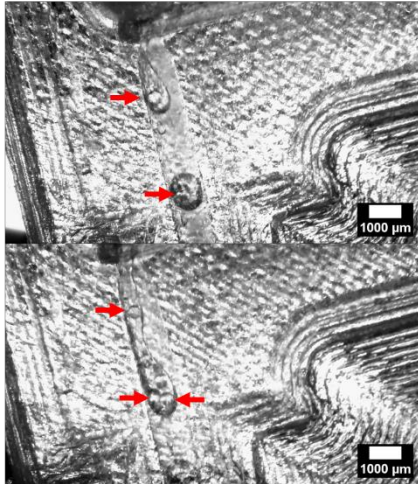
---

**Appendix 2.A.** Droplet Frequency data acquisition. The yellow line indicates the site of the droplet pinch-off. Each image corresponds to a single frame and the generated macro automatically measures the grey value mean intensity across the stack. As the droplet passes through the yellow line ROI, the mean intensity changes and was measured. Each number corresponds to one frame and is noted on the graph plotted by Image J of the grey value Mean intensity Vs the frame number.

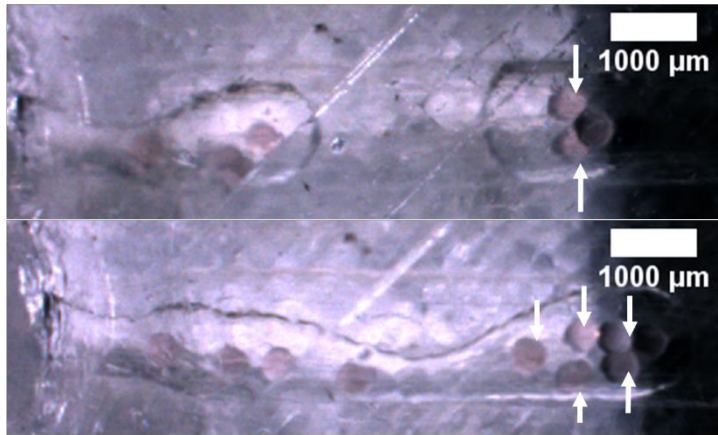


**Appendix 2.B.** Squeezing regime of multi-oil core experiments. The flow rates and experiment execution of the DE-MD for producing multi-core hydrogel capsules. The two experiments (LHS: **Figure 2. 8A** and RHS: **Figure 2. 8B**) established the jetting or squeezing regime at low (top) and high (bottom) OP2 flow rates.

**EXPNT : Figure 2. 8A experiment**



**EXPNT: Figure 2. 8B experiment**



**Appendix 2.C.** Tables that support the results in **Figure 2. 8A-C**. Production of multi-core O/H/O capsules using the DE-MD and the effect of different flow rates on the core encapsulation, SEM, and diameter. (i) Table A: The first experiment, shows that a small increase in the alginate flow rate increased the number of oil cores encapsulated in the alginate (highlighted orange rows). (ii) Table B: The increase of the inner oil phase increased the number of encapsulated oil cores, while the flow rates of alginate and carrier nanoemulsion were kept at 5 ml/hr and 10 ml/hr, respectively. (iii) Table C: Data showing that the incremental increase of the inner oil and alginate phase benefits the control over the core number.

**(i) Table A**

Inner Oil (ml/hr)	Alginate (ml/hr)	Av. Core number based on replicates $\pm$ SEM	Diameter $\pm$ SEM
Continuous carrier phase <b>8 ml/hr</b>			
0.1	2	0.6 $\pm$ 0.1	428.6 $\pm$ 8.5
0.2	2	1 $\pm$ 0	453.4 $\pm$ 15.6
0.3	2	1.8 $\pm$ 0.1	456.3 $\pm$ 13.0
0.4	2	1.4 $\pm$ 0.1	541.6 $\pm$ 11.4
0.5	2	2 $\pm$ 0	527.4 $\pm$ 10.7
0.6	2	2.1 $\pm$ 0.1	569.0 $\pm$ 3.6
0.7	2	2.5 $\pm$ 0.1	544.0 $\pm$ 10.2
0.7	3	3.6 $\pm$ 0.1	494.3 $\pm$ 11.8
0.7	4	3.4 $\pm$ 0.3	465.4 $\pm$ 12.7
0.8	2	2.2 $\pm$ 0.1	559.2 $\pm$ 7.2
0.9	2	2.7 $\pm$ 0.2	571.6 $\pm$ 6.0
1	2	2.4 $\pm$ 0.1	532.5 $\pm$ 7.5

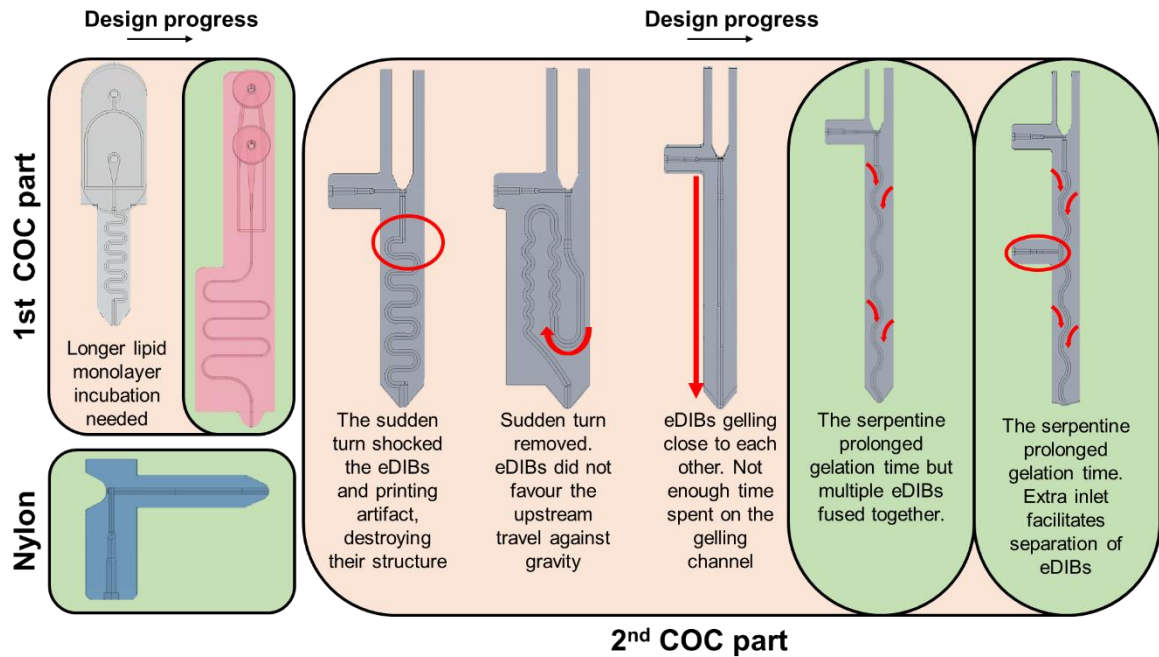
**(i) Table B**

Inner Oil (ml/hr)	Alginate (ml/hr)	Av. Core number based on replicates $\pm$ SEM	Diameter $\pm$ SEM
Continuous carrier phase <b>10 ml/hr</b>			
0.18	5	1 $\pm$ 0	432.4 $\pm$ 7.4
0.2	5	1.3 $\pm$ 0.1	395.1 $\pm$ 11.2
0.28	5	2.4 $\pm$ 0.1	378.2 $\pm$ 6.2
0.3	5	2.4 $\pm$ 0.1	390.0 $\pm$ 6.6
0.4	5	3.3 $\pm$ 0.1	391.7 $\pm$ 4.3
0.5	5	4 $\pm$ 0	423.0 $\pm$ 19.0
0.6	5	6.7 $\pm$ 0.2	323.5 $\pm$ 5.5

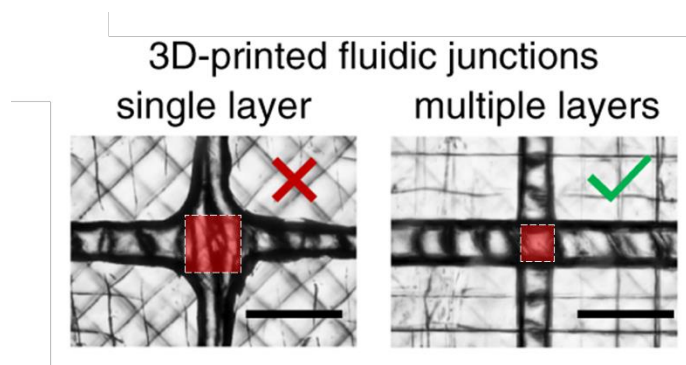
**(i) Table C**

Inner Oil (ml/hr)	Alginate (ml/hr)	Av. Core number based on replicates $\pm$ SEM	Diameter $\pm$ SEM
Continuous carrier phase <b>35 ml/hr</b>			
0.5	5	1 $\pm$ 0	336.0 $\pm$ 3.8
1	6	2 $\pm$ 0	324.7 $\pm$ 4.1
1.5	7.5	3 $\pm$ 0	344.4 $\pm$ 3.1
2.5	8.5	4 $\pm$ 0	362.4 $\pm$ 8.9
4	10	5 $\pm$ 0	354.1 $\pm$ 11.6

**Appendix 2.D.** Optimisation of the TE-MD design. The design progress of the TE-MD direction is from left to right (→). Even though the grey design of the 1<sup>st</sup> COC possessed the two-layer droplet-forming junction (Appendix 2. D), longer incubation of the water droplets in the lipid-containing oil was needed, because of observed merging between aqueous phases, leading to the final pink design. The blue Nylon design, did not change much from DE-MD, but it is mainly shorter. The 2<sup>nd</sup> COC part, facilitated in the gelation of the eDIBs, while maintaining their integrity.



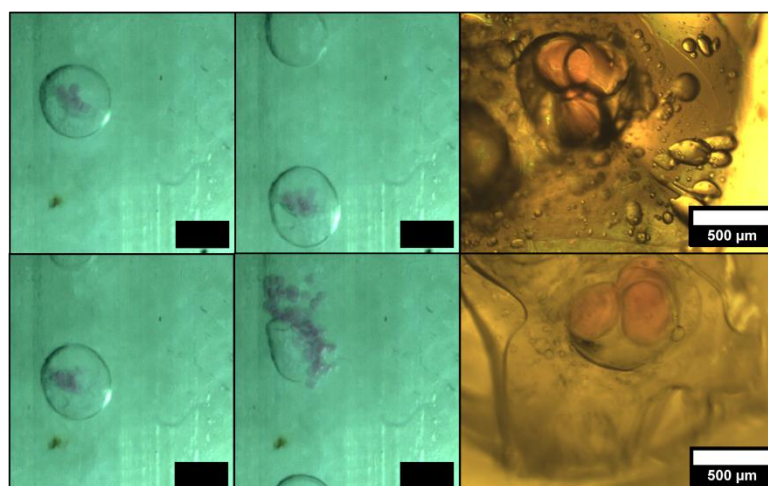
**Appendix 2.E.** Droplet-forming junction of a planar 3D-printed single layer junction and a non-planar two-layered junction. The red marked area, indicates the significant difference between the area of the droplet-forming orifices, which directly influences the size of the internal cores <sup>1</sup>.



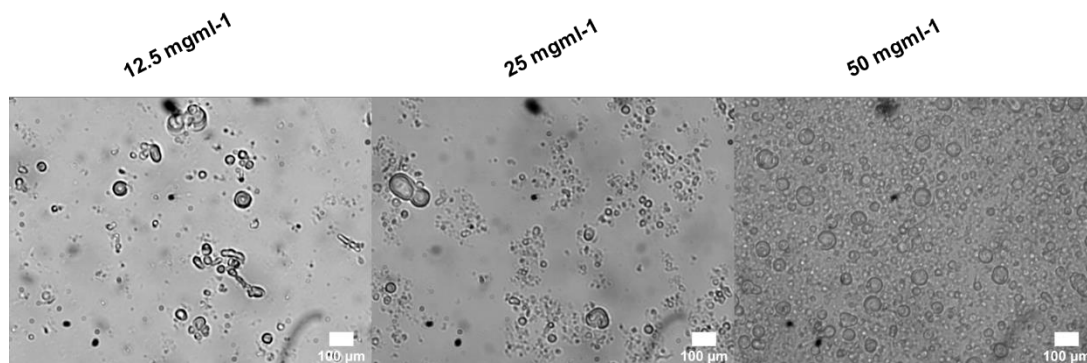
**Appendix 2.F.** Density, viscosity, and surface tension of oils used in this chapter.

	Density (g/mL) at 20 °C	Viscosity (mPa.s) at 20 °C	Surface tension (mN/m) at 20-25 °C
<b>Mineral oil</b>	0.83-0.89 <sup>2</sup>	2.6-14.2 (at 40 °C) <sup>2</sup>	26.1-29.3 <sup>3</sup>
<b>Hexadecane (Hex)</b>	0.77 <sup>4</sup>	3.4 <sup>4</sup>	27.4-28.1 <sup>5</sup>
<b>Silicone oil AR 20</b>	1.01 <sup>6</sup>	20 <sup>6</sup>	20.6 <sup>6</sup>

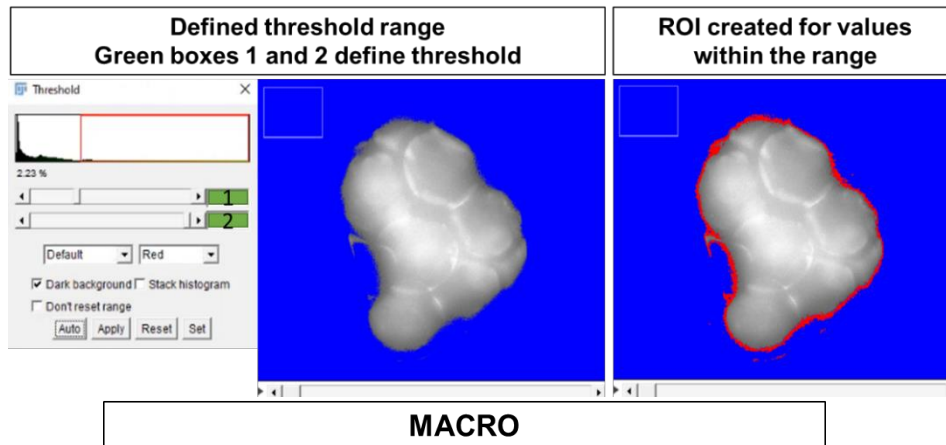
**Appendix 2.G.** eDIB formation with 1% Tween 20. Successful eDIB formation was achieved by adding 1% of synthetic surfactant in alginate. The eDIBs were produced using the TE-MD with only OC3. Although the eDIB formation was successful, their integrity was compromised. After consideration and efforts to avoid such surfactants, this concentration was converted to a concentration of DPPC and was slowly reduced until successful eDIB were formed at a low DPPC concentration.



**Appendix 2.H.** Microscopy images of different DPPC vesicle concentrations in buffer: DPPC vesicles were produced as mentioned in section 2.3.5.



**Appendix 3.A.** Thresholding method using the following Macro for intensity measurements only within the defined range, i.e., only fluorescent cores. Running the Macro below, lets the user define a threshold range to be applied through the whole stack of images. Depending on the threshold range, an ROI is created for each stack image, around the area that lies within the threshold range (red line around fluorescent cores). Subsequently the ROI areas and intensities are automatically measured.



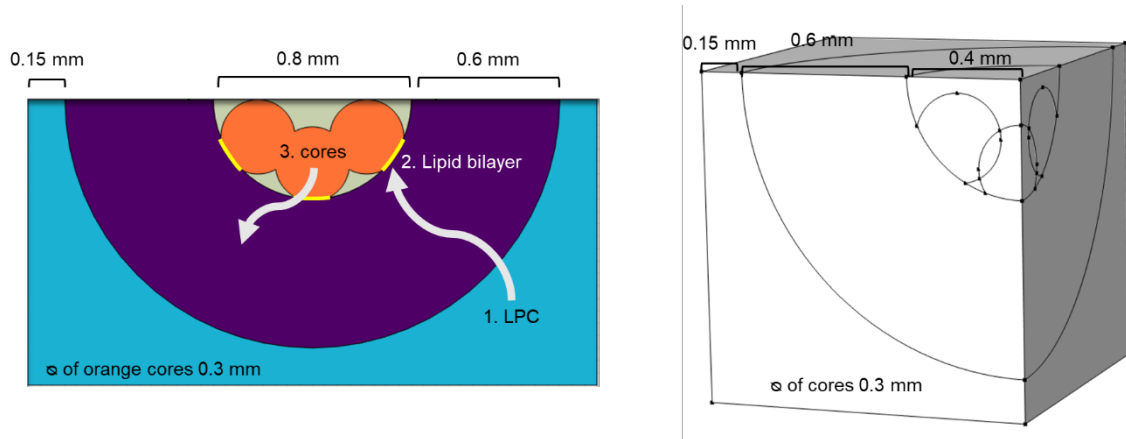
```

1  /* Define the intensity threshold range (45-255 in this case)
2  * The minimum intensity is measured at points where the intensity is between the defined values
3  */
4  run("Threshold...");
5  msga = "Set threshold values then click OK ";
6  waitForUser(msga);
7  /*The following command will run the function "Analyze Particles"
8  * Based on the defined threshold values it will find the edges of the area to analyse.
9  * If there is a stack open, it will analyse all of the slices
10 * and add the measured area to the ROI manager
11 */
12 run("Analyze Particles...", "size=0-infinity show=Masks stack");
13 rename("Mask");
14 n = getSliceNumber();
15 while (getSliceNumber()<nSlices){
16 run("Create Selection");
17 type = selectionType();
18 if (type==1)
19 run("Next Slice [>]");
20 else
21 roiManager("Add");
22 run("Next Slice [>]");}
23 run("Create Selection");
24 type = selectionType();
25 if (type==1)
26 run("Next Slice [>]");
27 else
28 roiManager("Add");
29 selectWindow("Mask");
30 close();
31 //selectWindow(name);
32 //resetThreshold();
33 msga = "Scroll through ROI manager to check segmentation of enamel. Click OK to see results.";
34 waitForUser(msga);
35 roiManager("Deselect");
36 //run("Set Measurements...", "area mean standard redirect=None decimal=1");
37 //roiManager("Measure");
38 //close();
39
40

```

**Appendix 3.B.** Additional information on the COMSOL computational simulations.

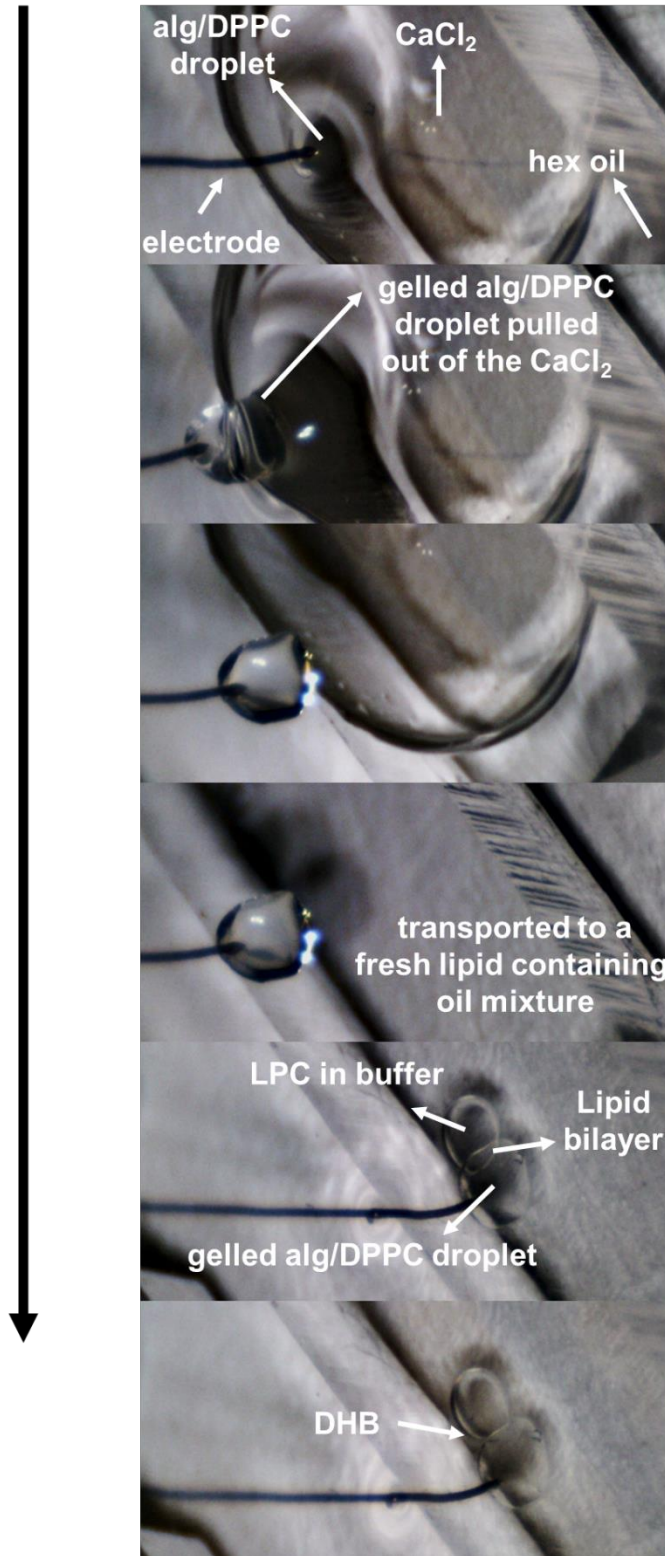
**A.** Dimensions of the 2D (LHS) and 3D (RHS) COMSOL model geometries.



**B.** To activate the release of the core's species  $c$  (orange cores in **A.**) through the lipid bilayers, a step function was created as shown below. This step function was imported in the diffusion coefficient of the species  $c$ , within the 'Thin diffusion barrier' boundary conditions, which represents the lipid bilayers. Hence, at this boundary conditions a relationship was created between the local concentration of LPC added to the exterior and the rate of the transport of species  $c$  through the bilayer. This dependent on the assigned threshold and the transition was set to 0.1 (this value is commonly used).

$$\text{step function location} = \text{threshold} + \frac{\text{transition}}{2}$$

**Appendix 3.C.** Method for gelling an alginate droplet on the electrode for DHB electrophysiology experiments.



**Appendix 3.D.** Light sensitive phospholipids.

In the interest to fabricate light sensitive eDIBs, a collaboration was initiated with Prof. Matthew Langton at Oxford University. Some of their work focuses on synthesis of light-sensitive lipids (redAzoPC), with structures similar to Chander, *et al.* 2021 and Morgan, *et al.* 1987<sup>7,8</sup>. By modifying the structure of the lipids, they claimed they were able to make them sensitive to specific wavelengths. As shown in the molecular structure below (**1A**), the lipids have two azobenzene bonds, N=N. If this molecule is exposed to red light with wavelengths around 625 nm, the azobenzene bonds will bend (Z-state). If then they are exposed to blue light of wavelength around 455 nm, the azobenzene bonds will return to their initial straight state (E-state).

Usual experiments with such lipids are conducted in liposomes, but their incorporation in the eDIB system was not able to work consistently. The lipid composition utilised for the experiments was 90 % DPPC and 10 % redAzoPC, as instructed, by the chemist who synthesised the lipids. For redAzoPC in a lipid-containing hexadecane phase, the following was prepared: 10 mM of 90% DPhPC and 10% redAzoPC in hexadecane. The use of silicone oil, would cause the lipids to crash (for unknown reason), as shown in **1B** below. For redAzoPC in lipid-containing buffer phase, to mix with alginate, the following was prepared: 1 mM of lipids, 90% DPhPC and 10% redAzoPC in buffer.

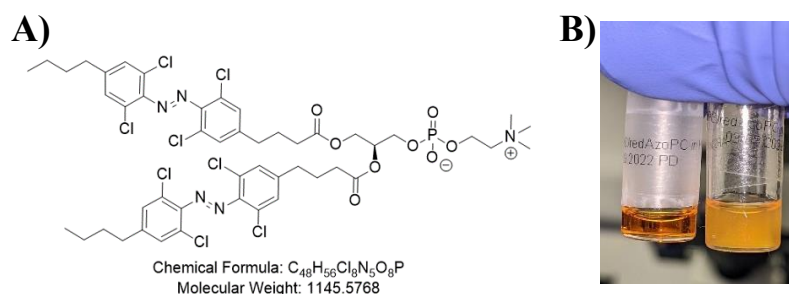


**Figure 3.D. 1:** **A)** The redAzoPC of molecular weight 1145.56 g/mol, in the E-state **B)** 10 mM 10% redAzoPC, 90% DPPC in 100 % hexadecane (LHS) and in 60 % hexadecane and 40 % silicon oil (RHS).

According to the team in Oxford the redAzoPC lipids were delivered in the E-state. To ensure that the lipids are in the E-state the lipids were exposed to UV light for 10 minutes prior to experiments. After performing the experiment 3 times, only 1 out of 3 showed leakage under the exposure to red light. This was not reliable because number of samples were limited. As shown in **Figure 3.D. 3A**, the redAzoPC lipids phase separate (orange particles). This occurred in the syringe and the vial, in which the lipids were in hexadecane oil or in buffer. In order for the lipids to not separate from the rest of the solution, they had to be warmed up at  $> 40\text{ }^{\circ}\text{C}$  and vortexed well. If left alone, they would separate from the rest of the solution quickly as the temperature dropped. **Figure 3.D. 3**, shows the experimental setup for the red light exposure tests (all the equipment were purchased from RS). RedAzoPC lipids in the mid-oil core, when

exposed to the red light, some rearrangement was shown, but the reason was unclear (**Figure 3.D. 2A**). The only successful experiment where there was a small indication of core release under red light exposure, is shown in (**Figure 3D.3B**).

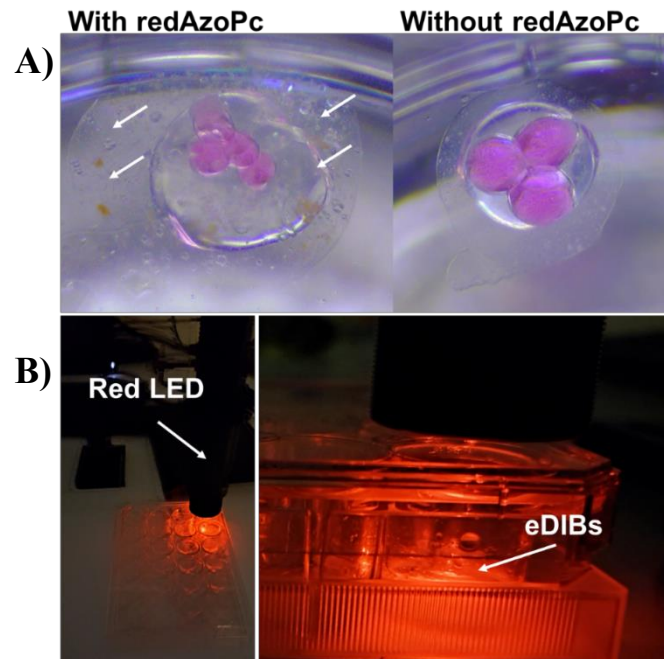


**Figure 3.D. 3: Experimental setup for red light exposure experiments.** *A) eDIBs produced using 90% DPPC and 10% redAzoPC in alginate/vesicle shell phase (LHS) or 100% DPPC vesicles (RHS). B) Red light exposure setup with eDIBs in a well plate. The LED was 5 -8 mm away from the top of the well plate. The LED light was slightly collimated, using a 100 mm lens and tubing.*

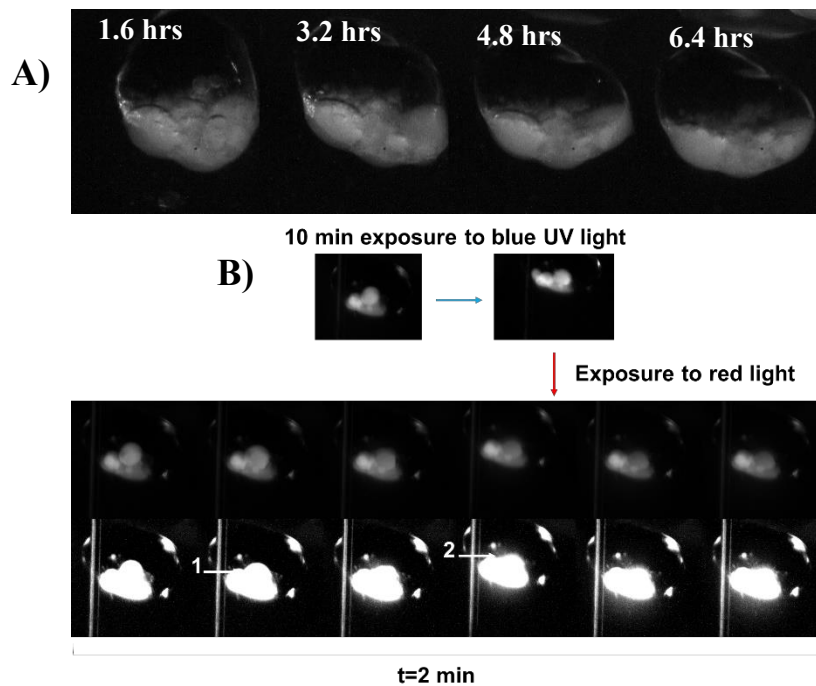
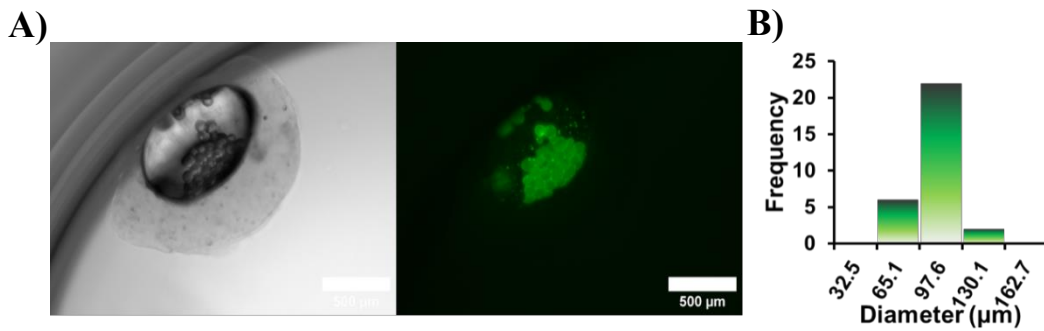


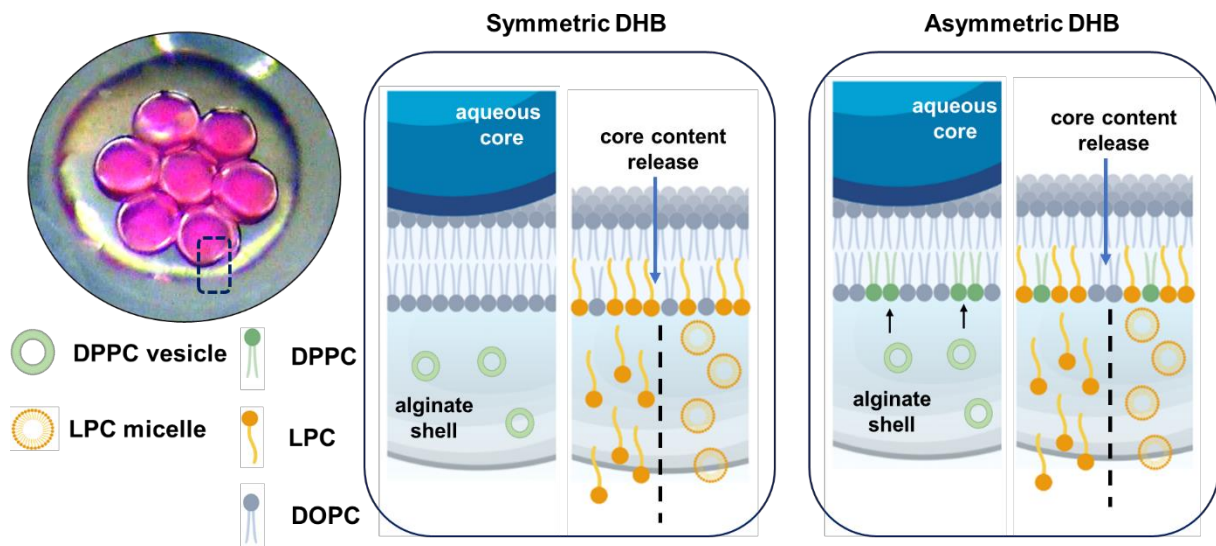
**Figure 3.D. 4: eDIBs formed with redAzoPC.** *A) 10% redAzoPC, 90% DPhPC in hexadecane as the mid-oil core. B) 10% redAzoPC, 90% DPPC the alginate shell solution. eDIBs were exposed to UV for 10 min and then exposed to red light for 1-2 hours. No fluorescence around the cores, 2. Some fluorescence around the core. The size of visible oil cores is 500-700  $\mu\text{m}$  in diameter.*

**Appendix 3.E.** A) BF and GFP images of eDIBs encapsulating quenched calcein dye in buffer at 70 mM. B) Histogram shows the distribution of the inner core sizes.



**Appendix 3.F.** Probable symmetric (DOPC) and asymmetric (DOPC/DPPC) droplet-hydrogel bilayer (DHB) formed within the microfluidically produced eDIB.

The following figure illustrates the symmetric and asymmetric bilayers, before and after the insertion of LPC monomers (<CMC) or fusion of micelles (>CMC). Top left: eDIB with pink sulfB cores with a box that locates a DHB. The asymmetric DHB is a result of DPPC vesicle fusion with the lipid bilayer before complete gelation. Core content release is achieved after the addition of LPC (monomers or micelles) and fusion with the lipid bilayer.



**Appendix 3.G.** Chung-Kennedy filtration of data.

The following macro was utilised to filter noisy DIB electrophysiology current, where  $K$  is the maximum forward/backward moving average filter length (samples),  $M$  is the prediction error analysis window size (samples) and  $p$  is the positive scaling of prediction error. For the filtration of the electrophysiology data in this Chapter, the inputs were set to  $K=400$ ,  $M=50$  and  $p=50$ . The code was adapted from Little, *et al.* 2011<sup>9</sup>, and by a colleague.

**Matlab code**

```
function CK_filtered_current = ckfilter_HB(current, K, M, p);

narginchk(4,4);

N = length(current);
prior = 1/(2*K);

xf = zeros(N,K);
xb = zeros(N,K);

% Create forward and backwards filters of length L = 1,2..K
L = (1:K)';
for k = (K+1):(N-K-1)
    xf(k,:) = cumsum(current(k+1:k+K))./L;
    xb(k,:) = cumsum(current(k-1:-1:k-K))./L;
end

CK_filtered_current = current;

for k = (max(K,M)+1):(N-max(K,M)-1)

    yb = repmat(current(k-M+1:k),1,K);
    yf = repmat(current(k:k+M-1),1,K);

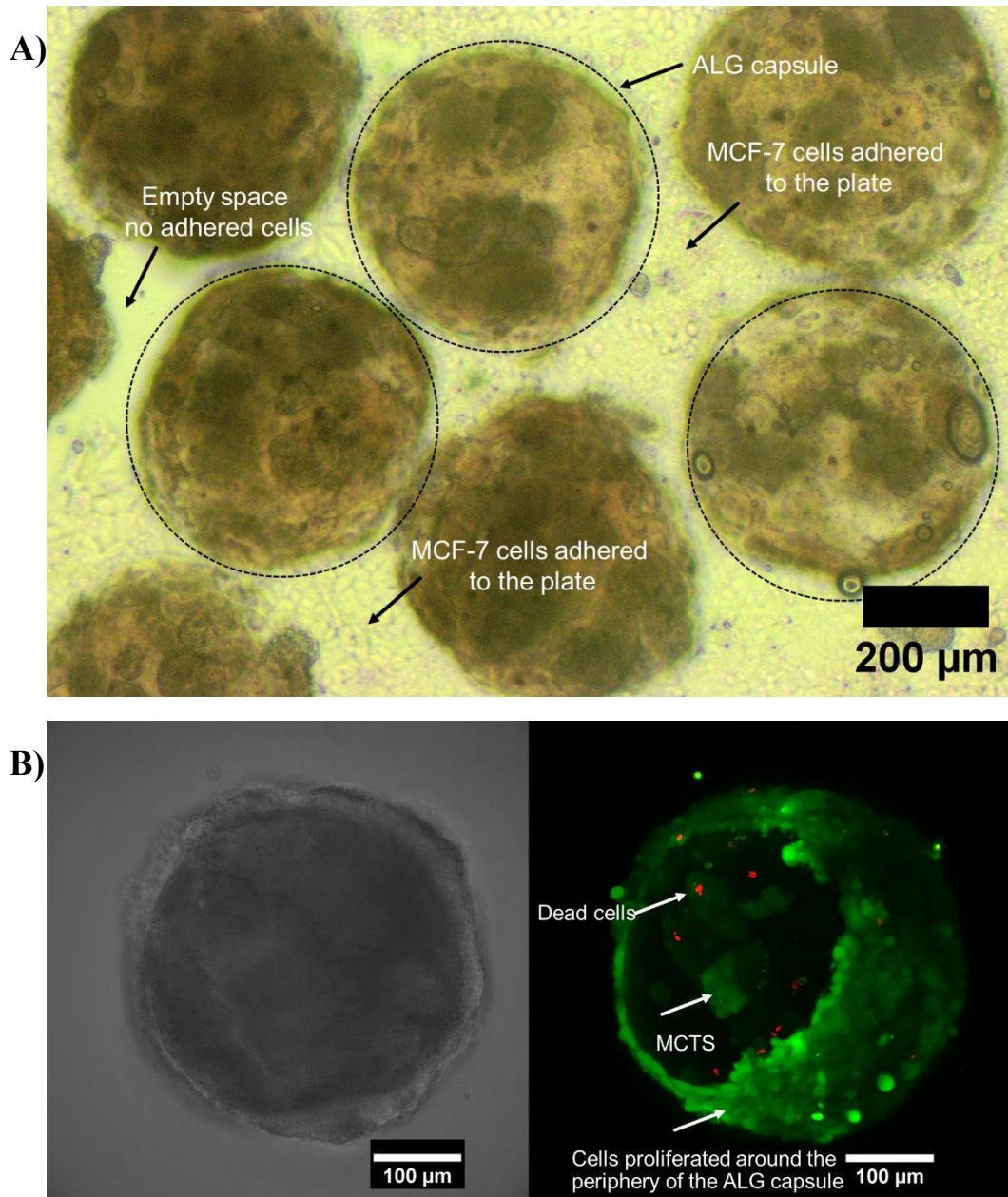
    f = prior*sum((yb-xf(k-M+1:k,:)).^2).^(-p);
    b = prior*sum((yf-xb(k:k+M-1,:)).^2).^(-p);

    if (any(isinf(f)))
        f(isinf(f)) = 1;
        f(~isinf(f)) = 0;
    end
    if (any(isinf(b)))
        f(isinf(b)) = 1;
        f(~isinf(b)) = 0;
    end

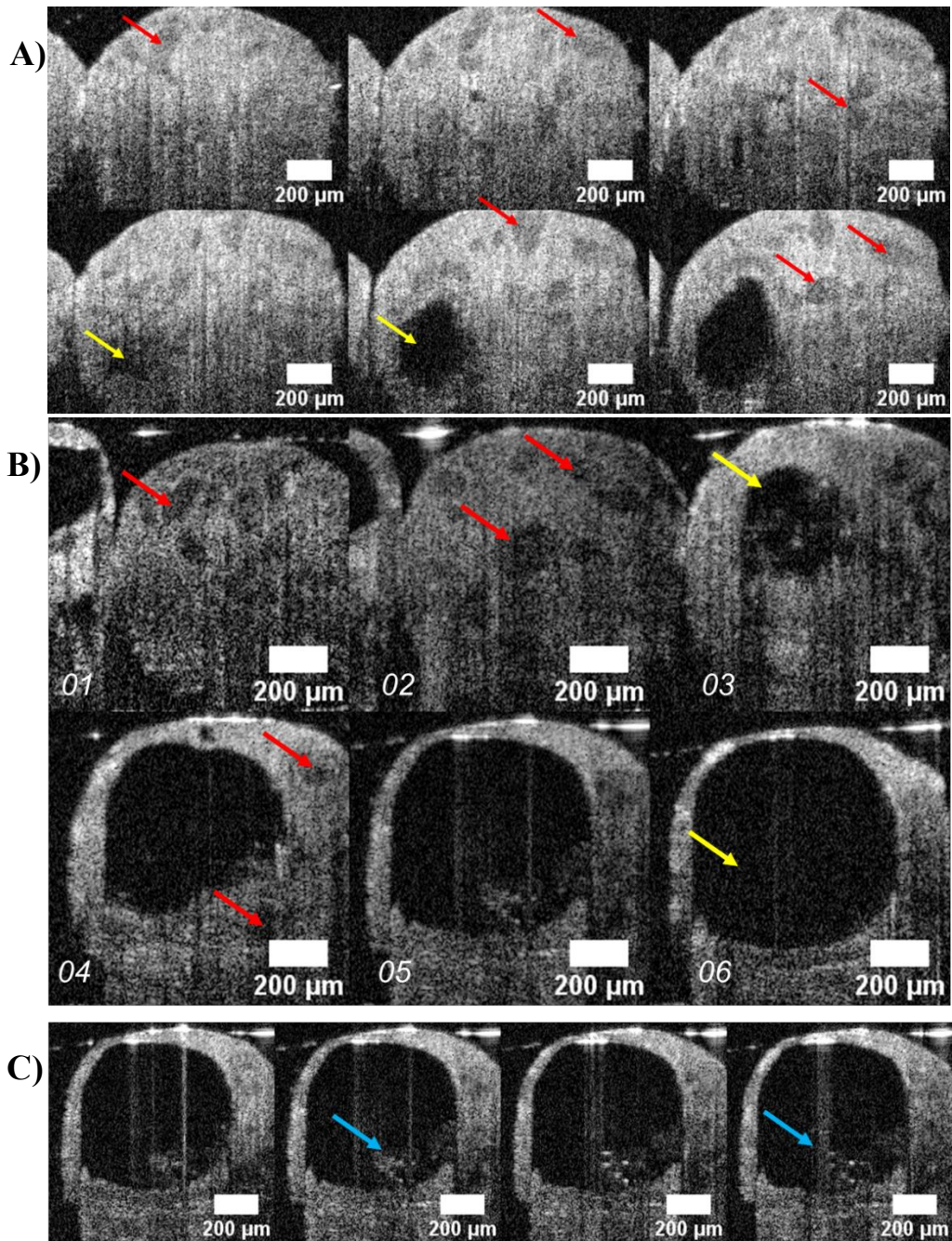
    fb = sum(f+b);
    f = f/fb;
    b = b/fb;

    CK_filtered_current(k) = f*xf(k,:)' + b*xb(k,:);
end
```

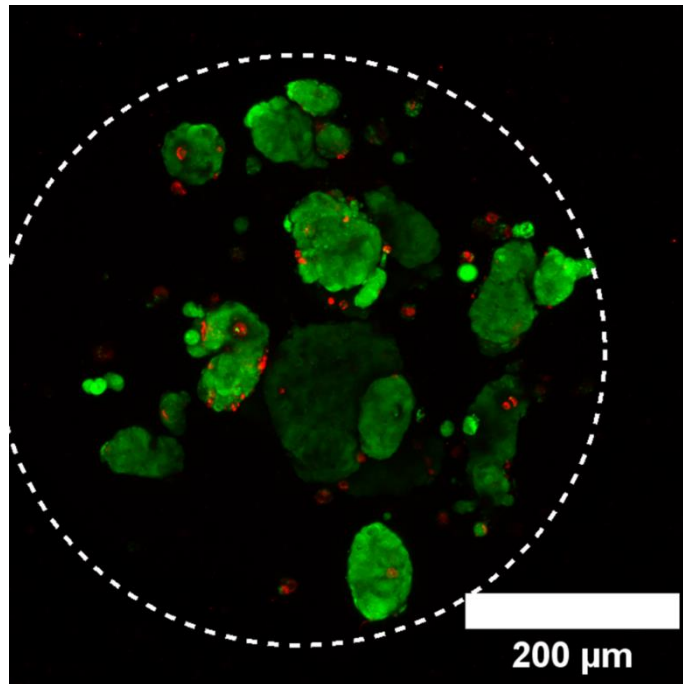
**Appendix 4.A.** Cell migration into the tissue culture substrate. Figure **A)** MCF-7 cell adhered to the tissue culture flask after they migrated away from the ALG capsules (Day 15). Initial sign of this behaviour was seen around 10 days after encapsulation. Figure **B)** Z-stack projection LSM image of ALG capsules on Day 15, showing MCF-7 cells migrated all around the periphery of the capsules, however some MCTSs can be visualised at the centre of the capsule.



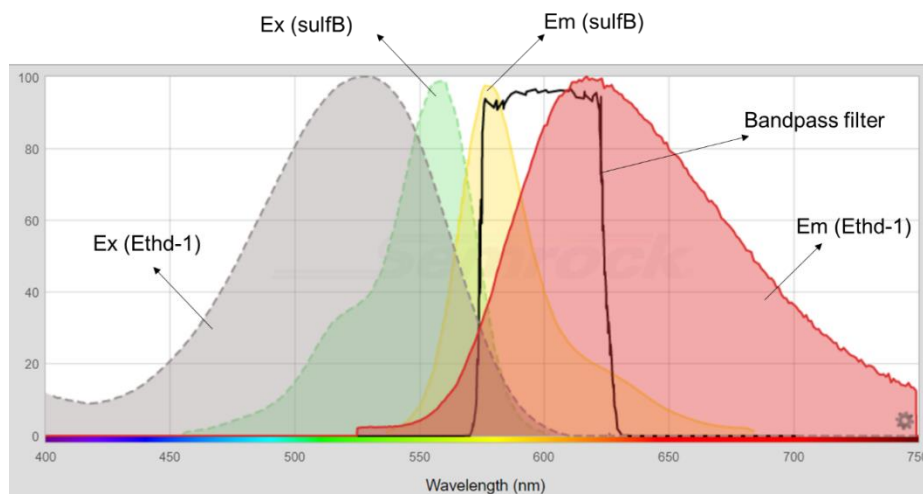
**Appendix 4.B.** OCT imaging of veALGCOL OCCs or eDIBs with MCF-7 tumour spheroids after 28 days of culture. OCT imaging was performed as described in Chapter 3, Section 3.1.2. Figure A) Yellow arrows indicate the oil core and red arrows note MCTSs. Spacing between each montaged (z01-z06) image is 12  $\mu\text{m}$ . Figure B) Yellow arrows indicate the oil core, red arrows note MCTSs. Spacing between each montaged image is 40  $\mu\text{m}$ . Figure C) Blue arrows possibly show aqueous cores. Spacing between each montaged image is 4  $\mu\text{m}$ .



**Appendix 4.C.** Example of image (z-projection) obtained using laser confocal microscopy (200  $\mu\text{m}$  depth, z-slicing 6  $\mu\text{m}$ ) showing high resolution MCTSs. Figure shows ALGCOL capsules imaged 11 days after encapsulation of MCF-7. Live cells appear green and dead cells appear red after staining with the live/dead cytotoxicity assay reagents (Calcein-AM and EthD-1). The white dashed line notes the boundary of the capsule. This capsule was immobilised on a confocal microscopy dish with alginate 1% and 0.2 M  $\text{CaCl}_2$ .



**Appendix 4.D.** Excitation emission spectra of SulfB and EthD-1. The bandpass filter used during LSFM is also indicated. The image was obtained from Searchlight Spectra Viewer from Semrock <sup>10</sup>).



***Appendices References***

1. Li, J. et al. Building programmable multicompartment artificial cells incorporating remotely activated protein channels using microfluidics and acoustic levitation. *Nat Commun* 13, 4125 (2022).
2. Bertrand, Y. & Hoang, L. C. Vegetable oils as substitute for mineral oils. in *Proceedings of the 7th International Conference on Properties and Applications of Dielectric Materials* (Cat. No.03CH37417) vol. 2 491–494 vol.2 (2003).
3. Mendonça, C. G. de, Raetano, C. G. & Mendonça, C. G. de. Surface tension of mineral oils and vegetable oils. *Eng. Agríc.* 27, 16–23 (2007).
4. Hardy, R. C. Viscosity of n-Hexadecane. (Department of Commerce, National Bureau of Standards, 1958).
5. Rolo, L. I., Caço, A. I., Queimada, A. J., Marrucho, I. M. & Coutinho, J. A. P. Surface Tension of Heptane, Decane, Hexadecane, Eicosane, and Some of Their Binary Mixtures. *J. Chem. Eng. Data* 47, 1442–1445 (2002).
6. Bazyar, H., Javadpour, S. & Lammertink, R. G. H. On the Gating Mechanism of Slippery Liquid Infused Porous Membranes. *Advanced Materials Interfaces* 3, 1600025 (2016).
7. Morgan, C. G., Thomas, E. W., Sandhu, S. S., Yianni, Y. P. & Mitchell, A. C. Light-induced fusion of liposomes with release of trapped marker dye is sensitised by photochromic phospholipid. *Biochim Biophys Acta* 903, 504–509 (1987).
8. Chander, N., Morstein, J., Bolten, J. S., Shemet, A., Cullis, P. R., Trauner, D. & Witzigmann, D. Optimized Photoactivatable Lipid Nanoparticles Enable Red Light Triggered Drug Release. *Small* 17, 2008198 (2021).
9. Little, M. A., Steel, B. C., Bai, F., Sowa, Y., Bilyard, T., Mueller, D. M., Berry, R. M. & Jones, N. S. Steps and Bumps: Precision Extraction of Discrete States of Molecular Machines. *Biophysical Journal* 101, 477–485 (2011).
10. SearchLight Spectra Viewer from Semrock. <https://searchlight.semrock.com/?sid=fb57073f-1b45-4517-b25b-2e50432f4db9#>.